Universidad de Granada

Departamento de Electrónica y Tecnología de Computadores

Analysis and characterization of pMOSFET as dosimetric sensor

Tesis Doctoral

María Sofía Martínez García

Editor: Editorial de la Universidad de Granada
Autor: María Sofía Martínez García
D.L.: GR 2224-2014
ISBN: 978-84-9083-297-4

Universidad de Granada

Departamento de Electrónica y Tecnología de Computadores

Análisis y caracterización del pMOSFET como sensor dosimétrico

Tesis Doctoral

María Sofía Martínez García

Miguel Ángel Carvajal Rodríguez y Jesús Banqueri Ozáez, profesores Titulares de Universidad, ambos del Departamento de Electrónica y Tecnología de Computadores de la Universidad de Granada,

CERTIFICAMOS:

Que el trabajo de investigación recogido en la presente memoria, titulada "Análisis y caracterización del pMOS como sensor dosimétrico", y presentada por María Sofía Martínez García para optar al grado de Doctor por la Universidad de Granada, ha sido realizado en su totalidad bajo nuestra dirección en el Departamento de Electrónica y Tecnología de Computadores de la Universidad de Granada.

Granada, Noviembre de 2014

Dr. Miguel Ángel Carvajal Rodríguez	Dr. Jesús Banqueri Ozáez
Profesor Titular de Universidad	Profesor Titular de Universidad

La doctoranda María Sofía Martínez García y los directores de la tesis Miguel Ángel Carvajal Rodríguez y Jesús Banqueri Ozáez, garantizamos, al firmar esta tesis doctoral, que el trabajo ha sido realizado por el doctorando bajo la dirección de los directores de la tesis y hasta donde nuestro conocimiento alcanza, en la realización del trabajo, se han respetado los derechos de otros autores a ser citados, cuando se han utilizado sus resultados o publicaciones.

Granada, Noviembre de 2014.

Director/es de la Tesis | Doctoranda

Fdo.: Miguel A. Carvajal Rodríguez | Fdo.: Mª Sofía Martínez García

Jesús Banqueri Ozáez

Agradecimientos

Me ha costado varios días ponerme a escribir estos agradecimientos, pues buscaba el momento adecuado sin estar “enfadailla” con ninguna de las dos personas que más tengo que agradecer en esta tesis: a mi “dire” Migue y a Fernando. Al final, he llegado a la conclusión que ese momento iba a ser muy difícil de encontrar, ya que “soy una enfadona”... Así que por si les quedaba alguna duda quiero decirles que no tengan en cuenta mis “regañinas”, pues eso solo lo hago con la gente que me importa.

En primer lugar quiero agradecer a mis directores a Migue y a Jesús. Migue, tengo tantas cosas que agradecerte, que escribiría otra tesis solo numerándolas: gracias por enseñarme tanto, por confiar en mí e insistirme que pidiera la beca, por tus lecciones magistrales con las que me quedo aún con la boca abierta, por tener siempre soluciones a mis problemas electrónicos, por elegirme “heredera” de tus algoritmos y del P3 y permitirme usarlos, por estar siempre dispuesto a ayudarme, por tu infinita paciencia conmigo, por decirme que no me agobie, por decirme que no trabaje tanto, por estar disponible 24 horas al día, por a pesar de mi insistencia no enfadarte, por tantas risas, por tantas horas de trabajo juntos, por tu actitud siempre positiva y optimista.... en resumen por ser el mejor director que nunca podría imaginar haber tenido, por todo eso y mucho más, Gracias “dire”.

A Jesús, por acordarte de mí y permitidme pedir la beca. También por tus chistes, porque encontrar tantos chistes no creo que es tarea fácil y porque a pesar de que me “chinches” sabes que no me enfado.

A Alberto, porque a pesar de no estar sobre el papel, me has dirigido la tesis como si lo estuvieras. Por enseñarme a investigar, a ser constante y a no rendirme. Por ser tan generoso, y por ayudarme a sacar fruto a mi trabajo aunque yo creyera que no había.

A Alberto y a Jesús agradeceros permitirme acabar el máster, a pesar de haberme concedido la beca en Granada. A los tres daros las gracias por las risas con "las cosicas de Migue", las bromas de Jesús y las miradas cómplices de Alberto. Porque sois grandes profesionales pero sobre todo mejores personas. Gracias por preocuparos por mí tanto en el ámbito laboral como personal, gracias de corazón.

También quiero agradecer a mis compañeros de departamento: A Antonio Martínez, por las risas, los "cotis" y por animarme cuando estaba de bajón, a Nuri por los cafés en el CITIC, a Pepe por estar siempre dispuesto ayudarme y por la bondad que tienes, a Almudena por renunciar a esta beca y permitir que la cogiera yo, a Diego, por las tapas de la Posada, a Miguel, por enseñarme a ser paciente, a Berta, porque siempre me rio con ella, a Antonio García y a Encarni por ayudarme con mis primeras clases como profesora,….y a todos los demás compañeros muchas gracias. Gracias por hacerme sentir parte de esta "familia electrónica".

Además quiero agradecer a la gente del Hospital que han permitido que pueda realizar gran parte de este trabajo: a Fernando, a Julia y a Damián, por hacerme sentir uno de vosotros y por tantas horas juntos en el bunker. A Antonio Lallena, por intentar introducirme en el mundo de la simulación Monte Carlo y por su continua disponibilidad.

Also, I would like to thank Aleksandar Jaksic and Nikola Vasovic, to let me work in Tyndall National Institute, and to let me work with their RADFETs. Of course, I would like to thank Ali, to make me have fun during the work time at Cork.

Quiero dar las gracias a mis amigos, tanto a "Las Niñas" como a mis "Amiguitos" porque cuando estoy con ellos me hacen olvidar los malos ratos y los agobios del trabajo.

Quiero agradecer infinitamente a mi familia: a mis padres, por confiar en mí, porque siempre habéis apoyado mis decisiones, por preocuparos

tanto por mí y por vuestro esfuerzo. A mi hermana, porque aunque a veces no lo entiendas, sé que me apoyas por encima de todo. A los tres, Gracias.

Gracias al resto de mi familia, en especial a mis abuelas, porque aunque no sepan lo que hago, sé que están muy orgullosas de mí….aunque “no me dé ni para comprarme ni un pisico…” .También agradecer a mi familia política, a Mari Sol y a Fernando, por tratarme como a una hija más, y a mis cuñados.

Y finalmente quiero agradecértelo a Ti, a Fernando, a Pete. Porque si con Migue me faltan páginas, contigo me faltan palabras. Gracias por estar siempre ahí, por soportarme, por apoyarme, por consolarme, por animarme, por ayudarme tanto profesional como personalmente. Gracias por ser tan “payaso”, por sacarme siempre una sonrisa, gracias por confiar en mí por encima de todo, y por hacerme creer que soy capaz de esto y de mucho más. Gracias, porque sin ti no sería lo que soy, ni habría llegado hasta donde estoy, gracias por ser mi mitad.

A todos,

MIL GRACIAS.

A mis padres.

A mi hermana.

Y a PT.

Resumen

El cáncer es una de las principales causas de muerte a nivel mundial. Su tratamiento está basado en tres estrategias fundamentales: cirugía, quimioterapia y radioterapia. La radioterapia consiste en usar haces de radiación de alta energía para destruir las células cancerígenas de un área concreta. Su efectividad reside en focalizar la mayor concentración de energía en la zona afectada, sin dañar los tejidos circundantes. Del cálculo de esa energía absorbida por el paciente proviene la dosimetría.

Existen varios tipos de radioterapia: externa e interna. Este trabajo se desarrolla fundamentalmente en el ámbito de la radioterapia externa donde se usan tanto haces de fotones como de electrones, dependiendo de la profundidad a la que se encuentre el tumor. La radioterapia externa se planifica normalmente con programas específicos para determinar la orientación de los campos en función del lugar exacto del tumor. Sin embargo, durante la aplicación del tratamiento es conveniente comprobar la dosis recibida por el paciente, lo cual es el principal objetivo de la dosimetría *in vivo*. Existen diferentes tipos de dosímetros usados para tal fin, cristales termoluminiscenes, diodos, cámaras de ionización, etc. Sin embargo en los últimos años se ha extendido el uso de transistores MOSFET como sensores dosimétricos, pues aportan una serie de ventajas sobre los sistemas dosimétricos tradicionales tales como lectura inmediata y no destructiva, bajo consumo de potencia, fácil calibración, almacenamiento permanente, y una razonable sensibilidad y reproducibilidad.

Existen MOSFET que se fabrican específicamente para detectar radiación ionizante, son los denominados RADFETs (RADiation

sensitive Field-Effect Transistors), los cuales tienen un óxido de puerta más ancho siendo así más sensibles a la radiación. El parámetro eléctrico más usado para la medida de dosis con MOSFET es la tensión umbral (V_t). Sin embargo uno de los mayores inconvenientes de este parámetro es su dependencia con la temperatura, especialmente en aplicaciones donde pueden darse cambios bruscos de temperatura como en el espacio o durante la aplicación de tratamientos de radioterapia.

Así, este trabajo se ha desarrollado en dos líneas fundamentales: el estudio de la respuesta de varios modelos MOSFET a la radiación ionizante y su influencia térmica cuando son usados como sensores dosimétricos.

En primer lugar se ha realizado una caracterización de sensores MOSFET comerciales tanto para haces de fotones como para haces de electrones, típicamente usados en los tratamientos de radioterapia. Dentro de los transistores comerciales, se han estudiado transistores con dos tipos de geometrías, transistores laterales y transistores verticales. Ya que normalmente este tipo de sensores no tienen mucha sensibilidad, también se han diseñado técnicas para mejorar la respuesta de los mismos, tanto polarizándolos durante el periodo de radiación como apilando varios transistores. Para reducir los efectos térmicos e incrementar la linealidad de los sensores, han sido aplicados algoritmos de polarización con múltiples corrientes previamente diseñados por el Departamento de Electrónica y Tecnología de Computadores (Universidad de Granada). El objetivo final ha sido encontrar la configuración y el modelo de MOSFET comercial óptimo, para cada tipo de radiación.

En la caracterización de radiación gamma, todos los tipos analizados han mostrado un comportamiento lineal con la dosis, con sensibilidades

entre 4.1 y 62 mV/Gy. Además se realizó un estudio preliminar, del circuito integrado CD4007 de su respuesta ante fotones, con vistas a ser usado posteriormente en la caracterización con electrones debido a que consta de un encapsulado no metálico. Finalmente se concluyó que la mejor configuración propuesta para este tipo de radiación en cuanto a linealidad, reproducibilidad y deriva temporal ("fading") a corto plazo es el transistor 3N163 doble polarizado a 10 V, que alcanza una sensibilidad de 62 $\pm$3 mV/Gy, casi comparable a la conseguida por transistores específicos RADFET.

En cuanto a la caracterización realizada con haces de electrones, todos los tipos estudiados, mostraron una sensibilidad entre 3 y 13 mV/Gy. En esta ocasión su linealidad e incertidumbre es comparable a la obtenida con transistores RADFETs, sin embargo la sensibilidad era menor. Esto no supuso un gran problema, puesto que el objetivo principal en la caracterización de electrones, era encontrar una configuración óptima para ser usada en RIO (Radioterapia Intraoperatoria) donde normalmente las dosis aplicadas en una sola sesión sobre el paciente oscilan entre 10 y 35 Gy, por tanto prima la reproducibilidad y linealidad que obtener sensibilidades elevadas. Así pues, la configuración óptima para este fin fue la apilada y polarizada a 0.6 V del circuito integrado CD4007.

A continuación se llevó a cabo un estudio de la respuesta ante radiación ionizante de transistores específicos, RADFETs, fabricados por el centro irlandés de investigación "Tyndall National Institute" localizado en Cork (Irlanda), con el que se ha colaborado estrechamente en la realización de este trabajo. Se realizó un estudio comparativo de cinco tipos de sensores, con espesores de óxido de puerta de 100 nm, 400 nm y 1 μm tanto para haces de fotones como para haces de electrones. Dentro de los modelos de 400 nm se

estudiaron tres tipos de RADFETs fabricados con diferentes procesos de oxidación para el óxido de puerta. Todos los transistores fueron medidos polarizados a la corriente constante I_{ZTC}, para minimizar la influencia de la temperatura. Los resultados experimentales han mostrado respuestas muy similares en cuanto a sensibilidad, reproducibilidad y fading a corto plazo en las condiciones de referencia en las que se caracterizaron los sensores. El fading a corto plazo ha mostrado que se podría considerar despreciable para los tamaños de óxido de 100 y 400 nm, sin embargo en 1µm el fading es importante y disminuye conforme aumenta la dosis acumulada. Se han observado dos efectos competitivos, por un lado la densidad de cargas atrapadas en el óxido que disminuye monótonamente a temperatura ambiente tras la irradiación, y la densidad de cargas de la interfase muestra un crecimiento inicial.

Finalmente se concluyó que estos modelos de RADFETs son también válidos para dosimetría con electrones, como por ejemplo RIO, y que la mayoría de las conclusiones de trabajos previos para fotones pueden ser extendidas para haces de electrones, dentro de los límites del estudio.

Además se ha propuesto uno nuevo parámetro dosimétrico: el desplazamiento de la pendiente subumbral con la dosis acumulada. Se ha demostrado que la pendiente subumbral es modificada por la dosis. Un tipo de transistor comercial, el 3N163, ha sido caracterizado en un rango de radiación gamma típica de tratamientos de radioterapia. Debido a que el parámetro dosimétrico ha mostrado una buena linealidad, sensibilidad y reproducibilidad podría ser utilizado como parámetro complementario al típicamente usado de incremento de la tensión umbral; aumentando la fiabilidad en la verificación de la dosis de los tratamientos de radioterapia.

A continuación se pasó al estudio de la influencia de la temperatura en el MOSFET cuando se usa como sensor dosimétrico. En primer lugar se ha presentado un modelo de la influencia de la temperatura en el transistor MOS. Dicho modelo ha sido experimentalmente validado y probado con transistores MOSFET tipo n (3N170) y tipo p (3N163) en sus específicos rangos de corriente. Así pues, se ha demostrado que la corriente de drenador puede ser calculada para obtener el coeficiente térmico adecuado en función del propósito para el que vaya a ser utilizado el transistor, por ejemplo como sensor dosimétrico, objetivo fundamental de este trabajo, o sensor de temperatura.

Basándonos en el modelo térmico expuesto se ha presentado un método para mejorar el coeficiente lineal de temperatura del voltaje de fuente en caso de que la corriente I_{ZTC} sufra un desplazamiento causado por la dosis acumulada o ciclos térmicos. Se han comparado los resultados de cinco tipos de transistores RADFETS medidos con el tradicional método de polarización a corriente constante I_{ZTC} o con el propuesto. Se ha conseguido una mejora entre el 33% y 80% con diferentes desfases de I_{ZTC}. Por tanto se concluye que los resultados conseguidos mejoran de la precisión en la medida de la dosis en caso de desfases de valores de la corriente I_{ZTC}.

Por último y como resultado del estudio térmico realizado, se ha llevado a cabo la aplicación de un sensor de temperatura. Han sido propuestos dos modelos de termómetro basados en MOSFET trabajando en la región de saturación: usando dos transistores tipo p y otra configuración usando dos transistores complementarios. Finalmente con esta última se ha obtenido una sensibilidad media de 5.27 mV/K dentro del rango industrial de temperatura.

Index

1 Motivation and objectives 29

1.1 Motivation 29

1.2 Objectives 31

1.3 Document outline 32

2 State of art 35

2.1 History 35

2.2 Dosimetry: basic concepts 36

2.2.1 Exposure 37

2.2.2 Electronic equilibrium 38

2.2.3 Dose and dose rate 42

2.2.4 Biological effects of radiation: equivalent and effective dose 43

2.3 Types of radiation 45

2.4 Radiotherapy 48

2.4.1 Radiation sources 50

2.5 Main ionizing detectors 51

2.5.1 Thermoluminescent dosimeters (TLDs) 51

2.5.2 Semiconductor detectors 53

2.6 Fundamentals of the Metal-Oxide-Semiconductor Field Effect Transistors (MOSFET) 58

2.6.1 Structure 59

2.6.2 *I-V* curves 61

2.6.3 Thermal dependency of *I-V* curve 65

2.7 Ionizing radiation effects in MOSFET 67
2.7.1 Hole creation and trapping 69
2.7.2 Influence on *I-V* curves 73
2.7.3 Commercial dosimetric systems based on MOSFET 94
3 Materials and methods 111
3.1 Transistor types 111
3.1.1 Commercial transistors 112
3.1.2 RADFETS 122
3.2 Radiation sources 126
3.2.1 Cobalt therapy unit (^{60}Co) 126
3.2.2 Lineal accelerator (LINAC) 128
3.2.3 Dose and electronic equilibrium conditions 131
3.3 Irradiation Setup 135
3.4 Experimental Setup of the electrical characterization 138
3.5 Experimental Setup of thermal characterization 145
3.6 Dosimetry System 147
3.6.1 Sensor module 148
3.6.2 Reader unit 154
3.6.3 Previous measurement algorithms of UGR 157
3.6.4 Methodology 163
3.7 Summary 164
4 Response to ionizing radiation 167
4.1 Validation of dosimetric system 169
4.2 Thermal characterization 171

4.2.1 3N163 ... 172

4.2.2 DMOS ... 173

4.2.3 CD4007 ... 175

4.2.4 RADFETs ... 177

4.2.5 Current setting for the 3CM/2CM ... 178

4.3 Response to radiation of commercial transistors ... 180

4.3.1 Response to photon beams ... 181

4.3.2 Response to electron beams ... 190

4.3.3 Study of the subthreshold swing as dosimetric parameter 203

4.4 RADFETs transistors ... 214

4.4.1 Experimental procedure ... 217

4.4.2 Study of the radiation response ... 218

5 Effects of the temperature on MOSFET as dosimeter ... 225

5.1 State of art ... 226

5.2 Theoretical Model of thermal effects on MOSFETs ... 228

5.2.1 Experimental validation of the theoretical thermal model 234

5.3 Thermal drift reduction with changes in I_{ZTC} ... 244

5.3.1 Experimental procedure ... 245

5.3.2 Experimental results ... 246

5.4 Application as temperature sensor ... 251

5.4.1 Results ... 253

6 Conclusions ... 261

6.1 Response to ionizing radiation 261

6.1.1 Commercial transistors 262

6.1.2 RADFETs transistors 265

6.2 Effects of temperature on MOSFET as dosimeter 267

6.3 Scientific Contributions 268

6.3.1 Journal papers 268

6.3.2 International Conferences 270

7 Conclusiones 273

7.1 Respuesta a la radiación ionizante 273

7.1.1 Transistores comerciales 274

7.1.2 Transistores RADFETs 278

7.2 Efectos de la temperatura en MOSFET como dosímetros .. 280

Bibliography 283

Figure index

Figure 2.1 Photons incident over a volume (Ortega Aramburu and Jorba Bisbal 1994). 38

Figure 2.2 Schematic representation of the electronic equilibrium concept (Ortega Aramburu and Jorba Bisbal 1994). 39

Figure 2.3 Ionization chamber scheme (Khan 1984) 40

Figure 2.4 Normalised response of ionization chamber with the thickness wall (Khan 1984). 41

Figure 2.5 Classification of radiation (Holmes-Siedle and Adams 1993) 45

Figure 2.6 IORT treatment (Medical 2014). 50

Figure 2.7 TLD band diagram a) unsensitised and b) sensitised process (Carvajal 2008). 52

Figure 2.8 LiF and CaF_2 glow curve (Ortega Aramburu and Jorba Bisbal 1994). 53

Figure 2.9 Intrinsic semiconductor detector (Carvajal 2008). 55

Figure 2.10 Electron-hole pairs creation in the depletion zone. 57

Figure 2.11 PIN diode (Ortega Aramburu and Jorba Bisbal 1994). . 58

Figure 2.12 MOSFET geometries: a) Lateral and b) Vertical. 60

Figure 2.13 a) pMOS in accumulation region. b) pMOS in inversion region (Carvajal 2008) 62

Figure 2.14 Biased pMOS with different voltages (Carvajal 2008)... 63

Figure 2.15 *I-V* curves in a pMOS transistor. a) Intensity versus drain-source voltage in different gate-source voltages. b) Intensity versus gate-source voltage for different values of the drain-source voltages (Carvajal 2008) 64

Figure 2.16 *I-V* curve in saturation, with $v_{GD} = 0$ for different temperatures (Carvajal 2008) 67

Figure 2.17 Pair production and trapping at interface traps. a) Ionizing radiation creates electro-hole pairs b) Electrons sweep out to the gate and holes to the bulk c) Holes move slower to the bulk e) Holes reach the bulk f) Trapped holes in the interface traps g) Superficial states, traps in the silicon interface (Carvajal 2008). 68
Figure 2.18 Electron – hole pairs separated by an electric field in the oxide. a) Positive bias on the gate b) No bias on the gate (Carvajal 2008)..70
Figure 2.19 Holes transport in the oxide: a) Transport through valence band b) Transport by tunnel effect with traps in band gap (Ma and Dressendorfer 1989)..72
Figure 2.20 Energy band diagram of traps created by radiation a) pMOS after irradiation with a flat band voltage. b) nMOS after irradiation with a flat band voltage. c) Strong inversion diagram in pMOS with negative bias on gate. d) Strong inversion diagram in nMOS with positive bias on gate. (Carvajal 2008)...........................76
Figure 2.21 nMOS and pMOS threshold voltage shift (Freeman and Holmes-Siedle 1978). 77
Figure 2.22 Shift in mind gap voltage for an MOS capacitor as a function of radiation dose showing saturation at high doses. Symbols are data points. Curves are a computer model fit with (solid) and without (dashed) trap filling (Boesch et al. 1986). 80
Figure 2.23 Carrier mobility normalised to the pre-irradiation mobility versus interface trap density (Sexton and Schwank 1985)....81
Figure 2.24 Ionizing radiation effect over *I-V* curves. a) pMOS transistor b) nMOS transistor (Carvajal 2008)..................................82
Figure 2.25 Absolute value of accumulated threshold voltage shift with the received dose for different bias gate (Soubra et al. 1994)......84
Figure 2.26 Sensitivity, V/Gy, versus the accumulated dose at different gate biases (Soubra et al. 1994)...85

Figure 2.27 MOS structure in detail with trapped charges in the oxide (Carvajal 2008)..86
Figure 2.28 Charges and electric field evolution when the oxide is irradiated. a) The electric field created by the space charge region is weak. b) Electric field is cancelled in the interface region with the gate and there is a region free of charge c) The free region of charge is expanded through the oxide (Carvajal 2008)......................................87
Figure 2.29 Thickness oxide influence in the sensitivity of MOSFET a) Biased MOSFET $V_{GB} > 0$ b) Unbiased MOSFET during irradiation (Sarrabayrouse and Siskos 1998)..90
Figure 2.30 Trapped hole recombination by tunnel effect (Carvajal 2008)..92
Figure 2.31 Recovering of threshold voltage shift with time for different oxide field (Oldman 1999)...93
Figure 2.32 Recovering of normalised threshold voltage shift with time in different temperatures (Oldman 1999). RmT denote the room temperature around 25ºC...93
Figure 2.33 pMOS configuration to measure the threshold voltage shift with constant current (Carvajal 2008)..95
Figure 2.34 Biased schematic diagram during irradiation of a Thomson and Nielsen sensor composed by two RADFETs (Thomson et al. 1991)..98
Figure 2.35 Measurement schematic diagram of Thomson&Nielsen sensor (Thomson et al. 1991). 98
Figure 2.36 a) Dosimetric sensor Thosmon&Nielsen b) mobileMOSFET reader c) portable Dosimeter (Canada 2014). 99
Figure 2.37 OneDose™ dosimetric system (Carvajal 2008)............ 103
Figure 2.38 OneDose™ sensor on the patient (Carvajal 2008)....... 103
Figure 2.39 Block diagram of OneDose system (Halvorsen 2005)... 104

Figure 2.40 The online MOSFET dosimetry system (Rosenfeld 2014a). 106
Figure 2.41 Schematic comparison of a MOSFET with epoxy bubble (left) and MOSkin (right) (Kwan et al. 2008). 108
Figure 2.42 Schematic diagram of the MOSkin detector (Kwan et al. 2009). 109
Figure 2.43 Diagram of a MOSFET threshold voltage thermo-stabilization circuit (Rosenfeld 2014b). 110
Figure 2.44 a) MOSkinTM detector on Kapton pigtail and b) Multiple MOSkinTM mounted on an Endo Rectal Balloon (Metcalfe et al. 2013). 110
Figure 3.1 Longitudinal section and button view of the 3N163 transistor. Terminal equivalence is (D) drain, (S) source, (C) substrate and (G) gate. Dimension are expressed in millimetres (Asensio et al. 2006). 115
Figure 3.2 Encapsulate SOT23 a) 3-pin b) 4-pin .Dimensions are expressed in millimetres (ZVP3306 , ZVP4525 , BS250F). 118
Figure 3.3 CD4007 a) Pin-out b) Functional diagram (CD4007UB). 119
Figure 3.4 Dimensions of SOP encapsulation (CD4007UB). Dimensions are expressed in millimetres. 120
Figure 3.5 Dimensions of PDIP encapsulation (CD4007UB). Dimensions are expressed in inches/millimetres. 121
Figure 3.6 Detailed schematic diagram of CD4007UB showing input, output and parasitic diodes (CD4007UB). 121
Figure 3.7 ESAPMOS4 layout. 122
Figure 3.8 ESAPMOS4 pin-out. 124
Figure 3.9 14-pin DIP packages with kovar lids. 124
Figure 3.10 3D model for an ESAPMOS4 RADFET. 125

Figure 3.11 Scheme of a teletherapy unit of ^{60}Co (Ortega Aramburu and Jorba Bisbal 1996). 127
Figure 3.12 Decay scheme of ^{60}Co (Carvajal 2008)........................ 127
Figure 3.13 Theratron-780 spectrum at the isocentre with different fields (Teimouri Sichani and Sohrabpour 2004)................................ 128
Figure 3.14 Lineal accelerator components (Ortega Aramburu and Jorba Bisbal 1996). 130
Figure 3.15 PDD of a Theratron-780 Cobalt therapy unit in water. It has been calculated for the isocentre (80 cm) with a radiation field of 10x10 cm^2 (Carvajal 2008) with data from (Panettieri et al. 2007).. 132
Figure 3.16 PDD of Siemen Mevatron KDS unit in water (Photons of 6MeV). It has been calculated for the isocentre (100 cm) with a radiation field of 10x10 cm^2.. 133
Figure 3.17 PDD of Siemen Mevatron KDS unit in water (Electrons of 6MeV). Calculated for the isocentre (100 cm) with field of 10x10 cm^2.. 134
Figure 3.18 Irradiation set-up: a) Biasing tests for electron beam in commercial transistors. b) Unbiased tests for commercial and RADFET transistors in photon and electron beams......................... 136
Figure 3.19 B1500 analysed semiconductor (Keysight). 139
Figure 3.20 SMU Triax connection B1500 with the test fixture 16442B (Agilent 2014).. 141
Figure 3.21 Connection jumper leads of 16442B with the MOS transistor (Agilent 2014). 142
Figure 3.22 Auxiliary PCB for linear region characterization. 143
Figure 3.23 Auxiliary PCB for saturation region characterization. 143
Figure 3.24 VCL3006 Climate chamber from Vötsch Industrietechnik (Vötsch 2014)... 146
Figure 3.25 Experimental setup of thermal characterization.......... 147

Figure 3.26 Sensor module configurations with a single pMOS. a) Unbiased mode: during radiation period the JFET is on and the terminals are short-circuited all together. b) Unbiased mode: during readout process the JFET is cut-off. c) Biased mode: during radiation period JFET2 is cut-off with a bias source between the gate and source. d) Biased mode: for readout process JFET2 is on and JFET1 is off. 149

Figure 3.27 Sensor module configurations for two stacked pMOSs. a) Unbiased mode: during radiation period the JFET is on and the terminals are short-circuited all together. b) Unbiased mode: for readout process the JFETs are cut-off. c) Biased mode: during radiation period JFET3 is cut-off with a bias source between the gate and source. d) Biased mode: for readout process JFET3 is on and JFET1 and JFET2 are off........ 151

Figure 3.28 Parts of sensor module: two stacked biased sensor (left) and single unbiased sensor (right)........ 152

Figure 3.29 Types of sensor configurations: a) Single unbiased b) Single biased c) Two stacked unbiased d) Two stacked biased........ 152

Figure 3.30 Types of sensor modules: a) 3N163 b) ZVP3306 c) RADFETs, with and without kovar lid........ 153

Figure 3.31 Biasing PCB. 153

Figure 3.32 UGR reader unit and sensor module........ 154

Figure 3.33 Block diagram of the reader unit and the sensor module (Carvajal et al. 2012) 155

Figure 4.1 *I-V* curve for a transistor of t_{OX}=100 nm in a temperature of 22°C. The line shows the used region to do the linear fit. 169

Figure 4.2 Typical subthreshold swing of a 3N163 as a function of temperature. Experimental data show with symbols and error bars and the line is the linear fit........ 172

Figure 4.3 *I-V* curves of a ZVP3306 transistor at different temperatures (symbols)........ 173
Figure 4.4 V_t of a ZVP3306 transistor (number 2) at different temperatures. Uncertainties are smaller than the size of symbol. Lines show the linear fits to data. 174
Figure 4.5 *I-V* curves of a CD4007 transistor at different temperatures........ 175
Figure 4.6 Typical thermal drift of a CD4007 dosimeter with (solid line) and without (dashed line) applying the thermal compensation method. The results of the corresponding linear regression are also given. Uncertainties are smaller than the size of symbol used. 176
Figure 4.7 *I-V* characteristics for the RADFET number 1, of the transistors with t_{OX}= 400nm_W7 and 300/50 type for I_{ZTC} extraction. 177
Figure 4.8 Increment of V_t as dose function for single unbiased CD4007 transistors........ 184
Figure 4.9 Sensitivities per irradiation session of single biased ZVP3306 transistor with 10 V versus dose........ 185
Figure 4.10 Short-term post-irradiation fading for dosimeter T1: 3N163 with bias 5 V........ 186
Figure 4.11 Short-term post-irradiation fading for dosimeter T1: 3N163 with bias 10 V........ 187
Figure 4.12 Accumulated threshold voltage shift of 3N163 as a function of the accumulated dose for four different devices, each one corresponding to the configurations studied in the present work........ 189
Figure 4.13 Sensitivities per irradiation session of single unbiased ZVP3306........ 193
Figure 4.14 Increment of V_t as dose function for ZVP3306 transistors. 194

Figure 4.15 Short-term post-irradiation fading for dosimeter T1: ZVP3306 with bias 5 V. 195
Figure 4.16 Short-term post-irradiation fading for dosimeter T1: ZVP3306 with bias 10 V. 196
Figure 4.17 Accumulated threshold-voltage shift as a function of the accumulated dose (solid squares) and sensitivity per session (open squares) for a CD4007 pMOS in the single biased configuration. The solid line represents the linear fit of experimental data, their uncertainties of ΔV_t (with a coverage factor $k=1$) is 0.5 mV/session. Average uncertainties in the measured dose D, 2.5 cGy, are smaller than the size of the symbols used. The horizontal dashed line shows the global sensitivity. 198
Figure 4.18 Short term fading post-irradiation fading for dosimeter CD4007 T1. 199
Figure 4.19 Accumulated threshold voltage shift as a function of the accumulated dose for four different devices, each one corresponding to the configurations studied in the present work. In all cases the manufacturer was Texas Instruments 200
Figure 4.20 Accumulated threshold voltage shift vs. accumulated dose for the five units used to analyse the response to the two stacked configuration for the CD4007 in IORT conditions 202
Figure 4.21 Drain current versus gate voltage in the subthreshold regime of MOSFET T78 as a function of the accumulated dose up to 51 Gy. Symbols are the experimental data and lines the linear fits. . 208
Figure 4.22 Subthreshold swing shift of MOSFET T80 as a function of the dose (experimental data in symbols with error bars and linear fit shown with the line) 209
Figure 4.23 Sensitivity per radiation session of MOSFET T80. Experimental data are shown with symbols and error bars and linear fit with the line. 210

Figure 4.24 Threshold voltage shift and sensitivity per radiation session of MOSFET T80 as a function of the dose (experimental data in symbols with error bars and linear fit shown with the line). 211
Figure 4.25 Residual thermal drift after compensation of temperature effects with equation (4.4) (experimental data in symbols with error bars and linear fit shown with the line).. 213
Figure 4.26 Accumulated threshold voltage shift as a function of the accumulated dose of RADFETs with tox =100 nm and W/L = 300/50 and 690/15, irradiated with photon (left) and electron (right) beams. 219
Figure 4.27 Accumulated threshold voltage shift as a function of the accumulated dose of RADFETs with tox =400 nm, with W/L = 300/50 irradiated with photon (left) and electron (right) beams...... 219
Figure 4.28 Accumulated threshold-voltage shift as a function of the accumulated dose of RADFETs with t_{OX} =400 nm, with W/L = 690/15 irradiated with photon (left) and electron (right) beams. 220
Figure 4.29 Accumulated threshold voltage shift as a function of the accumulated dose of RADFETs with tox =1 μm and W/L = 300/50 and 690/15, irradiated with photon (left) and electron (right) beams. 221
Figure 4.30 Short-term post-irradiation fading for RADFETs of t_{ox} =1 μm for photon (left) and electron (right) beams up to 350 s after irradiation. 221
Figure 5.1 MOSFET configurations for biasing at constant current in saturation region a) nMOS b) pMOS. 228
Figure 5.2 *I-V* characteristics of transistors at 20ºC: a) 3N163_T1 b) 3N170_T1 236
Figure 5.3 Threshold voltages as a function of the temperature of the transistors T1 of the groups 3N163 and 3N170................................ 237

Figure 5.4 *I-V* characteristics for MOSFSET T1 for I_{ZTC} extraction: a) 3N163 b) 3N170. 238
Figure 5.5 V_S for 3N163_T1 measured at 20 and 1000 μA. 239
Figure 5.6 α(ID) as a function of $ID^{1/2}$ for transistors 3N163_T1 and 3N170_T1. The dots represent experimental data and the thin black line is the theoretical model. 240
Figure 5.7 Thermal coefficients of the drain currents of interest with a ΔI_{ZTC}. The black line represents before the I_{ZTC} shift and grey line after. 244
Figure 5.8 $\alpha(I_D)$ as function of $I_D^{1/2}$ for RADFETs with different t_{OX} . The sample of 400 nm is form the 400nm_W8 type. The dots represent experimental data and the thin black line is the theoretical model given by equation (5.11). 247
Figure 5.9 Experimental thermal coefficients as a function of I_D for a RADFET with t_{OX}=1 μm, showing the shifts due to irradiation and the thermal cycles. Uncertainties (with a coverage factor $k=1$) in mV/ºC are smaller than the size of symbol used. 248
Figure 5.10 Temperature sensor schemas for differential measurements: a) Two pMOS b) Two complementary MOSFETs... 254
Figure 5.11 Source voltages at I_{D1}, I_{D2} and differential voltage, V_{PT}, as a function of temperature, for the dual pMOS (top figure) and the complementary MOS (bottom figure) sensor configurations. 258

Table index

Table 2.1 Mass Thickness to get the electronic equilibrium with photons of different energies (Knoll 2000). 41

Table 2.2 Radiation weighting factors (Knoll 2000). 43

Table 2.3 Radiation weighting factors of tissues and organs (Ortega Aramburu and Jorba Bisbal 1996). 44

Table 2.4. Sensitivity for model TN-502RD and TN-1002RD (Canada 2014)... 101

Table 2.5. Recommended bias setting and radiotherapy dose per model. 101

Table 2.6 Uncertainty in the dose determination with the OneDose system(Sicel 2005) 105

Table 3.1 Electrical characteristics of 3N163 transistor. Min, Typ and Max denote minimum, typical and maximum values. Minus sign indicate the direction of current and voltage (Siliconix). 114

Table 3.2 Electrical characteristics of ZVP3306 transistor (ZVP3306). 116

Table 3.3 Electrical characteristics of ZVP4525 transistor (ZVP4525). 117

Table 3.4 Electrical characteristics of BS250F transistor (BS250F).117

Table 3.5 Pin- out and description pins of ESAPMOS4. 123

Table 3.6 RADFETs types.. 125

Table 3.7 Range of energies of LINAC Mevatron KDS. 129

Table 3.8 PDD and build-up used for every transistor and beam type. 134

Table 3.9 Voltage range, resolution, and accuracy. 140

Table 3.10 Current range, resolution, and accuracy. 141

Table 3.11 Technical specifications of HP4148B. 144

Table 3.12 Biasing conditions for the pMOS in the lineal and saturation regions for the extraction of *I-V* characteristics.............. 145
Table 3.13 Groups of transistors for photon beam (6 MeV) study. 164
Table 3.14 Groups of transistors for electron beam (6 MeV) study.165
Table 4.1 Threshold voltage of a group of samples, measured with the semiconductor analyser B1500 and the UGR dosimetry system. 170
Table 4.2 Values of thermal coefficients. Uncertainties are given with a coverage factor k=1. 175
Table 4.3 I_{ZTC} and thermal coefficient of threshold voltage for the studied transistors CD4007 type. Uncertainties are given with a coverage factor k=1. 176
Table 4.4 I_{ZTC} currents and thermal coefficient for the different types of RADFETs... 178
Table 4.5 Selected currents for biasing with the reader unit to apply the 2CM or 3CM.. 179
Table 4.6 Sensitivities per sample in the group of single biased 3N163 biasing with 5 and 10 V, respectively... 184
Table 4.7 Dose sensitivity for the analysed pMOS in the various configurations for photon beams. 188
Table 4.8 Dose sensitivity for the analysed pMOS in the various configurations for electron beam. 196
Table 4.9 Sensitivies per sample in the group of CD4007 single unbiased and biased configuration.. 197
Table 4.10 Sensitivities and uncertainties of the subthreshold swing and threshold voltage shifts to radiation. Average values are also shown in the last two rows.. 212
Table 4.11 Fitting parameters of RADFET response, according to the power law model for every size and type for photon and electron ionizing radiation. ΔV_t was expressed in mV and D in Gy.............. 222

Table 5.1 Thermal parameters, $\alpha_{|Vt|}$ and I_{ZTC}, and their uncertainties in transistors 3N163 using linear fit (method 1) and the proposed thermal model (method 2).. 241
Table 5.2 Thermal parameters, $\alpha_{|Vt|}$ and I_{ZTC}, and their uncertainties in transistors 3N170 using linear fit (method 1) and the proposed thermal model (method 2).. 242
Table 5.3 I_{ZTC} and its shift, ΔI_{ZTC}, in percentage for each RADFET type and size and. Uncertainties are given with a coverage factor k=1. 249
Table 5.4 Linear thermal coefficients expressed in mV/ºC and cGy/ºC using two methods of dose readout for different I_{ZTC} shifts.. 251
Table 5.5 Experimental and predicted sensitivity of the source-drain voltage of a MOS transistor biased at current of interest. Predicted values using the thermal model and the averaged thermal parameters values are given in Table 5.1.. 256
Table 5.6 Temperature coefficients of the differential source voltage and errors of the temperature sensors for the two proposed configurations.. 257

Acronyms

CMRP	Centre for Medical Radiation Physics
CSDS	Clinical Semiconductor Dosimetry System
CT	Computer Tomography
DAC	Digital to Analog Converter
DMOS	Double Diffused Metal Oxide Semiconductor
EEPROM	Electrically Erasable Programmable
ERB	Endo-rectal Balloons
FSTs	Fast Switching Traps
FTs	Fixed Traps
HRSMU	High Resolution Source Monitor Unit
ID	Identification Number
IMRT	Intensity Modulated Radiation Therapy
IORT	Intraoperative Radiotherapy
JFET	Junction Field Transistor
LCD	Liquid Crystal Display
LINAC	Linear Accelerator
MCU	Microcontroller Central Unit
MOS	Metal Oxide Semiconductor
MOSFET	Metal Oxide Semiconductor Field Effect Transistor
MRI	Magnetic Resonance Imaging

nMOS	n channel MOSFET
PC	Personal Computer
PCB	Printed Circuit Board
PDD	Percentage Depth Dose
PET	Positron Emission Tomography
pMOS	p channel MOSFET
RH	Relative Humidity
RADFET	Radiation Sensitive Field Effect Transistor
SI	System International
SMD	Superficial Mounted Device
SMU	Source Monitor Unit
SSTs	Slow Switching Traps
STs	Switching Traps
TLD	Thermoluminiscent
UGR	University of Granada
USB	Universal Serial Bus
VDMOS	Vertical Double Diffused Metal Oxide Semiconductor
WED	Water Equivalent Depth
WHO	World Health Organization
W/L	Width/Length
ZTC	Zero Temperature Coefficient

2CM	2 Current Method
3CM	3 Current Method
3D	3 Dimensions
4D	4 Dimensions

1

Motivation and objectives

1.1 Motivation

Cancer for the World Health Organization (W.H.O.) is a generic term for a large group of diseases that can affect any part of the body. Other terms used are malignant tumours and neoplasms. One defining feature of cancer is the rapid creation of abnormal cells that grow beyond their usual boundaries, and which can then invade adjoining parts of the body and spread to other organs.

The cancer treatment is based on three fundamentals points: the surgery, the radiotherapy and chemotherapy. The surgery is the proceeding to remove the cancer. The radiotherapy uses beam of high energy to destroy the cancerous cells in a concrete area and the chemotherapy use medicine to destroy the malign cells in the human body.

In the radiotherapy the effectiveness in the treatment resides, between other factors, in focusing the major concentration of energy in the affected area; to destroy the tumour cells. From the calculation of this dose, that is the absorbed energy, comes the dosimetry.

In this work the external radiotherapy is involved, where generally electron or photons beams are used. This depends on the

depth of the tumour. In the external radiotherapy it is very important look for the right orientations and electric field to do not damage the surrounding healthy tissues of the tumour. Therefore, it is necessary to know the exact place of the tumour. For that, a previous planning is done, with a computer tomography (CT).

Although the geometry verification provides successful results, it is convenient to check the received dose by the patient during the radiotherapy sessions. This is the main objective of *in vivo* dosimetry. There are different dosimeters used for this aim: ionization chambers, thermoluminescent crystals (TLDs), diodes and the well-known in the electronic field, the Metal-Oxide-Semiconductor Field Effect Transistors (MOSFETs) (Ma and Dressendorfer 1989, Knoll and Bräunig 1988).

In the last few decades, commercial dosimetry systems for radiotherapy, based on p-channel MOSFETs (pMOSs), have been developed. MOSFETs present a series of advantages over traditional dosimetry systems in medical applications (Thomson 1987, Black 2003). The most important ones are an immediate and non-destructive readout, low power consumption, an easy calibration, a permanent storage of doses and a reasonable sensitivity and reproducibility (Holmes-Siedle and Adams 1986, Soubra, Cygler and Mackay 1994, Hughes et al. 1988, Amin et al. 2011). There are MOSFET, specifically manufactured for dosimetry systems are the so-called RADiation sensitive Field-Effect Transistors (RADFETs) (Ma and Dressendorfer 1989). They have oxides optimized for increased radiation sensitivity. This is usually achieved by growing very thick gate oxides with properties that enhance the trapping of radiation-induced holes (Kelleher et al. 1992, Ristic, Golubovic and Pejovic 1996,

Sarrabayrouse and Siskos 1998). They main inconvenient is their high cost of manufacturing, because they need specific process.

The most popular electrical parameter used for dose measurements with MOSFETs is the threshold voltage (V_t). However, the well-known thermal dependence of V_t is one of the major interference in the measured doses , especially in applications where changes in temperature are common as for example in radiotherapy treatments (environmental/skin temperature difference) or space applications, such as the case of satellites (cycles of sunlight/darkness). Because of that, this line has been widely studied by several authors (Haran et al. 2004, O'Sullivan et al. 1990, Buehler et al. 1993, Kimoto et al. 2003, Shoucair, Hwang and Jain 1984a, Shoucair, Hwang and Jain 1984b, Thomson et al. 1998, Soubra et al. 1994, Mackay et al. 1997, Shin et al. 1999, Soli et al. 1992, Sung-Joon et al. 2002, Tsividis 1987, Vettese, Donichak and Bourgeault 1996).

These variations make the thermal dependence in a non-negligible effect that can prevent the accurate measurement of the dose. The most typical procedure to avoid the thermal drift is to measure using the I_{ZTC} current of the transistor, where the thermal dependence is minimal, however this current can also suffer shift due to the accumulative dose and cycles of temperature.

1.2 Objectives

The main objective of this Ph.D. Thesis is to study the pMOS transistor as dosimetric sensor, both the response to ionizing radiation and the thermal effects of it, when it is used as dosimeter. In order to

reach this principal purpose, several particular objectives have been addressed:

1. Characterization of the response of commercial transistors to electron and photon beams. Two structures have been analysed, lateral and vertical geometries. The aim is to find out a valid commercial transistor, with enough sensitivity to work as dosimeter for each type of beam.
2. Comparative of the response of RADFET to electron and photon beams.
3. To propose a new dosimetric parameter: the subthreshold swing. This could be a complementary parameter to the traditional threshold voltage shift for enhancing the confidence of dose verification.
4. To make a thermal study of the effects of the temperature on MOSFET as dosimeter.
5. To look for a novel method based on the thermal study, to reduce the effect of possible changes in the zero temperature coefficient current, I_{ZTC}.

1.3 Document outline

This document has been organized as follows:

In chapter 2, an introduction, background and state of art to some general aspects involved in this Ph.D. Thesis are presented: the concept of dosimetry, types of radiation, the radiotherapy, main ionizing detectors, fundamentals of MOSFET and their degradation with the ionizing radiation.

In chapter 3, a description of the materials and methods of this Ph.D. Thesis are introduced: the types of transistors used (both commercial and RADFETs transistors), the radiation sources and the irradiation setups required to the response to radiation studies, also the experimental setup both thermal and electrical characterization and finally the dosimetry system and the algorithm used in the work.

In chapter 4, the responses of commercial and specific RADFETs to ionizing radiation are shown. Firstly a thermal characterization of the MOSFET types is shown; afterward the responses to photon and electron beams of the selected MOSFET are presented. Also a subthreshold study is carried out from which the subthreshold swing is proposed as dosimetric parameter, to be used as complementary parameter to the threshold voltage shift, used in dosimetry with MOSFET.

In chapter 5, a study of the thermal effects on MOSFET as dosimeter is carried out. Therefore, a theoretical thermal model is proposed, with their experimental validation for nMOS and pMOS transistors. From this thermal model, a method to reduce the thermal drift with changes in the zero temperature coefficient in a MOSFET has been obtained, and finally the application of the thermal model using the transistor as temperature sensor.

To sum up, in chapter 6, the conclusion of all the experiments and theoretical studies are exposed.

2

State of art

2.1 History

Radiotherapy starts with the X-ray invention at the end of XIX century by Röengent, a year later in 1896; it describes the first application in a malign breast tumour. By the same year Becquerel discovers uranium emits similar radiation to those described by Röengent. In 1898, Curie marriage discovers radium salts emits a same type of radiation and they studied the biological effect.

The need of characterizing the quality and amount of radiation, originate a new discipline in 1896, the *dosimetry*. Thanks to the cooperation between physicians and doctors, between 1896 and 1904, several dosimetric techniques were developed, to reproduce the exposure and to evaluate the ration between dose and effects.

At the beginning of century, X-rays were used to treat tumours, mainly dermatology tumours. During twenties or thirties, Regaud and Coutard developed treatment in sessions with external radiotherapy. From fifties started to quantify the effects of radiation with cell culture, and with the development of technology, in 1953 appeared the first lineal accelerator, which are currently used in radiotherapy treatment. In seventies, computers started to be a new tool of

controlling radiotherapy. Sterling and collaborators establish the first planned treatment in 3D (with calculation and modulated dose). In the eighties, with the creation of computer tomography (CT), the three dimension radiotherapy born. Finally, in nineties radiotherapy is assumed as a therapeutic tool for treating tumours, and positron emission tomography (PET), magnetic resonance imaging (MRI) and echography have been included in the planning of radiotherapy.

Intensity modulated radiation therapy (IMRT), is an advanced technique of radiotherapy in 3 dimensions, more accuracy, where the intensity of radiation is controlled, obtaining huge radiation dose in the tumour, and reducing the dose over the surrounding healthy tissues.

In XXI century, complex system of radiotherapy of 4D stars to appear, taking into account the physiological movements of organs, for example the lungs during the breathing (Castellanos 2006, De las Heras González 2008)

2.2 Dosimetry: basic concepts

Dosimetry tries to establish suitable magnitudes and units to estimate in a complete way the phenomena of radiation-matter interaction. This section introduces the dose concept and their different meanings, as well as some remarkable phenomena concerning to radiation.

2.2.1 Exposure

When the ionizing radiation reaches the material, it breaks the atomic or molecular structure, creating ion-electron pairs. Gamma radiation or X-rays interact with matter with three processes: photoelectric effect, Compton Effect and pair production. During these processes secondary electrons are generated, which lose the energy when they crash into the atoms in the material, leaving an ion trail.

When a photon beam incidents over a volume of matter, as in Figure 2.1 some of them go through the material without crashing with any atom, therefore they do not generate secondary electrons, for example γ_4. Other photons crash inside the volume and create secondary electrons that can escape from it, as in the cases γ_1 and γ_2. Also, there will be secondary electrons, which have been created outside the volume, go through it and they create charge inside, as in the case of γ_3.

Exposure, *X*, is defined as the quotient between the created charge, *dQ*, by the electrons that the radiation has created inside the irradiated volume and the mass, *dm*, inside the volume:

$$X = \frac{dQ}{dm} \tag{2.1}$$

dQ is the charge generated by γ_1 and γ_2, both inside and outside the volume, the charge generated by the electrons come from γ_3 is not included; although they have generated charge inside this volume. Neither new electrons created by the photons sent out during the stopping of secondary electrons are included.

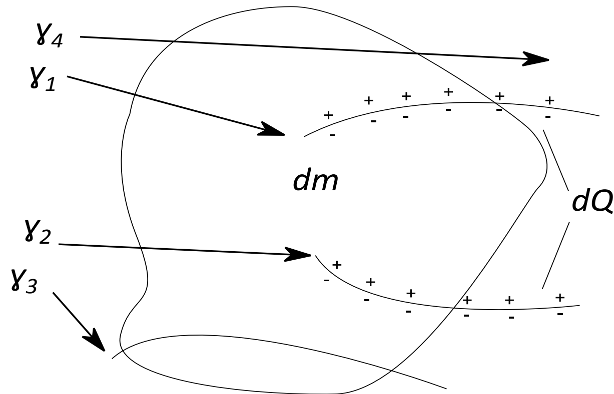

Figure 2.1 Photons incident over a volume (Ortega Aramburu and Jorba Bisbal 1994).

The unit of exposure in the S.I. is $C \cdot kg^{-1}$, although it is also used the *roentgen*, *R*, that according to (Knoll 2000) , is the radiation exposure of X or γ needed to produce an electrostatic charge (about $2.08 \cdot 10^{9}$ ions pair) in a cubic centimetre of air in normal conditions (273.15 K and one atmosphere of pressure). The ratio between both units is:

$$1R = 2.58 \cdot 10^{-4}\, C \cdot kg^{-1}$$

2.2.2 Electronic equilibrium

In a material that has been influenced by the photon beam, it is very difficult to identify the ions that come from the interaction of secondary electrons inside the volume or pairs produced by secondary electrons in the exterior. A new concept is introduced, *electronic equilibrium*, that establishes that the ionization produced outside of the reference volume by electrons generated inside of it are

compensated with the ionization produced inside by electrons produced in the exterior of the volume.

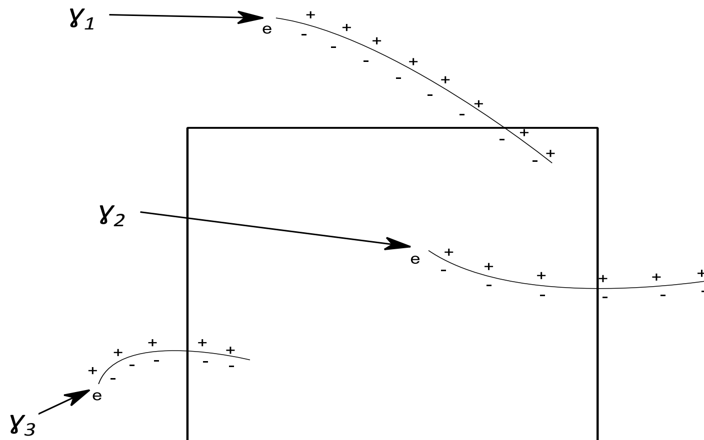

Figure 2.2 Schematic representation of the electronic equilibrium concept (Ortega Aramburu and Jorba Bisbal 1994).

The majority of radiation detectors measure the energy inside of volume of matter by the charge created inside of it. A suitable measurement must be done with the electronic equilibrium condition, where the charge entering to the volume by external process would be approximately equal to the loss of charge created by internal process.

Ionizing chambers are one of the most used instruments to measure the exposure to radiation. The detector material is a volume of air enclosed in a cavity. The cavity is manufactured with material with an atomic number similar to air. Secondary photons, electrons and positrons that reach the interior of chamber, depend on the photons incident energy and the thickness and composition of wall's chamber. Usually, the chamber works in the *build-up* zone, where the produced charge in the exterior of the cavity by secondary electrons

created inside, is higher than the produced charge inside by secondary electrons that come from exterior, then the exposure is under estimated (Figure 2.4).

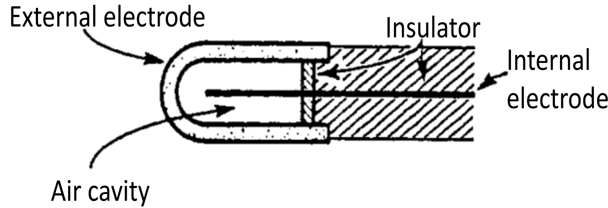

Figure 2.3 Ionization chamber scheme (Khan 1984).

When the width of walls increases, the contribution of charge created inside the chamber by secondary electrons, which come from the exterior, is equal to charge created outside. This exterior charge is created by secondary electron, which come from inside but they have been transferred to the outside of walls. Thicker walls, will also fulfil the electronic equilibrium condition, although the charge inside will be less because of beam attenuation.

Attenuation effects of radiation could be corrected by a suitable factor. Exposure, X, with the charge measured by an ionizing chamber in electronic equilibrium, has the ratio:

$$X = \frac{Q}{\rho \cdot V} \frac{1}{A} \tag{2.2}$$

with A as attenuation factor, ρ density of air, at pressure and temperature of room conditions and V the volume of air.

The thickness to get the electronic equilibrium depends on the kind and energy of ionizing radiation and the density of the material. In dosimetry, normally it is normalized the width multiply by the density of material that is known as *mass thickness*. Table 2.1 shows the

thickness to get the electronic equilibrium condition with different energies, as (Knoll 2000) says.

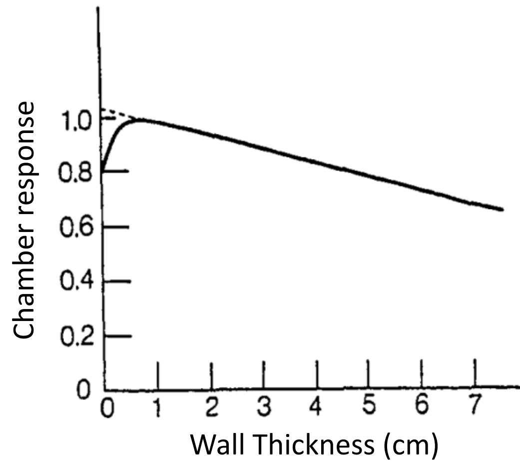

Figure 2.4 Normalised response of ionization chamber with the thickness wall (Khan 1984).

E (MV)	**Thickness (g/cm^2)**
0.02	0.0008
005	0.0042
0.14	0.014
0.2	0.044
0.5	0.17
1	0.43
2	0.96
5	2.5
10	4.9

Table 2.1 Mass Thickness to get the electronic equilibrium with photons of different energies (Knoll 2000).

2.2.3 Dose and dose rate

When ionizing radiation incident on a volume of matter, a part of the energy is deposited on it and another part escapes from it. *Absorbed dose* or *dose* is the energy absorbed from any type of radiation per unit mass of the absorber material:

$$D = \frac{d\varepsilon}{dm} \tag{2.3}$$

It is very important to highlight that the absorbed energy depend on the type of radiation, intensity and nature of irradiated material. The unit under the S.I. convention is gray, Gy (1 Gy=1 $J \cdot kg^{-1}$). Also could be expressed in rad (1 rad=1 cGy). The variation of dose during a time *dt*, is *dD*, and it is defined as *dose rate*, expressed in Gy/s:

$$\dot{D} = \frac{dD}{dt} \tag{2.4}$$

The absorbed dose in an irradiated material could be determined from the exposure, using an ionizing chamber. If the wall has the suitable thickness to get electronic equilibrium, the exposure and dose could be related to:

$$D = f_{med} \cdot X \cdot A_t \tag{2.5}$$

where A_t is transmission factor between the material and air, f_{med} the factor known as roentgen-to-rad, that establishes the ratio between absorbed coefficient of material and air. In dosimetry field, it is interesting to know the absorbed charge in the ionizing chamber under electronic equilibrium, that is proportional to dose.

2.2.4 Biological effects of radiation: equivalent and effective dose.

Biologic damage depends on the type of radiation. As an example, 1 Gy of α particles produce biologic effect twenty times higher than 1 Gy of X- rays. To establish this ratio, *quality factors*, w_R, of radiations, have been defined. This is a ponderation to be applied to dose of different irradiations to compare the effects between them. The severity and permanence of these changes are directly related to the local rate of energy deposition along the particle track, known as the *linear energy transfer*, *L*.

Type and Energy range	$\mathbf{w_R}$
Photons, all energies	1
Electrons and muons, all energies	1
Neutrons, energies:	
< 10 KeV	5
10 KeV to 100 KeV	10
>100 KeV to 2 MeV	20
> 2 MeV to 20 MeV	10
> 20 MeV	5
Protons, other than recoil protons, energy > 2 MeV	5
Alpha particles, fission fragments, heavy nuclei	20

Table 2.2 Radiation weighting factors (Knoll 2000).

The concept of *dose equivalent*, H_T, therefore, has been introduced to quantify more adequately the probable biological effect of the given radiation exposure over a tissue or organ, *T*.

$$H_T = D_{T,R} \cdot w_R \tag{2.6}$$

If there is a mix of radiations, then the total equivalent dose H_T is given by a sum over all irradiation types:

$$H_T = \sum_R D_{T,R} \cdot w_R \tag{2.7}$$

Under S.I. convention the unit of equivalent dose is J/kg, known as *sievert* (Sv). Also *rem* is used as measurement unit, 1 Sv=100 rem. To account the different radiosensitivity of various organs and tissues, a set of *tissue-weighting factors*, w_T, are introduced to allow calculation of what is now called the *effective dose*, *E:*

$$E = \sum_T w_T \cdot H_T \tag{2.8}$$

Tissue or Organs	$\mathbf{w_T}$
Gonads	0.20
Bone marrow	0.12
Colon	0.12
Lung	0.12
Stomach	0.12
Bladder	0.05
Mammary gland	0.05
Liver	0.05
Oesophagus	0.05
Bones	0.01
Skin	0.01
Others	0.05

Table 2.3 Radiation weighting factors of tissues and organs (Ortega Aramburu and Jorba Bisbal 1996).

The tissue-weighting factors are chosen to give greater weight to those organs and tissues that are most sensitive to radiation. Table 2.3, others, refers touterusn, small intestine, spleen, swindle, utero, kidney, muscles and extrathoratic region.

2.3 Types of radiation

Radiation is classified into two main categories, as shown in Figure 2.5: *non-ionizing and ionizing*, depending on its ability to ionize matter.

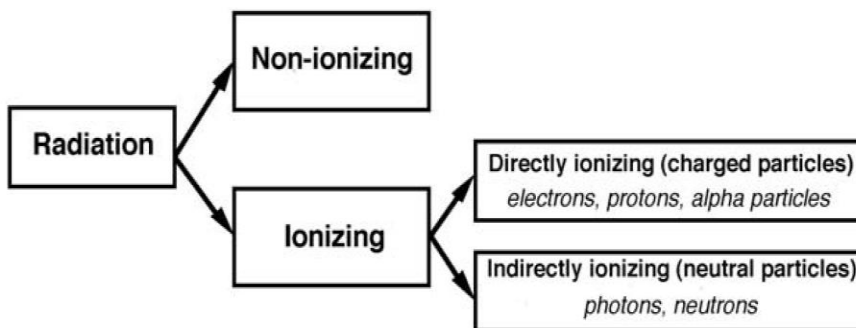

Figure 2.5 Classification of radiation (Holmes-Siedle and Adams 1993).

Non-ionizing radiation cannot ionize matter because its energy is lower than the ionization potential of matter.

Ionizing radiation can ionize matter either directly or indirectly because its energy exceeds the ionization potential of matter. It contains two major categories:

- *Directly ionizing radiation* (charged particles): electrons, protons, alpha particles, heavy ions. They deposit energy in the medium through direct Coulomb interactions between the

directly ionizing charged particle and orbital electrons of atoms in the medium.

- **Beta particles, electrons, positrons:** Beta particles have the same mass as an electron but may be either negatively or positively charged. With their small size and charge they penetrate matter more easily than alpha particles but are more easily deflected. Their velocity, normally approaching that of light, means they are lightly ionizing. The possible interactions of electrons and positrons with the medium are elastic scattering, inelastic collisions and bremsstrahlung emission; positron can also undergo annihilation, either in flight or at rest.
- **Protons:** The proton is the nucleus of a hydrogen atom and carries a charge of 1 unit. The proton has a mass some 1800 times that of an electron, and consequently is more difficult to deflect.
- **Alpha particles:** They are the nuclei of helium atoms. They have a mass of 4 and a positive charge of 2 units. Normally of high energy (in the MeV range), they interact strongly with matter and are heavily ionizing. They have low penetration power and travel in straight lines.

- *Indirectly ionizing radiation* (neutral particles) photons (X-rays, gamma rays), neutrons. In this case deposits energy in the medium through a two-step process: first charged particle is released in the medium (photons release electrons or positrons, neutrons release protons or heavier ions). Afterward, the released charged particles deposit energy to the medium

through direct Coulomb interactions with orbital electrons of the atoms in the medium.

- **Gamma rays and X-rays (photons):** These are short-wavelength form of photon or electromagnetic radiation. They have a different origin, a gamma ray come from nuclear interaction, whereas an X-ray originates from electronic or charge-particle collisions, where electron transitions between shells. Their behaviour with the matter is identical. They are lightly ionizing and highly penetrating and leave no activity in the material irradiated. The dominant physical processes are photoelectric effect, coherent (Rayleigh) scattering, incoherent (Compton) scattering and electron-positron pair production.
- **Neutrons:** A neutron has the same mass as a proton but has no charge and consequently is difficult to stop. The capture of a neutron results in the emission of a gamma ray. Neutrons are classified: thermal (<1 eV); intermediated; and fast (>100 keV).

Both directly and indirectly ionizing radiations are used in the treatment of disease, mainly but not exclusively malignant disease. The branch of medicine that uses radiation in treatment of disease is called *radiotherapy, therapeutic radiology or radiation oncology.* Electrons and gamma radiation play an important role in medical physics, since they are used directly as beams for cancer therapy, gamma beam for deepest and electron beams for superficial tumour, due to its deep in penetration. The branches of medicine that use ionizing radiation in diagnosis of disease are *diagnostic radiology* and *nuclear medicine* (Holmes-Siedle and Adams 1993, Podgosak 2006).

This work is mainly focused on dosimeters used in radiotherapy where the levels of energies are higher than in *diagnostic radiology;* and the sensitivities needed to detect the dose are smaller. Therefore, a deeper study of the radiotherapy is shown in the next section.

2.4 Radiotherapy

Radiotherapy uses ionizing radiation with a therapeutic finality. It is interested in the energy deposited in the patient by the radiation source. It is a basic treatment in the majority oncology protocols, and it is usually used to support other treatments. Only the 60% of oncology patients receive radiotherapy. Once the therapeutic decision of treating a patient with radiotherapy has been taken, six steps must be followed: simulation, planning, time check, radiation field check, doses administration and treatment registration.

The administration consists of a local and regional therapy to apply a dose to the minimum possible volume. The radiations cause cellular damage, reducing the cellular capacity of growing and reproducing. The maximum efficiency is obtained to apply the suitable dose to malign cells and producing as less damage as possible to the rest of surrounding tissue. Radiotherapy is only used when the tumour is located, and it is possible to use it in the majority of cancer. It could be used before surgery, to reduce the size of tumour, after surgery to remove possible reminiscent cells or during surgery knows as radiotherapy intra-operatory (IORT) (Castellanos 2006). Depending on the distance where the source is allocated, there are two types of radiotherapy:

- ***External radiotherapy:*** The radiation is applied on the distance. The source is located at a distance from the patient, and a beam is directed over the tumour. The dose is normally divided into sessions applied during several weeks. The applied dose per session is 1.8-2 Gy in short interval times. It depends on a dose rate of every source, but normally is around 0.5 to 5 minutes (Ortega Aramburu and Jorba Bisbal 1996). This division is used to reduce the secondary effects of radiation. The patient does feel pain and he must be immobilized.
    - Intra-operative radiotherapy (IORT): is a complementary technique to surgery, used just after removing the tumour, with the patient lying on the stretcher, and aiming at destroying the remaining cancer cells on the edge of the tumour (Aristu et al. 1999). This technique allows a visual and palpable tumour demarcation. It also permits normal dose-limiting tissues to be physically excluded from the treatment field either by displacement or by protection with lead shields (Cox 1994, Willet et al. 1999). In IORT, electron beams or low-energy X-rays are used as ionizing radiation sources. The absorbed dose range is from 10 Gy, in combination with external radiotherapy treatment, up to 30-35 Gy, in case of a single irradiation session. The beam energy depends on the depth of the tumour.

The combination of IORT and typical external radiotherapy, allows obtain advantages of both procedures: to treat wide areas use the external radiotherapy; to reduce the volume of the tumour; and selective tumoral area using IORT. All of

them could be combined with chemotherapy (Brady et al. 1990).

Figure 2.6 IORT treatment (Medical 2014).

- ***Brachytherapy:*** It consists of radioactive material in or near the tumour. The total dose is distributed in sessions with an average time of fifteen minutes.

2.4.1 Radiation sources

The machines more used in radiotherapy are: cobalt-60 source, lineal accelerator or cyclotron.

- **Cobalt-60 unit:** it consists of a source of radioactive cobalt that emits γ when the cobalt is disintegrating and it becomes Nickel-60. The average energy of photon beam is 1.25 MeV, and the maximum dose reaches a deep of 0.5-1 cm.
- **Linear Accelerator:** electromagnetic waves of high frequency are used to accelerate electron of high energies through a vacuum lineal tube. It is normally used to treat superficial tumours. The energies vary between 4 and 25 MeV, with 80 & of maximum dose in a depth of 2-6 cm.

- **Cyclotron:** is an accelerator of heavy particles to produce neutrons and proton beam. (Holmes-Siedle and Adams 1993)

2.5 Main ionizing detectors

There are different radiation detectors; however this work treats meanly in pMOS as radiation dosimeters. To understand the advantages of MOSFET, solid state dosimeters are briefly introduced.

2.5.1 Thermoluminescent dosimeters (TLDs)

These devices are based on the thermoluminescece phenomena. Light is emitted when the material is heated after exposure to radiation. An inorganic lattice could be explained as a characteristic band diagram composed of: valence diagram, with electrons bound to atoms, conduction band where the electrons are free to move, and between them, gap band with forbidden energetic states. When the lattice is doped, could appear intermediate states in the gap band. A *thermoluminescent dosimeter*, *TLD*, is normally doped with acceptor impurities which create allowed states in the gap band for electrons close to the conduction band; also with donor impurities that have a huge facility to give their electrons, and electronic state close to the valence band are created.

Light is emitted when electrons and holes recombine. When ionizing radiation is received over the lattice, electrons in the valence band are excited and promote to the conductive band (1), as it can be observed in Figure 2.7. The electron can move through the conduction band (2), until it is cached by traps (3), which have been created by acceptors impurities. At the same time, the holes are moving through

the valence band (2'), until an electron form donor impurities loses part of its energy and recombine with the hole (3'). Finally the electrons created by radiation are trapped by acceptors impurities close to the conduction band, and holes in the donor impurities close to the valence band. At room temperature, the device could be in this state during long periods of time.

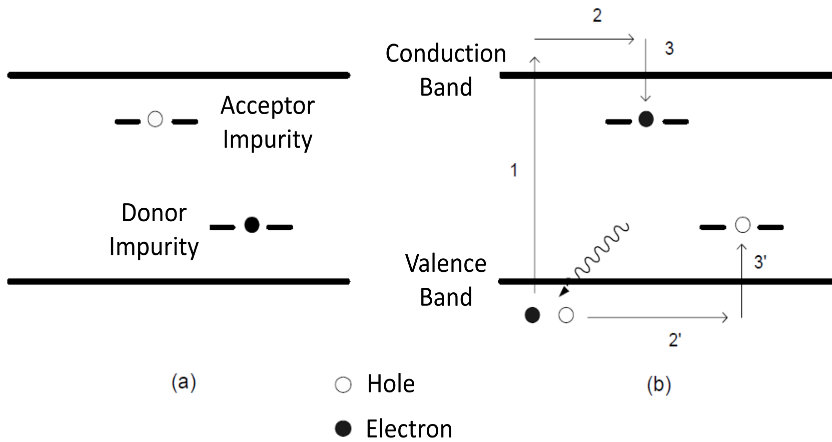

Figure 2.7 TLD band diagram a) unsensitised and b) sensitised process (Carvajal 2008).

To measure the absorbed energy, the lattice is heating, the thermal excitation of carriers is increased, and some of them get away from those states and they recombine, emitting a photon. The difference of energy between the initial state and final state is around 3-4 eV, so emitted photon is in the visible spectrum. This means the reading of dose is destructive. The photons are normally amplified with a photomultiplier and are registered during a time. The emitted light is characteristic of every material and temperature. The plot of light output versus temperature is known as the *glow curve* for that particular material (Figure 2.8).

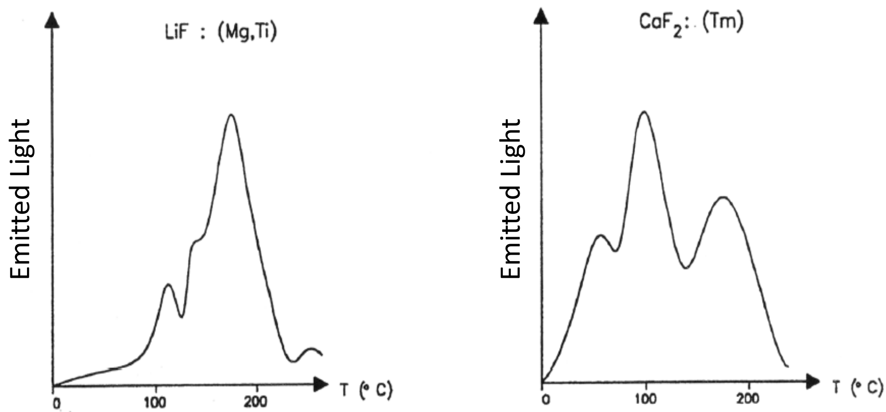

Figure 2.8 LiF and CaF_2 glow curve (Ortega Aramburu and Jorba Bisbal 1994).

Since the traps are emptied by heating, TLD are subject of fading; in the process of measuring the intensity of light in every temperature shows a high temporal dependency. During a time the holes-electrons pairs are recombining until the electronic traps are spent, and finishing the emission of light. Therefore, it is necessary a measurement protocol to avoid this fading, this is the main disadvantages of the TLD; the information is not in real time. TLDs can be reused after a further high-temperature annealing step, so long as the dose is low. They are widely used as personal or environmental dosimeters. (Carvajal 2008, Holmes-Siedle and Adams 1993, Ortega Aramburu and Jorba Bisbal 1994)

2.5.2 Semiconductor detectors

The sensing element to radiation is a semiconductor material, usually silicon or germanium. Electron-hole pairs are created when the ionizing radiation incident on the semiconductor. The pairs are moved by an electric field due to the difference of potential. Biasing the

semiconductor with special conditions, it is possible to obtain both the energy as the type of ionizing radiation.

The main advantages of semiconductor detectors are:

- Due to high density, the ionizing particles can lose the entire energy in a short path, so the efficiency per volume unit is huge.
- The needed energy to the production of electron-hole pairs is reduced, so the number of created photons or ionizing particle is higher than in other detectors. This makes statistic variation lower, and the uncertainty is reduced, because typical deviation depends on the square root of number of generating pairs. To produce an electron-hole pair is necessary only 3.5 eV for silicon, and 2.8 eV in the case of germanium. So if an incident particle with 5 MeV lose their energy in the silicon, it will produce $1.43 \cdot 10^6$ pairs. If an important number of photons of 5 MeV incident, it will be obtained a statistical distribution of the number of created pairs, N, per the population of incident photons. If it is assumed a Poisson distribution, the standard deviation of the number of pairs would be $\sqrt{N}$. In the example, a $\sigma = 1.2 \cdot 10^3$, that is 0.08% of the average number of created pairs.
- The mobility both free electron in the conduction band and holes in the valence band, is elevated. Since the detection volume is small, the recollection charge time is very short, and the resolution time is the order of nanoseconds.

(Ortega Aramburu and Jorba Bisbal 1994)

Homogeneous detector

A pure semiconductor is used as sensitive material to radiation, intrinsic semiconductor. It is normally known as *homogeneous detector* or *intrinsic detector*. The typical materials are Si or Ge between two electrodes, where electron-holes pairs are created by radiation. The pairs are separated by an electric field, originated by the difference in potential between the electrodes. The originated current goes through a resistor, where it generates a voltage proportional to the number of created pairs by ionizing radiation.

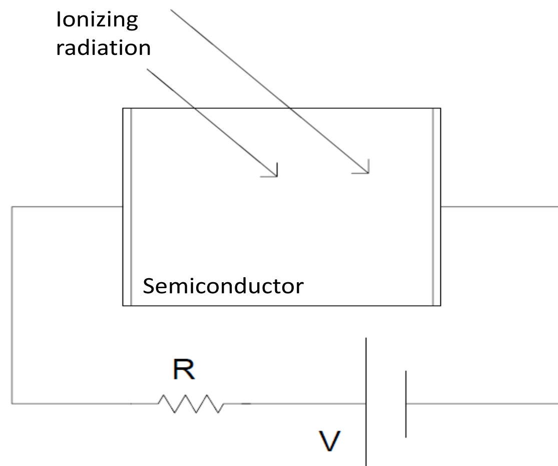

Figure 2.9 Intrinsic semiconductor detector (Carvajal 2008).

The carriers must be collected by the electrodes before an important number of them recombine. Then the recollected time must be neglected compared with the lifetime of carriers in the semiconductor. Recollected time could be estimated as:

$$t_c = \frac{x}{\mu \cdot E} \tag{2.9}$$

with μ carrier mobility in the semiconductor, E electric field and x the distance between electrodes. This time could be reduced, increasing carrier mobility, purifying the silicon or germanium and reducing the temperature. However, there are limits, because the hole or electron mobility has a maximum per temperature that cannot be exceeded. With 300 K the maximum mobility of electrons in the silicon is 1900 $cm^2V^{-1}s^{-1}$, and for holes, 550 $cm^2V^{-1}s^{-1}$. Considering this, it is necessary to increase the voltage between electrodes avoiding the recombination. The required voltage creates parasitic currents that mask the increasing current due to radiation. To avoid these currents it would be necessary a resistivity of material around 10^8 Ωcm, and the silicon has $2 \cdot 10^4$ Ωcm. This is the reason because these detectors are not very common (Carvajal 2008).

Detector junction

It is important to use material with high resistivity to reduce the parasitic currents in the semiconductor, when high electric fields are applied. Therefore, to obtain an area with great resistivity, rectifier diodes are used. It is widely known, putting in touch two semiconductors with impurities form different nature, donors (n type) and acceptors (p type), is created a region close to the junction where the number of free carriers is non-existent, as a result of migration to the other semiconductor zone in a diffusion process. This area is known as *depletion zone*, where the electric field is very high, and the created electron-hole pairs are separated.

To increase the detection volume, the junction is applied a reverse bias, where n type has more potential than p type. In this case, the current intensity through the junction is the leakage current of junction and the current of the pairs created by the radiation. With

the higher reverse bias, the bigger depletion zone, but it never could be more than the breakdown voltage of junction. Doped diodes have usually areas of micrometres or millimetres. The electric field in the junction is around thousands of voltages per centimetre, for reverse bias of hundreds of volts. Then, it is not very advisable to use this detector in vivo dosimetry, for security of patient (Carvajal 2008).

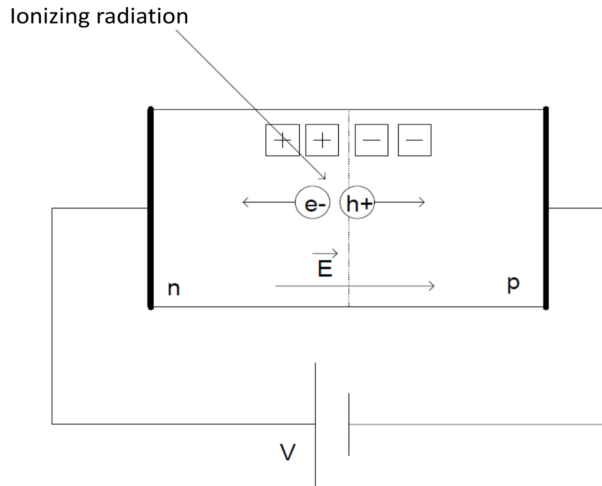

Figure 2.10 Electron-hole pairs creation in the depletion zone.

PIN diode

Junction detector needs an important voltage to get a depletion zone with the right dimension to detect ionizing radiation. To increase this area, a semiconductor without dope is included between n type and p type semiconductors. As impurity concentration in very reduced, the charge density is close to zero, and the electric field maintains constant. This structure is known as *PIN diode*, and it consists of a p type region, an intrinsic semiconductor area, and a n type region.

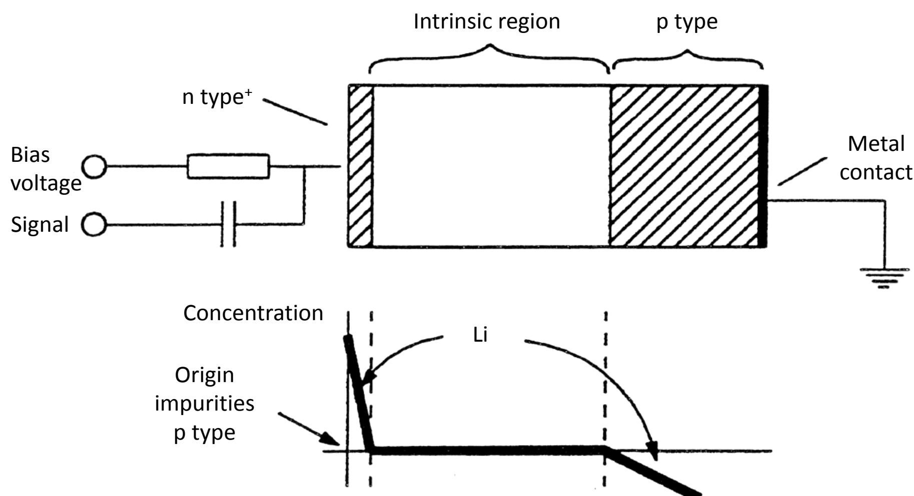

Figure 2.11 PIN diode (Ortega Aramburu and Jorba Bisbal 1994).

Because this new area, the absolute value of breakdown voltage is higher than in a normal diode, because of the significant increase of the potential barrier, reducing the leakage current due to the tunnel effect. These detectors have the advantage of immediate readings dose, very important in vivo dosimetry. However, they need high bias during irradiation periods (Carvajal 2008).

2.6 Fundamentals of the Metal-Oxide-Semiconductor Field Effect Transistors (MOSFET)

This section will explain the theoretical base to understand the transistor MOSFET as dosimetric sensor. A brief resume of electrical characteristic and structure, and the influence of radiation over them are exposed. Finally, two commercial systems based on MOSFET will be referenced.

2.6.1 Structure

The *metal-oxide-semiconductor field effect transistor* (MOSFET) is a four-terminal device, which are named as source (S), gate (G), drain (D) and body or bulk or substrate (B). In most common applications, the body is connected to the source, making it a three-terminal device. Its performance is based on the regulation of its conductivity between two of its terminals, drain and source, with a controlled electric field in a third terminal, gate. The transistors used in this work are *p type*s that are built over a *n type* semiconductor bulk. An elevated concentration of acceptor impurities is diffused to create the drain and source regions. These regions are p^+ type and normally source is used as reference terminal. An insulating layer is growing over the body. Silicon dioxide (SiO_2) is the material usually used. Over it, a metal, typically Aluminium (Al) or polycrystalline silicon builds the transistor gate. This structure is known as *Metal Oxide Semiconductor*, MOS (Carvajal 2008).

The traditional geometry used in MOSFET is the lateral one, commonly known as lateral transistor, where the distribution between drain, channel and source is planar Figure 2.12a. An especial type of lateral transistors manufactured specifically to detect radiation is *Radiation Sensing Field Effect Transistors* (RADFET). Their properties will be studied in the next sections.

Many other structures have been proposed to improve MOSFET performance with higher response speed, lower power consumption and more reliable operation. The second representative structures used in this work with the classical one is the double-diffused MOS (DMOS).

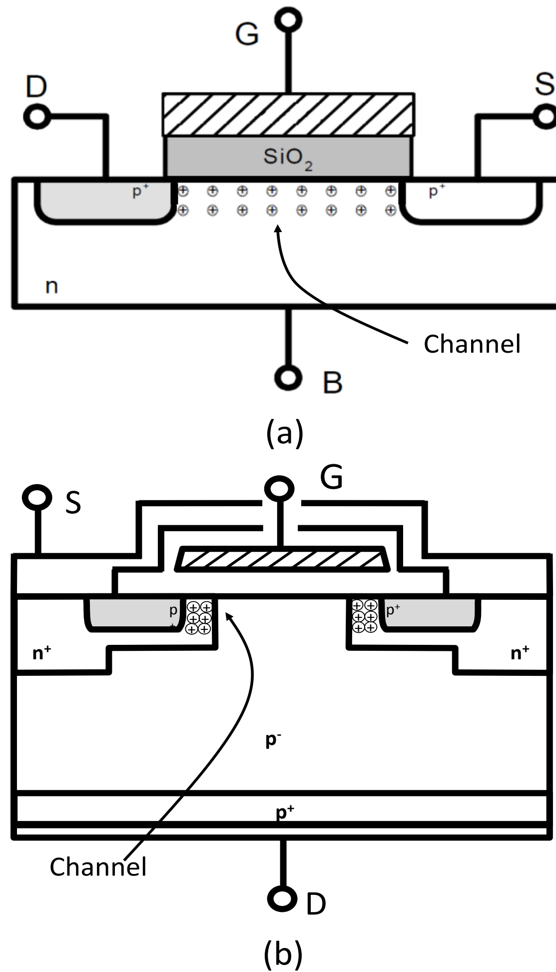

Figure 2.12 MOSFET geometries: a) Lateral and b) Vertical.

The distribution in a DMOS is vertical, therefore they are also known as VDMOS or Double-Diffused MOS or simply DMOS. In Figure 2.12b shows the physical structure of device, the source electrode is placed over the drain, resulting in a current mainly vertical when the transistor is in the on-state. A parasitic diode appears between the source and drain, and the bulk terminal is removed, resulting in a three terminals device. The diffusion refers to the manufacturing process, it is necessary a double diffusion process to get

the *p* and *n regions*. This structure has been fabricated in both a vertical (VDMOS) and horizontal direction, but the vertical is the structure more extended. In this geometry the voltage rating is a function of the doping, while the current is a function of the channel width (Sze 1981). This type has a short channel length, therefore less sensitive to radiation. This is due to the only sensitive parts are the region of channel below the gate.

2.6.2 *I-V* curves

When a positive voltage is applied to the gate, with the other three terminals short-circuited, an electric field is built, and the electron concentration near to Si-SiO_2 interface increases. The majority carriers in the *n* type substrate, has increased, and the transistor is in the *accumulation region*. When the gate voltage is negative, the electrons go to the bulk, and the holes concentration close to the interface increases, the transistor is in *weak* or *moderate inversion regions*. If the voltages are even more negative, and holes concentration is similar to electrons concentration, the transistor is in *strong inversion*. This elevated holes concentration, below insulator, and between source and drain is the *inversion channel*.

The minimum voltage in absolute value, to apply between gate and source, to create the channel it is known as threshold voltage, V_t, which is negative in case of pMOS transistors. Once the channel is created, if a small voltage is applied between drain and source, current flows between them. The carriers are holes, and this state of the transistor is the *linear region* or *triode* (equation (2.10)). If the voltage between the drain and source increase, $|v_{DS}|$, there is a point, when v_{GD}

$= V_t$, the channel is depleted. If v_{DS} is even more negative, the channel disappears near to drain, and the carriers have drastically reduced.

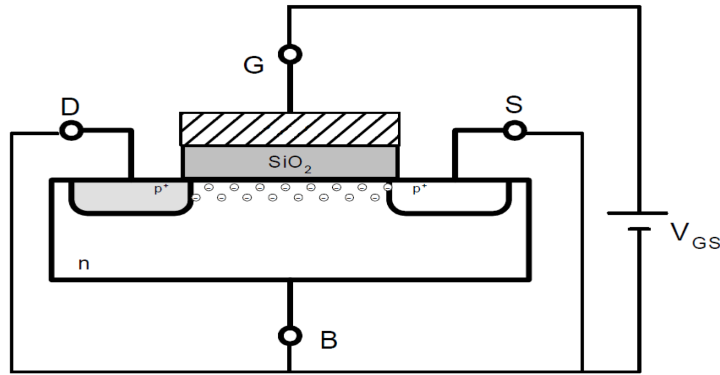

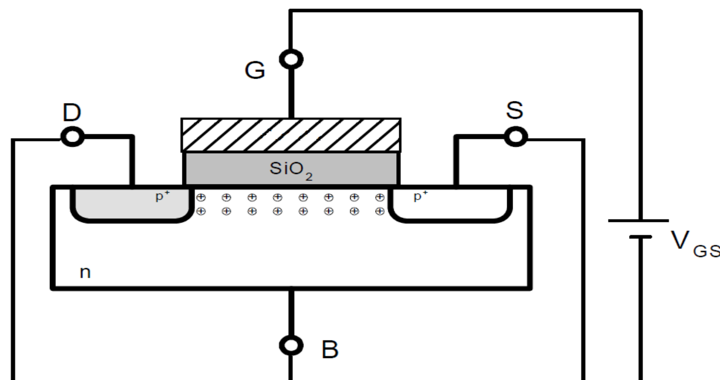

Figure 2.13 a) pMOS in accumulation region. b) pMOS in inversion region (Carvajal 2008).

This means a huge resistance and the variation between drain and source has low influence in the current flows by the channel; this region is known as *the saturation region* (equation (2.11)).

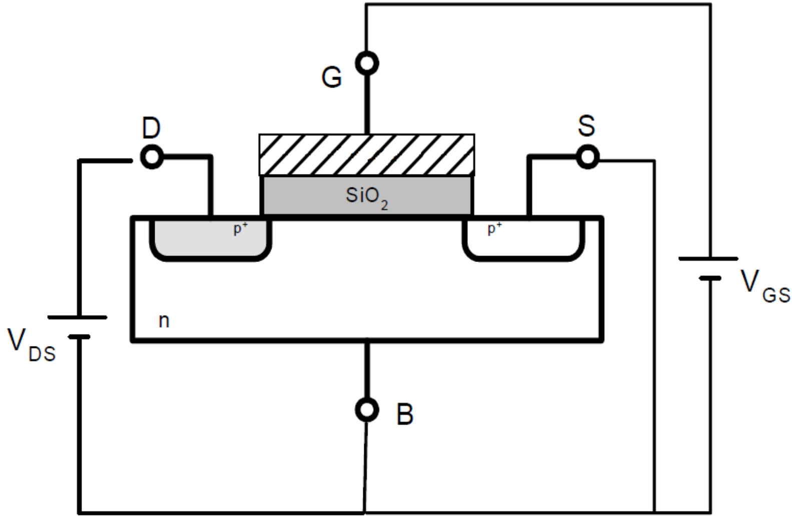

Figure 2.14 Biased pMOS with different voltages (Carvajal 2008).

In a pMOS transistor v_{GS}, v_{DS}, $v_t < 0$, to work with a simple notation, the absolute of these magnitudes is used. The current in the different regions describe is expressed as:

$$i_D = -\beta\left((|v_{GS}| - |V_t|) \cdot |v_{DS}| - \frac{1}{2}v_{DS}^2\right) \Leftrightarrow |v_{GS}| \geq |V_t|, |v_{DS}| < |v_{GS} - V_t| \quad (2.10)$$

$$i_D = -\frac{\beta}{2}\left((|v_{GS}| - |V_t|)^2(1 + \lambda \cdot |v_{DS}|)\right) \Leftrightarrow |v_{GS}| \geq |V_t|, |v_{DS}| \geq |v_{GS} - V_t| \quad (2.11)$$

Where β, is commonly accepted as transconductance, $\beta = k_p \frac{W}{L}$, with $k_p = \mu_p C_{ox}$. W and L are the width and length of channel, respectively, μ_p as hole mobility and C_{ox}, is the oxide capacity per surface unit. C_{ox} is defined as $C_{ox} = \frac{\varepsilon_{ox}}{t_{ox}}$, with dielectric constant, ε_{ox} and oxide thickness, t_{ox}. λ is the parameter to model the effective length of channel in saturation. The negative sign of current means that, i_D, in the pMOS transistor goes from source to drain (Carvajal 2008).

For the *I-V* characteristic curves, a first level model has been utilized for the pMOS transistor, except to model the effective length of channel. This model is enough to justify the results of this work. Figure 2.15 shows the typical curves in a pMOS transistor, both saturation and lineal region (Carvajal 2008, Sze 1981).

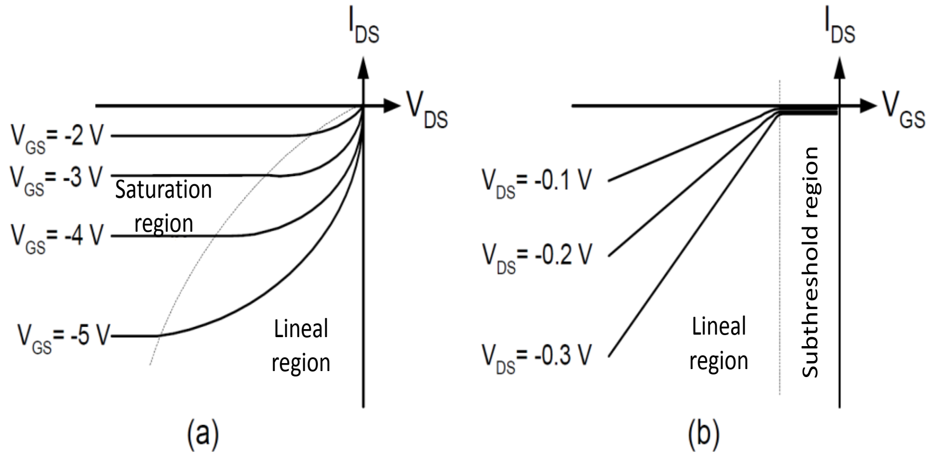

Figure 2.15 *I-V* curves in a pMOS transistor. a) Intensity versus drain-source voltage in different gate-source voltages. b) Intensity versus gate-source voltage for different values of the drain-source voltages (Carvajal 2008).

Subthreshold Region

Subthreshold regime deserves a specific section, because although it is not very typical to work with the transistor in this state, it is extremely interesting in dosimetric field, as it will be explained in the next sections.

When gate voltage is below the threshold voltage and the semiconductor surface is in weak inversion, the corresponding drain current is called the subthreshold current. In weak inversion, the drain

current is dominated by diffusion (Tsividis 1987, Overstraeten, Declerck and Muls 1975), that is defined as:

$$i_D = -\frac{W}{L}\mu_p \int_0^{v_{DS}} Q_I(\Phi_S)d\Phi_S \tag{2.12}$$

with μ_p holes mobility, Q_I gives the mobile hole charge per unit area in the inversion layer, Φ_s, surface potential. To evaluate the integer, Q_I must be known function of Φ_s. to maintain the condition of conservation of the electric potential; the ratio between gate source and Φ_s is:

$$v_{GS} = \Phi_{MS} - \frac{Q_{ox}}{C_{ox}} + \Phi_S - \frac{Q_I + Q_B}{C_{ox}} + \frac{qD_{it}}{C_{ox}}(\Phi_S - \Phi_{S0}) \tag{2.13}$$

where Φ_{MS} is the metal semiconductor work function difference, Q_B the depletion charge per unit area, C_{ox} is the oxide capacitance per unit area; Q_{ox} is the total oxide charge per unit area at flat-band voltage. D_{it} is the interface state density per unit area. Φ_{S0} is the surface potential when the charge in the interface state is non-existent (Sze 1981, Banqueri 1994).

2.6.3 Thermal dependency of *I-V* curve

The device temperature affects the parameters which define the *I-V* curve, as mobility and threshold voltage. The mobility in a semiconductor is reduced as the temperature increases, because the thermal movement (phonon scattering) in the lattice and the carriers increase the probability of crashing into them and with the net. The thermal dependency of carriers mobility in the silicon can be modelled by (Tsividis 1987):

$$\mu(T) = \mu(T_r)\left(\frac{T_r}{T}\right)^a \tag{2.14}$$

with $\mu(T)$ as mobility in temperature, T, $\mu(T_r)$ is carrier mobility to reference temperature, T_r, and a is a constant, between 1.2 and 2.0. The temperatures must be expressed in Kelvin.

Minority and majority carrier density in a semiconductor, increase with the temperature. This produces the strong inversion, and the channel creation, take place with gate-bulk voltages smaller in absolute value, and then the threshold voltage is reduced. The thermal dependency can me modelled with a lineal ratio (Tsividis 1987):

$$|V_t(T)| = |V_t(T_r)| - \alpha_{V_t}(T - T_r) \tag{2.15}$$

α_{Vt} is the thermal coefficient of threshold voltage.

Working in the saturation region, and neglecting channel length modulation, the *I-V* characteristic comes from (2.11):

$$|i_D| = \mu_p(T)C_{ox}\frac{W}{L}\frac{1}{2}(|v_{GS}| - |V_t|)^2 \tag{2.16}$$

In low levels of currents, with small values of $|v_{GS}|$ similar to the threshold voltage, the effect of decreasing voltage, $|V_t|$, dominates against the reduction of mobility. In low current, an increase of temperature, with $|v_{GS}|$ constant, results in an increase of drain current. When there is a considerable intensity, and $|v_{GS}|$ exceeds the threshold voltage value, the reduction of mobility with temperature dominates, therefore the intensity is decreased when the mobility increase and the gate-source voltage maintains constant.

There is a region of current, where the reduction in absolute value of threshold voltage and mobility with the temperature are compensated, and the ratio $|i_D|$ and $|v_{GS}|$ is constant with thermal variations. This region is named as *Zero Temperature Coefficient*, *ZTC*, and it shows in Figure 2.16. When the current in the MOSFET,

maintains in this *ZTC* region, the gate-source voltage is unchanged with variations in temperature. This has a special importance in this work (Carvajal 2008).

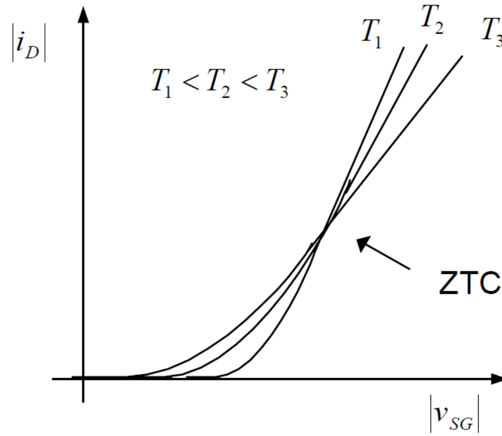

Figure 2.16 *I-V* curve in saturation, with $v_{GD} = 0$ for different temperatures (Carvajal 2008).

2.7 Ionizing radiation effects in MOSFET

The electron-hole pair creation and trapping of charges are the main mechanisms that take place to detect ionizing radiation with MOSFET. First, an electric field separates the pairs created by radiation and afterward the holes sweep along an area where there are a lot of traps and the holes stay placed (see Figure 2.17). The radiation damage in the MOSFET consists of three main components:

- the trapped charge build-up in the oxide
- an increase in the number of interface traps.
- an increase in the number of bulk oxide traps.

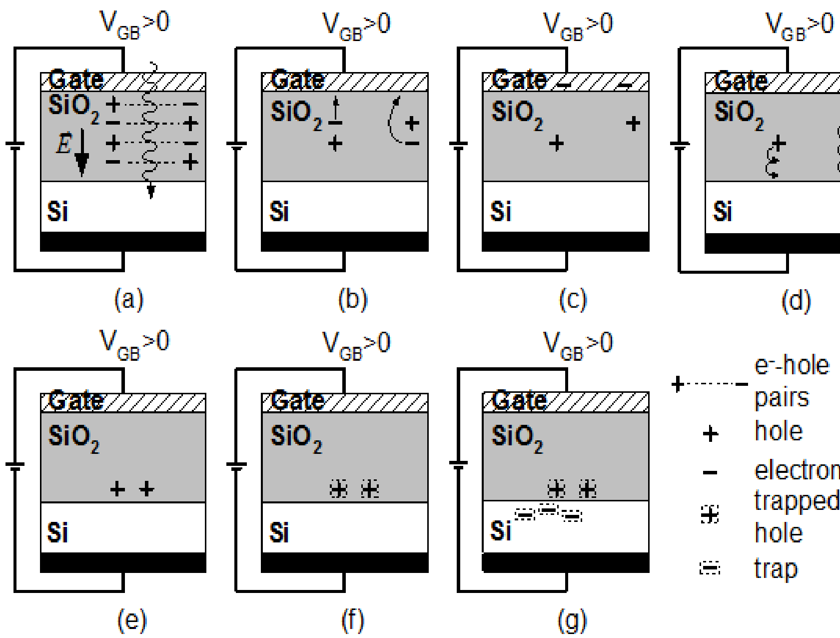

Figure 2.17 Pair production and trapping at interface traps. a) Ionizing radiation creates electro-hole pairs b) Electrons sweep out to the gate and holes to the bulk c) Holes move slower to the bulk e) Holes reach the bulk f) Trapped holes in the interface traps g) Superficial states, traps in the silicon interface (Carvajal 2008).

Electrons are very movable in SiO_2 and move quickly to the contacts, in contrast the holes have a very low effective mobility and its transport is via a complex stochastic trap-hopping process, some of them may be trapped within the oxide resulting in a positive charged net. The number of electron-hole pair generated is directly proportional to the absorbed energy by the material; the total damage is also roughly proportional to the total dose of radiation received by the device (Carvajal 2008).

2.7.1 Hole creation and trapping

Type p MOSFET, is mainly studied, because the threshold voltage in the n-channel transistors has no a monotonous behaviour with the radiation, thus is not very used in dosimetry. The part of a MOS structure most sensitive to ionizing radiation is the oxide insulation layer. MOS structure can be also used as radiation sensor (Yilmaz, Doğan and Turan 2008, Yilmaz and Turan 2008, Yilmaz, Kaleli and Turan 2007). When a positive voltage between gate and bulk, V_{GB}>0, is applied, an electric field appears, between the gate and bulk, as it can be observed in Figure 2.17 and Figure 2.18a. Electric field exists in the areas where the energy bands of semiconductors have bent, the oxide and nearby to the interface. When a positive voltage is applied V_{GB} >0, high electron density appears in the interface Si-SiO2, and the transistor is in accumulation region. The pairs created in the interface are separated by the electric field, the electrons are swept to the gate and the holes recombine with electrons of the bulk. In the oxide, the electric field is high enough to separate the pairs, in this case, the electrons go to the gate, and the holes are confined in the traps.

Also, when there is no bias in the gate of the transistor the radiation can be detected, because there is an electric field caused by the difference of working function of metal in the gate and the semiconductor in the bulk (Figure 2.18b). The electrons created by the ionizing radiation go to the gate, and the holes to the interface.

Due to the electric field, the holes are swept to the interface, and the density of charge Q_0 increases, that produces an increase of threshold voltage $|V_t|$. It is necessary to study in detail the creation and separation of holes in the oxide.

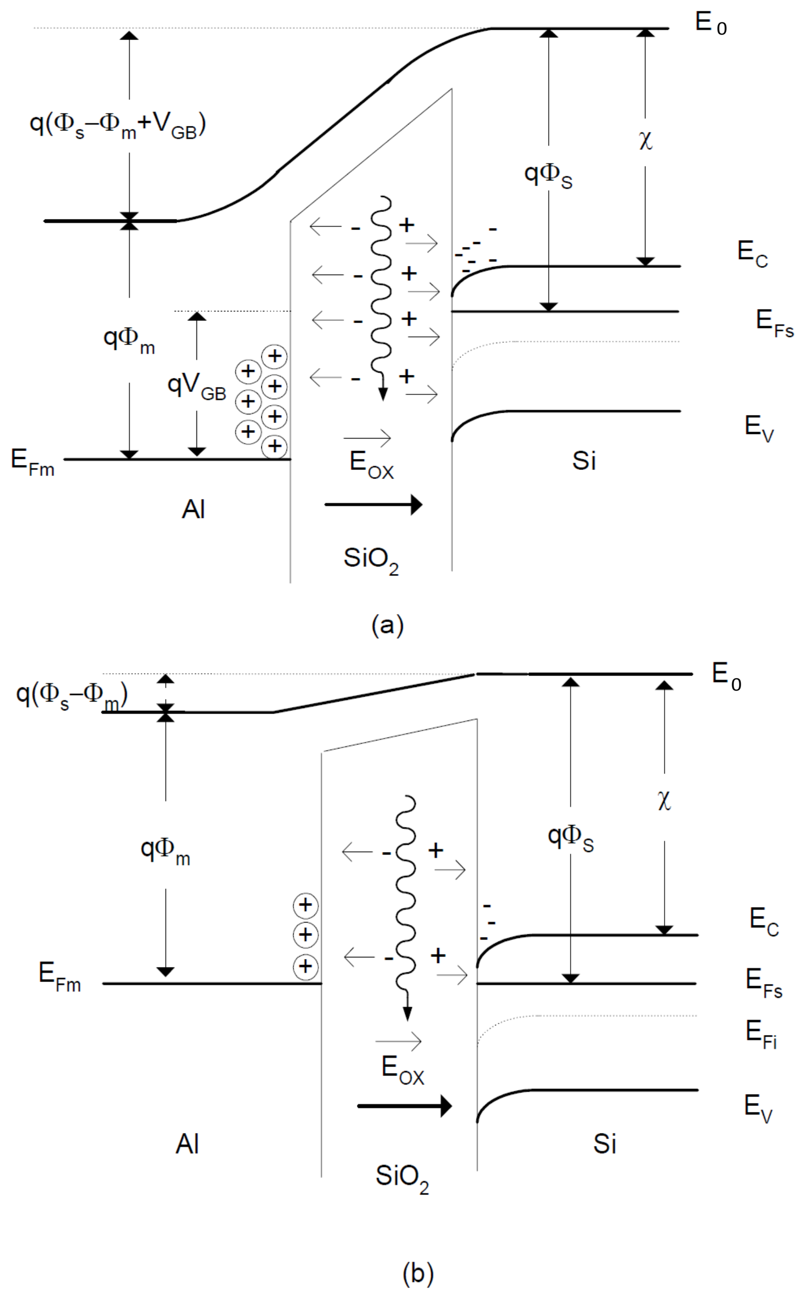

Figure 2.18 Electron – hole pairs separated by an electric field in the oxide. a) Positive bias on the gate b) No bias on the gate (Carvajal 2008).

As it has been said, ionizing radiation produces electron-hole pairs, to do that, the minimum energy to create a pair in the SiO_2 is (17 ± 1) eV, (Benedetto and Boesch 1986) says. (Oldman 1999) details that the number of pairs created per unit in the oxide volume produced by a rad could be calculated, resulting in $8.1 \cdot 10^{12}$ $cm^{-3}rad^{-1}$. The part of holes which escapes from the electric field is denoted as $fy(E_{ox})$. It depends on the electric field and the density of pairs created. By (Ma and Dressendorfer 1989), the fraction varies between 0.1 and 1.0. There are two analytic models to explain the recombination: the Smoluchowski Onsager (Onsager 1938) or *geminate* model and the columnar model (Jaffe 1929). In both cases the fraction of pairs that escapes to recombination increase with the electric field.

Electrons generated are much more movable than the holes, and they are swept out from the oxide to the gate in times of *ps*. The holes that escape to the initial recombination are relatively immobile. This difference is due to different mobilities of electrons and holes in the SiO_2, the electron mobility is much higher than the hole mobility. (Ma and Dressendorfer 1989) says the electron mobility is around 20 $cm^2V^{-1}s^{-1}$ in room temperature, and the maximum drift velocity could be 10^7 cms^{-1}, when high electric field are applied. In the case of hole mobility depends strongly on the electric field and temperature. In a room temperature, the mobility varies from 10^{-4}-10^{-11} $cm^2V^{-1}s^{-1}$ with the electric field. Accordingly the hole mobility is a hundred times slower than the electron one (Carvajal 2008).

The holes move slowly towards interface with two main transport mechanisms (Ma and Dressendorfer 1989): across the valence band or with energetic states in the band gap. The states created by radiation in the band gap of SiO_2, could be filled by electron comes from the valence band (see Figure 2.19). The hole created in the

valence band due to the occupation of the trap, moves to the interface by means of a new occupied trap, which donates its electron. When the trap has given its electron, and neutralizes the hole, starting again the process of transporting. This mechanism depends on the temperature and the energy of the states in the gap band. This time has a huge dispersion, because depends on random processes of occupying and emptying of states of energy. For high temperatures, these times at different levels of energy tend to be similar and the dispersion is reduced.

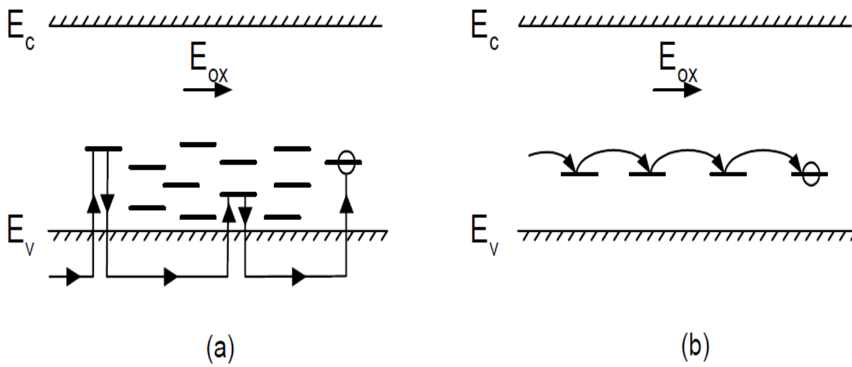

Figure 2.19 Holes transport in the oxide: a) Transport through valence band b) Transport by tunnel effect with traps in band gap (Ma and Dressendorfer 1989).

The second transport mechanism is based on the tunnel effect between holes states to others states in the band gap. This process is activated by temperature, and it has a new random behaviour, because it relies on the height and thickness of potential barrier, which depends on the spatial orientation of molecules in the SiO_2.

All traps created by radiation, are close to the interface, around 10 nm. Therefore, the response of the device hinges on the

manufacturing process, because it is based on superficial phenomena (Carvajal 2008).

2.7.2 Influence on *I-V* curves

Ionizing radiation creates electron-hole pairs and traps in the oxide, but also new allowed states are created in the bulk, in the vicinity of the interface. *I-V* curves are influenced by these new states; therefore MOSFET parameters affected by radiation will be studied along this section.

Threshold voltage effects

It is widely known threshold voltage in a pMOS transistor is defined as (Tsividis 1987):

$$V_t = -2\Phi_F + \Phi_{MS} - \frac{1}{C_{ox}}(Q_b + Q_{ss}) \tag{2.17}$$

where, $-2\Phi_F$[1] is the voltage needed in the gate of transistor to produce strong inversion in the bulk and in the vicinity of the interface (Sze 1981), Φ_{MS} is the difference in work functions of the metal (Φ_M) and the semiconductor (Φ_S) in a MOS structure. Q_b is the depletion charge that is the charge density at the interface when a negative voltage is applied to the gate, with the bulk as reference. Q_b in a pMOS is positive because the ionizing impurities are donors. It is defined from (Sze 1981, Tsividis 1987) as:

[1] In fact, this is the value of the beginning of moderate inversion, however in the ideal case; it is adopted as limit of strong inversion.

$$Q_b = \sqrt{2qN_D\varepsilon(2\Phi_F + v_{BS})} \tag{2.18}$$

with q as electron charge, N_D is the density of donor impurities in the bulk, ε the dielectric constant in the silicon, $\Phi_{F,}$ is the Fermi level and v_{BS} appears when the bulk is biased to a different voltage to the source (Body effect). This charge density creates an electric field, which repel the holes, thus the contribution to the threshold voltage is negative:

$$\Delta V_{GB}|_{Depletion\ charge} = -\frac{Q_b}{C_{ox}} \tag{2.19}$$

Finally, if the MOS structure is considered no ideal, a new factor due to imperfections, $Q_{ss,}$ must be taken into account, in the threshold voltage. These imperfections appear during the manufacturing process, and normally are positive. They have a negative influence in the threshold voltage, because they also repel the needed holes to build the channel.

$$\Delta V_t|_{Imperfetions} = -\frac{Q_{ss}}{C_{ox}} \tag{2.20}$$

Remembering C_{OX} is the capacity per oxide unit.

$$Q_{ss} = Q_0 + Q_G \tag{2.21}$$

Q_0 is the charge in the bulk-oxide interface, normally positive, and Q_G the charge in the metal-oxide interface, normally negative. Therefore, Q_{ss} is considered the factor of threshold voltage due to charge trapped in the MOS structure. This charge density could be changed caused for external factor, as for example ionizing radiation. If it is defined Q_{OT}, as the trapped charges in the oxide, and Q_{IT}, the trapped density charge in the interface, the shift in the density charge of the MOS could be written:

$$\Delta Q_{ss} = \Delta Q_{OT} + \Delta Q_{IT} \tag{2.22}$$

Then the threshold voltage shift could be defined:

$$\Delta V_t = -\frac{Q_{ss}}{C_{OX}} = -\frac{1}{C_{OX}}(\Delta Q_{OT} + \Delta Q_{IT}) \tag{2.23}$$

Usually the trapped charge in the oxide is positive, however, the trapped charges in the bulk need a detailed analysis. To understand the effects of traps over the threshold voltage, it is necessary to know some characteristics of them (Oldman 1999):

- Traps are commonly in the band gap.
- There are two types of traps: donor and acceptor traps, both neutral when they do not have a charge.
- The majority of traps over the half of band gap are acceptors and below are donors.
- A donor trap below Fermi level is occupied, thus in a neutral state. Acceptor traps are empty, therefore in a neutral state, when they are over the Fermi level.

Silicon traps are the main reason of the diverse performance between pMOS and nMOS transistors. In pMOS when the gate is biased with a negative voltage, the electrons in the nearby to the interface, goes to the bulk, and the band diagram curves upward. In a similar way, the energy band in the acceptor traps curves, then the traps which were filled before inversion (Figure 2.20a), now are over the Fermi level, thus empty and in neutral state (Figure 2.20c). Some donor traps, which were without ionizing because they were below the Fermi level (Figure 2.20a), now are over it, accordingly a positive ionizing of them happens (Figure 2.20c). This increase the effect of the positive traps charge in the oxide, therefore the threshold voltage is even more negative:

$$\left.\begin{matrix}\Delta Q_{IT} > 0\\ \Delta Q_{OT} > 0\end{matrix}\right\} \Rightarrow \Delta Q_{ss} > 0$$

In a nMOS, when the flat band voltage is applied, the situation (Figure 2.20b) happens, the majority acceptor traps are empty and donor traps are ionized, and some of them in neutral states.

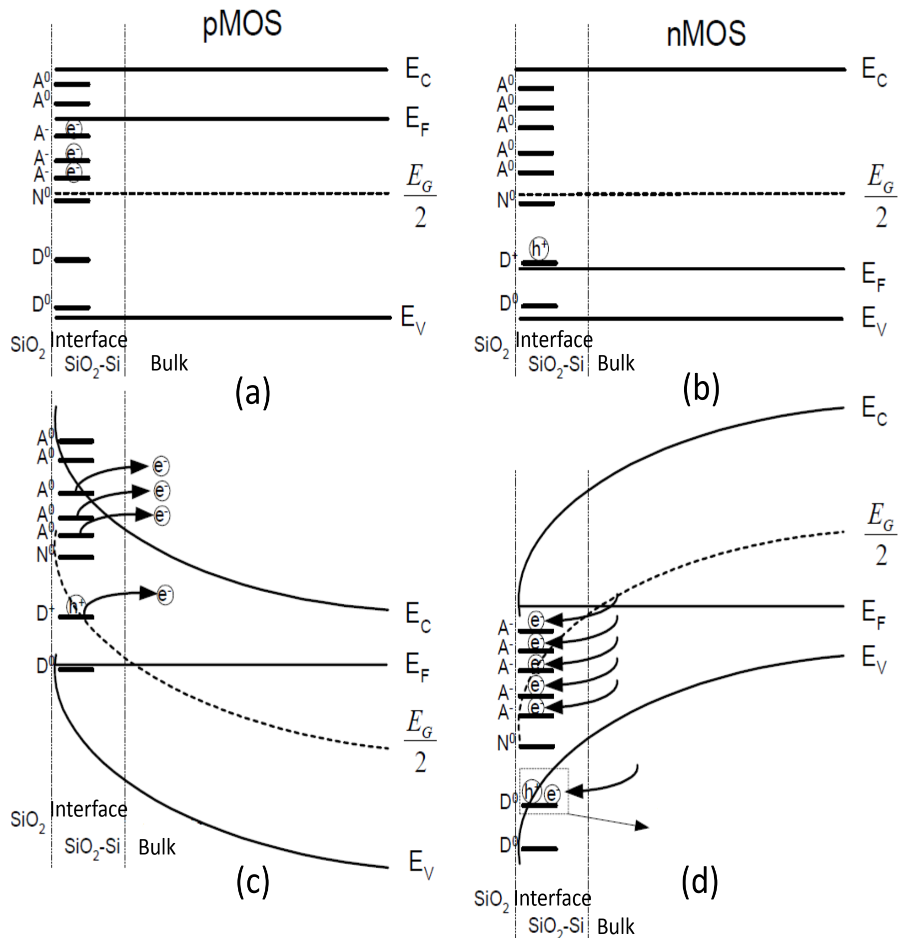

Figure 2.20 Energy band diagram of traps created by radiation a) pMOS after irradiation with a flat band voltage. b) nMOS after irradiation with a flat band voltage. c) Strong inversion diagram in pMOS with negative bias on gate. d) Strong inversion diagram in nMOS with positive bias on gate. (Carvajal 2008).

When the gate is biased with a positive voltage, the curves go into downward (Figure 2.20d). The donor traps are now below the Fermi level, thus they are occupied and neutral state. On the other hand, acceptor traps below the Fermi level are negatively ionized (occupied). Then, a negative density appears close to the interface due to superficial traps. Then, in a nMOS:

$$\left.\begin{array}{l}\Delta Q_{IT} < 0 \\ \Delta Q_{OT} > 0\end{array}\right\} \Rightarrow \Delta Q_{ss} > 0 \; or \; \Delta Q_{ss} < 0$$

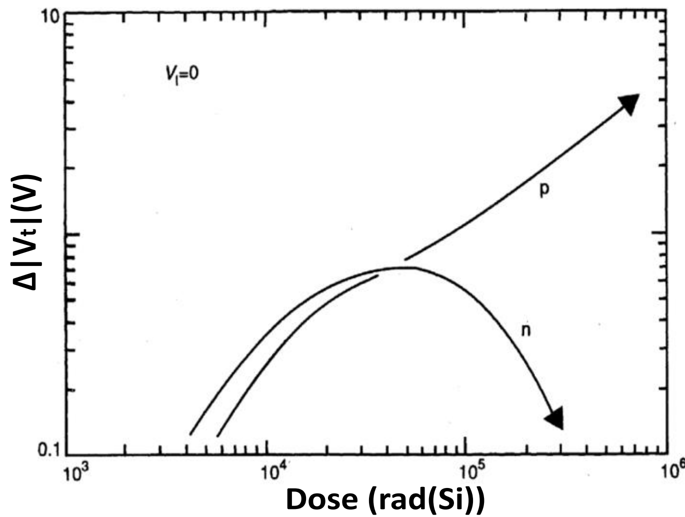

Figure 2.21 nMOS and pMOS threshold voltage shift (Freeman and Holmes-Siedle 1978).

The negative charge in the interface weakens the effect of positive traps in the oxide; therefore the threshold voltage in a nMOS could recover (see equation (2.23)). Figure 2.21 shows the experimental results of (Freeman and Holmes-Siedle 1978), where the threshold voltage shift is compared for pMOS and nMOS transistors. The rebound effect can be observed for the nMOS type. This is the reason

because commonly the pMOS transistors are used to detect radiation (Carvajal 2008).

In a pMOS trapped charge density requires an exhaustive analysis. They could be also defined as:

- **Fixed traps (FTs):** represent the traps created in the gate oxide that do not have the ability to exchange the charge with a channel (substrate) within the transfer/subthreshold characteristic measurement time frames. The shift in density of FTs is denoted as ΔQ_{FT}. FTs could contain a small amount of slow switching traps (SST) that are located deeper in the oxide; since there is not enough time for the carriers from the channel to reach them during measurement frames, this amount is normally underestimated. FTs are usually deeper in the oxide. During the long time post-stress annealing they can only be permanently recovered.
- **Switching traps (STs):** represent the traps crated near and at the oxide/substrate interface. In the interface capture the carriers from the channel (exchange charge with channel) during the time frames of electrical measurements. The shift in density of STs is denoted as ΔQ_{ST}. The STs created in the oxide, near interface are called the *slow switching traps* (SSTs) or border traps, while the STs created in this oxide/substrate interface are called either the *fast switching traps* (FSTs) or true interface traps (or only interface traps). Densities denoted as ΔQ_{SST} and ΔQ_{FST} respectively. FTs represent traps in the gate oxide that do not exchange the carriers from the channel, while the SSTs and FSTs, forming the STs, represent the traps that do exchange (communicate with) the carriers from the channel. FTs and SSTs are also known as the oxide trapped

charge (Q_{OT}), and FSTs as the interface traps (Q_{IT}). The deeper the trap is in the oxide, the slower is its electrical response.

The correlations with the density of oxide traps (oxide trapped charge density) ΔQ_{OT} and the interface traps density ΔQ_{IT} are:

$$\Delta Q_{OT} = \Delta Q_{FT} + \Delta Q_{SST} \tag{2.24}$$

$$\Delta Q_{IT} = \Delta Q_{ST} - \Delta Q_{SST} = \Delta Q_{FST} \tag{2.25}$$

The contributions of FTs and STs to the threshold voltage shift ΔV_t in a pMOS could be expressed as:

$$\Delta V_t = -(\Delta V_{FT} + \Delta V_{ST}) = -\frac{1}{C_{OX}}(\Delta Q_{FT} + \Delta Q_{ST}) \tag{2.26}$$

Where ΔV_{FT} and ΔV_{ST} are the contributions of FTs and STs to ΔV_t, respectively (Ristic et al. 2011, Ristic 2008).

Effects of bias conditions on threshold voltage

It is widely extended that the bias voltage applied to the structure during the irradiation has a major impact on the device response. The shift observed with a positive voltage applied to the gate are significantly larger than those with negative voltage, since under positive field the radiation-generated holes are driven toward the interface Si/SiO_2, and the holes trapped at this interface have a large effect on the voltage shifts and its linearity is improved (Figure 2.20) (Ma and Dressendorfer 1989).

The carrier transport is complex (Boesch et al. 1986), the response is not linear with the field. Several models for describing the response of MOS devices as a function of electric field and dose have been developed. These range from simple *charge sheet models*, in which

the holes are assumed to be trapped within a thin sheet near the oxide/silicon interface to dynamic computer models, where Poisson's equation and trap dynamics are used to calculate the time-dependent behaviour of holes, electrons, and traps in the oxide. These models help to understand threshold voltage shift tends to saturate at high doses. This is caused by increased recombination of holes and electrons. As more holes are trapped building up an internal space charge region that reduce the net internal field and filling of the limited number of hole traps (Ma and Dressendorfer 1989, Holmes-Siedle, Ravotti and Glaser 2007). An illustration of saturation effect and model fit is given in Figure 2.22.

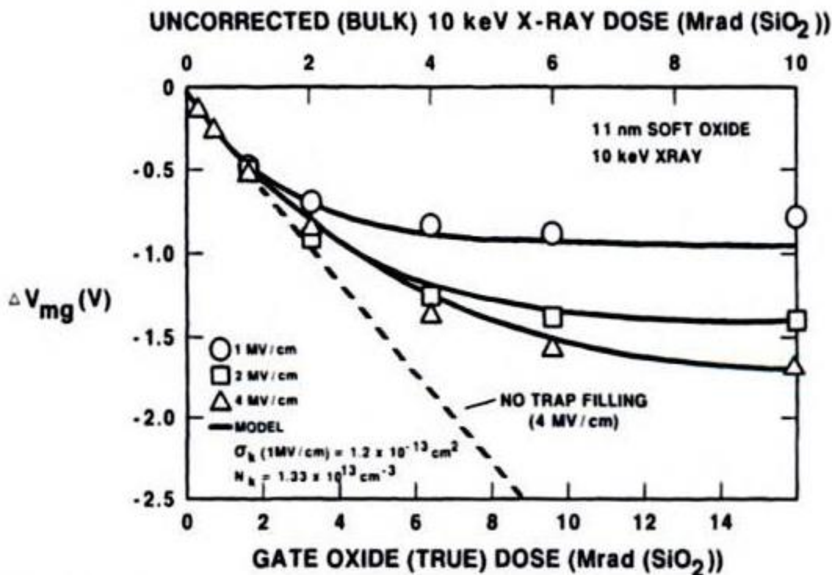

Figure 2.22 Shift in mind gap voltage for an MOS capacitor as a function of radiation dose showing saturation at high doses. Symbols are data points. Curves are a computer model fit with (solid) and without (dashed) trap filling (Boesch et al. 1986).

Accumulated response versus dose

Traps near to the interface produce degradation in the carrier mobility (Banqueri et al. 1993) and in consequence a variation of transconductance, β, happens.

$$\beta = \mu_p C_{OX} \frac{W}{L} \tag{2.27}$$

The carrier mobility degradation in the channel is mainly due to two simultaneous effects:

- Carrier recombination rate of channel increases with increasing of trap density or allowed states for these carriers.
- Occupied and ionized traps produce *coulomb* scattering.

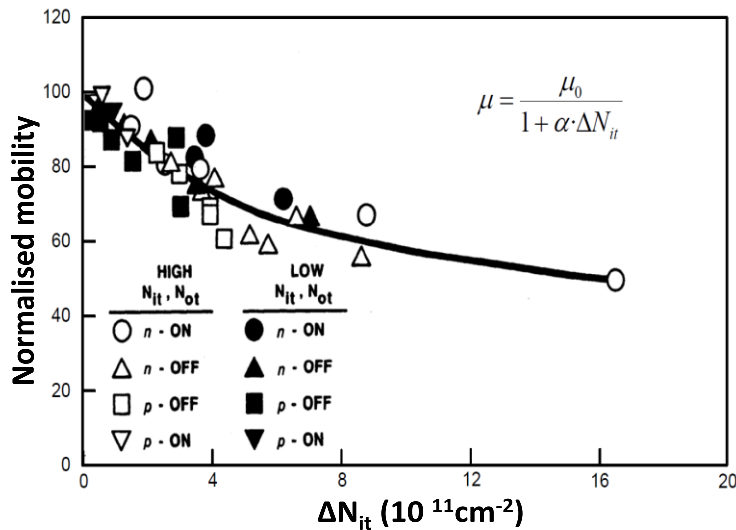

Figure 2.23 Carrier mobility normalised to the pre-irradiation mobility versus interface trap density (Sexton and Schwank 1985).

There is a relationship between the mobility and the interface trap density (Q_{IT}), also denoted in the literature as N_{it}, see Figure 2.23. It has been analysed ionizing radiation causes some effects over

threshold voltage and transconductance, and *I-V* curve changes both pMOS and nMOS.

In Figure 2.24 the slope decreases in absolute value, when the dose increases, due to damage in the channel transconductance. Threshold voltage in pMOS change with a monotonous behaviour with dose, however, in nMOS, this dependency is not monotonous (Carvajal 2008).

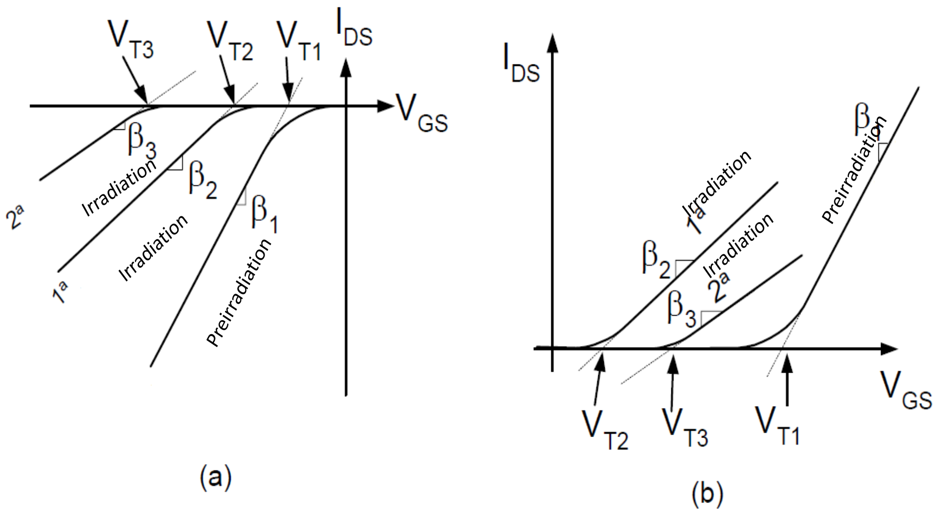

Figure 2.24 Ionizing radiation effect over *I-V* curves. a) pMOS transistor b) nMOS transistor (Carvajal 2008).

Accumulated response with dose

The accumulated dose is the sum of different shifts produce in each irradiation session. Thus, the accumulated dose can be expressed as:

$$\Delta|V_t| = \sum_i \Delta|V_{t,i}| \tag{2.28}$$

If total dose is defined as the sum of doses in every irradiation:

$$D = \sum_i D_i \tag{2.29}$$

The expected response of a pMOS dosimeter, to radiation-induced is the threshold voltage shift, thus, it is usually represented by a power-law:

$$\Delta|V_t| = A \cdot D^n \tag{2.30}$$

where A is a constant, D is the absorbed dose and n is the degree of linearity, ideally 1. n depends on the oxide thickness, the electric field and the absorbed dose. If $n = 1$ then A represents the sensitivity, S, of pMOS dosimeters:

$$S = \frac{\Delta|V_t|}{D} \tag{2.31}$$

It is widely known, that this power law could be considered lineal for low doses. However, this linearity depends on the gate oxide thickness, the accumulated dose and the bias gate condition of characterization. An example of the representation of the accumulated dose versus accumulated dose is observed in Figure 2.25, where a reduction of linearity is shown to high dose.

Although there are examples in the literature of reduction of this linearity in high dose (Sarrabayrouse and Siskos 1998, Boesch et al. 1986, Soubra et al. 1994), the threshold voltage shift is widely used as dosimetric parameter.

In low dose, the trap density oxide is almost non-existence; therefore the electric field in the oxide is the voltage difference between the gate and bulk, caused by an external bias of by the difference of work functions between gate and bulk materials. As it has been previously explained in following irradiations, the trap density oxide increases, and the electric field is shielded. The number of traps which

escapes to recombination is decrement and the sensitivity is reduced (Carvajal 2008).

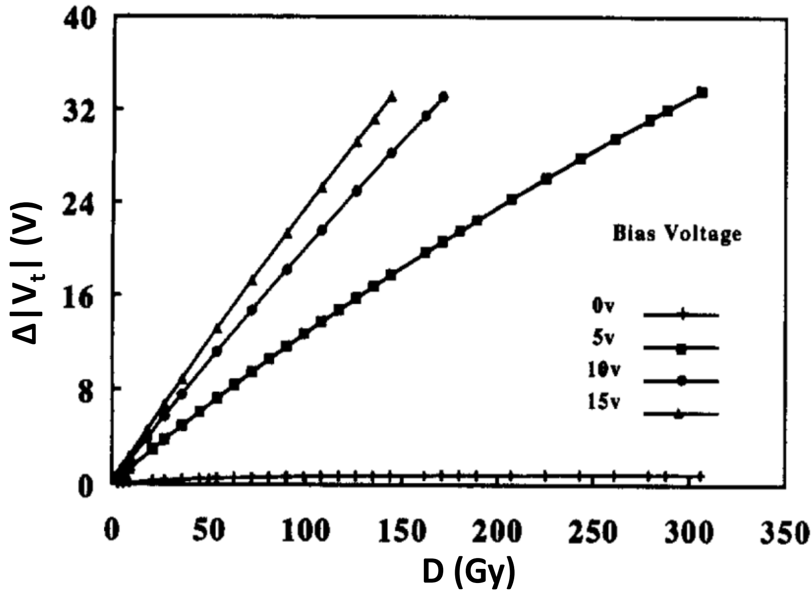

Figure 2.25 Absolute value of accumulated threshold voltage shift with the received dose for different bias gate (Soubra et al. 1994).

If it is supposed a positive and uniform spatial charge density in the oxide, the electric field can be defined:

$$E_{OX} = \frac{V_{OX}}{t_{OX}} + \frac{\rho_{OX}}{\varepsilon_{OX}}\left(x - \frac{t_{OX}}{2}\right) \tag{2.32}$$

with ρ_{OX} charge density in the oxide created by ionizing radiation, V_{OX} is the potential in the oxide and x is the distance from a point in the oxide to the gate, see Figure 2.27. More detailed description is provided in (Carvajal 2008).

By (2.32) the electric field is minimum with $x = 0$. When the charge density increases, the electric field could be zero, nearby to the gate. This happens if the charge density reaches a critical value of:

$$\rho_{OX}^{critical} = \frac{2\varepsilon_{OX} V_{OX}}{t_{OX}^2} \tag{2.33}$$

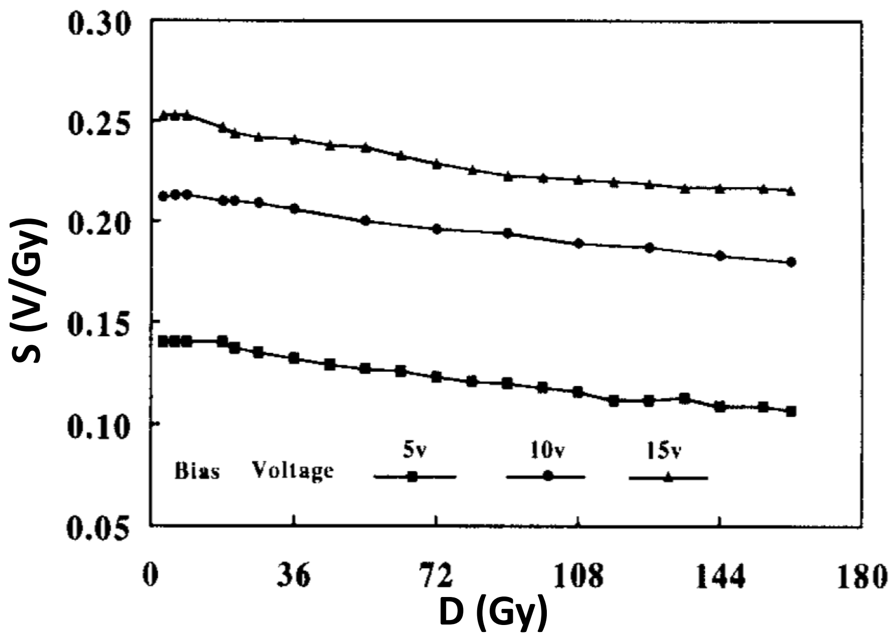

Figure 2.26 Sensitivity, V/Gy, versus the accumulated dose at different gate biases (Soubra et al. 1994).

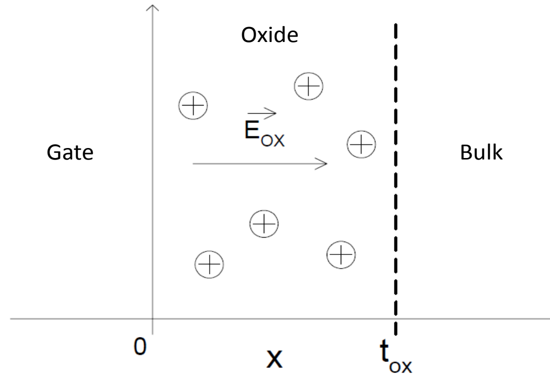

Figure 2.27 MOS structure in detail with trapped charges in the oxide (Carvajal 2008).

When ρ_{OX} is smaller than the critical density charge, there is an electric field through the entire oxide, then the recombination does not increase (Figure 2.28a). With more irradiations, the charge density is increasing, and the critical value, $\rho_{OX}^{critical}$ is reached. In this value, the electric field is null in the gate-oxide interface (Figure 2.28b).

In this area the recombination between the existing charges with the electrons goes to the gate increases because there is no electric field to avoid it. If the fixed charge increases even more, the area with null electric field also increases (Figure 2.28c). This is similar to have a MOSFET with less thickness oxide, then the sensitivity is lower (Carvajal 2008).

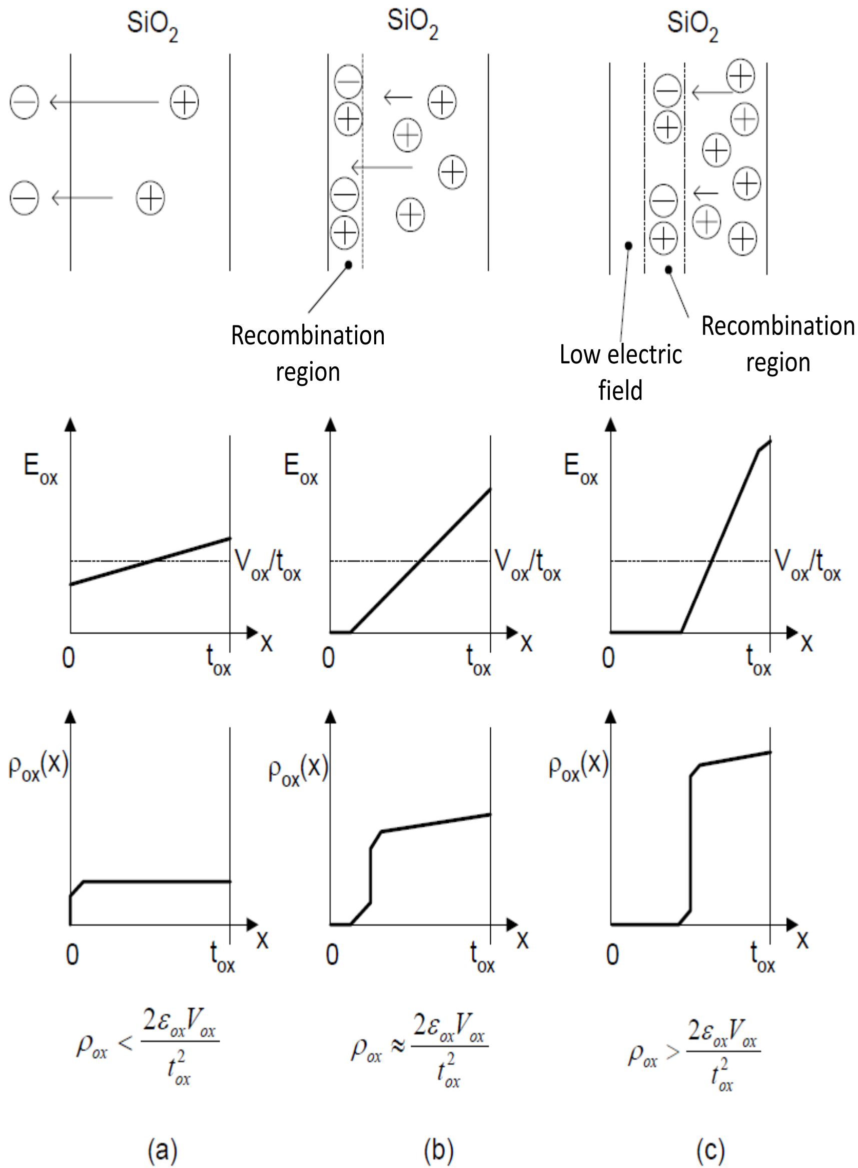

Figure 2.28 Charges and electric field evolution when the oxide is irradiated. a) The electric field created by the space charge region is weak. b) Electric field is cancelled in the interface region with the gate and there is a region free of charge c) The free region of charge is expanded through the oxide (Carvajal 2008).

Subthreshold swing

The subthreshold behaviour of a MOSFET is mainly influenced by the interface traps, decreasing the slope of *I-V* curves as the interface state density increases. Therefore, it could be expected a linear shift of the subthreshold characteristics which is very suitable for a dosimetric parameter. For a MOSFET in weak inversion, the drain current is dominated by the diffusion mechanism, remembering the expression (2.12). A useful parameter in the subthreshold regime can be defined as the gate voltage swing, S, needed to reduce the drain current by one decade, termed the subthreshold swing. Usually, this parameter can be approximated by (Ma and Dressendorfer 1989):

$$S = \frac{kT}{q}\left[1 + \frac{C_{SC}(\Phi_S)}{C_{OX}}\right] \tag{2.34}$$

In the absence of interface traps, with C_{SC} the space charges capacitance depending on the surface potential ϕs and C_{OX} the gate oxide capacitance. If interface traps are generated by radiation, then a change in the slope of the *I-V* curve would be produced, and therefore in the subthreshold swing. In this situation, the subthreshold swing is modified as (Ma and Dressendorfer 1989):

$$S_{IT} = S_0\left[1 + \frac{+C_{IT}(\Phi_S)}{C_{OX}+C_{SC}(\Phi_S)}\right] \tag{2.35}$$

where S_{it} and S_0 represent the subthreshold swings with or without interface traps, respectively, and $C_{IT}(\varphi_S) = qQ_{IT}(\varphi_S)$ is the capacitance associated with the interface traps. In a radiation session, it can be obtained the mean interface trap density created, ΔQ_{IT}, from Equations (2.34) and (2.35) as a function of the increase in the subthreshold swing given by:

$$\Delta Q_{IT} = \frac{C_{OX}}{kT}(S_{D2} - S_{D1}) = \frac{C_{OX}}{kT}\Delta S \tag{2.36}$$

where S_{D1} and S_{D2} are the subthreshold swing before and after a radiation session (Banqueri et al. 2012).

Influential factors pMOS sensitivity to radiation

One of the main objectives in a radiation detector is to get a high sensitivity. There are different techniques to increase the sensitivity with the radiation in a pMOS dosimeter:

- **Gate bias:** As it has been said, the number of pairs which escapes to recombination increase with a high electric field in the oxide. A technique to get high field in the oxide is to bias the gate of transistor with a positive voltage $V_{GB} > 0$. With more gate-bulk voltage, more sensitivity is the transistor (see Figure 2.25 and Figure 2.26).
- **Oxide thickness:** The thickness in the gate oxide is a crucial factor in the sensitivity of transistors. When the volume in the oxide is high, more space has the ionizing radiation to create electron-hole pairs. If it is assumed a uniform density of creating pair in the oxide, (Oldman 1999) confirms the threshold voltage shift is proportional to the square of the gate oxide thickness. (Sarrabayrouse and Siskos 1998) have found an empirical relationship between the sensitivity and the oxide thickness. The results are shown in Figure 2.29. Among the holes created by the radiation, only those that escapes to the recombination, influents in the threshold voltage shift. The high electric field in the oxide increases the portion of the holes that escapes to recombination, $f_y(E_{OX})$. By (Sarrabayrouse and Siskos 1998) the sensitivity is proportional to $f_y(E_{OX})$ and gate oxide thickness as power law:

$$S = \frac{|\Delta V_t|}{\Delta D} \propto t_{OX}^{n} \cdot f_y(E_{OX}) \tag{2.37}$$

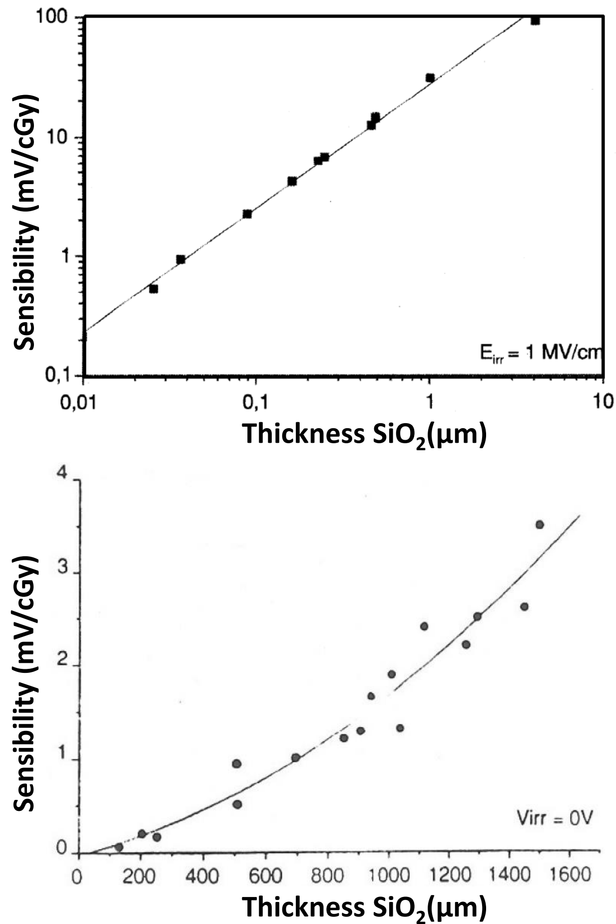

Figure 2.29 Thickness oxide influence in the sensitivity of MOSFET a) Biased MOSFET $V_{GB} > 0$ b) Unbiased MOSFET during irradiation (Sarrabayrouse and Siskos 1998).

- **Implanted and doped oxide traps:** Traps might be introduced by implanting or doping the oxide with impurity ions. The effect of the implant on the trapping properties of the oxide depended more upon the damage done to the SiO_2 network by the implantation process than on the specific ion

used (Ma and Dressendorfer 1989). This implantation enhances the response of the transistor, and the initial threshold voltage is reduced to an inferior value. This increase the dynamic range for radiation-induced threshold voltage (Haran et al. 2004).

RADFETs are transistor specially manufactured to detect ionizing radiation, therefore by equation (2.37), this kind of transistors are specific because they have an important gate oxide thickness, around 500nm, manufactured with conditions that have an elevated sensitivity (Ma and Dressendorfer 1989, Ristic et al. 1996, Sarrabayrouse and Siskos 1998, Kelleher et al. 1992).

Threshold voltage recovery: fading

After irradiation the threshold voltage reduces in absolute value to its initial value. This recovery is known as *fading*.

Usually the fading is defined as:

$$F = \frac{V_t(0) - V_t(t)}{V_t(0) - V_{t0}} = \frac{V_t(0) - V_t(t)}{\Delta V_t(0)} \tag{2.38}$$

where $V_t(0)$ is the threshold voltage immediately after irradiation, $V_t(t)$ is the threshold voltage after annealing time t, V_{t0} is the threshold voltage before irradiation and $\Delta V_t(0)$ is the threshold voltage shift after irradiation.

At room temperature, the electrons in the bulk can go by tunnel effect to the oxide closer to the interface, around 2 or 5 nm. Once in the oxide, they recombine with trapped holes, and the threshold voltage is reduced. This is normally named as *tunnelling annealing*. The recovery is generally very slow and approximately exponential with time. The temporal function depends on the probability in pass

the barrier by tunnel effect with the thickness of the barrier. As time passes, this thickness barrier increases. This is because the traps closer to the interface have been previously recombined. The extinction of accumulated trapped charge at the rate of 0.2 nm per decade is produced (Ma and Dressendorfer 1989).

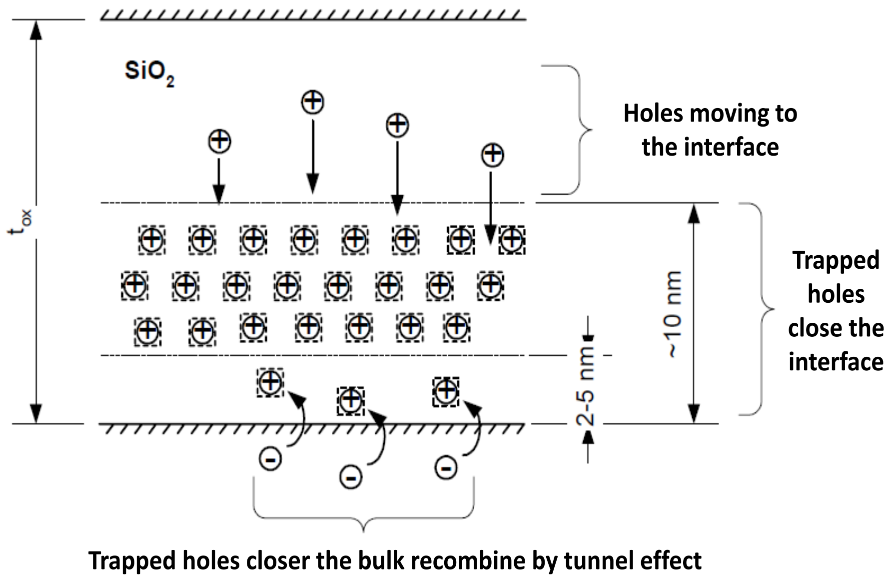

Figure 2.30 Trapped hole recombination by tunnel effect (Carvajal 2008).

When a positive voltage bias ($V_{GB} > 0$) is applied at the gate during the annealing, the barrier is reduced, and the electrons bulk can go to the oxide easily. Furthermore the number of electrons closer to the interface increases. Both reasons cause an increase in the recovery speed, it is normally known as *bias annealing*, see Figure 2.31 (Ma and Dressendorfer 1989).

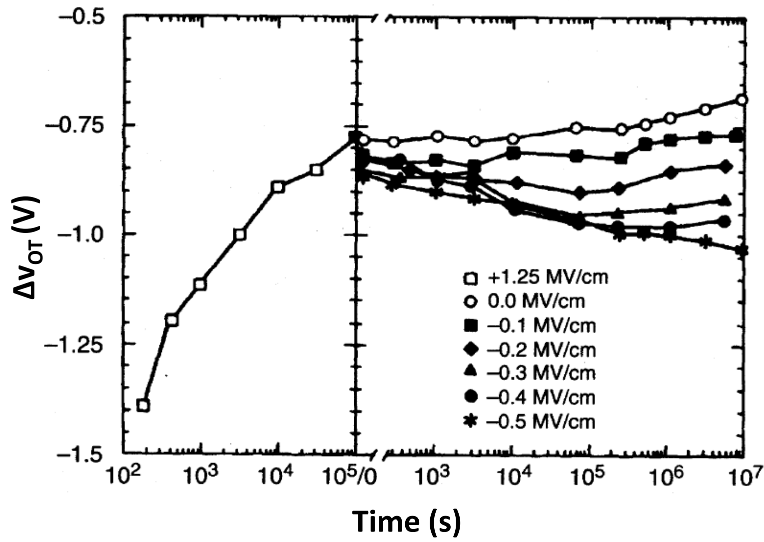

Figure 2.31 Recovering of threshold voltage shift with time for different oxide field (Oldman 1999).

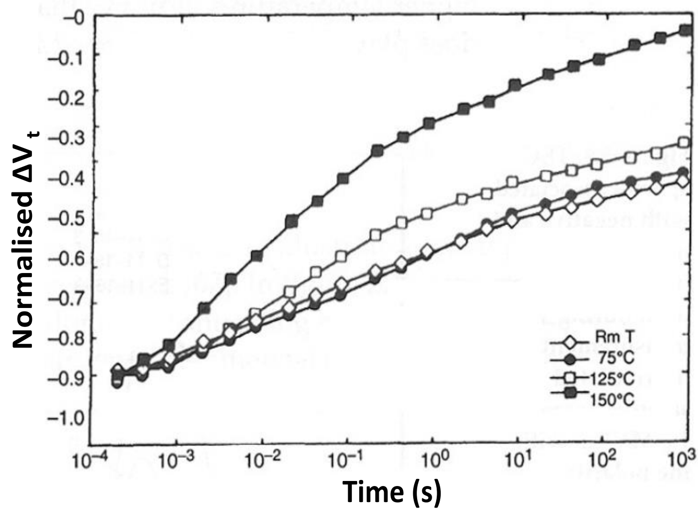

Figure 2.32 Recovering of normalised threshold voltage shift with time in different temperatures (Oldman 1999). RmT denote the room temperature around 25ºC.

Also annealing the transistor at high temperatures (over 100°C), the process would accelerate. As the temperature increases, the probability of a hole to escapes from its traps also increases. The ratio between the recovery and threshold voltage is exponential Figure 2.32.

Due to these reasons fading takes placed, although there is no gate bias, or high temperatures. Because of that, to work with dosimetric measurements it is necessary to wait a while (one or two minutes) after irradiation, to have the charges in the oxide close to the stationary situation (Carvajal 2008).

2.7.3 Commercial dosimetric systems based on MOSFET

Last few years, dosimetry based on MOSFET has evolved, originating several patents (Thomson 1984, Thomson 1987, Thomson, Mackay and Brown 1991, Kahilainen 1998, Knoll and Bräunig 1988, Kronenberg and Bard 1995, Kishi 1997, Gwynne 1993, Tarr and Thomson 2001, Black et al. 2005, Black 2003, Russell 2006, Polishchuk 2012, Rosenfeld 2014b, Asensio, Carvajal and Palma López 2008) from which commercial dosimetric systems have been created. Normally commercial systems use transistor with a gate oxide between 500 nm and 1 μm. Among developed systems, three of them have been commercialized by sector companies:

- Thomson&Nielsen system (Best Medical Canada)
- OneDose^{TM} from Sicel Technologies Inc. (USA)
- SkinMOS from Wollowong University (Australia)

Constant current measurement

Main commercial systems, to simplify the measurement of threshold voltage shift, use methods based on constant currents. The transistor is forced to operate in the saturation region, short-circuited and grounded gate and drain terminals, and tied source and bulk. A constant current flows by the transistors from source to drain (Figure 2.33).

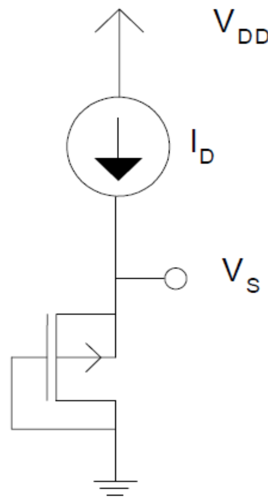

Figure 2.33 pMOS configuration to measure the threshold voltage shift with constant current (Carvajal 2008).

This technique is widely known (Sarrabayrouse and Siskos 1998, Jaksic et al. 2002). The reference terminal could be drain or source. Remembering the equation (2.11), and neglecting the effective module length of channel, the current in a pMOS, working in saturation region is:

$$i_D = -\frac{\beta}{2}(|v_{GS}| - |V_t|)^2 \tag{2.39}$$

If the transconductance is considered constant, neglecting its effects, the gate-source shift is equal to the threshold voltage shift, when the current is constant. Therefore,

$$\Delta|v_{GS}| \approx \Delta|V_t| \tag{2.40}$$

When the gate is grounded, then:

$$\Delta V_S \approx \Delta|V_t| \tag{2.41}$$

Best Medical Canada

Best Medical Canada has been the pioneer of dosimetry systems based on MOSFETs for in-vivo dosimetry for radiotherapy, brachytherapy and radiology applications for almost 30 years.

Dosimetric sensors used in this system have a pair of RADEFETs integrated into the same silicon substrate. Both transistors are identical and very close each other. Gate oxide of 500 nm or even more are used (Thomson et al. 1991), then the transistors are specially sensitive to radiation.

During irradiation each transistor is operable in a bias mode and a test mode (see Figure 2.34). Both transistors have gate-bulk biased in a positive voltage $V_{GB1,2} \geq 0$, to create an electric field that moves the holes created by radiation to the interface Si-SiO_2. Sensitivity is higher when the difference between gate and source increase, thus the transistor with highest bias would be the transistor more sensitive to radiation.

The operation mode can be observed in Figure 2.34, the simplest configuration of the sensor. All terminals are short-circuited, except the gate of transistor T1, which is biased with a positive voltage. Its sensitivity would be higher than the sensitivity in transistor T2, therefore threshold voltage shift would be higher for T1 than T2. With S1 and S2 are the sensitivities respectively, it can be written:

$$\Delta V_{T,1} = S_1 D$$
$$\Delta V_{T,2} = S_2 D \tag{2.42}$$

To measure the threshold voltage shift, both transistors are biased by the same constant current before and after irradiation, with two current sources (Figure 2.35). The shift in the drain voltage would be similar to the shift in the threshold voltage

$$\Delta V_{D,1} \approx \Delta V_{T,1}$$
$$\Delta V_{D,2} \approx \Delta V_{T,2} \tag{2.43}$$

Then,

$$\Delta V_D \equiv \Delta V_{D,1} - \Delta V_{D,2} \tag{2.44}$$

Substituting (2.42) and (2.43) in (2.44), it is obtained:

$$\Delta V_D = (S_1 - S_2) D \tag{2.45}$$

Therefore, the drain difference voltage is proportional to absorbed dose. The constant of proportionality is the difference of sensitivities of both transistors, and then when the difference of bias during irradiation is higher, the sensitivity will increase:

$$S = \frac{\Delta V_D}{D} \tag{2.46}$$

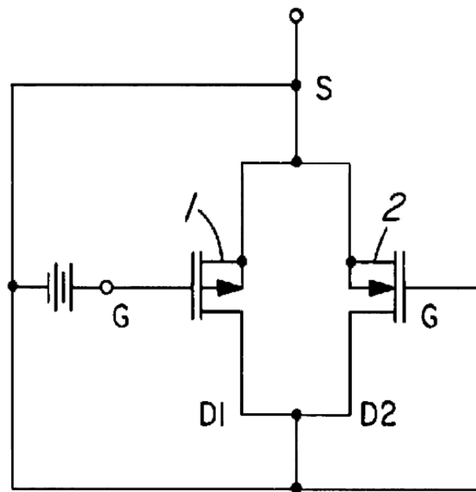

Figure 2.34 Biased schematic diagram during irradiation of a Thomson and Nielsen sensor composed by two RADFETs (Thomson et al. 1991).

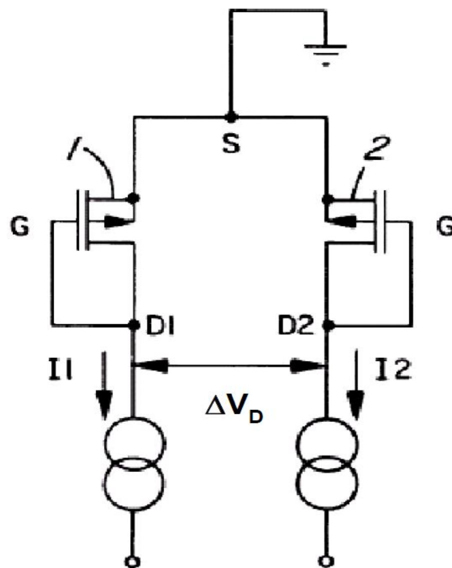

Figure 2.35 Measurement schematic diagram of Thomson&Nielsen sensor (Thomson et al. 1991).

This dual method of measuring has several advantages: the saturation effect of sensitivity is compensated with the saturation of the other RADFET, therefore the decrease of sensitivity of the whole sensor will appear for higher doses than for one only transistor. Another advantage is the thermal variations, which have the same effect in both transistors, both in drain voltage, thus they are cancelled each other.

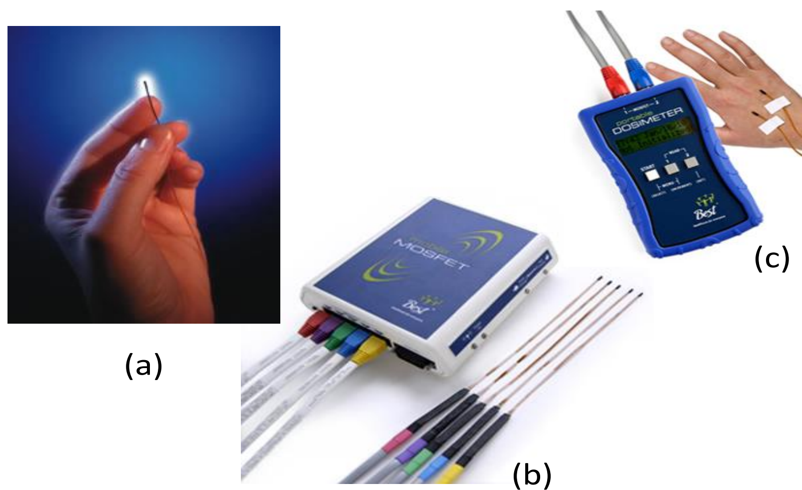

Figure 2.36 a) Dosimetric sensor Thosmon&Nielsen b) mobileMOSFET reader c) portable Dosimeter (Canada 2014).

Obviously, a previous calibration of each sensor is needed, before use the transistors as dosimeters. During calibration, the sensors are irradiated with a known dose, to establish the ratio with the increase of difference gate source. The manufacturer advises (Medical 2004) the calibration procedure must be done by the user with identical setting and conditions that dosimeter would have during its use. Bias voltage gate, type or radiation, energy, orientation and irradiation field; must be the same during calibration and measuring phases. Actually the

company offers a system to calibrate the sensor automatically, *MOSFET Calibration Jig.*

Once the dosimeter is calibrated, it could be used to measure the received dose in patients. To measure the dose is necessary to wait at least a minute after irradiation. This is caused because the voltage shows a decrease due to the *fading* of RADFETs.

Depending on size of sensor, the company offers three styles of MOSFET dosimeters: *standard MOSFET* (2.5x200x0.3 mm), *microMOSFET* (1x375x0.3 mm) and *Linear 5ive array* (1.5x460x1.3 mm). Every model has specific uses, but all of them have the same unique features, as, for example, an active region of 0.2x0.2 nm, an isotropic factor with a variation of ±3%, dose-rate and temperature independent, lightweight and flexible and multiple dosimeter capability with one reader.

Attending the gate oxide thickness the manufacturer offers different type of sensors with different sensitivities. Every model can be biased with different voltages to increase the sensitivity.

The high bias supply setting is when the bias gate-bulk in both transistors is around 10 V, when the sensitivity obtained is maximum. These dosimeters are suitable both radiotherapy and diagnostic x-ray, and energy error dependence is less than 5% and 10% respectively.

The Table 2.5 shows the type of setting depending on radiotherapy dose. This information is valid for *the standard MOSFET,* the *microMOSFET,* and the *Linear 5ive Array dosimeter.*

Dosimeter (*MOSFET dosimeter, microMOSFET and Linear 5ive Array*)	Bias Supply Setting	Nominal Sensitivity ^{60}Co (mV/cGy)	Nominal Sensitivity X-Ray (mV/cGy)
TN502RD, TN502RDM,TN252LA5	Standard	1	3
	High	3	9
TN1002RD, TN1002RDM, TN505LA5, TN1002LA5 (High sensitivity dosimeters)	Standard	3	10
	High	9	30

Table 2.4. Sensitivity for model TN-502RD and TN-1002RD (Canada 2014).

Dosimeter	Radiotherapy Dose	Recommended Bias Supply
High Sensitivity Dosimeter	1 to 20 cGy	High Setting
Standard Dosimeter	20 to 100 cGy	High Setting
Standard Dosimeter	>100 cGy	Standard Setting

Table 2.5. Recommended bias setting and radiotherapy dose per model.

A new calibration is needed when the voltage used as dosimetric parameter has increased 7 V after the last calibration. The manufacturer advises to change the dosimeter when the output voltage exceeds 20 V or when the *fading* is excessive. For example, if the fading in the first fifteen minutes after irradiation is over 3%.

The company offers two different readers, both adaptable for all dosimeters:

- *Mobile MOSFET*: is a wireless and portable dose verification system. It is entirely software driven, allowing for remote control of one or more systems from a PC. The system consist of remote monitoring dose verification software, wall-mounted Bluetooth™ wireless transceiver, and a small reader module that acts as a channel between the MOSFET and software, and provides a final dose report for patient records. Up to 5 MOSFETs or one *Linear 5ive Array* can be plugged into one module.
- *Portable Dosimeter*: is an economical, compact, stand-alone system for radiation dose measurement. Without needing for software or computer, the device shows the patient dosimetry measurements. It has a rechargeable battery powered dosimeter allows easy transportation. It supports two simultaneous dose points, and a continuously sample dose at a fixed time interval is possible.

OneDose™

The American company Sicel Technologies Inc. has developed a dosimetric system named as OneDose (Figure 2.37). It is based on a sensor with a single RADFET. The sensor is wireless, therefore the technology is different to Thomson&Nielsen system.

To measure the dose received by the patient, the sensor has to be connected to the reader unit before and after the irradiation. The threshold voltage shift is measured and it is related with the absorbed dose by the RADFET. The main advantage of this system is that does not need any connection during the irradiation. The sensor is fixed to the patient with an adhesive, as it is observed in Figure 2.38.

Figure 2.37 OneDose^{TM} dosimetric system (Carvajal 2008).

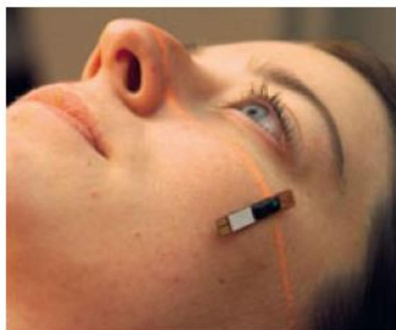

Figure 2.38 OneDose^{TM} sensor on the patient (Carvajal 2008).

The main problem is that the maximum received dose is only 5 Gy. The sensor is formed by a non-volatile memory EEPROM, which is recorded and electrically erased. The RADFET has a gate oxide of 400nm, with a gate of 300x50 μm^2. The memory is used to store the calibration and bias parameters for every sensor, and the corrector factors by the accumulative energy, thermal compensation, etc.

The diode D1 protects of possible electrostatics discharges, the resistors R1 and R2 drive the terminals source and drain to ground during the irradiation period. In the Figure 2.39, the gate and drain terminal are short-circuited, then the transistor is in saturation regime.

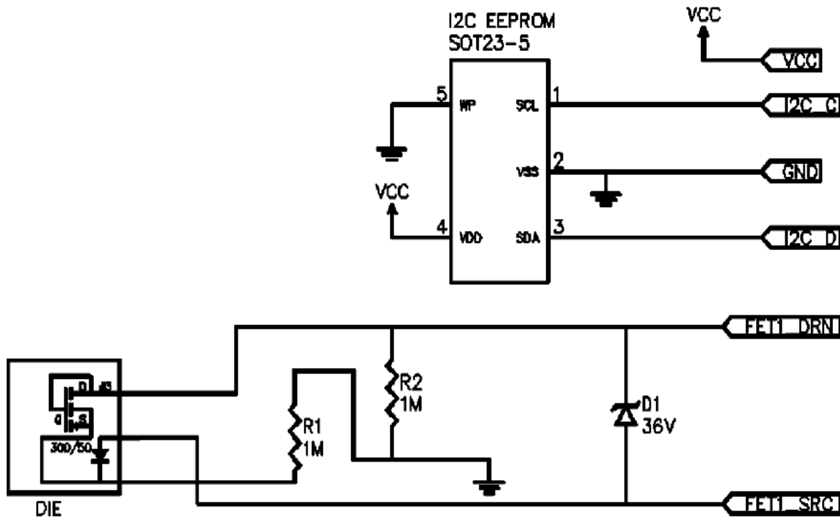

Figure 2.39 Block diagram of OneDose system (Halvorsen 2005).

The measurement process is based on biasing the transistor with a constant current in the ZTC region. This value is characteristic for every sensor, and it is stored in the memory. Before the irradiation, the sensor is connected to the reader unit, which look for the value of the intensity and bias the transistor. The drain-source voltage is measured and stored in the memory. Once the irradiation has been done, the process is repeated, and the difference between the drain-source voltages before and after irradiation is calculated. This shift in voltage is related to the received dose with the calibration factors for every sensor. Therefore, it is necessary a calibration per sensor, and its thermal study. This calibration process is done by the manufacturer and it is provided to the user with the coefficients stored in the memory.

The sensitivity of the transistors used for the sensor implementation is between 35-100 mV/Gy by (Halvorsen 2005). The

dispersion in the sensitivity values makes necessary the individual calibration for every sensor. The manufacturer (Sicel 2005), the errors in the dose measurement are summarized in the next table:

Dose (cGy)	Uncertainty
1-20	1 cGy
20-500	±5% (2σ)

Table 2.6 Uncertainty in the dose determination with the OneDose system(Sicel 2005)

The working temperature is between 20-40°C, where the thermal variation of the drain-source voltage is neglected. The uncertainty given by the manufacturer is in the acceptable range of use in the radiotherapy, where the uncertainty has to be less than 5%.

The main limitation is the maximum dose, which is 5Gy, thus the sensor can be only used once. The manufacturer makes unable the sensors after reading the voltage after irradiation. To avoid the measurement be affected by the short-term fading it is necessary to wait around 10 minutes.

It must be highlight this company is currently out of market; however a reference to this dosimetry system has been done, because it has been widespread in the dosimetry field (Halvorsen 2005, Kinhikar et al. 2006, Falco et al. 2012, Cheng et al. 2010, Best, Ralson and Suchowerska 2005).

MO*Skin*™ In Vivo Dosimeter

The MO*Skin*™ is a MOSFET based radiation detector that has been developed to provide real time on-line in vivo dose measurements during radiation therapy. The system has been developed at the

Centre for Medical Radiation Physics (CMRP) at Wollongong University, Australia. Due to this system is not a typical commercial one, the information that could be found about it, is that published in the recent literature (Metcalfe et al. 2013, Qi et al. 2007, Kwan et al. 2008, Kwan et al. 2009, Rosenfeld et al. 2001, Rosenfeld 2002, Rosenfeld 2014a). The system can be found in different versions.

It is necessary to make a difference between the MOSFET detectors and the reader system.

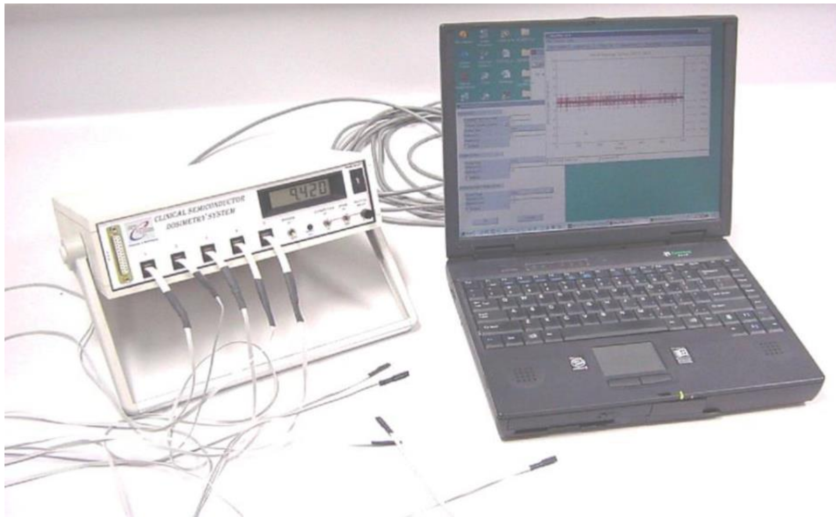

Figure 2.40 The online MOSFET dosimetry system (Rosenfeld 2014a).

The reader system, it is known as Clinical Semiconductor Dosimetry System (CSDS). In a first version the system reads ten MOSFETs sequentially online in a short time and the results are sent via RS232 link to a PC, where with specially developed software, are saved and presented graphically within seconds. The MOSFET reading can also be seen on the LCD display and sequenced (Rosenfeld et al. 2001), see Figure 2.40. The reader has the possibility of working with the MOSFET in active mode, when there is a positive gate bias

volt, this version provides +12 and +5 V. Two dosimeters can be connected to each channel, one having high and the other low sensitivity. The software, MosPlot 4.1, was designed using MATLAB for making profiles in quasi-static and pulsed radiation beams (Rosenfeld et al. 2001).

In this version, the sensor detectors were integrated MOSFET with two types of pMOS on the same chip, designed and produced by REM Oxford, U.K. (Holmes-Siedle 1999). These transistors are RADFET, specific for radiation detection.

The newest version of the system is composed of a modern reader and new detectors manufactured by CMRP. The new MO*Skin*™ reader can read out five devices at once in real time. Multiple data collection units may be used to operate more devices, and these may be connected to a computer in real time software-based analysis (Metcalfe et al. 2013). The new reader is a portable, battery-powered and was designed to accept several MOSkin designs and it can be set to apply either a +5 or +15 V bias voltage to the gate of the MOSFET sensor during irradiation.

The new MOSFET sensor has a gate oxide thickness of 0.55 μm, while the entire chip is approximately 400 μm thick. It is optimized to measure dose in a steep dose gradient. What makes this new design of unique is the design of the packaging, a recent patent describe the semiconductor detector, and the process of manufacturing (Rosenfeld 2014b). The MOSFET is dropped into a thin kapton layer and hermetically sealed with a water-equivalent flexible carrier of reproducible thickness. The film prevents damage to the electronics caused by moisture and acts as a carrier of the thin aluminium contact leads that are connected to the MOSFET sensor from the top-side.

This new package provides a highly reproducible water equivalent depth (WED) of approximately 0.07 mm (or the desired thickness) (Kwan et al. 2008). This new technology replaced the traditional epoxy bubble encapsulation, used in other commercial RADFETs (Figure 2.41). MOSkin detectors are available in either single or dual sensor designs. The dual MO*Skin*™ detector could incorporate two separate MOSFET sensors of different sensitivity. It is 10mm long and 1.8 mm wide. The chip on the detector itself is only around 400 μm, but the package is approximately 0.46 mm thick (Kwan et al. 2009) , see Figure 2.42.

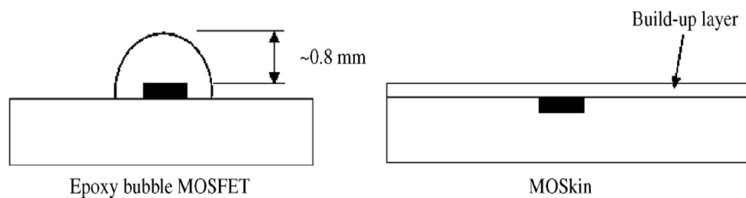

Figure 2.41 Schematic comparison of a MOSFET with epoxy bubble (left) and MOSkin (right) (Kwan et al. 2008).

An aspect not widely published in the literature, it is concerning the thermal compensation in MO*Skin*™. However, in (Rosenfeld et al. 2001) said a technique used with REM transistors, where a constant flow of hot air was used during the readout measurement, to maintain the transistors in the same temperature. In the recent patent (Rosenfeld 2014b), there is also a method for thermo-stabilizing a semiconductor detector comprising correcting threshold voltage drift arising owing to temperature changes according to the forward drop voltage of the source-substrate *p*-*n* junction.

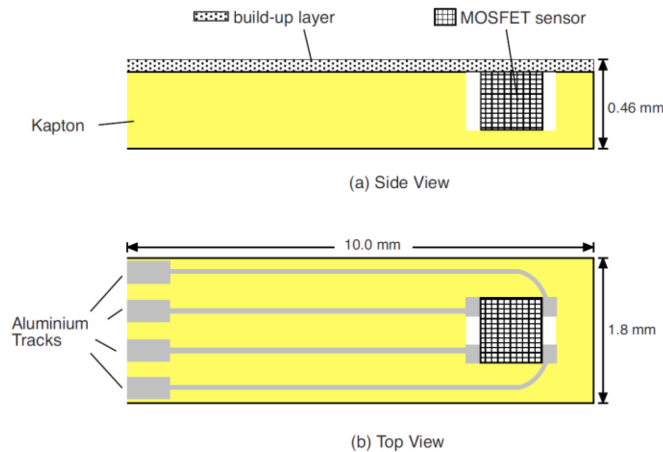

Figure 2.42 Schematic diagram of the MOSkin detector (Kwan et al. 2009).

The method comprises biasing a substrate of the semiconductor detector relative to the source to provide a substantially constant current for the *p-n* junction; scaling and sampling the change in the voltage drop across the source-substrate *p-n* junction; and subtracting the scaled change in the voltage drop from the threshold voltage during each readout cycle.

Figure **2.43** Diagram of a MOSFET threshold voltage thermo-stabilization circuit (Rosenfeld 2014b).

is a diagram of a MOSFET threshold voltage thermo-stabilization circuit.

The most recent published system (Metcalfe et al. 2013) has a 2.5 mV/cGy sensitivity to MV X-rays, and an 8 mV/cGy sensitivity to KV X-rays (~100 kVp), the difference is attributed to the detectors enhanced sensitivity to the photoelectric effect. The system has been tested for intra-cavity dosimetry during brachytherapy and external beam radiation therapy. Current works includes the continuing

development of the devices with endo-rectal balloons (ERBs) in order to assess in vivo rectal wall dose during prostate external radiotherapy. Future studies will be used in an eight-detector Octo-MOSkin configuration to track dose points around the rectal and anal wall interface.

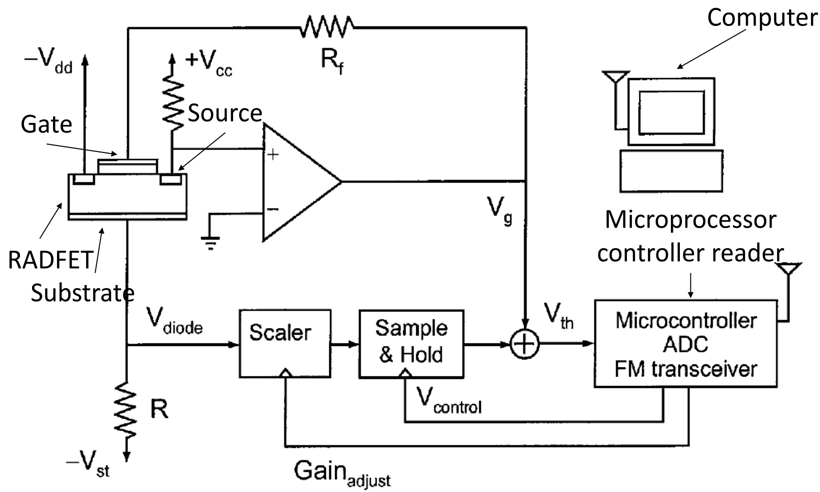

Figure 2.43 Diagram of a MOSFET threshold voltage thermo-stabilization circuit (Rosenfeld 2014b).

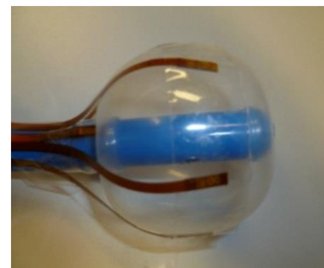

(a) (b)

Figure 2.44 a) MOSkinTM detector on Kapton pigtail and b) Multiple MOSkinTM mounted on an Endo Rectal Balloon (Metcalfe et al. 2013).

3

Materials and methods

In this chapter a detailed explanation concerning materials and methods is done including the description of all transistor types, the sources and the dosimetry system used to characterise the sensors. Also the different settings for the thermal, electrical and radiation study are described, together with the instrumentation used both in laboratory and hospital.

3.1 Transistor types

Traditionally, the commercial dosimetric systems based on MOSFET use specific transistors to detect ionizing radiation, called RADFETs. The main reason is because they have a thick oxide created with this purpose (Ma and Dressendorfer 1989, Kelleher et al. 1992, Ristic et al. 1996, Sarrabayrouse and Siskos 1998). Some authors (Vettese et al. 1996) say, commercial transistor do not match the requirements because they are not sensitive enough. However it has been shown (Asensio et al. 2006, Carvajal et al. 2012), commercial transistors have comparable sensitivities to some RADFETs. Furthermore a dosimetric system with commercial transistor could be significantly cheaper than those based on RADFETs.

Due to these reasons several types of transistors, low-cost commercial and RADFETs, have been characterized in this work, to compare their response with photon and electrons beams.

3.1.1 Commercial transistors

Several types of commercial transistors in different configurations have been characterized with two types of radiation beams: electrons and photons. The pMOSs availability in the market is huge, and there are transistors with different structures and configurations. Their sensitivity mainly depends on the thickness oxide, but other factors must be taken into account.

The thickness oxide and the dopant are rarely disclosed in the technical specifications of the component. Then, a parameter which indicates the oxide thickness is the maximum gate-substrate voltage ($V_{GB\ MAX}$) before broken; the greater the absolute value of $V_{GB\ MAX}$, the gate oxide can be expected to be thicker.

Another important factor to consider is the area underneath the gate oxide. The gate must be as much extensive as possible, because it indicates a wide oxide volume too, hence more sensitivity.

A third parameter to bear in mind is that the response to ionizing radiation is expected to be affected by the physical structure of each transistor. As it has been previously discussed in section 2.6.1, there are two main structures of the transistor in the market, but DMOS form the majority of single encapsulate transistor. In a DMOS (see Figure 2.12b) the channel is built just below a part of the gate, therefore only the trapped charge in this area of oxide, above the channel, influent to the *I-V* characteristic. This means an important

reduction of the effective oxide volume, only the regions on the channel. Then, as it is expected transistors with this structure are less sensitive to radiation. In lateral structure, the gate is between drain and source terminals, and the channel is built below all the surface of the gate terminal.

Finally, a very important consideration is the encapsulation. It is desired the radiation reach the transistor in conditions of electronic equilibrium. As well, the nature of the used beam in the characterization has to be considered. For example, it is widely known electron beams cannot be applied over metals. This is due to the fact that electron are absorbed by thin layers of metal or plastic, without reaching the target, the patient, in the radiotherapy treatment. In every type, the mass thickness equivalent is calculated, and if it is necessary a build-up is used to work in reference conditions, where the electronic equilibrium is fulfilled.

Attending these factors and depending the kind of study done with each type of transistor, they are next described.

Transistor 3N163

This type is a lateral enhanced pMOS transistor from Vishay Siliconix, (USA). Currently this transistor is provided by Linear System, (USA), because Vishay Siliconix has the transistor out of stock. However this thesis was done with Vishay Siliconix samples. It was characterized in previous works as dosimetric sensor in a single and unbiased configuration (Asensio et al. 2006, Carvajal et al. 2012). In this work, other studies and characterizations with the same type will be presented.

The device has a transient $V_{GB\ MAX}$ = -125V, more technical data provided by the manufacture are shown in Table 3.1.

Parameter	Symbol	Test conditions	Min	Typ	Max	Units
Threshold voltage	V_t	I_D=-10 mA, V_{GD}=0 V	2	2.5	5	V
Gate-Bulk Current	I_{GSS}	V_{GS}=-40 V, V_{DS}=0 V		2.5	10	pA
Drain Current (V_G=0)	I_{DSS}	V_{GS}=0 V, V_{DS}=-15 V		8	200	pA
Source Current (V_G=0)	I_{SDS}	V_{GD}= V_{BD}=0 V, V_{SD}=-20 V		10	400	pA
Break-Gate Voltage	$V_{G\,\mathrm{MAX}}$			125		V

Table 3.1 Electrical characteristics of 3N163 transistor. Min, Typ and Max denote minimum, typical and maximum values. Minus sign indicate the direction of current and voltage (Siliconix).

The transistor is contained in a cylindrical hermetic metal can, type TO-72. It is composed of an external nickel layer 0.25 mm thick and the height of the cylindrical wall is 4.5 mm. The MOSFET is placed on the surface of a cubic die with an area of 0.3x0.3 mm^2 and a height of 0.1 mm located at the centre of the cylinder. Its typical dimensions are shown in Figure 3.1.

(Carvajal 2008) concluded that taking into account the nickel density is 8.90 g/cm^3, the mass thickness for this type of transistor is 0.22 mm. Also says, from his study of sensitivity and interpolating the average sensitivity from Figure 2.29, concludes the gate oxide thickness of this device is around 200 nm. Actually the 3N163 pMOS has a unit price of less than 2.20 €. These transistors must not be characterized

with electron beams, due to its metal encapsulation.

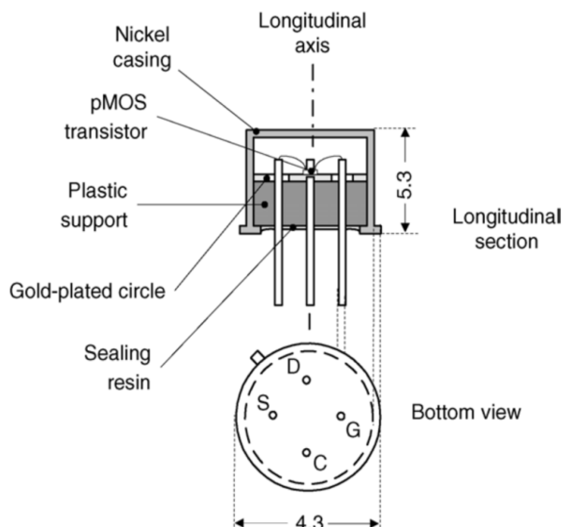

Figure 3.1 Longitudinal section and button view of the 3N163 transistor. Terminal equivalence is (D) drain, (S) source, (C) substrate and (G) gate. Dimension are expressed in millimetres (Asensio et al. 2006).

Transistors DMOS

A second option for the case of general purpose transistors in a single encapsulation are the Vertical Diffused MOS, also called Double-Diffused MOS or simply DMOS, which are mainly used as power MOSFETs. These devices have vertical geometry, which has been previously studied, with short channel dimensions, therefore less sensitive to radiation. During the last two decades some authors have studied the performance and capabilities of the DMOS in a radiation environment (Pejovic, Ristic and Jaksic 1997, Jaksic et al. 1998, Manic et al. 2001, Babcock et al. 1991). Special attention was paid because some of these transistors include body diodes as parasitic devices. Among the commercially available transistors, it had been considered those designed for small signal, having nonmetallic encapsulation (to

be characterized also with electron beams) and the maximum gate-source voltage, V_{GS}, (this last as an indication of a relatively thicker gate oxide).

The types selected were the very common DMOS transistors BS250F, ZVP3306 and ZVP4525, all of them manufactured by Diodes Incorporated (Plano, USA). Three transistors are p-channel enhancement with encapsulation SOT23. ZVP3306 and BS250F have 3-pin encapsulate, and ZVP4525 4-pin SOT89 encapsulate.

Table 3.2, Table 3.3 and Table 3.4 show the electrical characteristics of these devices. Min, Typ and Max denote minimum, typical and maximum values. Minus sign indicate the direction of current and voltage.

Parameter	**Symbol**	**Test conditions**	**Min**	**Typ**	**Max**	**Units**
Threshold voltage	V_t	I_D=-1 mA, V_{GS}=V_{DS}	-1.5		-3.5	V
Gate-Bulk Leakage	I_{GSS}	V_{GS}=±20 V, V_{DS}=0 V			20	nA
Drain Current	I_{DSS}	V_{GS}=0 V, V_{DS}=-60 V V_{GS}=0 V, V_{DS}=-48 V			-0.5 -50	μA
Gate-source Voltage	V_{GS}			±20		V

Table 3.2 Electrical characteristics of ZVP3306 transistor (ZVP3306).

Parameter	Symbol	Test conditions	Min	Typ	Max	Units
Threshold voltage	V_t	I_D=-1 mA, V_{GS}=V_{DS}	-0.8	-1.5	-2	V
Gate-Bulk Leakage	I_{GSS}	V_{GS}=±40 V, V_{DS}=0 V		±1	±100	nA
Drain Current	I_{DSS}	V_{GS}=0 V, V_{DS}=-250 V		-30	-500	nA
Gate-source Voltage	V_{GS}			±40		V

Table 3.3 Electrical characteristics of ZVP4525 transistor (ZVP4525).

Parameter	Symbol	Test conditions	Min	Typ	Max	Units
Threshold voltage	V_t	I_D=-1 mA, V_{GS}=V_{DS}	-1		-3.5	V
Gate-Bulk Leakage	I_{GSS}	V_{GS}=-15 V, V_{DS}=0 V			-20	nA
Drain Current	I_{DSS}	V_{GS}=0 V, V_{DS}=-25 V			-0.5	μA
Gate-source Voltage	V_{GS}			±20		V

Table 3.4 Electrical characteristics of BS250F transistor (BS250F).

Due to the reduced dimensions of this well-known superficial mounted device (SMD), SOT23, it has been considered the silicon die, where the transistor is allocated, is just in the centre of encapsulation, and the surrounding material is considered epoxy. The epoxy has a density between 1.1 and 1.4 g/cm^3. The 3-pin encapsulate has dimensions of 2.8x1.05x1.32 mm^3, and in the case of 4-pin are

4.5x1.50x2.42 mm. Considering an epoxy density of 1.25 g/cm^3 and a distance in encapsulate of 0.525 mm and 0.75 mm (half of height), the mass thickness is around 0.06 g/cm^2 and 0.09 g/cm^2 respectively. The unit cost is between 0.49 € and 0.57 €.

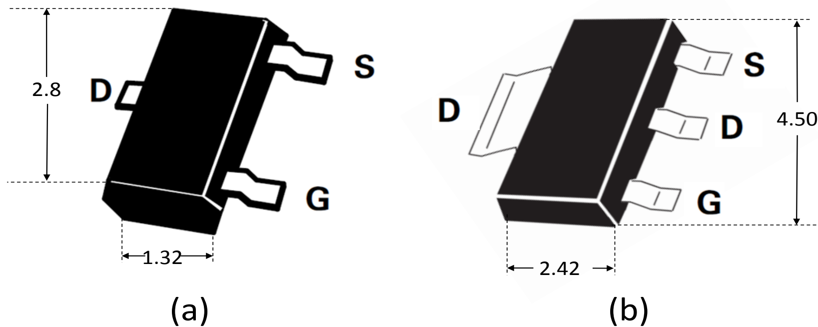

Figure 3.2 Encapsulate SOT23 a) 3-pin b) 4-pin .Dimensions are expressed in millimetres (ZVP3306 , ZVP4525 , BS250F).

CD4007

In this thesis, it has been worked not only with single encapsulated transistors, but also with multiple integrated transistors. Among the integrated circuits with pMOS transistors, it has been decided as a candidate the well-known lateral CD4007. This integrated circuit is composed of six transistors, three nMOS and three pMOS (see Figure 3.3), and is available from several semiconductor manufacturers. Other authors have studied the influence of ionizing radiation in this integrated circuit (Pejović, Jakšić and Ristić 1998, Siebel et al. 2014).

One more time, the technological parameters cannot be obtained from the manufactures, but in this case, some data have been published in the literature. (Pejović et al. 1998) describes an integrated circuit manufactured by 'Ei-Microelectronics', Nís, Serbia. The gate oxide is 100 nm and length (L) and width (W) channel are 4.4 and 100

μm respectively. On the other hand, (Foty and Titcomb 1987) talks about a thickness oxide of 120 nm, and channel size of W= 190 μm and L=4 μm. This version of the device has a boron implantation N_A=2.8x10^{16} cm^{-3}. Both designs have an Al-gate terminal. Therefore, although there are slight differences, it is concluded that the main parameter, gate oxide thickness, is around 100-120 nm.

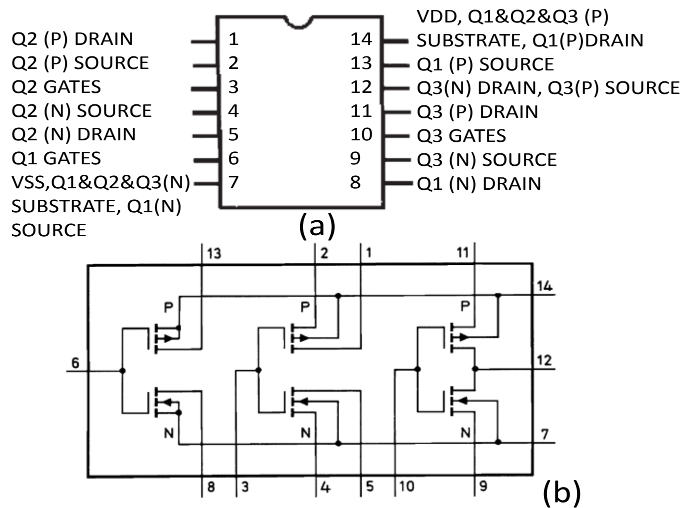

Figure 3.3 CD4007 a) Pin-out b) Functional diagram (CD4007UB).

As (Siebel et al. 2014) explains, which also characterized the device as dosimetric sensor with photon beams, this size of gate oxide provides the sensor with two important characteristics: their radiation sensitivity is around 7 mV/Gy, suitable for radiotherapy treatment applications, and operation with relatively reduced supply voltage since $|V_t|$ is around 1.6 V.

In the present work devices manufactured by Texas Instruments (Dallas, USA) and NXP Semiconductors (Eindhoven, Netherlands) were chosen. Also, two versions nonmetallic packages, of this device were tested: surface-mounted (SMD), Figure 3.4, and through-hole

(DIP), **Figure 3.5**. The silicon die was considered to be situated in the middle of geometry, and the surrounded material was considered epoxy. Then the mass thickness of SMD and DIP encapsulate are around 0.125 g/cm^2 and 0.317 g/cm^2, respectively. The unit cost is around 0.25 € for the surface-mounted and 0.3 € in the case of through-hole version.

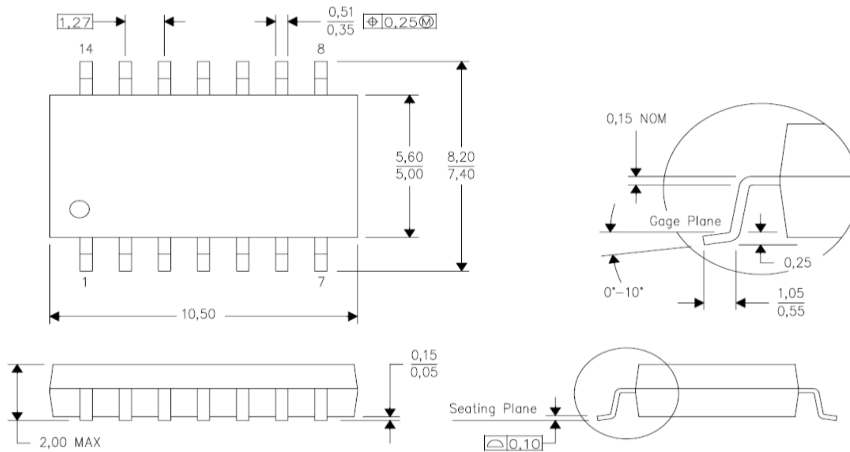

Figure 3.4 Dimensions of SOP encapsulation (CD4007UB). Dimensions are expressed in millimetres.

From Figure 3.3b, it is observed only the *p* type transistor Q2 and Q3 could be used in saturation configuration (remembering Figure 2.33), which is the typical configuration used to detect radiation. Q1 transistor cannot be used because it has short-circuited the bulk and drain terminals.

The internal schematic diagram (Figure 3.6) of this integrated circuit must be taken into account, because protection diodes affect to the possible bias of this device. There is a protection diode between the source and the gate of MOSFET Q2 and Q3, which turns on if a

voltage higher than 0.6 V is applied in the gate.

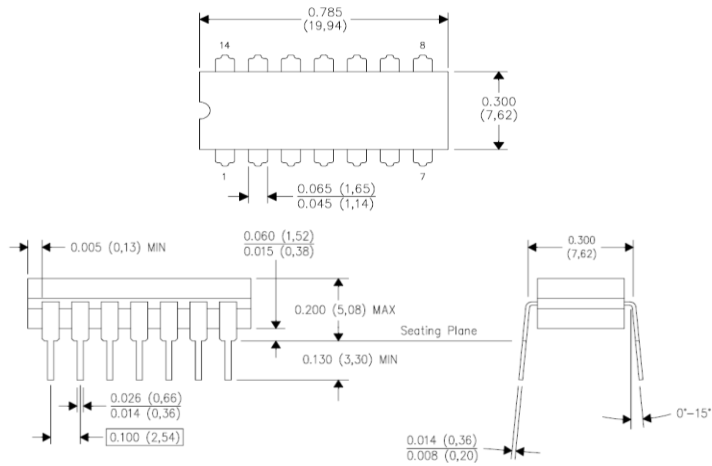

Figure 3.5 Dimensions of PDIP encapsulation (CD4007UB). Dimensions are expressed in inches/millimetres.

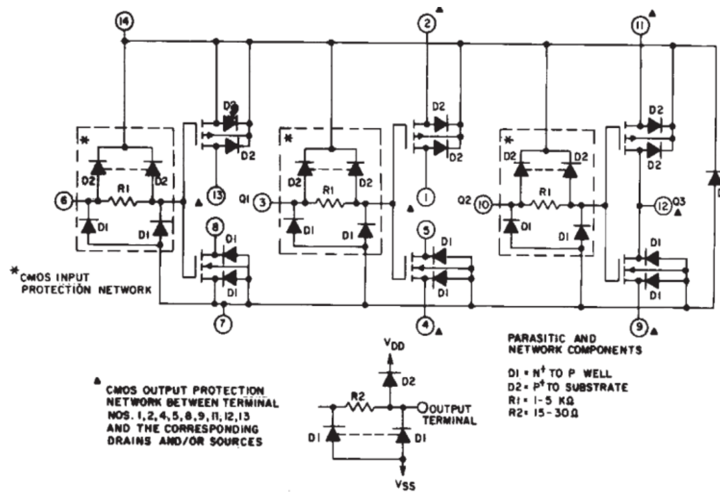

Figure 3.6 Detailed schematic diagram of CD4007UB showing input, output and parasitic diodes (CD4007UB).

3.1.2 RADFETS

The RADFEs in this work are divided in five types, manufactured and provided by Tyndall National Institute, Cork, Ireland. The samples are Al-gate p-channel MOS transistors and all of them are the type named ESAPMOS4. Gate oxides of 100 nm, 400 nm and 1µm were grown as pure thermal oxides (100 nm and 400nm) or a combination of thermal and CVD oxide (1μm). Three types of 400nm with different process of oxidation were tested in this work. To differentiate the three different types, they are referenced as 400 nm_W5, 400 nm_W7 and 400 nm_W8. 400 nm_W5 can be called a “standard” process; 400 nm_W7 and 400 nm_W8 are identical to the standard process, except for higher post-oxidation anneal temperature and duration.

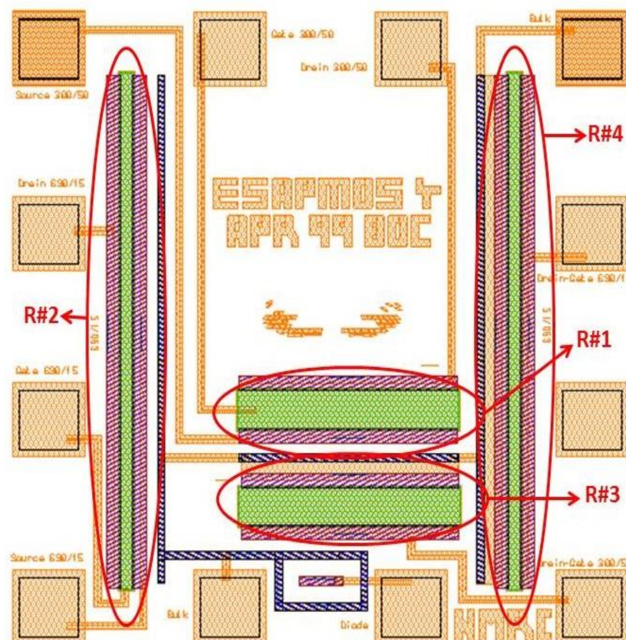

Figure 3.7 ESAPMOS4 layout.

Bond-pad No.	Label as Figure 3.8	Description
1	Bulk	Substrate connection (common)
2	Drain 300/50	Drain of 300/50 W/L RADFET#1
3	Gate 300/50	Gate of 300/50 W/L RADFET#1
4	Source 300/50	Source of 300/50 W/L RADFET#1
5	Drain 690/15	Drain of 690/15 W/L RADFET#2
6	Gate 690/15	Gate of 690/15 W/L RADFET#2
7	Source 690/15	Source of 690/15 W/L RADFET#2
8	Bulk	Another bulk connection (as 1)
9	Diode	P+ diode
10	Drain-Gate 300/50	Common drain & gate of 300/50 W/L RADFET#3
11	NC	No connection
12	Drain-Gate 690/15	Common drain & gate of 690/15 W/L RADFET#4

Table 3.5 Pin- out and description pins of ESAPMOS4.

Each chip contained four individual RADFETs, organized as two pairs with unique geometry (see Figure 3.7). Two of them had a channel width of W = 300 μm, and a channel length of L =50 μm (300/50 type), and another two transistors were 690/15 type. Two transistors (one of 300/50 and another of 690/15 type) had a common substrate pin, while the other terminals (gate, drain and source) were independent. The other two RADFETs of each type are internally connected to the source and bulk, and drain and gate, respectively. Boron implantation was done through the gate oxide to reduce the initial, pre-irradiation threshold voltage for the types of 400 nm and 1 μm. All of them were packaged in standard ceramic 14-pin DIP packages with kovar lids (see Figure 3.9). The pinout is observed in

Table 3.5 and Figure 3.8. The mass thickness for this kind of encapsulate is 0.21 g/cm^2 with kovar Lid or 0.00029 g/cm^2 without kovar lid.

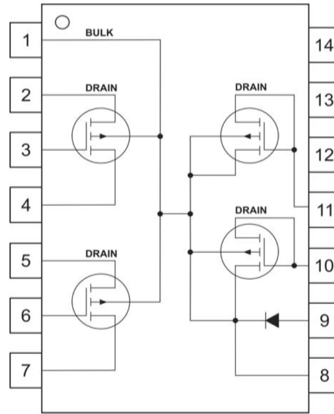

Figure 3.8 ESAPMOS4 pin-out.

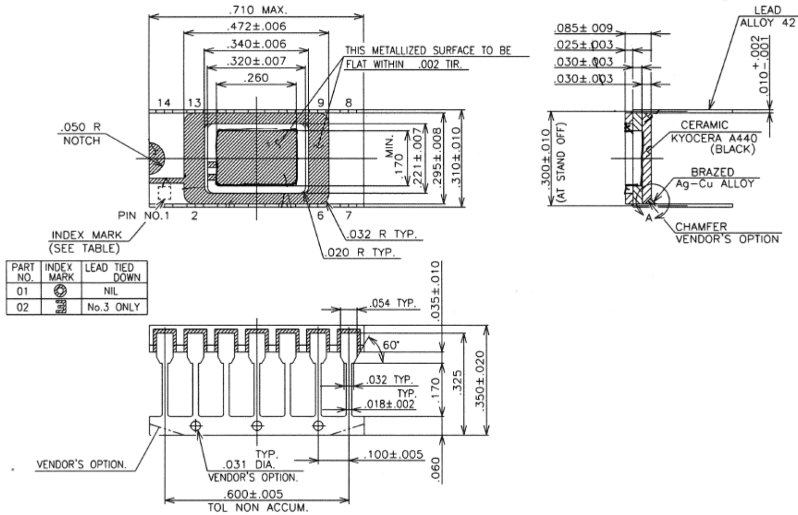

Figure 3.9 14-pin DIP packages with kovar lids.

In Figure 3.10, a 3-dimension model for this device is observed. The model was realized in a text file for Montecarlo simulations (PENELOPE code in our case) and it has been visualized with

GVIEW2D and *GVIEW3D*, which are geometry viewers that display 2 or 3 dimensional images of the geometry respectively. In the cross-section, it is observed in the central part, the silicon die (orange and blue region) where the four RADFETs are built.

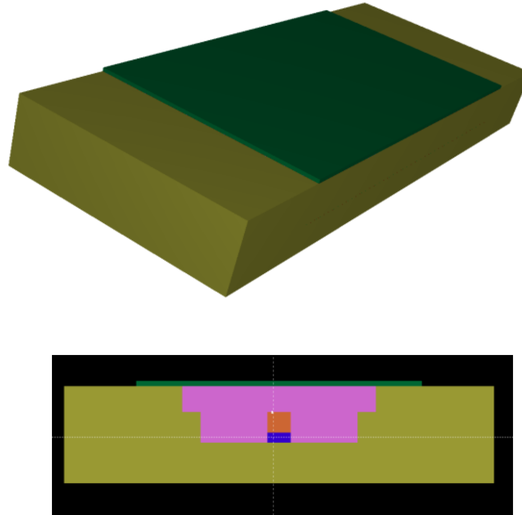

Figure 3.10 3D model for an ESAPMOS4 RADFET.

Type	**Size**
100 nm	300/50
	690/15
400 nm implanted: 400 nm_W5, 400 nm_W7 and 400 nm_W8	300/50
	690/15
1 μm	300/50
	690/15

Table 3.6 RADFETs types.

To sum, five types of RADFETs transistor were characterized. The transistors are referenced hereinafter as Table 3.6 shows. To specify the size of channel, in every name a suffix is added, with

300/50 or 690/15, which indicates the width and length respectively. Previous published papers mention the threshold voltages of the 100nm type is around 3.3 V (Ristic et al. 2011). In case of implanted 400nm the threshold voltage is around 0.5 and 2 V for sizes of 300/50 and 690/15 respectively (Benson et al. 2004, Jaksic et al. 2005).

3.2 Radiation sources

Two irradiation sources have been used in this work, a Cobalt therapy Unit for irradiation with quasi monoenergetic photons and a Linear accelerator used in clinical treatments.

3.2.1 Cobalt therapy unit (^{60}Co)

The cobalt therapy unit was an AECL Theratron-780 located at University Hospital of San Cecilio in Granada (Spain). This is a teletherapy unit with a ^{60}Co source. This source provides gamma radiation. The isocentre is placed to 80 cm from treatment head, where is situated the radioactive isotope. The teletherapy unit can turn the treatment head ±180°C, with rectangular irradiation field, with a maximum size of 30x30 cm^2. ^{60}Co decays by beta decay (β^-) to stable isotope ^{60}Ni.

The decay scheme is shown in Figure 3.12. With an elevated probability (99%), the ^{60}Co after decaying became ^{60}Ni with energy of 2.50 MeV over the fundamental state. During the process, two photons of 1.17 MeV and 1.33 MeV are emitted.

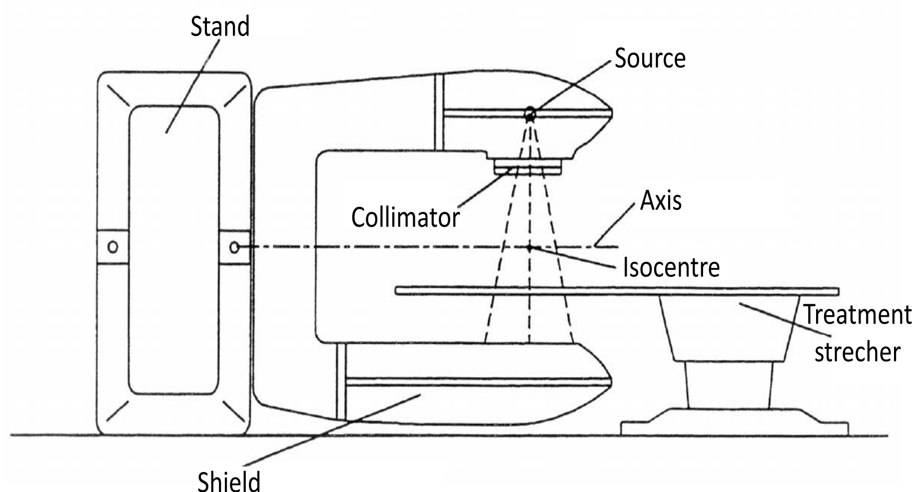

Figure 3.11 Scheme of a teletherapy unit of ^{60}Co (Ortega Aramburu and Jorba Bisbal 1996).

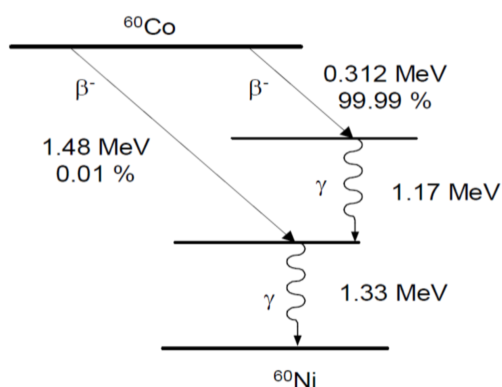

Figure 3.12 Decay scheme of ^{60}Co (Carvajal 2008).

There is a very low probability that the ^{60}Co became directly the state of Ni of 1.33 MeV. In this process, a beta particle (β^{-}) with higher energy is emitted. In the cobalt therapy unit, only photons are emitted, because the electrons (β^{-}) are absorbed by the elements which form the source and head. In dosimetric calculations, it is normally considered photons with an average energy of 1.25 MeV.

However, the emitted spectrum by Theratron-780 is slightly different from the ^{60}Co spectrum due to filters and collimators used to get a uniform radiation field. Figure 3.13 shows the spectrum produces in the isocentre of this machine with several radiation fields, obtained by (Teimouri Sichani and Sohrabpour 2004) with Monte Carlo simulations. As higher radiation field, the contribution of low energies is more important because more photons, which have lost energy by angular deflection, reach the isocentre of source.

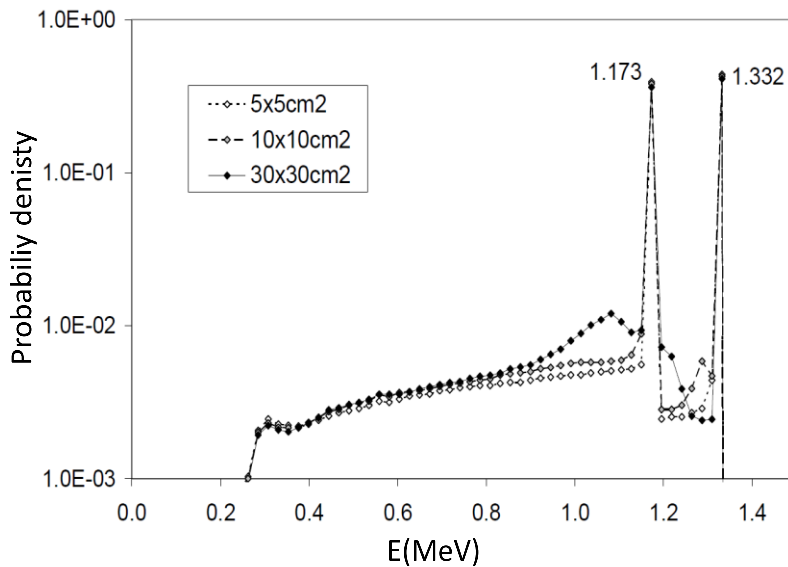

Figure 3.13 Theratron-780 spectrum at the isocentre with different fields (Teimouri Sichani and Sohrabpour 2004).

3.2.2 Lineal accelerator (LINAC)

The linear accelerator (LINAC) Mevatrons KDS (Siemens, Berlin, Germany), also operated at the University Hospital of San Cecilio in Granada (Spain). This is a linear accelerator used for radiotherapy treatments. The majority of modern LINACs work with

power source of 3000 MHz. Its isocentre is placed to 100 cm from the source. The maximum field in the distance to isocentre is 40x40 cm^2. LINACs are capable of generating photon and electron beams. This model has two nominal energies of photons, 6 and 18 MeV (with dose rate of 200 and 300 monitor units per minute). In the case of electron beams, where different square and circular applicators could be used, the ranges of energies is described in Table 3.7 where the dose rate are 300 monitors unit per minute, with the possibility of high dose rate to 900 um/min.

<table>
<tr><th>Type of beam</th><th>Electric field</th><th>Dose Rate (m.u./min)</th></tr>
<tr><td rowspan="2">Photons</td><td>6 MeV</td><td rowspan="2">200 and 300</td></tr>
<tr><td>18 MeV</td></tr>
<tr><td rowspan="6">Electrons</td><td>6 MeV</td><td rowspan="6">300 or 900 (high dose rate)</td></tr>
<tr><td>8 MeV</td></tr>
<tr><td>10 MeV</td></tr>
<tr><td>12 MeV</td></tr>
<tr><td>15 MeV</td></tr>
<tr><td>18 MeV</td></tr>
</table>

Table 3.7 Range of energies of LINAC Mevatron KDS.

The operating principle is based on electron acceleration. The electrons are injected into a cavity, normally a waveguide with finite dimensions, where a previous wave has been created by a high frequency resonator (*klystron*), see Figure 3.14. The cathode provides electrons to an accelerator tube in “packages” during pulses produces by the modulator. The modulator, also controls, the microwave emissions regulating the generation of them (*klystron*) also with electric pulses simultaneous those controlling the electron emission. The microwaves, whose objective is the acceleration of electrons, are driven by the waveguides to accelerator tube, where the electrons also arrive

synchronised with the microwaves. The waves must have an electric field component in the direction of the propagation of the particle, which is fundamental to accelerate the electron.

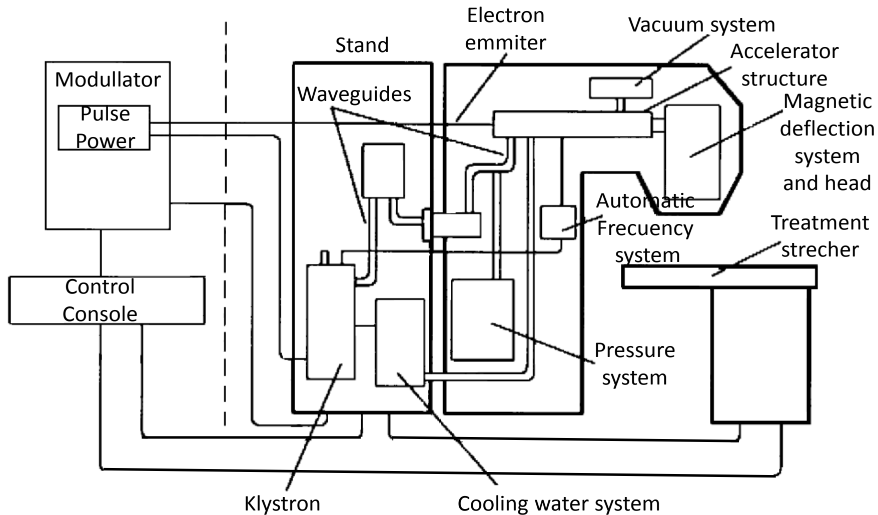

Figure 3.14 Lineal accelerator components (Ortega Aramburu and Jorba Bisbal 1996).

After the acceleration, the electrons reach the treatment head, where are directed by an electric field that produces a deflection of 270°. Now the beam is conformed to the treatment: if it is an electron beam, only it is necessary to extend and make uniform the beam. In the case of photon beam, the electrons are sent to a target with elevated atomic number, i.e. tungsten, and X-rays of high energy have obtained (Ortega Aramburu and Jorba Bisbal 1996).

In the case of electrons, it is necessary to add a second collimation, with electron applicators, to adapt the size of the field for the radiation treatment. X-rays are not emitted in a uniform distribution in all directions. With more electron energy, smaller angle

of emission in photon. To make uniform the beam, equalizers filter in the output of target are used.

3.2.3 Dose and electronic equilibrium conditions

The electronic equilibrium conditions must be particularized to every source and type of the transistor.

Co^{60} source

The mass thickness equivalent to ensure the electronic equilibrium with photons of 1.25 MeV is 0.56 g/cm^3 (Knoll 2000). Due to the Theratron-780 emits photons with lower energies, therefore the maximum dose, where the electronic equilibrium condition is fulfilled, is reached in a lower depth. (Panettieri et al. 2007) obtained the percentage depth dose (PDD) curve for Theratron-380 with experimental and simulated data. They say the maximum dose with electronic equilibrium in the isocentre of source and with a field of 10x10 cm^2 is reached in 0.35 mm in water. Figure 3.15 shows the experimental results from these authors.

As it has been previously explained, the cobalt therapy unit was used with the type of transistors 3N163. The mass thickness equivalent of the encapsulation of this type is 0.223 g/cm^2, where the dose is 99.5% of the maximum value, extracted by (Carvajal 2008) using the PDD reported by (Panettieri et al. 2007). Thus, as the electric field used is higher than 10x10 cm^2, the electronic equilibrium is covered, because with higher electric fields, smaller depth is necessary. Accordingly, in a field of 30x30 cm^2, this condition is ensured.

As the technological parameters of the transistor are unknown, (Carvajal 2008) overestimated the mass thickness from the source of ^{60}Co to oxide in the transistor. The mass thickness was 0.22 g/cm^{2,} where the PDD in this distance is 99.5%.

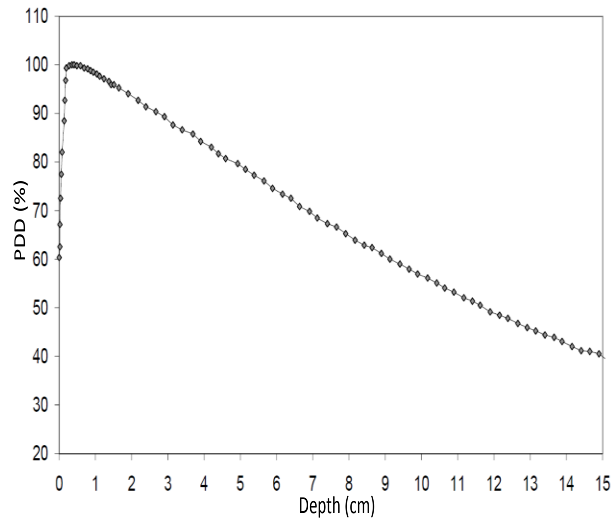

Figure 3.15 PDD of a Theratron-780 Cobalt therapy unit in water. It has been calculated for the isocentre (80 cm) with a radiation field of 10x10 cm^2 (Carvajal 2008) with data from (Panettieri et al. 2007).

LINAC

In the case of the lineal accelerator (LINAC), it has been made a difference between photon beams and electrons beam. The PDD curves for Mevatrons KDS with experimental data both photons and electrons beams are shown in the Figure 3.16 and Figure 3.17, respectively. These experimental data were transferred by the Radiophysic department from University Hospital San Cecilio, Granada. The curves belong to the lineal accelerator used in the experiments. The maximum dose in photons beams with electronic equilibrium in the isocentre to 100 cm from the source and a field of 20x20 cm^2 is reached in 1.6 cm

water. In the case of electrons beams, the maximum dose with a field of 15x15 cm^2 is to 1.7 cm.

The situation is quite different for LINAC than for ^{60}Co unit, both photon and electron beams. The PDD measured with the different types of transistors and their encapsulation in a radiation field of 10x10 cm^2 for photons and for electrons beams are shown in Table 3.8. Due to the electronic equilibrium conditions are not fulfilled, in some cases, a build-up of water-equivalent RW3 (PTW, Germany), is necessary to be used. The size of this build-up and the new PDD, are also shown in the Table 3.8.

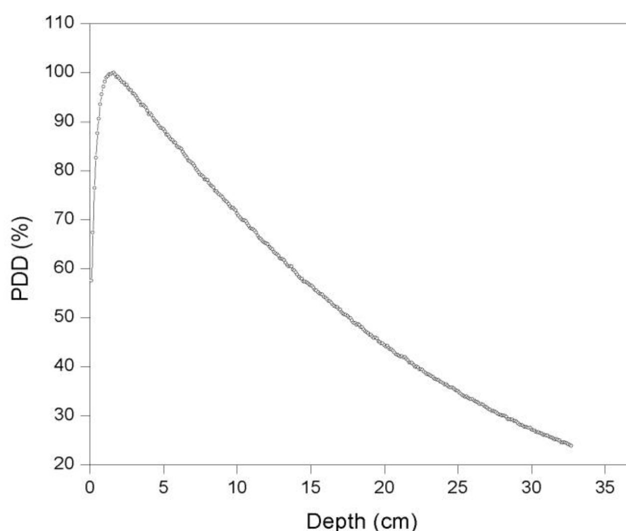

Figure 3.16 PDD of Siemen Mevatron KDS unit in water (Photons of 6MeV). It has been calculated for the isocentre (100 cm) with a radiation field of 10x10 cm^2.

Therefore, as the electric field used is equal or higher than 10x10 cm^2, the electronic equilibrium is covered, because similarly to Co^{60}; with higher electric fields, smaller depth is necessary. Then, in a field of 25x25 cm^2 or 15x15 cm^2 this condition is ensured.

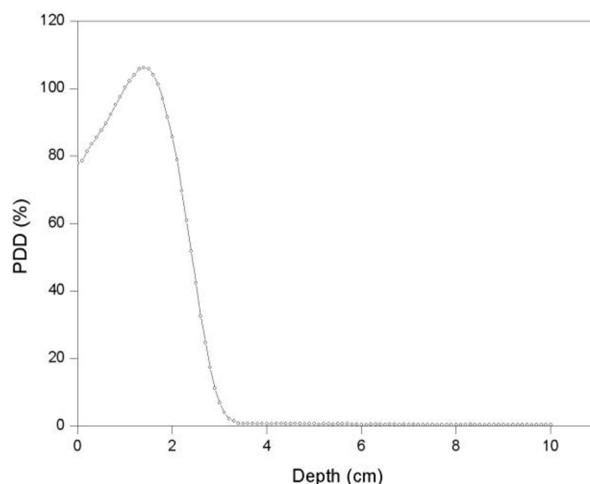

Figure 3.17 PDD of Siemen Mevatron KDS unit in water (Electrons of 6MeV). Calculated for the isocentre (100 cm) with field of 10x10 cm^2.

Beam type	Type	Mass thickness (g/cm^2)	PDD(%)	Build-up (cm)	Total build-up (cm)	$PDD_{with\ Buil\text{-}up}$(%)
Photons (10x10 cm^2)	3N163	0.225	64.5	1	1.225	98.9
	ZVP3306 /BS250F	0.065	47.5	1	1.065	97.7
	ZVP4525	0.093	50.6	1	1.093	97.9
	CD4007 (SMD)	0.125	54.1	1	1.125	98.1
	RADFET	0.210	63.4	1.5	1.710	99.8
Elec-trons (10x10 cm^2)	ZVP3306	0.065	78.4	-	0.065	78.4
	CD4007 (SMD)	0.125	79.3	-	0.125	79.3
	CD4007 (DIP)	0.317	83.9	-	0.317	83.9
	RADFET (NO LID)	0.00029	77.9	1.3	1.30029	105.9

Table 3.8 PDD and build-up used for every transistor and beam type.

3.3 Irradiation Setup

As it has been previously explained, two irradiation sources were used to characterize the radiation sensors. The response to radiation under reference conditions or in the situation more similar to electronic equilibrium is analysed.

Theratron-780 was used for the transistor 3N163 in the subthreshold region. All the radiations were carried out at a constant temperature with all four transistor terminals connected to each other, hence without gate voltage. The transistors were irradiated with a 35x35 cm^2 field and were located at a distance of 80 cm from the gamma-ray source. The doses were 2, 4 or 6 Gy per radiation session, up to a limit of 58 Gy and a constant dose rate of 0.22 Gy/min under normal incidence. The ionizing chamber PTW23332 (PTW, Freiburg, Germany) was used in every irradiation session to control the dosimetry.

Linear accelerator Mevatrons KDS was used in the major part of this work. All the irradiations were carried out with the pMOS transistors (in the case of unbiased tests) or the biasing board, situated at the isocentre, at 100 cm from the source. Transistors were characterized both under electron and photon beams, depending on the experiment that is carried out. Always with normal beam incidence, over a squared slab phantom made of water-equivalent RW3 (PTW, Germany) with dimensions which varies with the experiment. This information is provided in every case in next chapter. To control the stability of the accelerator, also an ionization chamber was needed in all irradiation sessions for photon and electron beams. Two models were used in this work, also the PTW23332 and the IBA SCANDITRONIX CC13 ionization chamber (IBA, Schwarzenbruck,

Germany). During this work, these chambers served also to determine the measured dose.

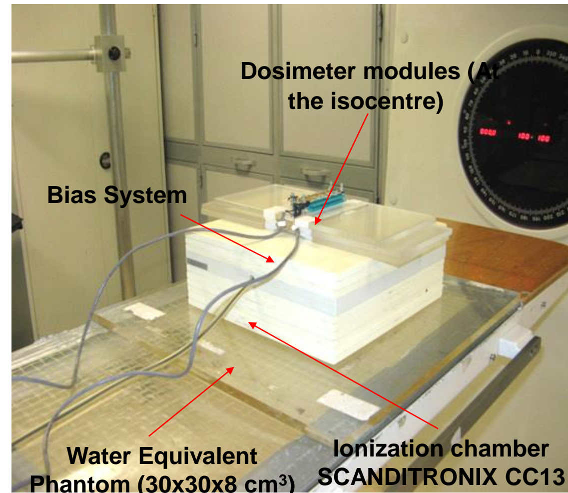

(a)

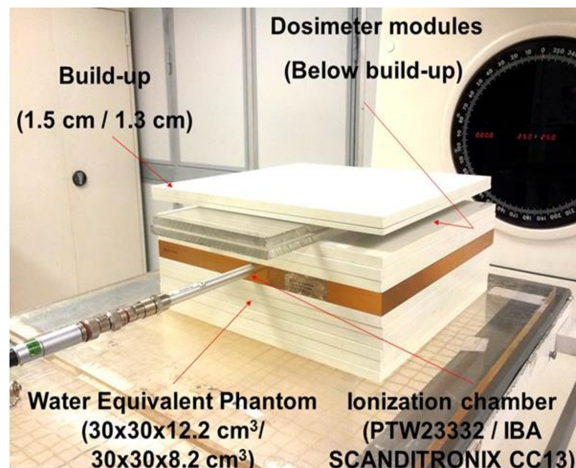

(b)

Figure 3.18 Irradiation set-up: a) Biasing tests for electron beam in commercial transistors. b) Unbiased tests for commercial and RADFET transistors in photon and electron beams.

Tests were always carried out with a field of 6 MeV for both photon and electron beams. In the case of commercial transistor, the

characterization was done with an irradiation field of 25x25 cm^2 for electron beams (without collimator) and 10x10 cm^2 for photons beams. For RADFET characterization, it was using an irradiation field of 25x25 cm^2 for photons and for electron beams was performed using a collimator and an irradiation field of 15x15 cm^2. The differences in size of irradiation field are due to the size of the analysed transistor, and if it is necessary use some auxiliary board, as in the case of biasing characterization. Some cases require a wider size, to get maintain all the sensor inside the irradiation field.

A picture of the irradiation setup is shown in Figure 3.18 for the bias (a) and unbiased test (b). Sensor modules were irradiated with dose between 1.9 and 20 Gy in each session depending of the experiment. A dose rate of 3.36 cGy/s or 4.85 cGy/s for photon and electron beams, respectively, up to a limit between 55 Gy or 275 Gy in the special case of RADFET with t_{OX} = 100 nm, manufactured to detect high radiation dose.

The build-up used is extremely dependent of the type of transistor. Every build-up must be calculated depending on the material and distance between the silicon die, where is allocated the transistor, and the source. Some experiments, for example in case of electron characterization with commercial transistors, no build-up was used on the MOSFETs to prevent the target volume from shadowing (Bloemen-van Gurp et al. 2006). However for the rest types a build-up also of water-equivalent was used: 1 cm (commercial transistors) or 1.5 cm (RADFETs) for photon beams and 1.3 cm (in RADFETs) for electrons beams, as it has been previously explained in Table 3.8.

During the characterization and to avoid fading effects, voltage measurements were carried out between six or ten minutes after the

irradiation. This elapsed time was enough to obtain stable values with our dosimetry system which will be described below.

In each session, transistors were irradiated in groups of 5 transistors or 4 chips, which contain 4 RADFETs each, thus a total of 16 transistors are irradiated simultaneously.

3.4 Experimental Setup of the electrical characterization

B1500A Semiconductor Device Parameter Analyser (Keysight Technologies, Santa Clara, USA), see Figure 3.19 supports various measurement capabilities for *I-V*, *C-V*, pulsed *I-V* and fast *I-V* measurement and enables a wide range of electrical characterizations and evaluations for device, material, semiconductor, active/passive component, and any electric devices. Its modular architecture allows configuring and upgrading the measurement modules up to ten slots. It was used to measure the *I-V* characteristics of the transistors and to bias constant drain currents. This instrument measures in the range from 0.1 fA to 1 A, and from 0.5 μV to 200 V.

EasyEXPERT is graphical user interface (GUI) based essential software working on the B1500A embedded Windows XP. It provides hundreds libraries named application tests. The operation is available through the 15-inch wide touch screen in addition to keyboard and mouse operation for ease of use. The EasyEXPERT software also provides an efficient test environment for intuitive operation, analysis and exploration in device characterization. The test condition and measurement data are automatically recorded in the workspace.

Therefore, the B1500 is controlled by the EasyEXPERT, where application tests are created for every type of study.

Figure 3.19 B1500 analysed semiconductor (Keysight).

The uncertainty in the B1500 semiconductor analyser depends on the source/monitor unit (SMU) or terminal used. For the *I-V* curves, B1517A High resolution module (HRSMU) was selected. This module has a range in voltage up to 100 V and in current up to 0.1 A with 4-quadrant operation. The minimum measurement resolution is 1 fA / 0.5 μV. In the specifications of the manufacture, in this concrete module the resolution and accuracy, depends on the voltage range (Table 3.9) and current range (Table 3.10). Also, it must be considered, when the SMU is measuring (Measure mode) or is forcing a measure (current or voltage) (Force mode). The temperature range of working is 5°C to 40°C and humidity range 20% and 70% RH, non-condensing.

Voltage range	Force resolution	Measure resolution	Force accuracy[1]	Measure accuracy[1]	Maximum current
±0.5 V	25 μV	0.5 μV	±(0.018% +150 μV)	±(0.01% +120 μV)	100 mA
±2 V	100 μV	2 μV	±(0.018% +400 μV)	±(0.01% +140 μV)	100 mA
±5 V	250 μV	5 μV	±(0.018% +750 μV)	±(0.009% +250 μV)	100 mA
±20 V	1 mV	20 μV	±(0.018% +3 mV)	±(0.009% +900 μV)	100 mA
±40 V	2 mV	40 μV	±(0.018% +6 mV)	±(0.01% +1 mV)	[2]
±100 V	5 mV	100 μV	±(0.018% +15 mV)	±(0.012% +2.5 mV)	[2]

[1] ± (% of reading value + offset voltage V).

[2] 100mV ($V_0 \leq 20$V), 50mA (20V<$V_0 \leq 40$V), 20mA (40V<$V_0 \leq 100$V), V_0 is the output voltage in volts.

Table 3.9 Voltage range, resolution, and accuracy.

The transistor is placed in a test fixture in the 16442B, which is basically a Faraday box designed for testing electronic devices. This allows the electrical connection between the transistor and the semiconductor analyser B1500, with a suitable socket module, which allows user to easily connect various devices to the measurement units. Figure 3.20 picture shows the typical connection between the semiconductor analyser ant the test fixture. Some types of transistors, for example 3N163 and RADFETs have no protection against accidental electrostatic charge injection. So, to prevent injection of charge, that changes the electrical characteristics of the device, a wrist strap was used to handle all the transistors. In spite of precautions, some of them were damaged during the electrical and thermal characterization.

Current range	Force resolution	Measure resolution	Force accuracy[1]	Measure accuracy[1]	Maximum voltage
±1 pA	1 fA	100 aA	±(0.9% +15 fA)	±(0.9% +12 fA)	100 V
±10 pA	5 fA	1 fA	±(0.46%+30 fA +10 aA x V_0)	±(0.46%+15 fA +10 aA x V_0)	100 V
±100 pA	5 fA	2 fA	±(0.3%+100 fA +100 aA x V_0)	±(0.3%+30 fA +100 aA x V_0)	100 V

[1]±(% of read value + offset current (fixed parte determined by the output/measurement range + proportional part that is multiplied by V_0).

Table 3.10 Current range, resolution, and accuracy.

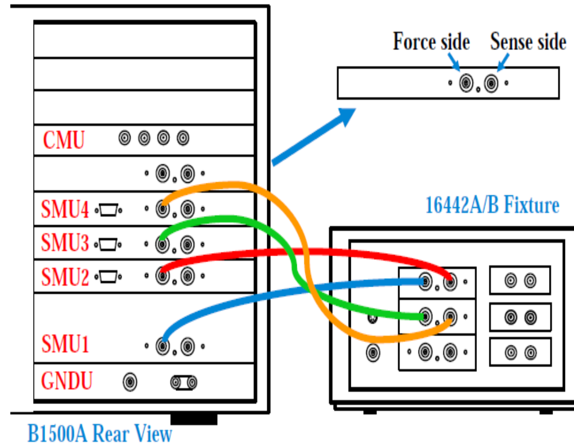

Figure 3.20 SMU Triax connection B1500 with the test fixture 16442B (Agilent 2014).

The *I-V* curves in linear and saturation regimes are obtained with this semiconductor analyser (see Table 3.12). It must be highlighted the range of currents or sweep could vary with the type of

the transistor. Typical configurations are shown in the Table 3.12. In the lineal regime a constant voltage of 100 mV in source and bulk, which are short-circuited and drain to ground, and a sweep in the gate from 0 to -10 V is done. In the saturation regime, the terminal source and bulk, and drain and gate are tied, respectively, and a sweep in current from 0 to 10 mA is applied with drain terminal grounded. In Figure 3.21 an example of the connections between transistor terminals and the test fixture is shown, but these connections will change with the pinout and test for the different types of transistors. Auxiliary PCBs have been manufactured, both for lineal and saturation regime (see Figure 3.22 and Figure 3.23). In saturation region, only a manual switch is used, to change between the source terminals of all transistors. However, in the linear range, two switches are needed to change the terminals sources and gates. The final connections are connected to the test fixture.

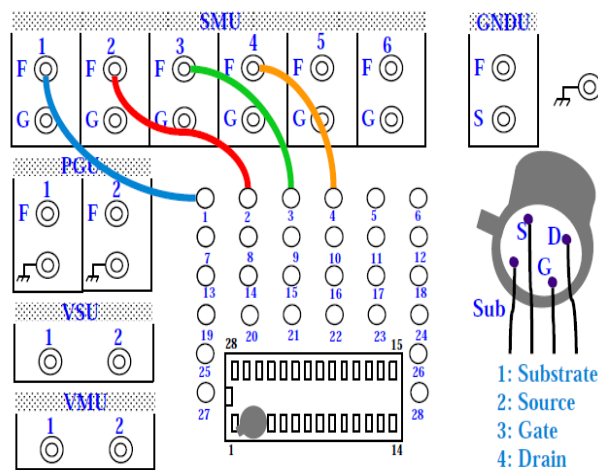

Figure 3.21 Connection jumper leads of 16442B with the MOS transistor (Agilent 2014).

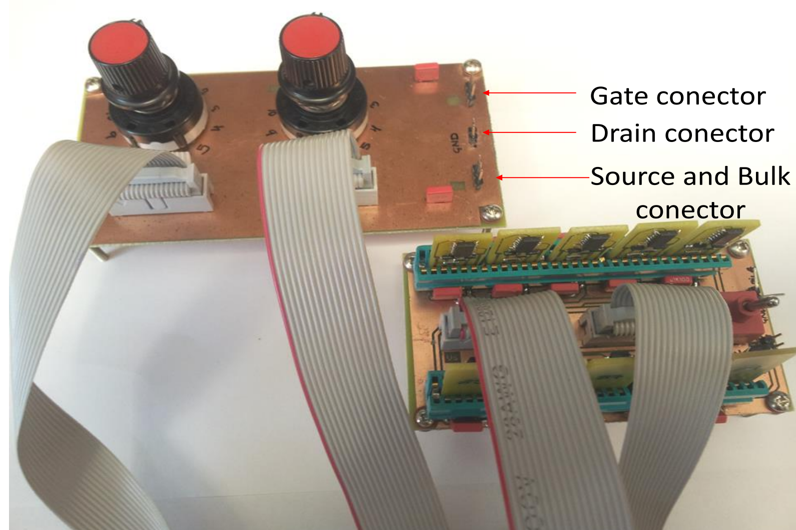

Figure 3.22 Auxiliary PCB for linear region characterization.

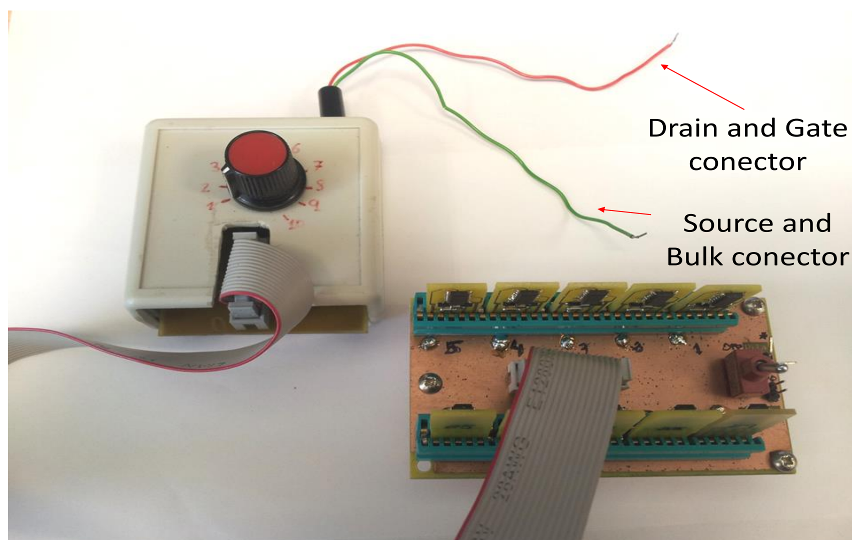

Figure 3.23 Auxiliary PCB for saturation region characterization.

In the subthreshold study another semiconductor parameter analyser HP-4145B (Hewlett Packard, Palo Alto, CA, USA) was used. It has four source monitor units (SMU). Similarly to B1500, each one

could be programed as voltage source and to measure the current or current source and to measure the voltage, in that terminal. The extractor parameter is controlled by a PC with a bus GPIB. In particular, the drain current I_{DS} as a function of the gate voltage, V_{GS}, was obtained for each transistor. The curves were extracted in subthreshold and the saturation regime with a drain source voltage of V_{DS} = -100 mV. Substrate and source terminals were shorted. During the curve measurement, transistors were also placed in an electromagnetic-shielded test fixture HP16085A (Hewlett Packard, Palo Alto, CA, USA). This is another Faraday box, which allows the electrical connection between the HP-4145B and the device.

Range	**Accuracy**	**Uncertainty (±3σ)**
±20 V	1 mV	$\pm(0.001 \cdot V_0 + 10\ mV + 0.4 \cdot I_0)$
±100 mA	100 μA	$\pm(0.003 \cdot I_0 + 100\ \mu A + 2.10^{-6} \cdot V_0)$
±10 mA	10 μA	$\pm(0.003 \cdot I_0 + 10\ \mu A + 2.10^{-7} \cdot V_0)$
±1 mA	1 μA	$\pm(0.003 \cdot I_0 + 1\ \mu A + 2.10^{-8} \cdot V_0)$
±100 μA	100 nA	$\pm(0.003 \cdot I_0 + 100\ nA + 2.10^{-9} \cdot V_0)$
±10 μA	10 nA	$\pm(0.003 \cdot I_0 + 10\ nA + 2.10^{-10} \cdot V_0)$
±1 μA	1 nA	$\pm(0.003 \cdot I_0 + 1\ nA + 2.10^{-11} \cdot V_0)$
±100 nA	100 pA	$\pm(0.005 \cdot I_0 + 100\ pA + 2.10^{-12} \cdot V_0)$
±10 nA	10 pA	$\pm(0.005 \cdot I_0 + 10\ pA + 2.10^{-13} \cdot V_0)$
±1 nA	1pA	$\pm(0.005 \cdot I_0 + 1\ pA + 2.10^{-14} \cdot V_0)$

Table 3.11 Technical specifications of HP4148B.

The error extractor depends on the scale and the value of measurement. By the manufacturer, the specifications of HP4145B the uncertainty of measurements are summarized in Table 3.11. V_0 and I_0 are the voltages and currents registered in every case in V and A respectively. If the temperature of the extractor is different to 23±5°C,

the uncertainty is multiplied by a factor 2. The minimum and maximum working temperatures are 10°C and 40°C respectively.

The configurations in the semiconductors analyser, for every configuration are summarized in Table 3.12. For subthreshold regime, the range of current between 1 nA and 1 μA in the lineal configuration was selected.

Regime	SMU	Terminal	Mode	Value (source as reference)
Lineal	2	Source (S)	Constant	100 mV
	3	Drain (D)	Constant	0 V
	4	Gate (G)	Sweep	0 V -->-10 V, Step -0.01 V
	2	Bulk (B)	Constant	100 mV
Saturation	2	Source (S)	Sweep	0mA -->10 mA, Step 10 μA
	3	Drain (D)	Constant	0 V
	3	Gate (G)	Constant	0 V
	2	Bulk (B)	Sweep	0mA -->10 mA, Step 10 μA

Table 3.12 Biasing conditions for the pMOS in the lineal and saturation regions for the extraction of *I-V* characteristics.

3.5 Experimental Setup of thermal characterization

The application of our algorithms requires the thermal characterization of the MOSFETs in order to determine the biasing currents during readout and the I_{ZTC}.

Figure 3.24 VCL3006 Climate chamber from Vötsch Industrietechnik (Vötsch 2014).

To do that, it is necessary to measure the *I-V* curves at different temperatures in the saturation region, with bulk and source short-circuited; and drain and gate pins grounded. The semiconductor analyser B1500 (Agilent Technologies, Santa Clara, USA) was used to measure the *I-V* characteristics of the transistors and to bias constant drain currents. For the temperature control, a climate chamber VCL4006 (Vötsch Industrietechnik, Balingen-Frommern, Germany) was used, capable of varying the temperature from -40 to 180°C, with a temperature deviation in time of ±0.3 to ±1.0 K and a temperature homogeneity in space of ±0.5 to ±2.0 K (see Figure 3.24). To monitor the transistor temperature with a better accuracy, a digital thermometer RS206-3722 (Amidata S.A., Madrid, Spain) with an accuracy of 0.1ºC was placed inside the chamber next to the transistors. However, in the thermal study of subthreshold characterization a NAW880EXL thermometer (Oregon Scientific, Tualatin, OR, USA), with accuracy of ±0.1°C and uncertainty of $\pm 3\sigma$

= ±1°C, was placed in the test fixture, in contact with the transistor for thermal monitoring.

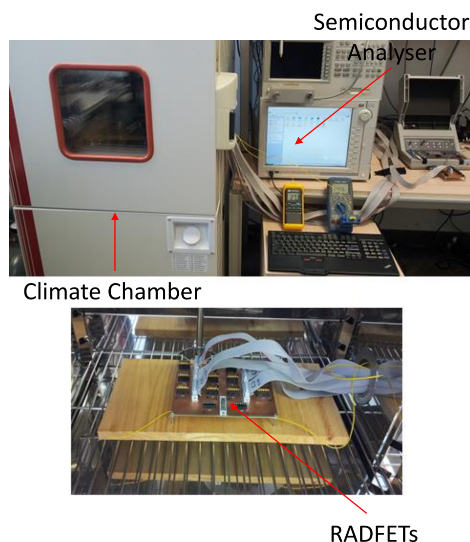

Figure 3.25 Experimental setup of thermal characterization.

Figure 3.25 shows a setup for thermal characterization of RADFETs transistors. The semiconductor analyser, the climate chamber, the thermometer and a board to place the transistors inside the chamber are shown. In the thermal characterization, groups of four or five transistors per type, different those which used to radiation characterization are measured.

3.6 Dosimetry System

Except of the subthreshold study, because its low current range, the radiation characterization, have been done with a compact, portable and low-cost dosimetry system based on MOSFET for in-vivo radiotherapy, previously designed by our research group (Carvajal et al. 2012).

This electronic system consists of a wireless sensor module containing the MOSFET under test and a microcontrolled reader unit.

3.6.1 Sensor module

Commercial MOSFETs show usually small oxide thicknesses and biased and stacked configurations are expected to increase the sensor sensitivity (Ma and Dressendorfer 1989, Holmes-Siedle and Adams 1986, Price et al. 2004b, Kelleher, Lane and Adams 1995, O'Connell et al. 1995, Sarrabayrouse and Siskos 1998, Holmes-Siedle et al. 2007). In the present work different biased (with different gate voltages) and single and stacked (with two transistors) configurations, have been analysed, with four configurations for each one of the different pMOS considered.

The sensor module is based on the previous design form (Carvajal et al. 2012) where a single general-purpose pMOS transistor, (the 3N163), is soldered onto a printed circuit board (PCB) with additional elements that are described below. In this work we built up sensor modules including a single pMOS (see Figure 3.26) or two stacked pMOSs (see Figure 3.27) depending the transistor and type of study. These transistors have no any protection against accidental electrostatic charge injection. Therefore, electrostatic charge can damage the device or, at least, cause spurious increases in V_t. Therefore, in the simplest configuration (single and unbiased), an n-channel, three Junction Field-Transistors (JFET) (see Figure 3.28), with a surface-mounted-device (SMD) case element; that maintains the terminal of the source connected to bulk, and the drain connected to the gate, short-circuited during irradiation and storage periods, has been included in the sensor module.

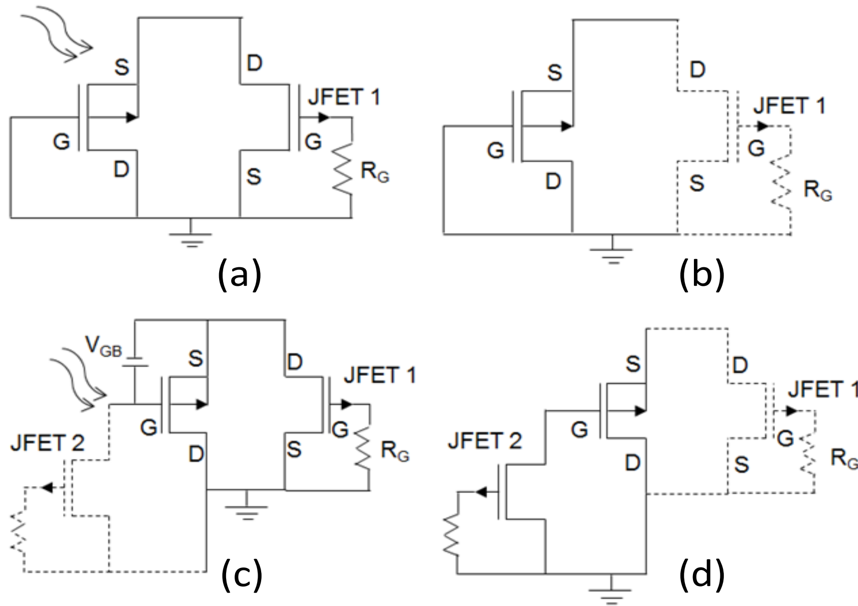

Figure 3.26 Sensor module configurations with a single pMOS. a) Unbiased mode: during radiation period the JFET is on and the terminals are short-circuited all together. b) Unbiased mode: during readout process the JFET is cut-off. c) Biased mode: during radiation period JFET2 is cut-off with a bias source between the gate and source. d) Biased mode: for readout process JFET2 is on and JFET1 is off.

The JFET MMBF4391 of NXP Semiconductor (Eindhoven, Netherlands) is used, with an individual cut-off voltage of -10 V and ON resistance of 30 Ω, welded in the PCB. JFET has the function of a switch to short-circuit or open the terminals. This transistor keeps normally on and keeps the source and bulk terminals connected to the drain and gate. However, during the readout process, the transistor works in the saturation region, and the connection between the source and drain must be interrupted by the polarization of the JFET gate to at least -10 V (Figure 3.26b). The JFET gate capacitance discharges through R_G, and all of the pMOS transistor terminals become

connected again, when the sensor module is removed from the reader unit.

However, for the biased mode, and the unbiased and biased modes with two stacked pMOSs, the design became more complex. Therefore, the modules consist of one or two pMOS and one, two or three (JFETs), with the corresponding discharging resistor, depending on the particular configuration. For the biased mode, another JFET was added. This transistor is situated between the gate and drain of the pMOS. It is normally on and keeps these two terminals short-circuited, during the readout process; it is open during the radiation period, when a bias is applied between the gate and the source.

In the two pMOSs configuration, two of these JFETs are added between the source and drain of the two pMOSs connected in series. These two JFETs are short-circuited by the gate, and it is necessary a voltage cut-off of -24 V to open both JFETs at the same time. In all the cases, a resistor R_G was included in the gate of the JFET to restore the connection between the terminals.

As its prior version during the readout, the pMOS transistors operated in the saturation region and it was necessary to maintain short-circuited the gate and the drain terminals. This short-circuit was also produced by polarizing the JFETs. In the case of the configuration including two stacked pMOS devices, the drain and source connected to JFETs belong to different transistors (see Figure 3.27b and d). To open the source and the drain terminals, these JFETs had to be cut-off. During the radiation process, all the terminals were short-circuited except the biased terminals of the transistor: the source and the gate. Therefore, it was necessary to open the gate and drain terminals cutting-off those JFETs. In the modules with two stacked transistors,

the sources of the two pMOSs were connected with the JFET1 during the radiation process. This made difficult the independent control of the bias of the two pMOSs and it was decided to bias only one of the two transistors (see Figure 3.29 shows the four different configurations of sensor with the transistor CD4007 and Figure 3.30 some of sensors with other types of transistors. Auxiliary PCB is needed to bias the transistor during the radiation period in the bias characterization. Figure 3.31 shows the auxiliary board manufactured to do this.

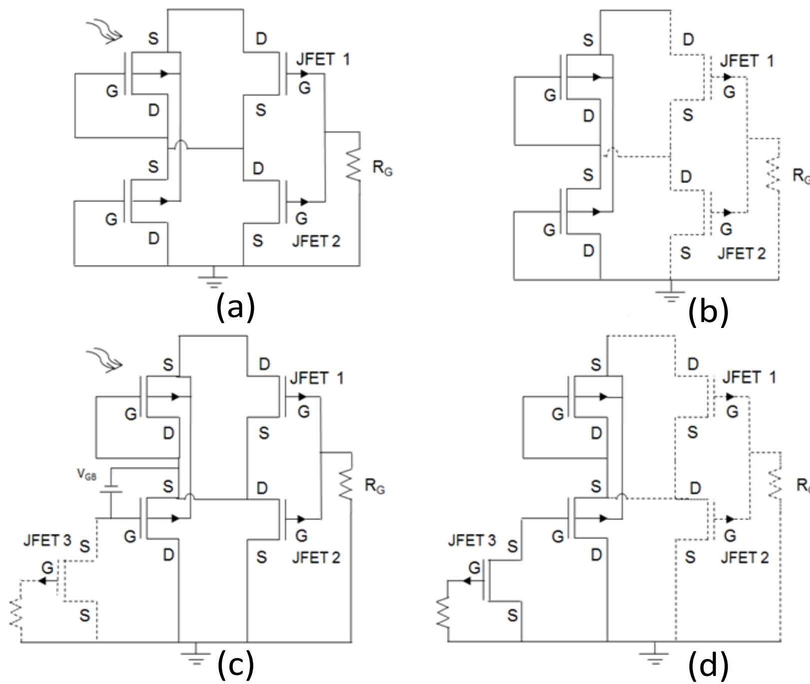

Figure 3.27 Sensor module configurations for two stacked pMOSs. a) Unbiased mode: during radiation period the JFET is on and the terminals are short-circuited all together. b) Unbiased mode: for readout process the JFETs are cut-off. c) Biased mode: during radiation period JFET3 is cut-off with a bias source between the gate and source. d) Biased mode: for readout process JFET3 is on and JFET1 and JFET2 are off.

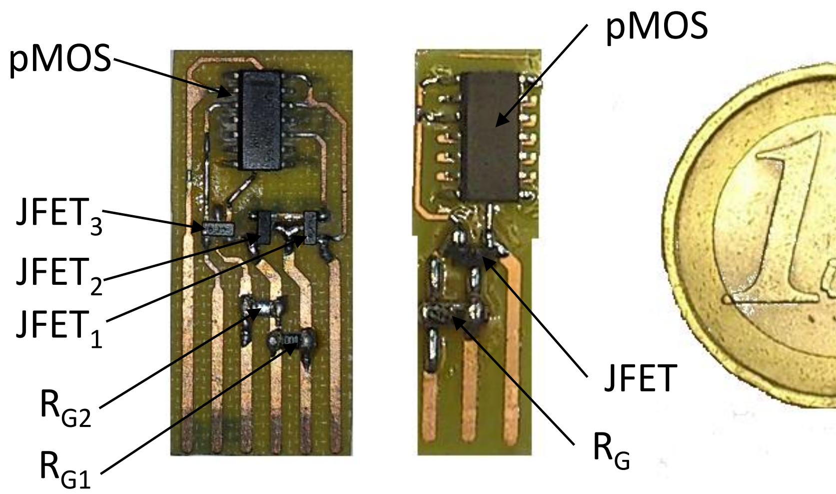

Figure 3.28 Parts of sensor module: two stacked biased sensor (left) and single unbiased sensor (right).

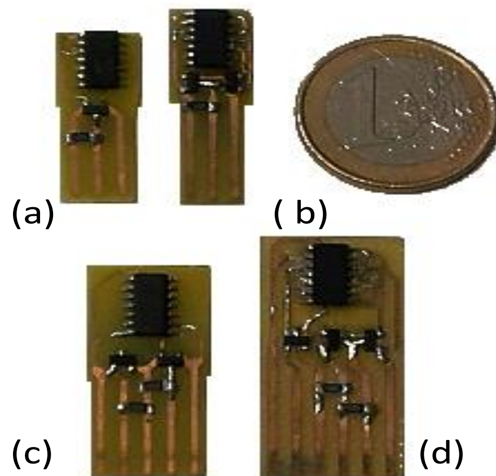

Figure 3.29 Types of sensor configurations: a) Single unbiased b) Single biased c) Two stacked unbiased d) Two stacked biased.

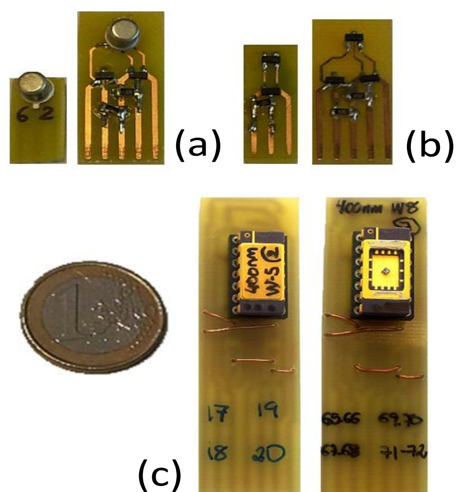

Figure 3.30 Types of sensor modules: a) 3N163 b) ZVP3306 c) RADFETs, with and without kovar lid.

.

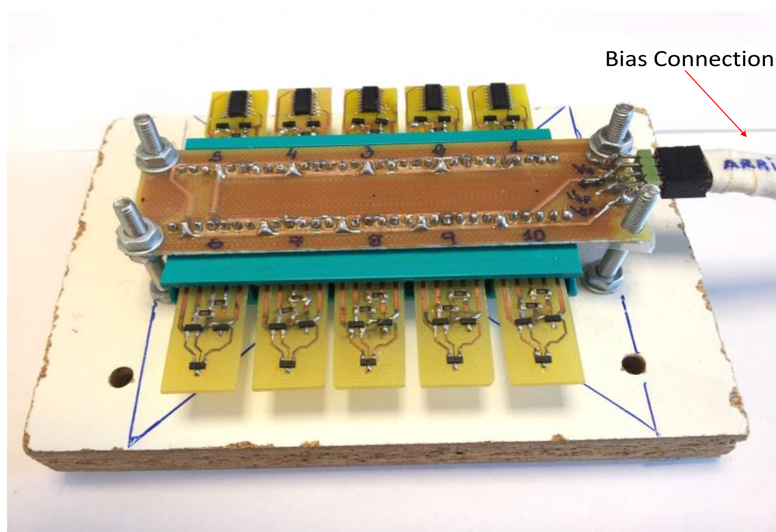

Figure 3.31 Biasing PCB.

3.6.2 Reader unit

A compact and low-cost dosimetry system based on MOSFET for in-vivo radiotherapy has been developed by Electronic and computer technology department of Granada University (Carvajal et al. 2012). This system is the main tool used for the dosimetric studies done in this work. This thesis is a continuation of an existing research line in this department, and previously tools and algorithms have been used in this work. This electronic measurement system consists of a reader unit and a set of wireless sensor modules containing a general-purpose MOSFET (see Figure 3.32).

Figure 3.32 UGR reader unit and sensor module

During the readout process, the gate and the drain terminals of the MOSFET are short-circuited and grounded, and the bulk and the source are also inter-connected. In this configuration, the transistor operates in the saturation region, and the MOSFET is biased with constant currents. The dosimetry system implements several measurement methods developed in previous works (Carvajal et al.

2011, Carvajal et al. 2010), to extend the linear range and reduce noise and thermal drift have been implemented and tested in the present system. The system provides suitable values for monitoring in-vivo radiotherapy treatments in a reliable way.

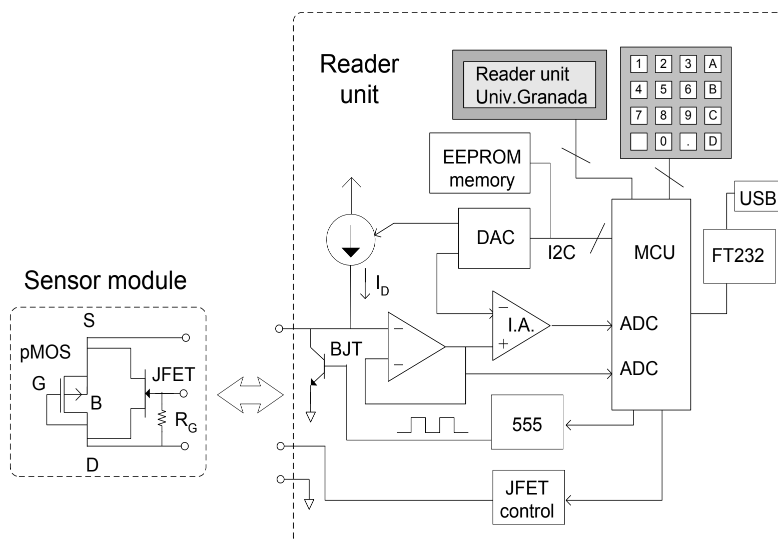

Figure 3.33 Block diagram of the reader unit and the sensor module (Carvajal et al. 2012)

The reader unit, whose block diagram is shown in Figure 3.33 consists of three functional blocks: the user interface, the microcontroller central unit (MCU) with an external memory, and the analog circuitry. The user interface includes an LCD screen, a keypad, and the circuitry necessary for computer connection via a USB port. An EEPROM memory is included in order to store different parameters of up to 256 different sensor modules. Each sensor module must be identified by entering its identification number (ID) using the keypad for zeroing and for dose measurements.

As can be seen in Figure 3.33, the MOSFET bias is provided by a programmable current source. Its output current is controlled by the MCU with a digital-to-analog converter (DAC). The DAC8551 of Texas Instruments (Dallas, Texas; USA) is used, because it has 16-bit resolution, two output channels, and an I2C communication port. In addition, drain currents can be applied in the switching mode to reduce the 1/f noise and improve linearity. This is done by diverting the current using a bipolar transistor (BJT) controlled by a pulsed signal generated by a 555 timer.

The source voltage is connected to the non-inverting input of an instrumentation amplifier (IA) with a buffer stage for impedance decoupling. The second channel of the DAC is connected to the inverting input of the IA to increase system resolution Figure 3.33. For each drain current, the calculation of the source voltage shifts is needed for applying the multiple current algorithm (Carvajal et al. 2011). Before irradiation, for the zeroing step, the pre-irradiation source voltage is detected and the microcontroller calculates the DAC output voltage necessary to reduce the IA output down to tens of millivolts. The digitized source voltages and the DAC words are stored in the EEPROM, which is mapped depending on the sensor module ID. After irradiation and charge stabilization in the pMOS transistor, the dose can be measured. The sensor ID is introduced on the keypad and then the post-irradiation source voltage is measured and subtracted from the DAC word stored in the zeroing step. Subsequently, it is amplified with a factor G (the gain of the IA).

Subtracting digitalised IA outputs from the two steps, the source voltage shift can be calculated with an amplification factor of G. The current values and the calibration parameters are loaded from the

EEPROM and the dose is calculated. Finally the results are shown on the display or can be downloaded to a computer.

Given the dose sensitivity S, the system resolution δ is given as:

$$\delta = \frac{\Delta}{G \cdot S} \tag{3.1}$$

where Δ is the ADC resolution in volts. Obviously, a better resolution is achieved if G and S increase and Δ reduces. In our case, with a 10-bit ADC (powered to 5 V), an IA gain of 20 and a minimum sensitivity of 20 mV/Gy, a resolution of 2 cGy is obtained. Electronic noise has also been kept lower than the ADC resolution (0.1% in this case) by averaging 512 replicas for each source voltage measurement. Therefore, this noise has a negligible contribution to the final total error.

3.6.3 Previous measurement algorithms of UGR

This section summarizes briefly the previous measurement algorithms developed by Electronic and Computer Technology Department of University of Granada. The algorithms are multiple currents methods based on biasing the MOSFET with one, two or three currents. As (Carvajal et al. 2011) explains; it is a very common practice in MOSFET dosimetry to neglect the contribution to source-voltage increments due to changes in the β (Sarrabayrouse and Siskos 1998, Rosenfeld 2002). However if this effects is taken into account the linear range can be increased. From (Carvajal et al. 2010) threshold voltage shifts can be found from voltage increases measured with two different currents, separating the contribution to the source-voltage shifts due to $\Delta\beta$ and $\Delta|V_t|$. If a third current is applied, the thermal-

compensation method and the extension of the linear range can be used simultaneously.

In the UGR dosimetric system, the sensor module has the transistor gate and the drain terminals are short-circuited and grounded, and the bulk and the source are also inter-connected. In this configuration, the transistor operates in the saturation region, remembering the equation (2.39), and neglecting the effective module length of channel, I_D-V_S can be modelled for pMOS as (Sze 1981):

$$i_D = -\frac{\beta}{2}(|v_{GS}| - |V_t|)^2$$

Note that, in this configuration, v_{GD}=0, then v_{GS}=v_{DS}. Therefore, the equation (2.39) could be rewritten as:

$$i_D = \frac{\beta}{2}(v_S - |V_t|)^2 \quad (3.2)$$

The radiation dose is calculated from the threshold voltage shift by means of measurements of the drain-source voltage at constant drain current. The first step is to study the thermal dependency of V_S and V_t at constant currents. It has been assumed the thermal dependence of the threshold voltage can be modelled by the usual linear model (Sze 1981, Tsividis 1987, Asensio et al. 2006):

$$\Delta|V_t| = \Delta|V_t^0| + \alpha_{|V_t|}\Delta T \quad (3.3)$$

where ΔV_t^0 represents the increase in the absolute value of the threshold voltage due to irradiation, which is independent of temperature, α_{Vt} is the thermal coefficients of V_t and ΔT is the temperature increase. In the same way, the shift of source voltage could be also modelled with a linear expression:

$$\Delta V_S = \Delta V_S^0 + \alpha(I_D)\Delta T \quad (3.4)$$

where ΔV_S^0 represents the increase in the absolute value of the source voltage due to irradiation, which is also independent of temperature, $\alpha(I_D)$ is the thermal coefficients of V_S ,dependent on the drain current. If the change in β produced by radiation can be considered as negligible, and the drain current is constant, the shift of the absolute value of threshold voltage, ΔV_t, is equal to the source voltage increment, ΔV_S (Buehler et al. 1993, Sarrabayrouse and Siskos 1998) .

From (Carvajal et al. 2010) and using (3.2), the threshold voltage can be calculated before (pre) and after (post) as:

$$|V_t|^{pre} = V_{preS} - \sqrt{2I_D}\sqrt{\frac{1}{\beta^{pre}}} \quad (3.5)$$

$$|V_t|^{post} = V_{post} - \sqrt{2I_D}\sqrt{\frac{1}{\beta^{post}}} \quad (3.6)$$

Therefore, the voltage threshold shift can be calculated as follows:

$$\Delta|V_t| = \Delta V_S - \sqrt{2I_D}\sqrt{\frac{1}{\beta^{post}} - \frac{1}{\beta^{pre}}} \quad (3.7)$$

Two-current method

If the increase in the source voltage is measured for two different currents, it can be written:

$$\Delta|V_t| = \Delta V_{S1} - \sqrt{2I_{D1}}\sqrt{\frac{1}{\beta^{post}} - \frac{1}{\beta^{pre}}} \quad (3.8)$$

and

$$\Delta|V_t| = \Delta V_{S2} - \sqrt{2I_{D2}}\sqrt{\frac{1}{\beta^{post}} - \frac{1}{\beta^{pre}}} \quad (3.9)$$

where ΔV_{S1} and ΔV_{S2} are the source voltage shifts measured at constant current I_{D1} and I_{D2}. Matching (3.8) and (3.9) gives:

$$\Delta|V_t| = \Delta V_{S1} + \frac{\Delta V_{S2} - \Delta V_{S1}}{1 - \sqrt{\frac{I_{D2}}{I_{D1}}}} \tag{3.10}$$

Equation (3.10) determines the threshold voltage from the drain-source voltage in absolute value measured at two different drain currents. This two current method increases the linear range.

However, using two drain currents, the thermal dependence also could be removed, instead of extending the linear range. To obtain the thermally compensated source voltage shift at the drain I_{D1}, an additional drain current is introduced, I_{D2}. Thus, similarly to (3.4), these sources voltages for these currents also can be modelled with a linear expression:

$$\Delta V_{S1} = \Delta V_{S1}^{0} + \alpha(I_{D1})\Delta T \tag{3.11}$$

$$\Delta V_{S2} = \Delta V_{S2}^{0} + \alpha(I_{2})\Delta T \tag{3.12}$$

Therefore, for ΔT it is obtained

$$\Delta T = \frac{(\Delta V_{S2} - \Delta V_{S1}) - (\Delta V_{S2}^{0} - \Delta V_{S1}^{0})}{\alpha(I_{2}) - \alpha(I_{D1})} \tag{3.13}$$

As it has been previously said, the threshold voltage shift due to radiation $\Delta|V_T^0|$, could be approximate to the source-voltage shift, ΔV_S^0, so:

$$\Delta\left|V_T^0\right| \sim \Delta\left|V_{S1}^0\right| \sim \Delta\left|V_{S2}^0\right| \tag{3.14}$$

ΔT is given by

$$\Delta T = \frac{\Delta V_{S2} - \Delta V_{S1}}{\alpha(I_{D2}) - \alpha(I_{D1})} \tag{3.15}$$

Therefore using equations (3.11) and (3.12) it can be seen that

$$\Delta V_{S1}^0 = \Delta V_{S1} + \frac{\Delta V_{S2} - \Delta V_{S1}}{1 - \frac{\alpha(I_{D2})}{\alpha(I_{D1})}} \quad (3.16)$$

On the other hand, if equations (3.11) and (3.12) are substituting in (3.10), it is obtained:

$$\Delta|V_t| = \Delta V_{S1}^0 + \frac{\Delta V_{S2}^0 - \Delta V_{S1}^0}{1 - \sqrt{\frac{I_{D2}}{I_{D1}}}} + \left[\alpha(I_{D1}) + \frac{\alpha(I_{D2}) - \alpha(I_{D1})}{1 - \sqrt{\frac{I_{D2}}{I_{D1}}}}\right]\Delta T \quad (3.17)$$

Comparing (3.17) with (3.3), it can be concluded that, the thermal coefficient of threshold voltage is:

$$\alpha_{|V_t|} = \alpha(I_{D1}) + \frac{\alpha(I_{D2}) - \alpha(I_{D1})}{1 - \sqrt{\frac{I_{D2}}{I_{D1}}}} \quad (3.18)$$

If (3.18) is rewritten for an arbitrary drain current $I_{D1}=I_D$, and $I_{D2}=I_{ZTC}$, where $\alpha(I_{ZTC})=0$, the following equation can be obtained:

$$\alpha(I_{D1}) = \alpha_{|V_t|}\left(\sqrt{\frac{I_D}{I_{ZTC}}} - 1\right) \quad (3.19)$$

If the thermal coefficients of $|V_t|$ and I_{ZTC} are known, the value of the thermal coefficient of the source voltage for any drain current can be calculated. This equation also allows us to determine the thermal compensation of the source voltage at the constant drain. Evaluating the expression (3.19) for I_{D2} and I_{D1}, the ratio $\alpha(I_{D2})/\alpha(I_{D1})$ can be obtained. Substituting it into equation (3.16), the thermally compensated source voltage shift can be found as a function of electric magnitudes that can be easily measured:

$$\Delta V_{S1}^0 = \Delta V_{S1} + (\Delta V_{S2} - \Delta V_{S1})\frac{\sqrt{I_{D1}} - \sqrt{I_{ZTC}}}{\sqrt{I_{D1}} - \sqrt{I_{D2}}} \quad (3.20)$$

Therefore, to evaluate equation (3.20), it is necessary to perform measurements of the increases in the source voltage at two currents,

with I_{ZTC} previously known. As (3.14) is applicable, then the threshold voltage shift can be also calculated from (3.20).

Three-current method

(Carvajal et al. 2011) an algorithm with three currents is described. Two currents are need to evaluate (3.10), I_{D1} and I_{D2}, and an additional current, I_C, is required for the thermal compensation of the source voltage shift measured at I_{D1} and I_{D2}. Equation (3.21) for I_{D1} and I_{D2}, gives:

$$\Delta V_{S1}^{0} = \Delta V_{S1} + (\Delta V_{SC} - \Delta V_{S1})\frac{\sqrt{I_{D1}} - \sqrt{I_{ZTC}}}{\sqrt{I_{D1}} - \sqrt{I_C}} \tag{3.21}$$

$$\Delta V_{S2}^{0} = \Delta V_{S} + (\Delta V_{SC} - \Delta V_{S2})\frac{\sqrt{I_{D2}} - \sqrt{I_{ZTC}}}{\sqrt{I_{D2}} - \sqrt{I_C}} \tag{3.22}$$

Then according to equation (3.10):

$$\Delta\left|V_t^{0}\right| = \Delta V_{S1}^{0} + \frac{\Delta V_{S2}^{0} - \Delta V_{S1}^{0}}{1 - \sqrt{\frac{I_{D2}}{I_{D1}}}} \tag{3.23}$$

Evaluating equations (3.21),(3.22) and (3.23) sequentially, allows both the thermal compensation and the linearity improvement methods to be taken into account, and provides the thermally compensated threshold voltage shift from the source-voltage increments measured for three different currents. If one of the currents, I_{D1} or I_{D2}, is equal to I_{ZTC}, equation (3.23) is simplified. For example, if $I_{D2}=I_{ZTC}$, the source voltage shifts at I_{D2} are thermally compensated, and all that is left is to evaluate equation (3.23) for ΔV_{S1} and ΔV_C in order to find ΔV_{S1}^{0}.

3.6.4 Methodology

The procedure followed to radiate the sensors was:

a) First of all, the dosimetric system was programmed with the different currents (one, two or three) used to bias the transistors. The algorithms have been detailed above. Every type was programmed to be characterized with one, two or three currents according to their thermal behaviour. The configuration of each transistor will be explained in the next chapter.
b) Next, the transistors are carried to the University Hospital San Cecilio, where the irradiation sources are allocated.
c) Before irradiation, a zeroing is done for each sensor, where the system measures and stores the source voltage (V_s^{pre}).
d) Irradiation of sensors.
e) After the irradiation, the sensors must wait for a time of 6 to 10 minutes and then, the source voltage after irradiation is measured with the dosimetric system (V_s^{post}).
f) The system calculates the threshold voltage shift for every dosimeter, and the sensitivity and dose are calculated from this shift.

The system is capable of measuring simultaneously 256 sensors, only they must be identify with their number by the keyboard. Also, the device can measure the performance of source voltage with the time (*fading).*

3.7 Summary

A brief summary of the different types and configurations, both for photon and electrons beams, are shown in Table 3.13 and Table 3.14.

Type	Field	Source	Build-up	Configuration	Bias (V)
3N163	35x35 cm^2	^{60}Co	No	Single	0
3N163	10x10 cm^2	LINAC	1 cm	Single	0
3N163	10x10 cm^2	LINAC	1 cm	Single	5
3N163	10x10 cm^2	LINAC	1 cm	Single	10
3N163	10x10 cm^2	LINAC	1 cm	Two stacked	0
3N163	10x10 cm^2	LINAC	1 cm	Two stacked	10
ZVP3306	10x10 cm^2	LINAC	1 cm	Single	5
ZVP3306	10x10 cm^2	LINAC	1 cm	Single	10
CD4007 (SMD)	10x10 cm^2	LINAC	1.5 cm	Single	0
RADFETs (5 Types)	25x25 cm^2	LINAC	1.5 cm	Single	0

Table 3.13 Groups of transistors for photon beam (6 MeV) study.

Type	Field	Source	Build-up	Configuration	Bias (V)
CD4007 (SMD)	25x25 cm^2	LINAC	-	Single	0
CD4007	25x25 cm^2	LINAC	-	Single	0.6
CD4007	25x25 cm^2	LINAC	-	Two stacked	0
CD4007	25x25 cm^2	LINAC	-	Two stacked	0.6
CD4007 (Texas Instruments)	25x25 cm^2	LINAC	-	Two stacked	0
CD4007 (Texas Instruments)	25x25 cm^2	LINAC	-	Two stacked	0.6
CD4007 (NXP Semiconductor)	25x25 cm^2	LINAC	-	Two stacked	0.6
BS250F	10x10 cm^2	LINAC	1 cm	Single	0
ZVP4525	10x10 cm^2	LINAC	1 cm	Single	0
ZVP3306	10x10 cm^2	LINAC	1 cm	Single	0
ZVP3306	10x10 cm^2	LINAC	-	Single	5
ZVP3306	10x10 cm^2	LINAC	-	Single	10
ZVP3306	10x10 cm^2	LINAC	-	Two stacked	0
RADFETs (5 Types)	15x15 cm^2	LINAC	1.3 cm	Single	0

Table 3.14 Groups of transistors for electron beam (6 MeV) study.

4

Response to ionizing radiation

During radiotherapy treatments, in order to avoid the damage to healthy tissues during the radiation sessions, the dosimeters are used to measure the dose of incident energy. As it has been previously explained, in the last few years, commercial dosimetry systems for photon beam radiotherapy, based on p-channel MOSFETs (pMOSs), have developed (Thomson 1987, Rosenfeld 2008, Rosenfeld 2014b). These devices show a number of advantages over traditional dosimetry systems in medical applications. The most important ones are an immediate and non-destructive readout, low power consumption, easy calibration, permanent storage of doses and a reasonable sensitivity and reproducibility (Holmes-Siedle and Adams 1986, Soubra et al. 1994, Hughes et al. 1988, Price et al. 2004b).

For increasing the sensitivity of MOSFETs to radiation, they are manufactured with special fabrication processes in order to achieve a thick gate oxide, between other characteristics. This type of MOSFETs is known as RADiation sensitive Field-Effect Transistors (RADFETs).

As it has been explained, the radiotherapy treatments use electrons and photons beams (gamma radiation), depending on the depth of the tumour. For superficial tumours electrons beam are used,

however, for the deepest cancers, the treatment with photons is more effective. In both cases the treatment is divided by several sessions of radiation. On the other hand, the intra operative radiotherapy (IORT) is a complementary technique used just after the cancer extraction. IORT aims to destroy the remaining tumour cells on the edge of the cancer using electron beams. The dose must be applied in only one session and just after the operation with the patient lying on the stretcher. Electron beam or low-energy X-rays are used as ionizing radiation sources and the absorbed doses range from 10 Gy, in combination with external radiotherapy treatments, up to 30-35 Gy, in case of a single radiation session.

In the last chapter, the sensing principle of these devices was described. It is based on the electron-hole pairs that are radio-induced in the gate-oxide of the transistor and create additional oxide trapped charge, producing a threshold voltage shift, ΔV_t. Taking this advantage and using the reader unit (Carvajal et al. 2012) to measure the increment of V_t; the response to ionizing radiation of several types of transistors is studied. The unit has implemented algorithms to reduce the thermal drift and the noise (Carvajal et al. 2010, Carvajal et al. 2011). This instrument is able to bias the transistors at one, two or three different currents sequentially measuring the source voltage at these currents to extract the information on radiation dose.

In this chapter, the response of different commercial MOSFET transistors and RADFETs to photon and electron beams is described, in order to check their capabilities as radiation sensors. Also a study of the degradation of the subthreshold swing is carried out to evaluate its use as dosimetric parameter. The main characteristics of the radiation response, such as sensitivity and reproducibility, have been determined using measuring algorithms previously developed by our research group

for photon beams and which allow, among other advantages, the thermal compensation of the devices. Although the experimental set-up was detailed in chapter 3, a brief summary for every study will be done for clarity in this chapter.

4.1 Validation of dosimetric system

Firstly, UGR dosimetry system has been validated using several types of transistors and the Semiconductor Analyser B1500. With this validation, it is justified the usage of this dosimetry system to further perform the characterization of sensors.

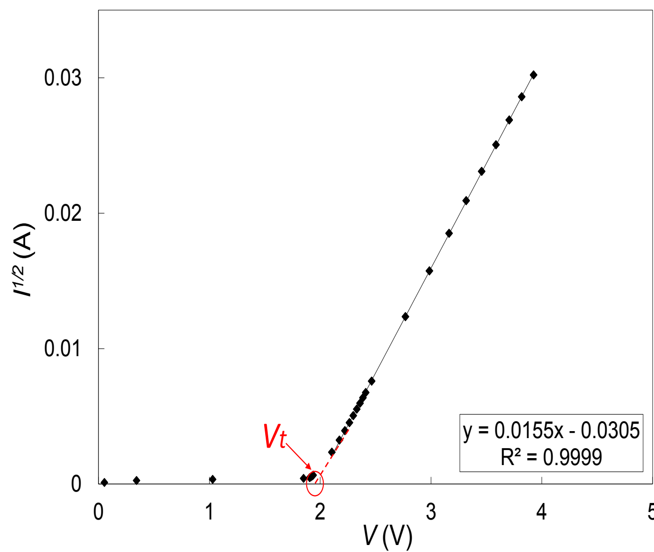

Figure 4.1 *I-V* curve for a transistor of t_{OX}=100 nm in a temperature of 22°C. The line shows the used region to do the linear fit.

Threshold voltages are obtained from the *I-V* curves of MOSFETs in the saturation region, using the B1500 Semiconductor

Analyser and also with the UGR dosimetry system at room temperature (22°C).

Type	Nº Chip	Size	Sam-ple	Vt_B1500 (V)	Vt_UGR (V)
100 nm	1	690/15	T2	1.9841±0.0006	2.047±0.006
		300/50	T3	1.9480±0.0002	1.951±0.004
		690/15	T4	1.9664±0.0006	1.986±0.009
	2	300/50	T5	1.9322±0.0002	1.933±0.006
		690/15	T6	1.9707±0.0007	2.02±0.13
		300/50	T7	1.9561±0.0002	1.959±0.003
		690/15	T8	1.9628±0.0006	2.05±0.25
400nm_W5	1	300/50	T9	0.2382±0.0001	0.21±0.01
		690/15	T10	0.1418±0.0003	0.18±0.02
		300/50	T11	0.1864±0.0001	0.16±0.01
		690/15	T12	0.1283±0.0003	0.17±0.02
	2	300/50	T13	0.1875±0.0001	0.16±0.01
		690/15	T14	0.1710±0.0003	0.20±0.01
		300/50	T15	0.1821±0.0001	0.16±0.01
		690/15	T16	0.1529±0.0003	0.18±0.01
400nm_W8	1	300/50	T17	0.9256±0.0002	0.93±0.02
		690/15	T18	0.6871±0.0005	0.69±0.05
		300/50	T19	0.4821±0.0002	0.48±0.021
		690/15	T20	0.3361±0.0004	0.34±0.04
	2	300/50	T21	0.8804±0.0002	0.88±0.01
		690/15	T22	0.6362±0.0005	0.63±0.05
		300/50	T23	0.4322±0.0002	0.43±0.021
		690/15	T24	0.2552±0.0004	0.25±0.04

Table 4.1 Threshold voltage of a group of samples, measured with the semiconductor analyser B1500 and the UGR dosimetry system.

The threshold voltage is extracted from the linear fit of square root of intensity with the gate-source voltage, V_{GS}, where it crosses the x axis (see Figure 4.1). This calculation is done for the complete range of currents applied with the B1500, and with the three programmed

current (see Table 4.5) in the dosimetry system from University of Granada. As it is observed in Table 4.1, the values of threshold voltages with both devices are similar; therefore the dosimetry system is validated.

The errors show in Table 4.1 and in the rest of thermal characterization of this work, are the statistic errors because are the maximum between it and the experimental error of the Semiconductor Analyser B1500.

4.2 Thermal characterization

It is important to highlight that the application of the algorithm to reduce the thermal drift (Carvajal et al. 2011) requires the thermal characterization of every MOSFET in order to determine the optimal currents I_1 and I_2 and the I_{ZTC} current. To do that, it was necessary to measure the *I-V* curves at different temperatures in the saturation region, with bulk and source short-circuited and drain and gate pins grounded. With the *I-V* curves are also calculated the thermal dependency of threshold voltage, α_{Vt}.

Groups of four or five transistors per type, were selected, (other than those irradiated for the characterization with dose). Different temperature sweeps were made between -40 and 85°C, measured in increments of 5 or 10°C. In every case, I_{ZTC} currents, were the I-*V* curves cross and the thermal coefficient of threshold voltage, α_{Vt} were calculated.

4.2.1 3N163

Due to this transistor in its simplest version (single and unbiased) was previously studied by (Asensio et al. 2006, Carvajal et al. 2011) with gamma beams; the thermal characterization was already done, where their main parameters are I_{ZTC} , which is 230±3 μA and the thermal coefficient of threshold voltage, α_{Vt}, -3.5±0.4 mV/°C.

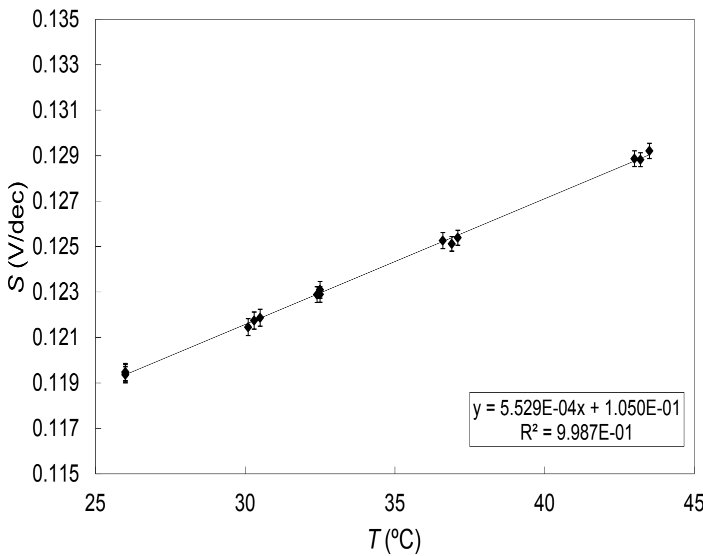

Figure 4.2 Typical subthreshold swing of a 3N163 as a function of temperature. Experimental data show with symbols and error bars and the line is the linear fit.

The dependence with temperature in the subthreshold swing (equation (2.34)) has also been characterized in this thesis because a subthreshold study is done in this type. The thermal behaviour of the subthreshold swing in the range from 25 to 45ºC has been measured for three transistors. Experimental data (symbols) and the linear fit are shown in Figure 4.2 for one of the transistors analysed. This behaviour was very similar to the rest of the 3N163 samples. The

average linear thermal coefficient calculated was $\alpha_{S,}$ $5.7 \pm 0.3 \cdot 10^{-4}$ V/dec · K for temperatures between 25 and 45ºC.

4.2.2 DMOS

As it has been previously mentioned, the analysed vertical transistors were BS250F, ZVP3306 and ZVP4525. Five transistors of each type were used in this analysis with the temperature.

Figure 4.3 shows the *I-V* curves in saturation for one of the transistors ZVP3306. A sweep was made ranging from 15 to 45°C. As can be seen, no crossing point was found, what did not allow obtaining I_{ZTC} in the current range studied. This is due to the presence of the parasitic diode in this device. Similar results were obtained for all other DMOS types.

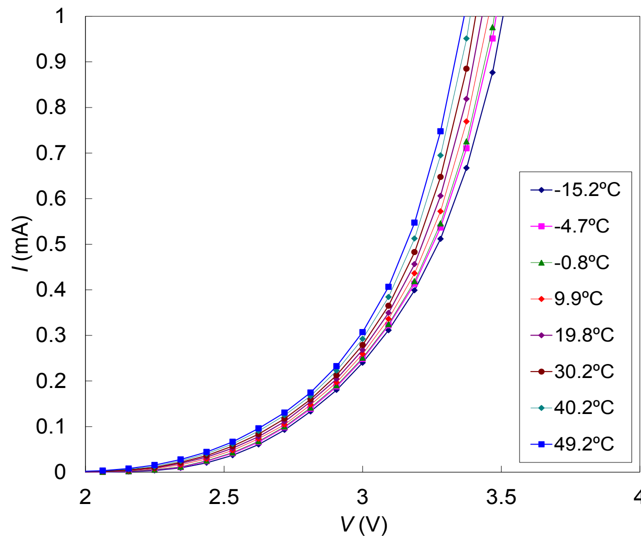

Figure 4.3 *I-V* curves of a ZVP3306 transistor at different temperatures (symbols).

Thermal compensation of DMOS transistors using the two or three current algorithm cannot be carried out due to there is no I_{ZTC}. Thus, in these cases, the thermal compensation has been made finding experimentally the thermal coefficient of V_t with temperature, α_{Vt}. The ΔV_t has been calculated with two current and subtracting the thermal contribution calculated from the temperature before and after irradiation (Asensio et al. 2006). α_{Vt} has been found for the three types, registering the V_t in a range of temperatures and using the thermal chamber. Figure 4.4 shows the thermal dependency of threshold voltage for the transistor number 2 of this group, the type is ZVP3306. In Table 4.2, some samples results, and the average and the uncertainty of the thermal coefficients of these three types are summarized.

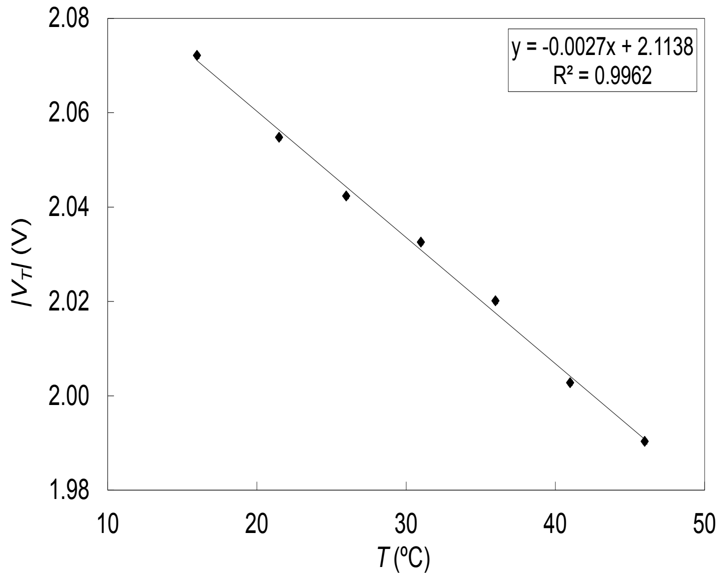

Figure 4.4 V_t of a ZVP3306 transistor (number 2) at different temperatures. Uncertainties are smaller than the size of symbol. Lines show the linear fits to data.

Type	T1	T2	T3	α_{Vt} (mV/°C)
BS250F	-2.3±0.1	-2.14±0.06	-2.45±0.06	-2.2±0.2
ZVP4525	-3.39±0.06	-3.4±0.1	-3.3±0.1	-3.38±0.06
ZVP3306	-2.67±0.07	-2.62±0.08	-2.39±0.08	-2.5±0.2

Table 4.2 Values of thermal coefficients. Uncertainties are given with a coverage factor k=1.

4.2.3 CD4007

A group of five pMOS transistors were analysed for this type. Figure 4.5 shows the curves *I-V* in case of the CD4007. Now, it was possible to obtain the I_{ZTC} that resulted to be 145 ± 4 μA, and then the three current algorithm for thermal compensation could be applied to these transistors.

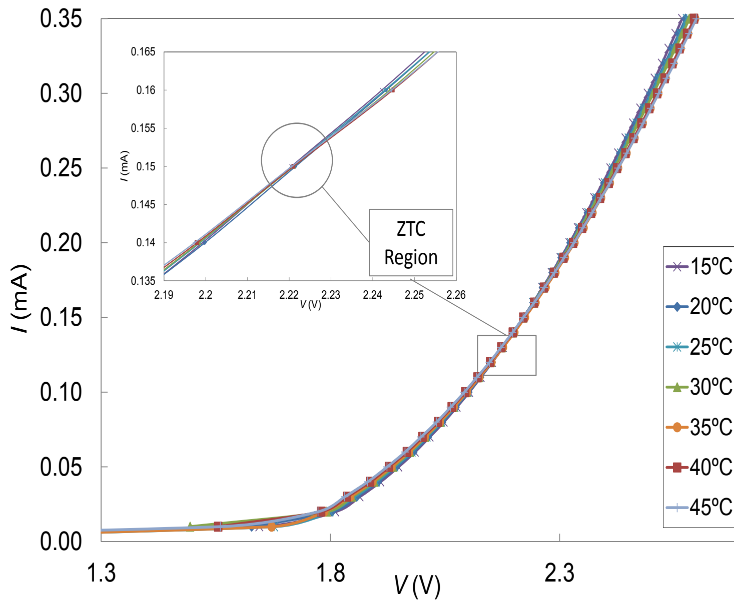

Figure 4.5 *I-V* curves of a CD4007 transistor at different temperatures.

Sample	I_{ZTC} (μA)	α_{Vt} (mV/°C)	α_{Vt0} (mV/°C)
T1	140.4	-2.2±0.1	0.1±0.1
T2	149.5	-1.8±0.3	0.01±0.1
T3	145.4	-2.1±0.1	0.2±0.2
T4	146.4	-1.86±0.06	-0.2±0.06
Average	145	-2±0.3	0.05±0.3

Table 4.3 I_{ZTC} and thermal coefficient of threshold voltage for the studied transistors CD4007 type. Uncertainties are given with a coverage factor k=1.

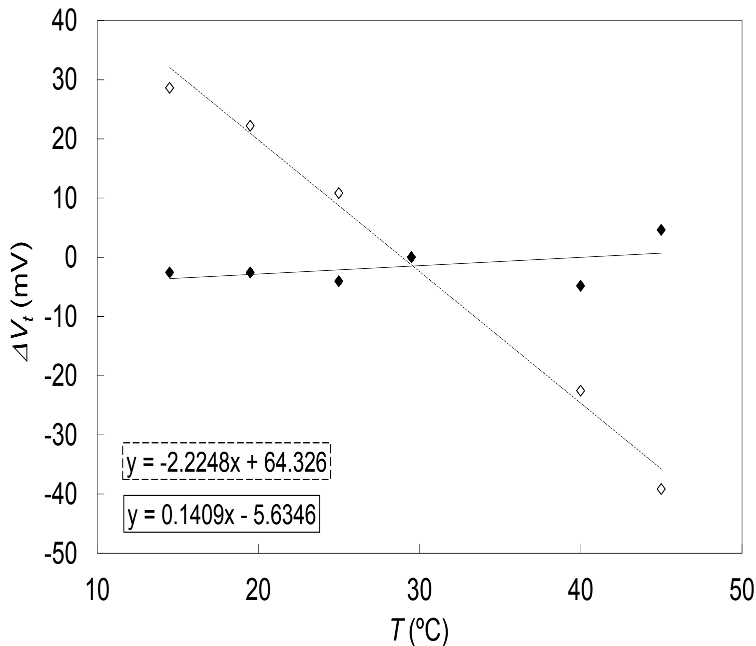

Figure 4.6 Typical thermal drift of a CD4007 dosimeter with (solid line) and without (dashed line) applying the thermal compensation method. The results of the corresponding linear regression are also given. Uncertainties are smaller than the size of symbol used.

The linear thermal coefficient was reduced from -2±0.3 mV/°C, without compensation, to 0.05±0.3 mV/°C when the compensation method of three current was applied, whose parameter is denoted as

α_{Vt0}. Table 4.3 summarizes the results for this type. Moreover, Figure 4.6 shows the thermal drift with and without compensation of the sample number 1.

4.2.4 RADFETs

Thermal characterization for every RADFET type and size was also carried out to find their I_{ZTC} currents. A temperature sweep was made from -40 to 85°C, with a range of currents between 10 nA and 1 mA. Four transistors of each type and size were used for this analysis.

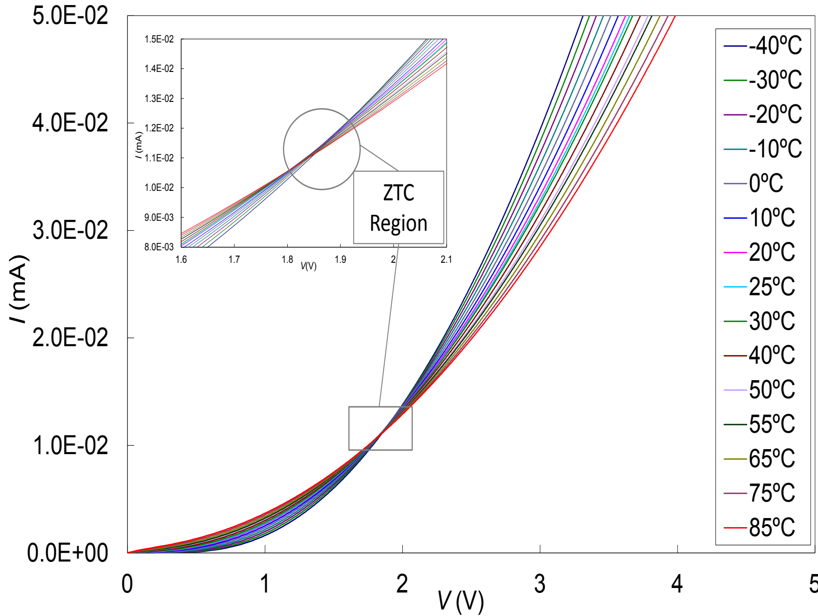

Figure 4.7 *I-V* characteristics for the RADFET number 1, of the transistors with t_{OX}= 400nm_W7 and 300/50 type for I_{ZTC} extraction.

In Table 4.4, I_{ZTC} are shown for each RADFET type and size. In Figure 4.7, the *I-V* curves in saturation for the RADFET with oxide of 400 nm and size of channel 300/50, as a function of the temperature

are depicted, showing the zero temperature coefficient zone. Similar behaviours were found for the rest of RADFETs.

Table 4.4 summarizes the I_{ZTC} currents and the thermal coefficients of these types of transistors.

Type	W/L	I_{ZTC} (μA)	α_{Vt}(mV/°C)
100nm_W8	300/50	16 ± 1	-2.10 ± 0.06
	690/15	183 ± 10	-2.2 ± 0.1
400nm_W5	300/50	12.2 ± 0.3	-5.03 ± 0.05
	690/15	127± 4	-4.62 ± 0.06
400nm_W7	300/50	10.8 ± 0.1	-4.84 ± 0.01
	690/15	109 ± 2	-4.32 ± 0.02
400nm_W8	300/50	11.2± 0.3	-4.86 ± 0.04
	690/15	115 ± 3	-4.41 ± 0.03
1um	300/50	10.9 ± 0.1	-10.1± 0.1
	690/15	120 ± 4	-8.4± 0.1

Table 4.4 I_{ZTC} currents and thermal coefficient for the different types of RADFETs.

4.2.5 Current setting for the 3CM/2CM

The application of the algorithms, previously explained in section 3.6.3, requires the selection of three drain currents, one of them the zero-temperature coefficient drain current, I_{ZTC}. From equation (3.22), if $I_{D1}=I_{ZTC}$, the current I_C andI_{D2} must be selected. Usually these currents are selected as the half or a quarter of I_{ZTC}. Except in the case of RADFETs with size 300/50 of channel, whose I_{ZTC} are lower, then I_C and I_{D2} are chosen around the half and double of I_{ZTC}. Finally the equations (3.22) and (3.23) with the selected currents are:

$$\Delta V_{S2}^{0} = \Delta V_{S2} + (\Delta V_{SC} - \Delta V_{S2}) \frac{\sqrt{I_{D2}} - \sqrt{I_{ZTC}}}{\sqrt{I_{D2}} - \sqrt{I_{C}}} \quad (4.1)$$

$$\Delta |V_{t}^{0}| = \Delta V_{S,ZTC}^{0} + \frac{\Delta V_{S2}^{0} - \Delta V_{S,ZTC}^{0}}{1 - \sqrt{\frac{I_{D2}}{I_{ZTC}}}} \quad (4.2)$$

with $\Delta V_{S,ZTC}$, $\Delta V_{S,C}$ and $\Delta V_{S,2}$ source voltage shift for currents I_{ZTC} , I_C and I_2 respectively.

Type	**W/L**	I_C **(μA)**	I_{D2} **(μA)**	$I_{D1}=I_{ZTC}$ **(μA)**
3N163	-	30	120	230
BS250F	-	30	120	-
ZVP4525	-	30	120	-
ZVP3306	-	30	120	-
CD4007	-	40	80	145
100nm	300/50	8	32	16
	690/15	45	91	183
400nm_W5	300/50	6	24	12.2
	690/15	31	63	127
400nm_W7	300/50	6	22	10.8
	690/15	27	54	109
400nm_W8	300/50	6	24	11.2
	690/15	28	57	115
1μm	300/50	6	22	10.9
	690/15	30	60	120

Table 4.5 Selected currents for biasing with the reader unit to apply the 2CM or 3CM.

Only in case of DMOS transistor, where the I_{ZTC} was not found, the three current algorithm cannot be applied, and the dosimetric characterization was carried out, only with two currents (equation (3.20) to enhance the linear range) was used to calculate de ΔV_t and

the thermal compensation was done numerically as it has been explained in section 4.2.2.

4.3 Response to radiation of commercial transistors

The use of general purpose transistor, as dosimeter, would reduce the cost of the final dosimetry system. In order to find a cheaper alternative, it is worth to study the behaviour of low-cost (<3 €) general purpose commercial MOSFETs as dosimeters. In previous studies (Asensio et al. 2006, Carvajal et al. 2010, Lee et al. 2000, Edgecock et al. 2009), the response to gamma radiation of this kind of MOSFETS was analysed. To our knowledge, this characterization has not been extended to electron beams (Amin et al. 2011, Bloemen-van Gurp et al. 2006, Manigandan et al. 2009).

Considering this, it is worth to present different techniques to increase the sensitivity of the commercial MOSFETs to demonstrate their potential as dosimetry sensors with electrons beams and gamma radiation. Different types of commercial MOSFET are irradiated in different configurations: unbiased and biased mode, single and two stacked pMOS; to select the best candidate and configuration for each type of radiotherapy. In all cases, as it was explained in section 3.6.1, the sensor module consists of the MOSFETs and one or two JFETs, in the unbiased and biased mode respectively. The JFETs transistors are cut off or on, which depends on the radiation process or the readout process of V_t. The techniques consist on different configurations and polarization. As it was previously studied; the pMOS polarization during radiation is a crucial factor in sensor sensitivity. The pMOS transistor can be biased or unbiased during the radiation sessions. In

the biased mode, a positive difference of voltage is applied and reducing the recombination probability of electron-hole pairs produced by the radiation in the gate-oxide and increasing the trapped charge creation (Ma and Dressendorfer 1989). The unbiased mode is characterized by no connections during radiation; usually all terminals are short-circuited together.

4.3.1 Response to photon beams

Different configurations and types of commercial pMOS are shown in order to enhance the sensitivity of this and other types of low-cost transistors. Increasing the sensitivity of the dosimeter, its use could be extended not only for radiotherapy treatments but also for X-rays applications or industrial setting with gamma radiation.

Experimental procedure

Three current method has been used to measure the ΔV_t in the 3N163 and CD4007, while to the DMOS type ZVP3306 two current method has been applied due to the I_{ZTC} for this geometry was not found. Four different configurations, single and two stacked transistors, in unbiased and biased mode, were tested to increase the sensitivity.

Forty five transistors (five per group) were irradiated with photons of 6 MeV with LINAC accelerator. The 3N163 were irradiated with 1.92 Gy per radiation session up to 25 Gy with a field of 10x10 cm^2. The ZVP3306 transistors were irradiated also with 1.89 Gy per radiation session up to 20 Gy with a field of 10x10 cm^2. It was used 1 cm of solid water above the MOSFET, to ensure the electronic equilibrium conditions.

Also a preliminary characterization of CD4007 in single and unbiased configuration was done to check their reliability as a dosimetric sensor with photons, however, its main objective was to use this type with electron beams, because its encapsulate, as it will be explained next. Anyway, the sensors were irradiated with a field of 10x10 cm^2 and a build-up of solid water of 1.5 cm. This type was irradiated with 3, 4 or 5 Gy per session, up to an accumulated dose of 25 Gy.

Both types were placed to 100 cm of the source, at the isocentre, with normal angle of incidence over a squared slab phantom with dimension of 30x30x10.5 cm^3. The source was LINAC Siemens Mevatrons KDS. The ionizing chamber PTW23332 was used in this experiment to control the dosimetry. During the characterization and to avoid fading effects, voltage measurements were carried out six minutes after the irradiation.

The drain current values have also been settled for the readout process Table 4.5, equations (4.1) and (4.2) have been evaluated before and after each irradiation session to calculate the threshold voltage shift and determine the absorbed dose.

The average sensitive of each pMOS was evaluated as the slope of the linear fit of ΔV_t as a function of the dose. Global sensitivity is calculated as the mean value of the average sensitivities for each dosimeter set. Uncertainty included the experimental error and one standard deviation of the values found for each transistor.

Single pMOS

3N163, ZVP3306 and CD4007 have been tested under gamma radiation with different configurations of polarizations. In a previous work (Asensio et al. 2006), it had been evaluated the response to gamma radiation in the single and unbiased mode of the 3N163 type. Now it was checked the enhancement of the sensitivity in the biased mode, comparing with another two commercial MOSFET, the ZVP3306 and the integrated circuit CD4007. In the different sessions of radiation, the ΔV_t as dose function was calculated, finding a lineal dependence. The DMOS transistors were thermally compensated using the thermal coefficient of V_t..

The analysed transistors showed a linear performance with the received dose. Among them, the 3N163 transistor has the highest sensitivity (see Table 4.7). For all the types the improvement is almost lineal with the biasing. Figure 4.8 shows the linear performance of the CD4007 in single and unbiased configuration. The sensitivity of ZVP3306 (see Figure 4.9) and CD4007 presents a low dispersion for photons beams; however, his averaged value is much lower than the sensitivity of 3N163. The sensitivity without bias of the 3N163 is already higher than the sensitivity with the highest bias of ZVP3306. In the 3N163 this parameter is improved by a factor 5 and 4 for the ZVP3306 and CD4007 respectively. This is probably caused by the effective area of oxide in every type. The 3N163 is a lateral one, whereas that ZVP3306 is a DMOS transistor. The case of CD4007 will be studied deeply for electron characterization. Table 4.6 shows the sensitivities for the group of single and biased with 5 and 10 V in the case of 3N163, where it is observed the reproducibility of this type and their high value of sensitivity.

In the following results, the uncertainties of threshold voltage shift (with a coverage factor k=1) are 0.5 mV/session for ΔV_t and 2.5 cGy for D in average. Uncertainties in D are smaller than the size of symbol used. Lines show the linear fits to data.

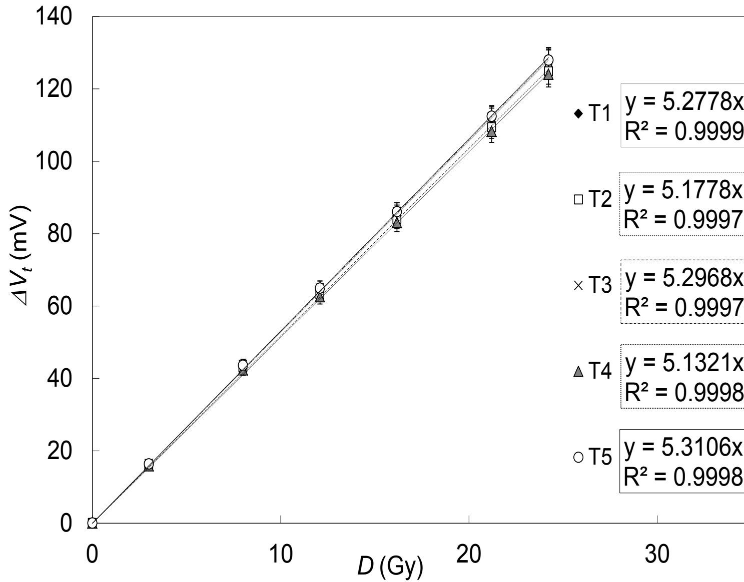

Figure 4.8 Increment of V_t as dose function for single unbiased CD4007 transistors.

Sample (Bias 5 V)	**Sensitivity (mV/Gy)**	**Sample (Bias 10 V)**	**Sensitivity (mV/Gy)**
T1	49.1±0.1	T1	57.7±0.5
T2	55.1±0.2	T2	54.7±0.6
T3	44.1±0.1	T3	52.1±0.7
T4	42.3±0.2	T4	51.2±0.6
T5	43.1±0.1	T5	57.0±0.7
Average	46.7±5.4	Average	54.5±2.9

Table 4.6 Sensitivities per sample in the group of single biased 3N163 biasing with 5 and 10 V, respectively.

The DMOS ZVP3306 and the CD4007 were discarded due to its low sensitivity. In addition, an additional thermal compensation should be carried out in the case of ZVP3306, due to the three currents algoritm cannot be applied. The two stacked configuration was only studied with the more sensitive transistor, 3N163 and for the highest biasing, 10 V.

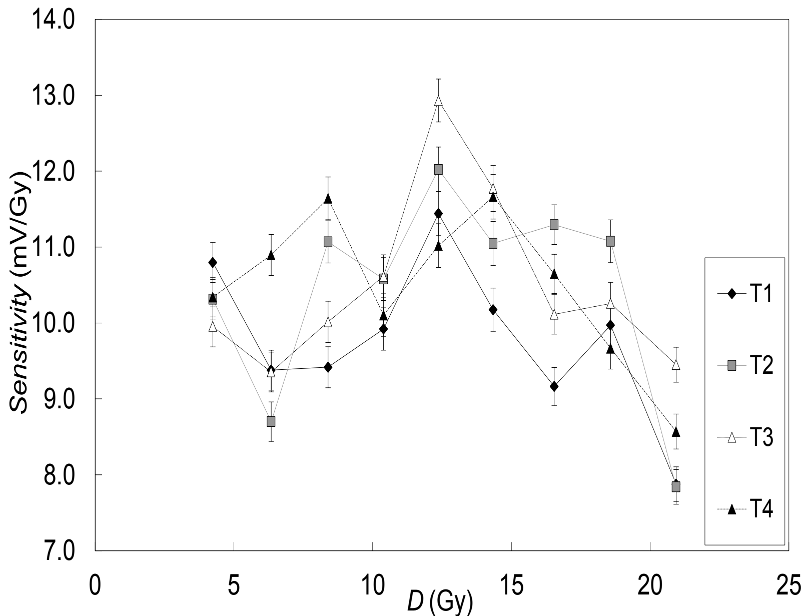

Figure 4.9 Sensitivities per irradiation session of single biased ZVP3306 transistor with 10 V versus dose.

The short-term fading of 3n163 pMOS for several accumulated doses was studied for of 5 and 10 V biasing respectively. The threshold voltage shift (in mV) is measured as a function of the time elapsed, in intervals of 30 s, since the moment of connection of the sensor module to the reader unit. The time between the end of the irradiation and the connection of the sensor module to the reader unit was proximately 30 s. The results indicate that, after 270 s, V_t has not yet stabilized (as Figure 4.10 and Figure 4.11 shown), however in (Carvajal et al. 2012)

showed as the single unbiased configuration of this type can be considered stable after the first 120 s. As it was expected, the fading with bias is higher than in the case of unbiased mode. From (Carvajal et al. 2012), the maximum shift of threshold voltage was around -3 mV; now with the biasing the maximum has increased form -16 mV to -30 mV, with 5 V and 10 V respectively. Also, it can be observed as the fading is decreasing in absolute value, when the accumulate dose increases. There are two competing effects, the density of oxide trapped charge decreases monotonically after irradiation by annealing (thus reducing the threshold voltage, low doses in the figures), while the density of interface traps exhibits the initial increase, (resulting in lower decrease of threshold voltage, high accumulated doses).

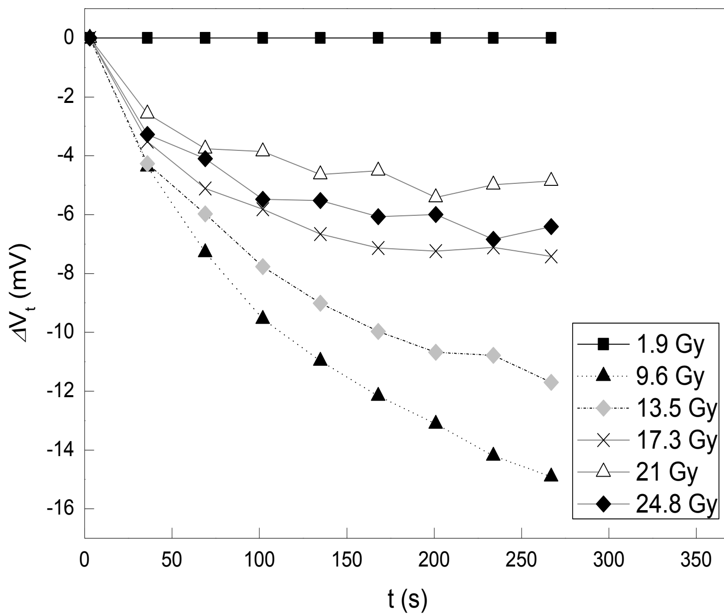

Figure 4.10 Short-term post-irradiation fading for dosimeter T1: 3N163 with bias 5 V.

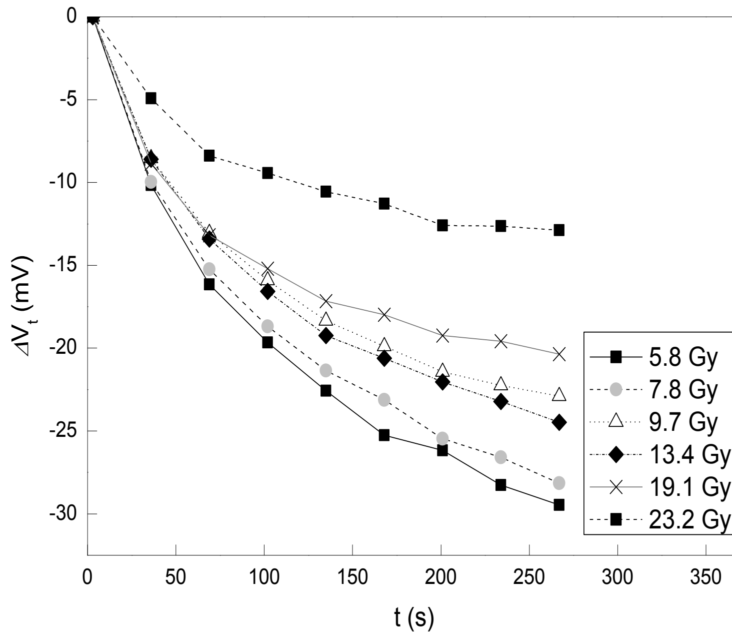

Figure 4.11 Short-term post-irradiation fading for dosimeter T1: 3N163 with bias 10 V.

Two stacked pMOS

3N163 is analysed both unbiased and biased two stacked configuration. Table 4.7 shows the results obtained for the sensitivity in all configurations. As it was expected the sensitivity has improved with the biased mode, both single and two stacked configurations. The two stacked transistors mode compared with the single mode has better results both biased and unbiased configurations.

As a summary, Figure 4.12 shows the accumulated V_t shift as a function of the accumulated dose for the four configurations studied in the case of the 3N163 pMOS. The increase in the sensitivity is apparent and it is worth pointing out how the linear behaviour is maintained in all situations.

Configuration	Type	Bias (V)	Sensitivity (mV/Gy)
Single	3N163	0	21±2
		5	47±5
		10	55±5
	ZVP3306	0	4.1±0.4
		5	7.5±0.6
		10	10.5±0.4
	CD4007	0	5.27±0.07
Two stacked	3N163	0	33±2
		10	62±3

Table 4.7 Dose sensitivity for the analysed pMOS in the various configurations for photon beams.

Once the final configuration has been selected for photon beams, the two stacked biased configuration has been compared to commercial dosimetry systems that use RADFETs as dosimeters with gamma radiation. The parameters of two commercial systems previously explained in the chapter 2, section 2.7.3 , OneDose^{TM} manufactured by Sicel Technologies Inc. and Thomson&Nielsen; have been obtained from their manufacturers.

According to the manufacturer, Sicel Technologies dosimeters have sensitivity, in unbiased mode, between 35 and 100 mV/Gy. In the case of the Thomson and Nielsen Electronics dosimeters the sensitivity with the standard dosimeter is between 100 mV/Gy and 300 mV/Gy for the standard and high bias supply setting, respectively. In our case, the sensitivity was 33±2 mV/Gy and 62±3 mV/Gy, for two stacked setting in unbiased and biased mode.

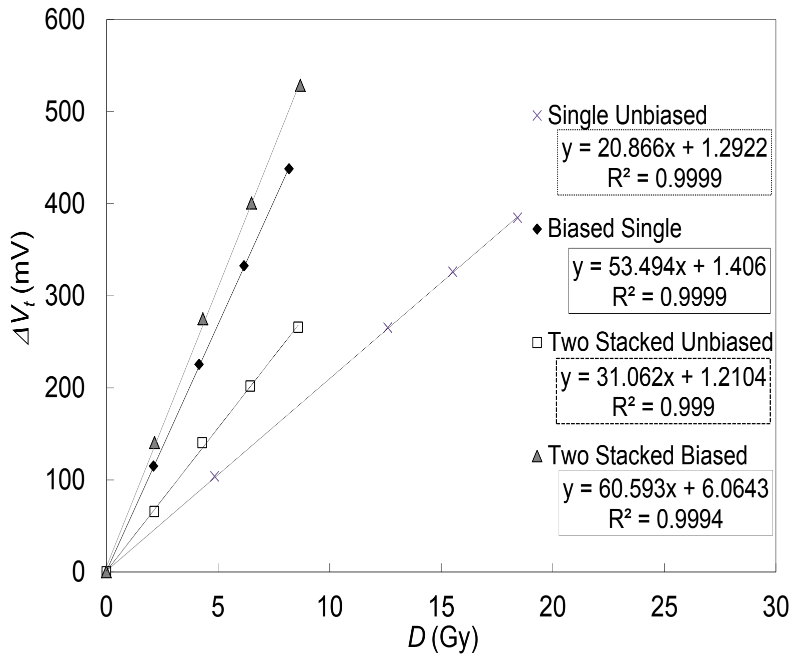

Figure 4.12 Accumulated threshold voltage shift of 3N163 as a function of the accumulated dose for four different devices, each one corresponding to the configurations studied in the present work.

Both cases are comparable to the sensitivity of Sicel Technologies dosimeters and slightly lower in the case of the proposed biased mode compared to the Thomson &Nielsen dosimeter in the standard bias supply. Furthermore, Sicel Technologies dosimeters allow a maximum received dose of 5 Gy, on the other hand the linearity of our sensor has been shown with accumulated dose of 30 Gy. Therefore linearity of our sensors is comparable to the commercial RADFETs. It has been shown as the designed sensor with commercial transistors has not many differences with the commercial system in the market.

4.3.2 Response to electron beams

Electrons beams are normally used for superficial tumours, but also with IORT. The dose delivered must be as controlled as possible. As it has been said, some authors tested commercial dosimetric system based on MOSFET with electron beams dosimetry (Amin et al. 2011, Bloemen-van Gurp et al. 2006, Manigandan et al. 2009). Also recently, reliable MOSFET dosimetry systems for IORT have been analysed (Consorti et al. 2005, Ciocca et al. 2006). They found good agreement with others dosimetry techniques.

IORT usually involves a single irradiation session; the reliability of the dosimeter must be higher than in case of conventional external treatments, in order to guarantee a reliable measurement of the delivered dose. During the IORT, the temperature of the pMOS could change because the thermal contact between the MOSFET and the patient's body may not be good nor repetitive, therefore temperature compensation is needed to reduce errors in the reading process.

A very important consideration is that pMOSs must be used without metal encapsulation, because, as it is well known, electron beams cannot be applied over metals during radiotherapy treatments. This is due to the fact that electron are absorbed by thin layers of metal or plastic, without reaching the patient (Knoll 2000). Due to this, the 3N163 transistor is not a good candidate for this radiation because the metallic encapsulate is incompatible with the electrons radiation.

The response of different types of low-cost commercial pMOS transistors that could be good candidates as radiation sensors for electron beams are studied. Finally the selected candidate; is

characterized, reproducing typical intra-operative radiotherapy treatment sessions. These results have been published in the paper (Martínez-García et al. 2014).

Experimental procedure

As mentioned, several types of transistors, CD4007, BS250F, ZVP3306 and ZVP4525 were tested in different configurations in order to study their response to electron beams. In case of CD4007, samples from different manufacturers and packages were analysed. The four different configurations considered were unbiased single, unbiased two stacked, biased single and biased two stacked (remembering section 3.6.1). In Figure 3.29, the four configurations for the CD4007 sensors are shown.

In each session, transistors were irradiated in groups of five units each, simultaneously, ensuring that all of them were affected by the same radiation beam. During the radiation period, the voltage between gate and source (V_{GS}) was chosen to be 0, 5 and 10 V. The CD4007 transistor could be studied at 0 and 0.6 V only because there is a protection diode between the source and the gate of this MOSFET that turns on if a voltage higher than 0.6 V is applied. For the biased mode, additional circuits were necessary to supply the various V_{GS} values during the radiation period.

Transistors were irradiated also with the linear accelerator Mevatrons KDS. The characterization of the transistors was performed using an irradiation field of 25x25 cm^2, placed over a squared slab phantom made of water-equivalent RW3 with dimensions 30x30x8 cm^3. This wide field, unusual in IORT, was used to irradiate simultaneously as many sensors as possible, but the transistors must be enough remote

one from the rest to prevent mutual influence. Sensor modules were irradiated with a dose between 1.8 Gy and 5.6 Gy in each session, achieving a total accumulated dose of around 59.4 Gy. During the characterization and to avoid fading effects, voltage measurements were carried out six minutes after the irradiation. No build-up caps were used on the MOSFETs to prevent the target volume from shadowing (Bloemen-van Gurp et al. 2006). Also the ionizing chamber PTW23332 was selected in this experiment.

In a similar way to the case of photon radiation, the drain current values have also been settled for the readout process Table 4.5. The average and global sensitivity have been calculated with the same procedure than in the case of gamma radiation. Also the uncertainty included the experimental error and one standard deviation of the values found for each transistor.

Single pMOS

It is started analysing the single unbiased configuration. First of all the response of the DMOS types: BS250F, ZVP3306 and ZVP4525 have been found out. In a similar process than before; after the different sessions of radiation, the ΔV_t as dose function was calculated, finding a lineal dependence for all studied transistor. These types were thermally compensated using the thermal coefficient of V_t.

Table 4.8 summarizes the average sensitivity and the standard deviation for the set of irradiation sessions. The analysed transistors showed a lineal performance with the received dose. Among them, the ZVP3306 transistor has the highest sensitivity and the better reproducibility (see Figure 4.13).

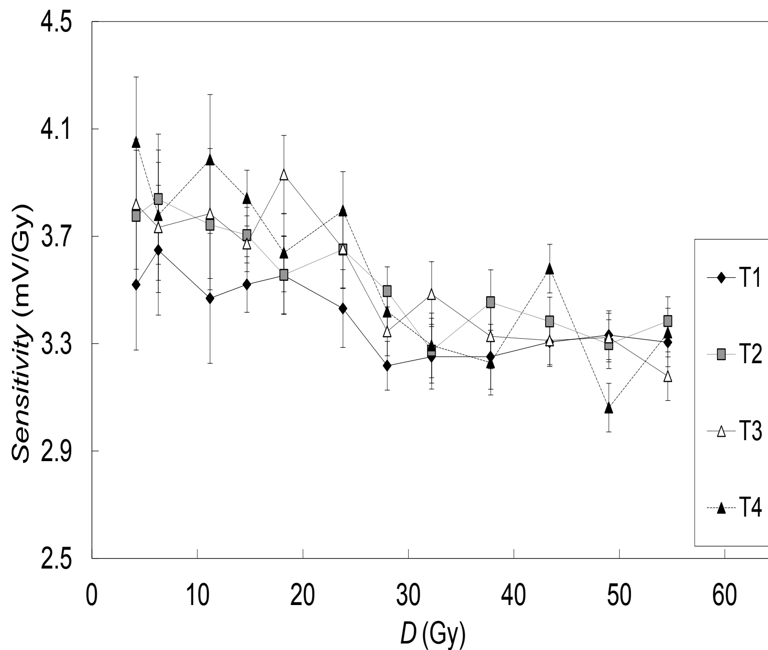

Figure 4.13 Sensitivities per irradiation session of single unbiased ZVP3306.

The ZVP3306 transistor has a greater sensitivity; while the types BS250F and ZVP4525 have 16% and 10% respectively lower. Even the ZVP3306 presents less standard deviation and a lineal performance, as it is shown in the Figure 4.14. That is the reason because hereafter, it has been continued analysing only the ZVP3306 pMOS in the single biased configuration, discarding the other two DMOS transistor. In the figure, the accumulated V_t shift versus the dose is plotted for four units of the ZVP3306 pMOSs in the saturation region. The results for the other DMOS transistors are similar. Therefore, the ZVP3306 is a possible candidate as dosimeter for radiotherapy with electron beams.

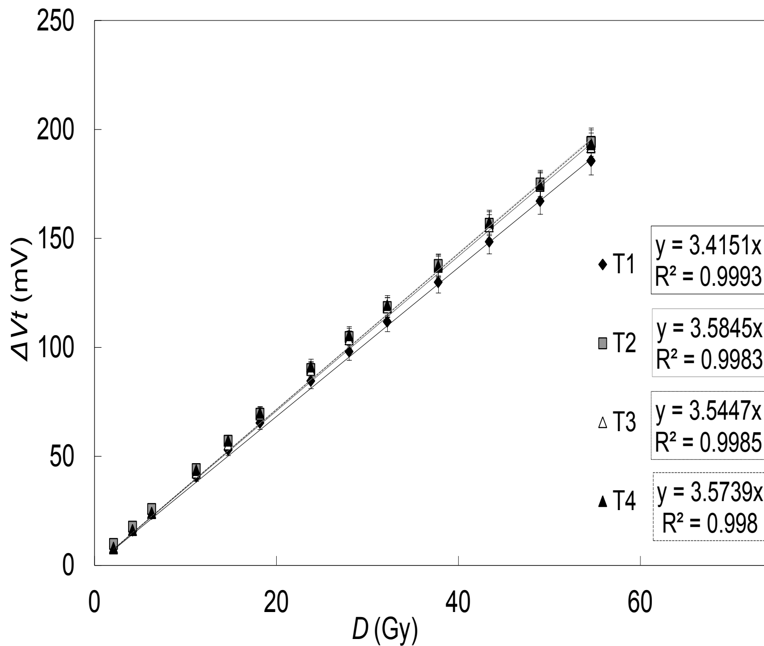

Figure 4.14 Increment of V_t as dose function for ZVP3306 transistors.

The fading of the ZVP3306 transistor for electrons beams with different bias has been analysed (see Figure 4.15 and Figure 4.16). Also the threshold voltage transient (in mV) is measured in intervals of 30 s. No more than 30 s has been since the end of the irradiation and the connection of the sensor module to the reader unit. Similar behaviour, than in the case of 3N163 short-term fading, previously analysed for photon beams. As it was expected, the shift of the threshold voltage is higher with high bias during irradiation. In this case, it can be concluded that V_t can be considered stable after the first 200 s. Also with the accumulated dose the threshold voltage shift is decreasing due to the increase in the density of interface traps versus the density of oxide traps charge. This effect is clearly observed in Figure 4.15, where the threshold voltage shift becomes positive for an

accumulated dose of 18 and 20 Gy. The same tendency is depicted in Figure 4.16.

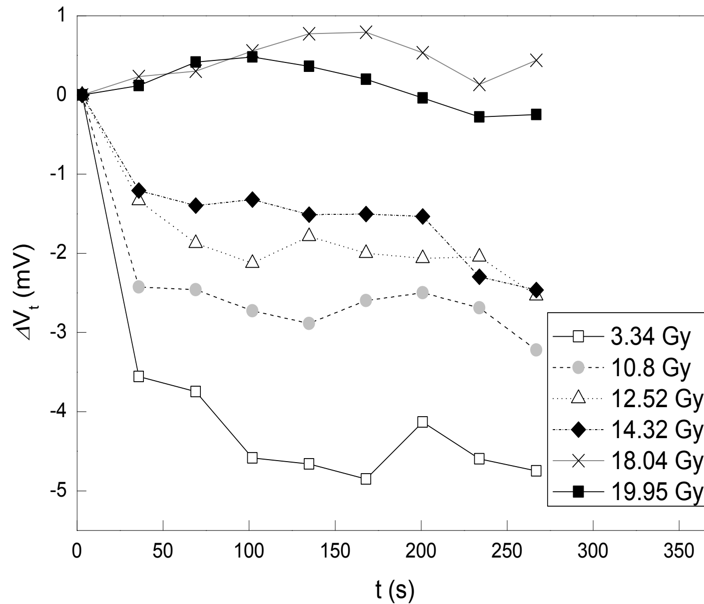

Figure 4.15 Short-term post-irradiation fading for dosimeter T1: ZVP3306 with bias 5 V.

Comparing the sensitivity and the thermal coefficient, the thermal drift can be obtained, giving 0.60±0.07 Gy/ºC, that is too high to be used without an additional thermal algorithm. Thus an additional thermal compensation method is required. In addition, linear range must be found in order to limit the use range of dosimeters. Therefore, others types of transistors, no DMOS, are being tested looking for a high sensitivity and a thermal behaviour that can be modelled easily.

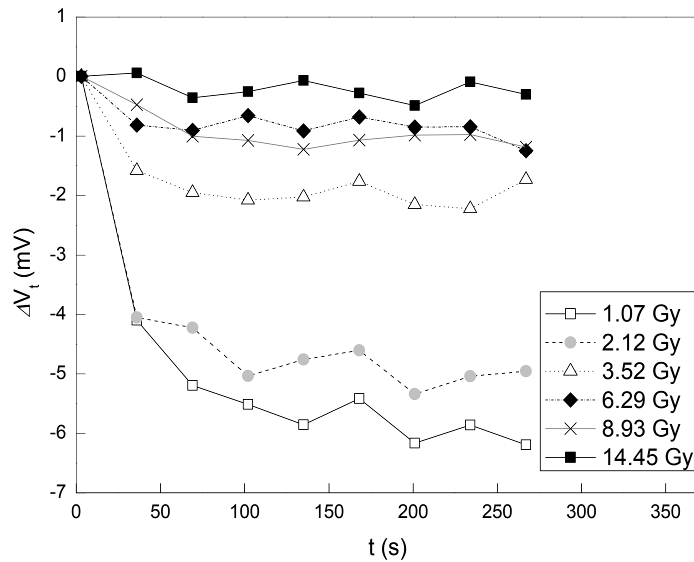

Figure 4.16 Short-term post-irradiation fading for dosimeter T1: ZVP3306 with bias 10 V.

Configuration	Type	Bias (V)	Sensitivity (mV/Gy)
Single	BS250F	0	3.1±0.4
	ZVP4525	0	3.4±0.4
	ZVP3306	0	3.7±0.3
		5	7.0±0.3
		10	9.0±0.9
	CD4007	0	4.6±0.1
		0.6	7.4±0.1
Two stacked	CD4007 (Texas Instruments)	0	9.5±0.7
		0.6	13.1±0.8
	CD4007 (NXP Semiconductors)	0.6	9.3±0.9

Table 4.8 Dose sensitivity for the analysed pMOS in the various configurations for electron beam.

The integrated circuit CD4007 in unbiased single configuration showed the highest sensitivity, 4.6 ± 0.1 mV/Gy with a very good linear behaviour of the accumulated shift V_t versus the dose. Table 4.9 shows the average sensitivities, for individual samples in this group. As the thermal compensation can be applied, this transistor can be also considered as a promising candidate to use as dosimeter in IORT.

The accumulated V_t shift for one of the CD4007 transistors in the saturation regime, in the single biased configuration and with 0.6 V bias is plotted, as a function of the accumulated dose, Figure 4.17. The data present a linear behaviour (R^2=0.9981) showing that this pMOS configuration is suitable for electron beams dosimetry.

Sample	**Sensitivity (mV/Gy) (Single Unbiased)**	**Sample**	**Sensitivity (mV/Gy) (Single Biased)**
T1	4.50±0.01	T6	7.5±0.1
T2	4.50±0.02	T7	7.6±0.1
T3	4.43±0.02	T8	7.3±0.1
T4	4.57±0.02	T9	7.4±0.1
T5	4.50±0.01	T10	7.4±0.4
Average	4.56±0.13	Average	7.4±0.1

Table 4.9 Sensitivies per sample in the group of CD4007 single unbiased and biased configuration.

Also the short-term fading of this MOSFET type in the single unbiased configuration was analysed. Figure 4.18 show the study for the sample number 1 (T1) of this group. The threshold voltage shift for an accumulative dose of 16.4 Gy is in the interval between -1 and 1.6 mV, Also with the dose increases, the threshold voltages shift become more positive, due also to the increase of in the interface charge density versus the oxide charge density. In these cases, the

difference is not significant, possibly due to a thinner oxide, and the threshold voltage fading could be considered as negligible.

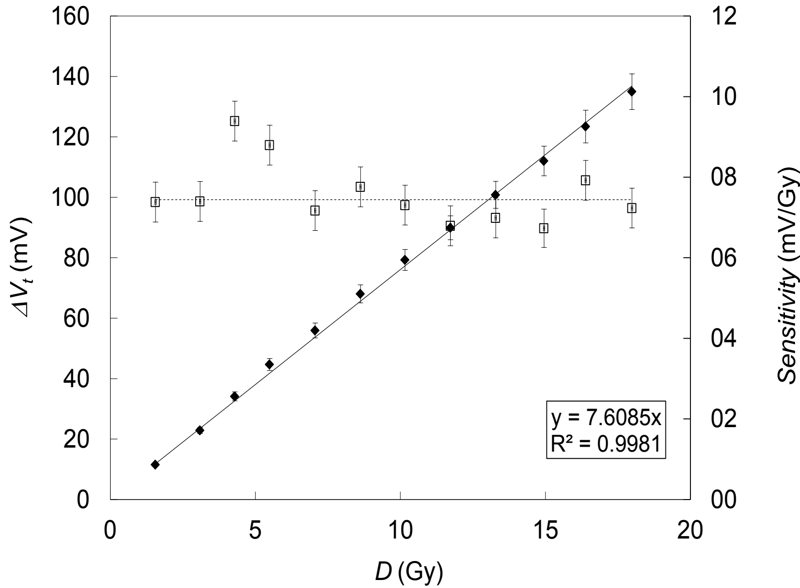

Figure 4.17 Accumulated threshold-voltage shift as a function of the accumulated dose (solid squares) and sensitivity per session (open squares) for a CD4007 pMOS in the single biased configuration. The solid line represents the linear fit of experimental data, their uncertainties of ΔV_t (with a coverage factor $k=1$) is 0.5 mV/session. Average uncertainties in the measured dose D, 2.5 cGy, are smaller than the size of the symbols used. The horizontal dashed line shows the global sensitivity.

Table 4.8 also shows the results obtained for the sensitivity in the single biased configuration for different voltage biases. As expected, the pMOSs under study, ZVP3306 and CD4007, have increased their sensitivities by a factor between 1.5 and 2.5 respectively. In the case of the ZVP3306, the sensitivity increased with the bias voltage, but a larger dispersion was found in the results obtained. This contrasts with the large reproducibility observed in the case of the CD4007 which maintains a dispersion of 0.1 mV/Gy as in

the single unbiased configuration. For this reason, together with the absence of I_{ZTC} current that avoids the possibility of applying the three current thermal compensation, the ZVP3306 has been discarded in the subsequent analysis of the two stacked configurations.

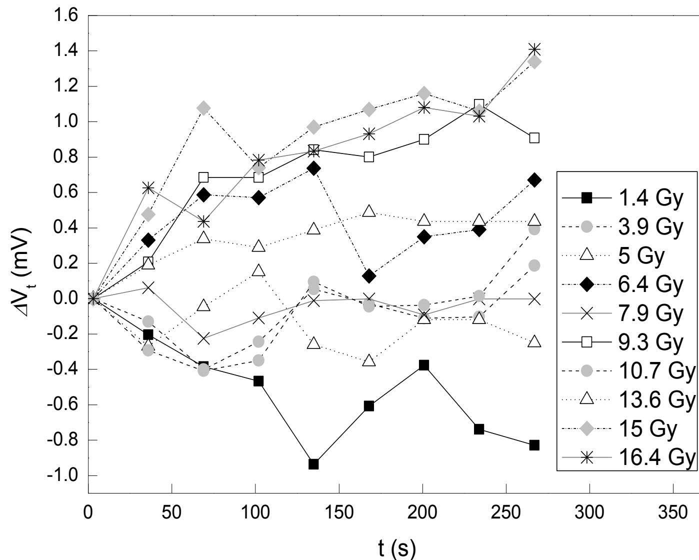

Figure 4.18 Short term fading post-irradiation fading for dosimeter CD4007 T1.

Two stacked pMOS

It is analysed both unbiased and biased two stacked configuration for the CD4007 integrated circuit. In case of biased MOSFETs, it is also studied the differences in their response, according to the manufacturer (Texas Instrument or NXP Semiconductors). Table 4.8 shows the results obtained for the sensitivity. Also in this case the voltage bias produces an increase of the sensitivity with a larger dispersion of the results. Texas Instrument devices show sensitivity about 45% larger than those from NXP

Semiconductors though these present a better reproducibility. This may be due to a different process of manufacturing or to differences in the geometry of the device. The two usual mounting configurations of the CD4007, these are the surface mounted and the through-hole package, have not shown significant differences in their sensitivities.

As a summary, Figure 4.19 shows the accumulated V_t shift as a function of the accumulated dose for the four configurations studied in the case of the CD4007 pMOS. The increase in the sensitivity is apparent and it is worth pointing out how the linear behaviour is maintained in all situations.

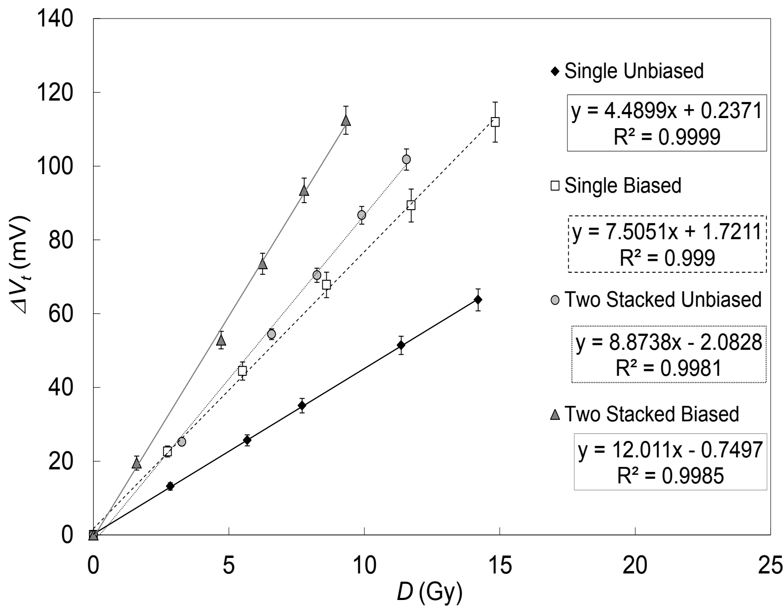

Figure 4.19 Accumulated threshold voltage shift as a function of the accumulated dose for four different devices CD4007, each one corresponding to the configurations studied in the present work. In all cases the manufacturer was Texas Instruments.

According to the results discussed above and published in (Martínez-García et al. 2014), the best candidate for electron beams

dosimetry is the CD4007 in the two stacked biased configuration. Once the optimal configuration was found, a final characterization was carried out reproducing IORT irradiation conditions. The goal was to measure the dose at the surface of a phantom, simulating the working situation of the dosimeters during this radiotherapy procedure. In this radiotherapy treatment, the doses delivered varies from 10 Gy, in combination with external radiotherapy, up to 30-35 Gy, in a sole treatment, and then it has been considered 22 Gy per session. In this high dose case, fading effects were minimized by measuring the V_t shifts 30 minutes after the end of the irradiation session.

Figure 4.20 shows the threshold-voltage shift versus the accumulated dose for the five units used in this analysis. The linear behaviour is clear also in the present irradiation circumstances. The global sensitivity of the set of these transistors, up to 90 Gy, was 12.7±0.3 mV/Gy. This value is similar to that found in the previous analysis with low doses (see Table 4.8) but shows a much better reproducibility with a dispersion reduced by more than 50%.

Once our sensor has been characterized and analysed, it has been compared to commercial dosimetry systems that use RADFETs as dosimeters. Typically, these systems are used with gamma radiation and not many RADFETs have been used with electrons in medical applications. In any case, this comparison has been done for electron beams with energy similar to that used in IORT applications (Consorti et al. 2005, Halvorsen 2005). The results obtained with two systems manufactured by Sicel Technologies Inc. (Halvorsen 2005) and Thomson and Nielsen Electronics (Consorti et al. 2005) were analysed and compared with ours.

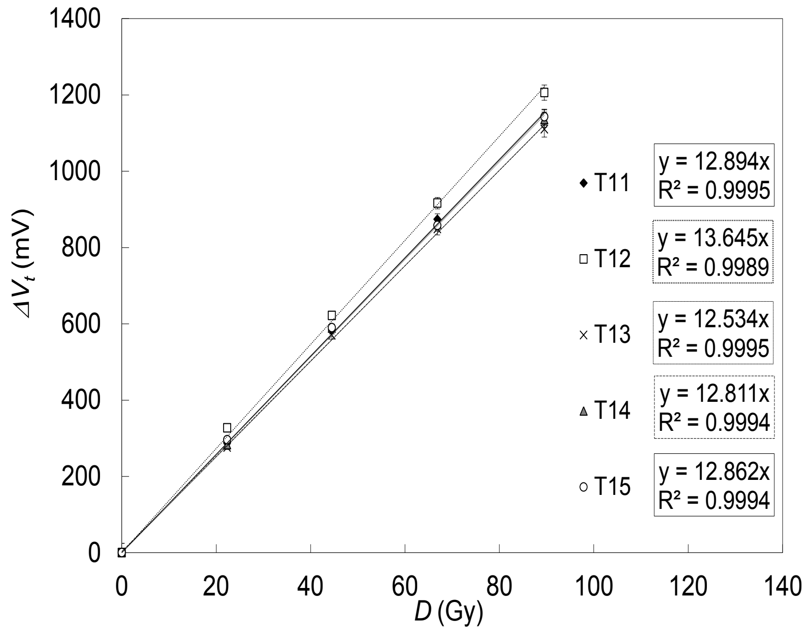

Figure 4.20 Accumulated threshold voltage shift vs. accumulated dose for the five units used to analyse the response to the two stacked configuration for the CD4007 in IORT conditions..

The comparisons are qualitative because the irradiation setups are not the same as ours. Thomson and Nielsen Electronics dosimeters were tested with an energy of 7 MeV, different to the 6 MeV used in (Halvorsen 2005) or in the present work. Transistors were situated in depth in a water phantom or over the surface, in both cases, using a source to dosimeter distance of 100 cm.

According to the manufacturer, Sicel Technologies dosimeters have a sensitivity, in unbiased mode, between 35 and 100 mV/Gy, with an uncertainty of 5% (k=2) for doses between 20 and 400 cGy (Halvorsen 2005). In the case of the Thomson and Nielsen Electronics dosimeters the sensitivity is around 90 mV/Gy, in a standard biased mode, with an overall uncertainty within 3.5% (k=1) in the range of doses between 1 to 25 Gy (Consorti et al. 2005). In our case, the

sensitivity was 12.7±0.3 mV/Gy, lower than in commercial systems. It is worth noting that both commercial dosimeters were characterized for low dose, while in the present study also doses similar to those used in IORT conditions were considered, with 22 Gy per session until a total dose of 90 Gy. In addition, Sicel Technologies dosimeters allow a maximum received dose of 5 Gy, and cannot be used for IORT. The linearity of our sensors is comparable to the commercial RADFETs. As well as in this work, methods to reduce the thermal drift dependence are considered in all the mentioned papers.

4.3.3 Study of the subthreshold swing as dosimetric parameter

In the general-purpose pMOSFET 3N163, a study of the degradation of the subthreshold swing is carried out to evaluate its use as a dosimetric parameter. Its reliability in terms of sensitivity, linearity, and reproducibility is also experimentally tested and compared with the threshold voltage shift under gamma rays.

It is well known that ionizing radiation causes degradation of the I_{DS}-V_{GS} (drain current vs. gate voltage) characteristics in MOSFETs (Ma and Dressendorfer 1989). Several electrical parameters of the transistor are influenced by this degradation. The technique usually applied, as in previous sections, has based on the measurement of the threshold voltage shift, ΔV_t, related to the radiation dose, D. This electrical magnitude is influenced by both kinds of radiation-induced charges: fixed oxide charge and interface traps. The dynamics of creation of these charges are different as the accumulated dose increases with significant incidence in the linear trend of the ΔV_t, particularly in the

unbiased regime, (without gate voltage during radiation, previously called unbiased mode).

Recently, it has been demonstrated for thin-gate oxide pMOSFETs, in the unbiased mode, that the creation of interface states presents a more linear trend with dose than the fixed oxide charge (Ristic et al. 2011). This linear trend is highly appropriate for obtaining transistors with a high linear range not requiring frequent recalibrations in the unbiased mode (recall the short linear range of MOSFETs in unbiased regime compared with being polarized during radiation). This fact only allows pMOSFETs to be used in the unbiased mode in the very short dose range before requiring costly recalibration. The subthreshold behaviour of a MOSFET is mainly influenced by these interface traps, decreasing the slope of I-V curves as the interface state density increases. Therefore, it could be expected a linear shift of the subthreshold characteristics which is very suitable for a dosimetric parameter.

In this subsection, the effects of ionizing radiation on the subthreshold behaviour of a general-purpose MOS transistor has been analysed and the direct dependence of the subthreshold swing on radiation dose studied for determining the limitations of using this response as a reliable dosimetric parameter. The typical range of dose of radiotherapy treatments, below 60 Gy has been applied. Of course, the response of the subthreshold current as a function of the accumulated dose has been widely studied both theoretically and experimentally, but in most cases restricted to the calculation of the dynamics of the interface trap creation/annealing (Ristic et al. 2011, Dozier et al. 1986, Shaw et al. 1992, Johnson et al. 1994, Gnana Prakash, Ke and Siddappa 2003) based on the experimental methodology by (McWhorter and Winokur 1986).

In a MOSFET in weak inversion, the drain current is dominated by the diffusion mechanism, and the *I-V* relationship can be approximated by an exponential relationship (Overstraeten et al. 1975). In that case, as it has been explained in section 2.7.2, a parameter in the subthreshold regime can be defined as the gate voltage swing, *S*, needed to reduce the drain current by one decade, termed the subthreshold swing. From equations (2.34), (2.35) and (2.36) and in accordance with a previous report (Ristic et al. 2011), a linear relationship between the creation of interface traps (ΔQ_{IT}) and the dose is proposed, which implies the same kind of relationship between the subthreshold swing shift and the radiation dose,

$$\Delta Q_{IT} = A \cdot D \Rightarrow \Delta S \propto D \tag{4.3}$$

In this subsection, the increase in the mean interface trap density according to Equation (4.3) has been studied as a dosimetric parameter. It has been analysed and tested the linear relationship between the subthreshold swing shift, ΔS, and the accumulated dose, *D*, equation (4.3), in terms of sensitivity, linearity, reproducibility, and thermal drift in a similar way as is usually done for the voltage threshold shift (Banqueri et al. 2012).

Experimental procedure

3N163 was the commercial pMOS under test. A total of eleven transistors (labelled T78 to T88) were irradiated with an AECL Theratron-780. All the radiations were carried out with all four transistor terminals connected to each other, hence without gate voltage, in the unbiased regime. The transistors were irradiated with a 35 x 35 cm^2 field and were located on the stretcher and at a distance of 80 cm from the gamma-ray source. These eleven transistors were

irradiated with different doses of 2, 4, or 6 Gy per radiation session, up to a limit of 58 Gy under normal incidence. For dose calculations, it has been considered that electronic equilibrium was achieved in the transistor. In fact, no angular dependence was found in previous work experimentally (Asensio et al. 2006) and by Monte Carlo simulations (Carvajal et al. 2009) for these transistors for different incidence directions with the Theratron-780. The ionizing chamber PTW23332 was used in this experiment to control the dosimetry

In order to quantify the response to radiation, the electrical characteristics of the pMOS transistor were measured before and after each radiation session. In particular, the drain current, as a function of the gate voltage (I-V), was obtained for each transistor using a computer-controlled semiconductor parameter analyser HP-4145B. These curves were extracted in subthreshold and saturation regime with a drain-source voltage of V_{DS}=-100 mV. Substrate and source terminals were shorted. During the curve measurement (readout period), transistors were placed in an electromagnetic-shielded test fixture HP 16085A. Short-term fading effects are overcome due to a delay of more than thirty minutes between radiation and the curve measurements. During radiation and storage periods, the transistors were placed on a prototyping board with all the terminals short-circuited together to prevent electrostatic charge from damaging the device. From the I-V curve, the slopes of the I_D logarithm were calculated in the current range from 1 nA to 1 μA (into the subthreshold region for this transistor) before and after radiation (see Figure 2.21). The increase in the inverse of these slopes was calculated for every radiation session. Uncertainties were taken to be twice the corresponding standard deviations. Quadratic error propagation was considered whenever required.

The temperature was recorded during the readout period, before and after radiation, in order to apply the thermal drift correction. A NAW880EXL digital thermometer, was placed inside the test fixture, in contact with the transistors for thermal monitoring. For thermal correction, it has been assumed a linear model:

$$S(T) = S_{T_0} + \propto_S (T - T_0) \quad (4.4)$$

where T is the temperature in degrees Celsius, and T_0 is the temperature during the measurement of the current-voltage curve before the radiation session. To find the linear thermal coefficient of S, α_S is needed. The average coefficient from thermal characterization, $\alpha_S = 5.7 \pm 0.3 \cdot 10^{-4}$ V/dec · K, was used to evaluate equation (4.4) before and after radiation and, therefore, to find the ΔS increase reducing the effect of the temperature (see Figure 4.2).

Response to radiation

In this subsection, the radiation response has been analysed in terms of linearity, sensitivity, and reproducibility among individual transistors, measuring in the subthreshold regime during readout (Banqueri et al. 2012). These parameters have been compared with those calculated for the threshold voltage shift for exactly the same transistors with the aim of discussing the reliability of the subthreshold swing, S, in relation with ΔV_t.

In Figure 4.21, the characteristic current-voltage curves are shown in the subthreshold regime for the transistor labelled as T78 (from 1 μA to 1 nA) for an accumulated dose of up to 51 Gy. These curves reveal a linear trend of *Log[I]* versus V (depicted in absolute values), and the well-known slope decrease for increasing dose (curves

from left to right in Figure 4.21). This behaviour is also evident in the rest of the analysed transistors with R^2 correlation factors higher than 0.999. The influence of the range of currents has been analysed taken from the slope calculations, repeating them for currents between 300 nA and 30 nA. A negligible change has been obtained, indicating that the measured subthreshold region is not critical in the determination of radiation effects.

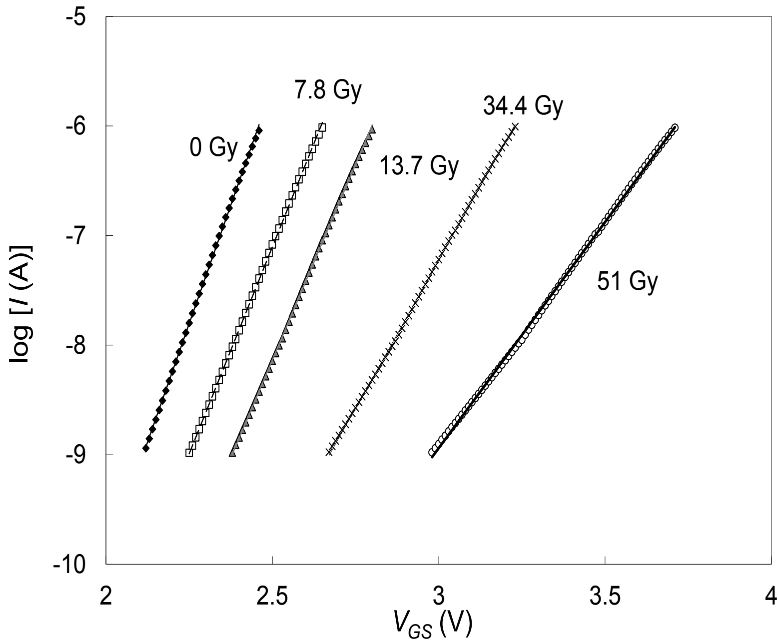

Figure 4.21 Drain current versus gate voltage in the subthreshold regime of MOSFET T78 as a function of the accumulated dose up to 51 Gy. Symbols are the experimental data and lines the linear fits.

In Figure 4.22, the response of the subthreshold swing shift is shown for transistor T80 as a function of the accumulated dose with symbols and their error bars. The line is the linear fit. This linear trend has also been obtained for the rest of the transistors.

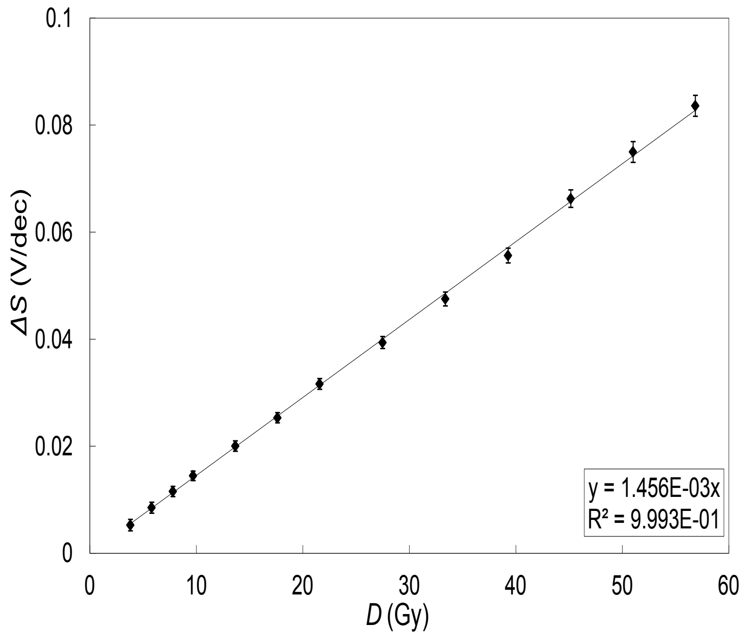

Figure 4.22 Subthreshold swing shift of MOSFET T80 as a function of the dose (experimental data in symbols with error bars and linear fit shown with the line).

In order to have better data on the reliability of ΔS as a dosimetric parameter, Figure 4.23 shows the typical behaviour of the sensitivity per radiation session for this magnitude. These data are simply obtained from the subthreshold swing shift per grey induced in each radiation session and correcting for the thermal drift. Although some data dispersion occurs, there is no significant decay in sensitivity; therefore, in the typical range of an individual radiotherapy treatment, this magnitude shows a constant response to radiation.

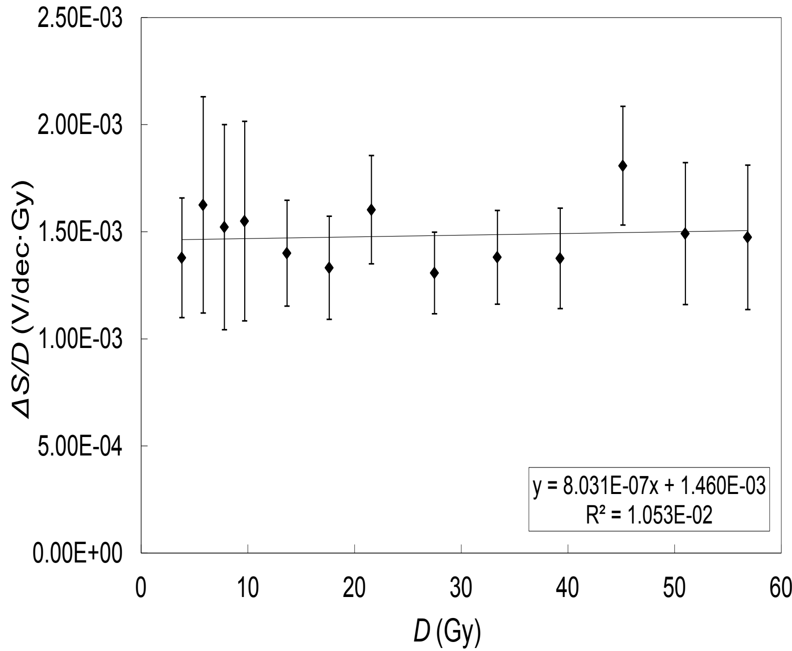

Figure 4.23 Sensitivity per radiation session of MOSFET T80. Experimental data are shown with symbols and error bars and linear fit with the line.

To compare the behaviour of the subthreshold swing as a dosimetric parameter, Figure 4.24 depicts the threshold voltage shift due to radiation and the sensitivity per radiation session for the same transistor T80, also showing the expected linear trend. The transistor threshold voltage was determined before and after radiation by the transfer characteristics in saturation, that is, as the intersection between the V_{GS}-axis and the extrapolated linear region of the $(I)^{1/2}–V$ curves (Asensio et al. 2006). Very good linearity was obtained in the studied range of radiation, confirming the reliability of the threshold voltage as a dosimetric parameter of this transistor as previously shown (Asensio et al. 2006).

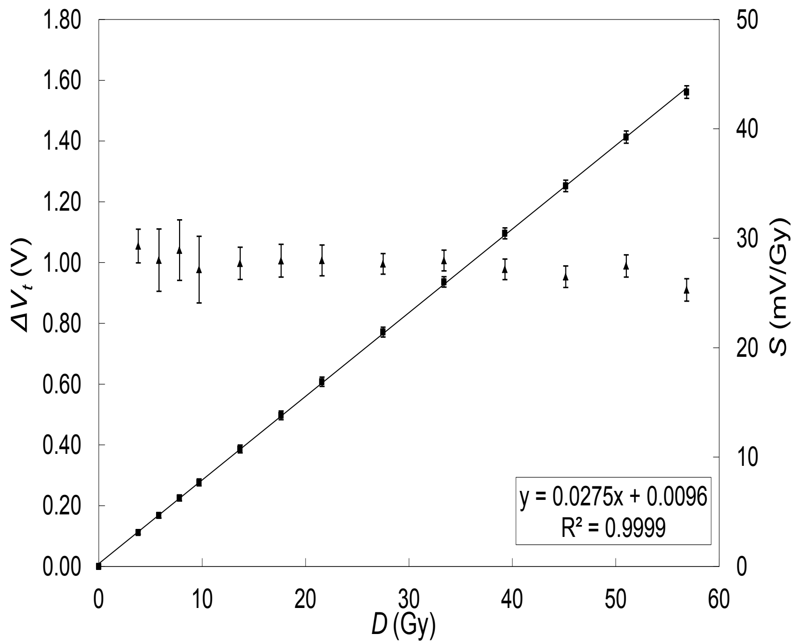

Figure 4.24 Threshold voltage shift and sensitivity per radiation session of MOSFET T80 as a function of the dose (experimental data in symbols with error bars and linear fit shown with the line).

Table 4.10 shows the sensitivity to radiation for the set of analysed transistors for both the subthreshold swing shift and the threshold voltage shift. The uncertainties of all experimental data are also shown as twice the standard deviations. Average values and uncertainties are calculated in the last two rows.

According to the average radiation sensitivity of $1.4 \cdot 10^{-3}$ V/dec · Gy given in Table 4.10 and the linear thermal coefficient previously calculated is α_S=5.7 ± 0.3 · 10^{-4} V/dec · K, it would have an equivalent thermal drift in radiation units of 40 cGy/K, which is an

unacceptable value for using the subthreshold swing as a dosimetric parameter without thermal compensation.

Transistor[1]	**78**	**79**	**80**	**81**	**83**	**84**	**85**	**86**	**87**	**88**
Sensitivity of ΔS (mV/dec · Gy)	1.37	1.258	1.46	1.32	1.420	1.44	1.544	1.55	1.337	1.554
Uncertainty (mV/dec · Gy)	0.01	0.007	0.01	0.01	0.006	0.01	0.009	0.02	0.007	0.008
Sensitivity of ΔV_t (mV/Gy)	25.5	29.2	27.9	29.3	29.6	27.9	30.0	28.6	29.2	28.5
Uncertainty (mV/Gy)	0.2	0.2	0.2	0.2	0.2	0.2	0.2	0.2	0.2	0.2
Average for ΔS (mV/dec · Gy)	1.4±0.2 (2SD)									
Average for ΔV_t (mV/dec · Gy)	29±2 (2SD)									

[1] Transistor T82 stopped working due to accidental ESD.

Table 4.10 Sensitivities and uncertainties of the subthreshold swing and threshold voltage shifts to radiation. Average values are also shown in the last two rows.

The direct technique to carry out this compensation is the monitoring of temperature during the readout period and using equation (4.4) for extracting the independent term with the temperature, S_{T0}. For operability of this method, the linear thermal model has to be applied with the average thermal coefficient. With this method of thermal compensation, a typical thermal-compensated subthreshold swing is plotted (see Figure 4.25). In the set of three thermal-compensated transistors, it has been obtained thermal-

compensated coefficients between $-1.7 \cdot 10^{-5}$ and $3.0 \cdot 10^{-5}$ V/dec · K, resulting in a reduction factor between 35 and 19 (in absolute value) of the thermal drift or 2 cGy/K (in radiation units) in the worst case. This value would be acceptable in the controlled temperature environment of a radiotherapy unit.

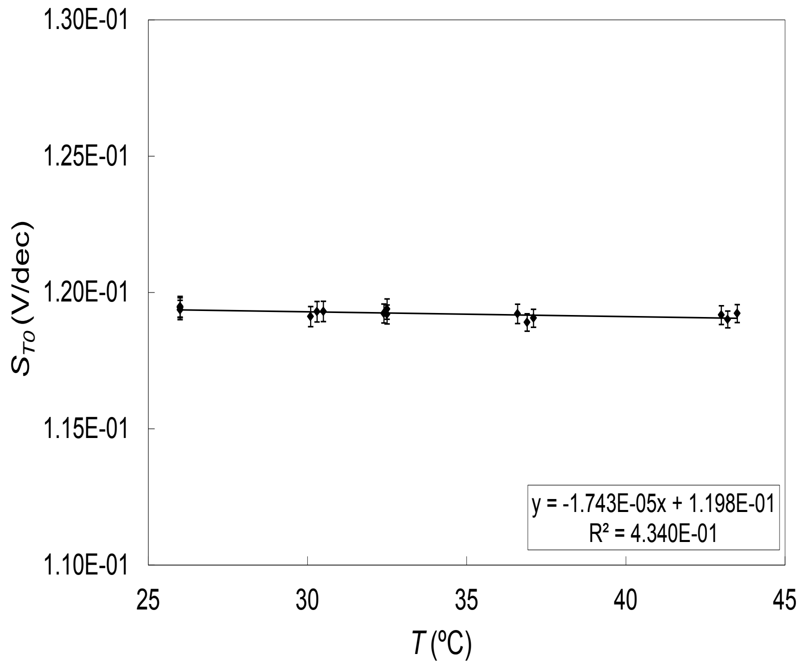

Figure 4.25 Residual thermal drift after compensation of temperature effects with equation (4.4) (experimental data in symbols with error bars and linear fit shown with the line).

Experimental results of the response to radiation of the subthreshold swing have shown to be a very promising dosimetric parameter to be taken into account as complementary to the monitoring of the threshold voltage shift. This response presents high linearity in the analysed range of dose, compared with the threshold voltage shift in Figure 4.24, and sensitivity per radiation session with quite constant behaviour. This fact could allow its use for a complete

radiotherapy treatment without additional calibration. The linear behaviour of S with temperature is also very helpful for easing modelling and the required compensation of the temperature influence. One weak point of the subthreshold swing shift, from the point of view of the practical implementation of the parameter determination, is greater difficulty in measuring than the threshold voltage shift, requiring at least two currents in the subthreshold current region and the additional polarization of drain compared with the usual extraction of V_t at constant drain current in saturation regime (shorting drain and gate terminals). Another weak point is the higher scattering of individual sensitivities as shown in Table 4.10, but this is likely not a significant drawback due to the required individual calibration of sensors as in the case of the threshold voltage shift.

In any case, and taking into account the current capability of electronics for signal processing, it would be possible to design a reader unit that implements the measurement of both dosimetric parameters: threshold voltage and subthreshold swing shifts. Data from the two electrical magnitudes would provide more robust results of the delivered dose, which would enhance the confidence of dose verification systems based on MOSFETs.

4.4 RADFETs transistors

The radiotherapy treatments require an accurate dosimetric control and RADFETs show a number of advantages over traditional dosimetry systems (Thomson 1987, Black 2003). RADFETs have oxides optimized in order to increase the radiation sensitivity. For that, a very thick gate oxide is grown (even more than 1 μm (Ristic et al. 1996, Ristic, Jaksic and Pejovic 1997)), that enhances the trapping

of radiation-induced holes. It is known that voltage shift with the dose has a power law relationship given by equation (2.30) (Ristic, Golubovic and Pejovic 1993, Ristic 2009):

$$\Delta V_T = A \cdot D^n$$

Different works have shown in unbiased mode, without external polarization, the typical linear range of RADFET dosimeter is up to several Gy or two tens of Gy, depending on the model. The linear range can be enhanced with external polarization (biased mode) (Ma and Dressendorfer 1989, Sarrabayrouse and Siskos 1998, Pejovic et al. 2013b). To provide a reliable procedure of measurement, the loss of dosimetric information during spontaneous annealing, the fading (F), has to be characterized and analysed (Pejovic et al. 2011, Jaksic et al. 2005, Ristic et al. 1996, Ristic et al. 1997, Haran et al. 2004). Remembering the equation (2.38), the fading is defined as:

$$F = \frac{V_t(0) - V_t(t)}{V_t(0) - V_{t0}} = \frac{V_t(0) - V_t(t)}{\Delta V_t(0)}$$

Another important matter that has to be addressed is the dependence of the RADFET response to different types of radiation beams (photon, electrons, protons…) and energies. In this point, the response for photons has been widely characterized with ^{60}Co sources (Pejovic et al. 2013b, Pejovic et al. 2011, Jaksic et al. 2002, Ristic et al. 2011, Pejovic, Pejovic and Jaksic 2013a, Pejovic, Pejovic and Jaksic 2012) and linear accelerators (Benson et al. 2004, Benson et al. 2006, Price et al. 2004b, Price 2005). This characterization has also been extended to electron beams (Nurul Amin et al. 2011, Bloemen-van Gurp et al. 2006, Manigandan et al. 2009); as well as recently to other types of particles like proton and neutrons (Price 2005, Price et al. 2004a, Jaksic et al. 2005).

In the present section, a comparative study of the response to photon and electron radiation beams of different RADFETs types (gate oxide thicknesses and sizes) manufactured by the Tyndall National Institute (Cork, Ireland) has been carried out and modelled using equation (2.30) and (2.38). They were experimentally characterized with beams produced by a linear accelerator over a range of doses typical of radiotherapy treatments under reference conditions. The influence of the gate oxide thickness, device size, oxide sensitivity enhancement process and radiation type have been analysed in terms of calibration parameters and short-term fading. One of our aims was to study the feasibility of these RADFETs for routine dose verification in electron beams comparing with the photon beam response. To minimize thermal drift, devices have always been biased with the zero temperature coefficient drain current, I_{ZTC} during readout (O'Sullivan et al. 1990, Buehler et al. 1993). For this models the 3CM, does not improve the response in linearity and reproducibility. This is due to the 3CM improve the linearity, taking into account $\Delta\beta$. In RADFETs ΔV_t is mainly caused by the oxide traps. As this type of transistors has a thick oxide the effect of oxide traps hide the possible improvement over the interface traps, so only the thermal compensation could be solved. Therefore, finally for simplicity, it has been decided to use the method of constant current $I_{ZTC.}$ To measure the increment of V_t with dose, the portable dosimetry system developed by (Carvajal et al. 2012) was also used. As the objective of this section is to compare the response to photon and electron beams of the same types, this study has been conducted in parallel.

4.4.1 Experimental procedure

In each session, transistors were irradiated in groups of 16 RADFETs (4 chips as shown in Figure 3.30c) simultaneously, ensuring that all of them were affected by the same radiation beam. Transistors were characterized both for electron and photon beams of 6 MeV. 40 individual RADFETs were used for each type of beam. A build-up layer made of 1.5 cm in the case of photon beams and 1.3 cm in the case of electron beam were placed over the RADFETs to reach the electronic equilibrium and the depth of dose maximum at the gate oxide. The linear accelerator Mevatrons KDS was used to irradiate RADFETs. All the irradiations were carried out with the RADFETs transistors situated at the isocentre, at 100 cm from the source, with normal beam incidence, over a squared slab phantom made of water-equivalent RW3 with dimensions 30x30x12.2 cm^3 for photon beams and 30x30x8.2 cm^3 for electron beam. The characterization of the transistors was performed using a gamma beam of 6 MV, with an irradiation field of 25x25 cm^2. Sensor modules were irradiated with a dose of 2.05 Gy or 4.24 Gy for 400 nm and 1 μm and 10.48 Gy and 23.03 Gy for 100 nm and in each session, achieving a total accumulated dose around 55 Gy for 400 nm and 1 μm and 275 Gy for 100 nm RADFETs. For electron beams the characterization of the transistors was performed using an electron beam of 6 MeV, with a collimator and an irradiation field of 15x15 cm^2. Sensor modules were irradiated with a dose of 2.06 Gy or 4.66 Gy for 400 nm and 1 μm and 10.79 Gy and 22.73 Gy for 100nm and in each session, achieving a total accumulated dose around 50 Gy for 400 nm and 1 μm and 208 Gy for 100 nm types. During the characterization of the stationary response and to avoid fading effects, voltage measurements were carried out ten minutes after the irradiation. This elapsed time was

enough to obtain stable values with our dosimetry system. The threshold voltage transient just after each irradiation session, the so-called short-term fading, was measured in intervals of 60 s during 360 s for different accumulated dose.

4.4.2 Study of the radiation response

Once the I_{ZTC} drain currents have been measured and settled for the readout processes (see Table 4.5 of section 4.2.5), the source voltages were measured before and after each irradiation session to calculate the threshold voltage shift and determine the calibration curves. The short-term fading has been also studied to set a reliable measurement procedure which reduces the effects of the voltage transients appearing after irradiations.

A comparative study of the response of RADFETs to 6 MV photon and electron beams has been carried out. In Figure 4.26, the accumulated V_t shift versus the dose for the type with 100 nm oxide of both sizes (W/L= 300/50 and 690/15 μm) are plotted and fitted to equation (2.30) for photon (left) and electron (right) beams. Hereafter, in all the figures showing threshold shift as a function of the dose, uncertainties (with a coverage factor $k=1$) are 0.5 mV/session for ΔV_t and 2.5 cGy for the dose on average. Dose uncertainties are smaller than the size of symbol used. Lines will show the potential fits to the data. The response of different type of RADFETs with 400 nm of gate oxide thickness has been also studied. Figure 4.27 and Figure 4.28 depict the results for a device of the three types of 400 nm showing the accumulated V_t shift versus the dose for W/L = 300/50 and W/L = 690/15 respectively. The responses of the other RADFETs of every group were very similar.

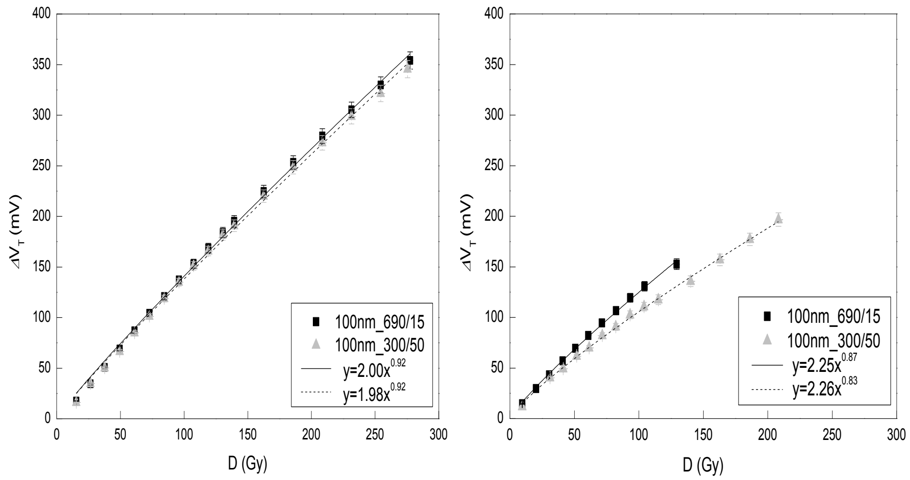

Figure 4.26 Accumulated threshold voltage shift as a function of the accumulated dose of RADFETs with tox =100 nm and W/L = 300/50 and 690/15, irradiated with photon (left) and electron (right) beams.

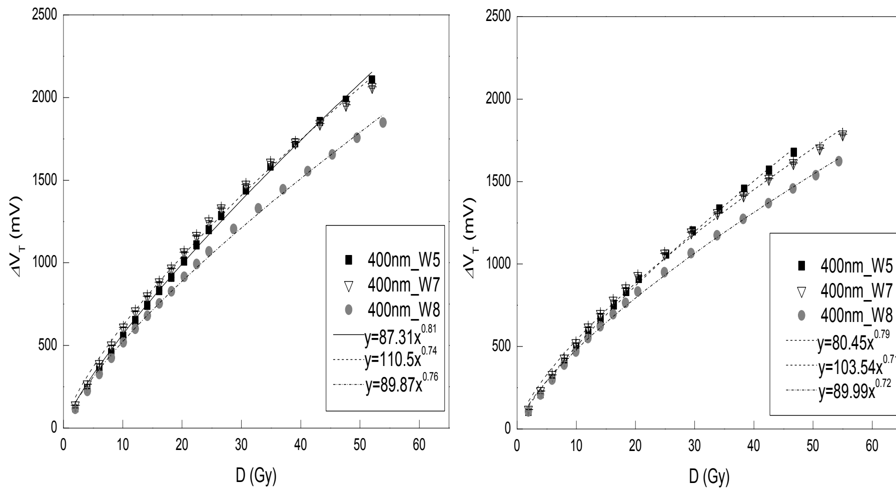

Figure 4.27 Accumulated threshold voltage shift as a function of the accumulated dose of RADFETs with tox =400 nm, with W/L = 300/50 irradiated with photon (left) and electron (right) beams.

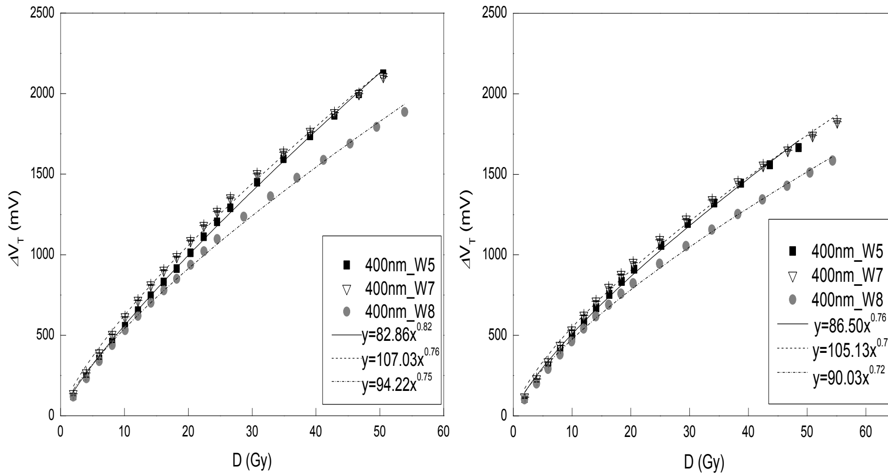

Figure 4.28 Accumulated threshold-voltage shift as a function of the accumulated dose of RADFETs with t_{OX} =400 nm, with W/L = 690/15 irradiated with photon (left) and electron (right) beams.

Experimental results and fittings are also shown in Figure 4.29 for RADFETs with t_{OX} =1 μm. As in the previous figures, very good agreements between the standard model of equation (2.30) and the response to radiation were achieved with a $R^2 > 0.999$.

Moreover, threshold voltage transients were measured as a function of the time elapsed, in intervals of 60 s, since the moment of the connection of the sensor module to the reader unit up to 360 s. The time between the end of the irradiation and the connection of the sensor module to the reader unit was also approximately 30 s. Among the studied RADFEts, short-term fading were only remarkable for t_{OX} =1 μm. In Figure 4.30, they are shown for several accumulated doses with photon (left) and electron (right) beams. Maximum fading of 100 nm and 400 nm RADFETs were less than 1% and 0.12% respectively for photon beams and less than 0.3% in RADFETs with the latter mentioned thicknesses for electron beams.

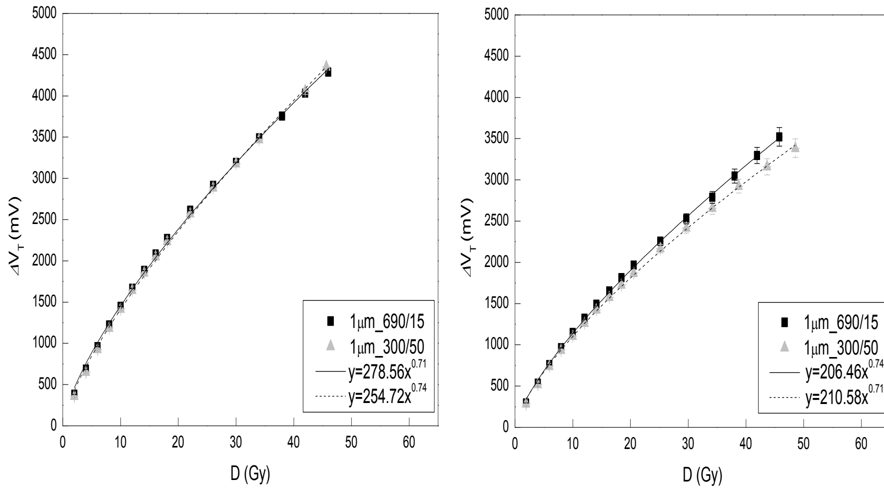

Figure 4.29 Accumulated threshold voltage shift as a function of the accumulated dose of RADFETs with tox =1 μm and W/L = 300/50 and 690/15, irradiated with photon (left) and electron (right) beams.

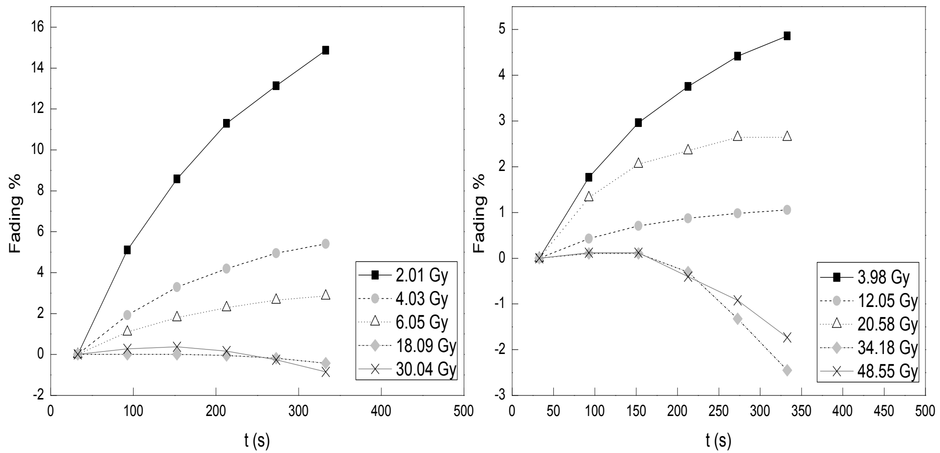

Figure 4.30 Short-term post-irradiation fading for RADFETs of t_{ox} =1 μm for photon (left) and electron (right) beams up to 350 s after irradiation.

Type	Size (W/L)	Photon Beam		Electron Beam	
		$\Delta V_T = A \cdot D^n$			
		A	**n**	**A**	**n**
100 nm	**300/50**	2.04 ± 0.34	0.91 ± 0.03	2.2 ± 0.3	0.83 ± 0.03
	690/15	2.03 ± 0.19	0.92± 0.02	2.2 ± 0.3	0.87 ± 0.03
400 nm_W5	**300/50**	91 ± 5	0.80 ±0.01	79 ± 3	0.79 ± 0.01
	690/15	81 ± 4	0.83 ± 0.01	83 ± 6	0.78 ± 0.02
400 nm_W7	**300/50**	113 ± 8	0.74 ±0.02	104 ± 6	0.73 ± 0.01
	690/15	103 ± 5	0.77 ± 0.02	105 ± 6	0.72 ± 0.01
400 nm_W8	**300/50**	73 ± 11	0.81 ±0.05	79 ± 10	0.73 ± 0.01
	690/15	86 ± 10	0.77 ± 0.02	85 ± 7	0.73 ± 0.01
1 μm	**300/50**	239± 23	0.76 ± 0.02	213 ± 9	0.72 ± 0.01
	690/15	248 ± 47	0.74 ± 0.04	202 ± 9	0.74 ± 0.01

Table 4.11 Fitting parameters of RADFET response, according to the power law model for every size and type for photon and electron ionizing radiation. ΔV_t was expressed in mV and D in Gy.

First, the method of constant ZTC current to minimize thermal drift has been considered valid, because I_{ZTC} did not significantly change as a result of the irradiation in the studied range. In our case, it has been measured a maximum shift of 17% for the 1 μm gate oxide type after 60 Gy of electron or photon radiation. A previous work also reported a similar shift of the ZTC current for 400 nm and 500 nm gate oxide RADFETs irradiated in the unbiased mode as well (O'Sullivan et al. 1990).

Table 4.11 lists the parameters A and n, for the calibration curves of the different studied types under photon and electron beams in reference conditions. Generally speaking, in all the studied cases there is a sub-linear behaviour, $n<1$, mainly due to the electric field screening produced by the radiation-induced oxide charges (Holmes-

Siedle et al. 2007). Only in RADFETs with 100 nm gate oxide, where this effect is less important, have a n parameter close to 1 mostly for photon beams. Moreover, as it was expected, the A parameter increases and n decreases with the gate oxide thickness for both ionizing sources in accordance with others experimental studies with photon beams (Benson et al. 2004, Ristic et al. 2011, Pejovic et al. 2012, Pejovic et al. 2011) . Bigger sensitive volumes provide higher A values due to higher radiation-induced oxide charge which enhances the electric field screening in the oxide, decreasing the exponent n.

In Figure 4.27 and Figure 4.28, it has been observed slight differences in sensitivity among the types of 400 nm. This can attributed to the different technological processing of these chips (W5 vs. W7/W8), but also lot-to-lot differences (W7/W8), which are typical for the RADFET technology and can be accounted for during the calibration process. Concerning the channel dimension, there are no significant differences between the performances of both sizes.

Regarding the short-term fading at room temperature, experimental results indicate that it can be neglected in case of t_{OX} =100 nm and 400 nm for both radiation beams, showing a threshold voltage drift always below 1% after 360 s. However, in case of 1 μm the influence of fading is important and decreasing when the accumulate dose increases (see Figure 4.30). There are two competing effects, the density of oxide trapped charge decreases monotonically after irradiation by annealing (thus reducing the threshold voltage in absolute value, giving a positive fading), while the density of interface traps exhibits the initial increase, (resulting in an increase of the absolute value of threshold voltage and, therefore a negative fading). It is widely known that switching oxide traps are particularly important in RADFETs, because of that they have the dominant influence on the short-term fading at

high accumulate dose (Jaksic et al. 2002, Savic et al. 1995). When the device has a concrete accumulated dose the induced positive charge by interface state build-up become comparable and even higher than the annealing of oxide traps and the fading show negative values (Price et al. 2004a, Jaksic et al. 2002, Ristic et al. 1996). Taking this fact into account, it is mandatory to set a delay time after irradiation to achieve a reliable measurement. For the thickest oxides studied, a delayed acquisition time of more than 10 minutes are required, because from Figure 4.30 it can be observed for high doses after 360 s has not been stablished.

Undoubtedly, the major novelty of this study is the possibility of the direct comparison of the calibration parameters of different gate oxide RADFETs for photon and electron radiation beams. According Table 4.11, RADFETs from Tyndall National Institute with t_{OX} between 100 nm and 1 μm showed a very similar calibration curve with independence of the radiation particle (photon or electron) at the studied energy. In most cases, calibration parameters A and n presents comparable values, within the uncertainty, for each RADFET type and for both types of beams. Therefore, this experimental study shows that analysed RADFETs can be suitably used for routine dose verification in electron beams, when applying the correction factors in case of not being used in reference conditions. It has been expected a very similar behaviour as in photon beams in terms of sensitivity and short-term fading.

5

Effects of the temperature on MOSFET as dosimeter

This chapter presents a model of the effects of the temperature on MOSFETs when they are used as dosimeters. This model is based on a previous algorithm for thermal drift reduction with multiple bias current for MOSFET (Carvajal et al. 2011). After the theoretical model, the description of the temperature dependence of Metal-Oxide-Semiconductor Field-Effect Transistor (MOSFETs) in saturation regime, is justified and experimentally tested in n-channel and p-channel transistors (Carvajal Rodríguez et al. 2014). This thermal model provides the linear temperature coefficient of source-drain voltage as a function of experimental transistor parameters and the drain current. To do so, an exhaustive thermal characterization of p-channel MOSFET and n-channel MOSFET is carried out in the industrial temperature range. Afterwards, the change of ZTC current caused by the integrated dose and alternating cycles of temperature is studied. Then the influence of changes of I_{ZTC} in the thermal coefficient of threshold voltage with two different methods: the proposed one and biasing with the I_{ZTC} current are compared, showing an significant reduction of the thermal drift applying the proposed method. As consequence of this study, the thermal model is also

applied to design a temperature sensor based on differential measurements of source-drain voltages in a pair of MOSFETs, configuration used for dosimetry as well.

5.1 State of art

The thermal dependence of electrical parameter of MOSFET or RADFETs, is one of the major concerns when they are used as dosimeters. The thermal drift can be an important factor in the dosimetry field, especially in applications where changes in temperature are common as for example in radiotherapy treatments (environmental/skin temperature difference) or space applications, such as the case of satellites (cycles of sunlight/darkness). These variations make the thermal dependence in a non-negligible effect that can prevent the accurate measurement of the dose.

Traditionally, there have been three ways to reduce the effect of temperature on the dosimetric response: the first one consists of setting the drain current at the point where the effect of the temperature is expected to be minimal, that is, where the temperature coefficient is zero, the ZTC current (Haran et al. 2004, O'Sullivan et al. 1990, Buehler et al. 1993, Kimoto et al. 2003, Shoucair et al. 1984a, Shoucair et al. 1984b, Tsividis 1987, Vettese et al. 1996). Another compensation method is based on differential measurements of the source-drain voltage of two identical MOSFETs on the same chip operating at two different positive biases on the gate, but the same current during readout. They have different source-drain voltage shifts, but the thermal fluctuation is expected to be the same in the two transistors. With the differential measurement of the source-drain voltage shift the thermal fluctuation is cancelled (Soubra et al. 1994, Mackay et al.

1997, Thomson et al. 1998, Shin et al. 1999). The last method is the subtraction of the temperature contribution to the acquired data. In this method, the thermal dependence of the dosimetric parameter must be found and the measurement must be corrected (Shin et al. 1999, Lin and Buehler 1991, Soli et al. 1992, Sung-Joon et al. 2002).

Concerning to the method based on biasing with I_{ZTC}, it must be taken into account a possible variation of this current. Two main reasons could cause a shift of the ZTC current: accumulative dose and extreme temperature cycles (Sarrabayouse and Siskos 2008, Haran et al. 2004, Holmes-Siedle et al. 2007). However the influence could be more significant in space application where the dose is higher. Also on space application, annealing may occur because of the temperature cycles in satellites, this is another main reason for the possible fluctuations in the I_{ZTC}. Therefore, in the space applications operates exactly at the ZTC current through an entire mission is almost impossible (Haran et al. 2004). The possible shift of I_{ZTC} could be solved with the method based on differential measurements but this solution is more complex and it requires two pMOS, with possible concerns on transistor asymmetry. Finally the method based on the subtraction requires a previous analysis of transistor in the laboratory to find out the dosimetric parameter to be corrected afterwards.

Recently, our research group proposed a thermal compensation method based in multiple current biasing during readout period (Carvajal et al. 2011). That procedure showed a reduction of the thermal drift in around a factor of 50 assuming no change in I_{ZTC}.

5.2 Theoretical Model of thermal effects on MOSFETs

It has been considered a general enhancement MOSFET (n or p type) biased at constant drain current with drain and gate short-circuited and, therefore, in the saturation region, as Figure 5.1 shows.

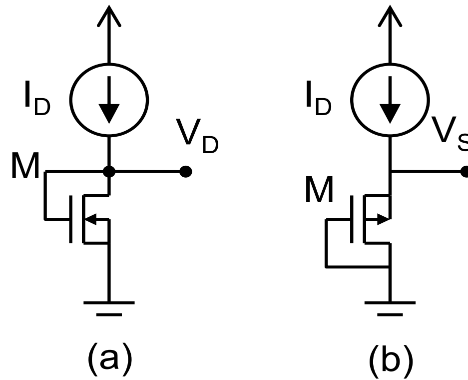

Figure 5.1 MOSFET configurations for biasing at constant current in saturation region a) nMOS b) pMOS.

In this case, neglecting the modulation channel effect, the I_D-V_{GS} characteristic is given by equation (2.39), previously studied:

$$i_D = -\frac{\beta}{2}(|v_{GS}| - |V_t|)^2$$

In this configuration, v_{GD}=0, then v_{GS}=v_{DS}. It is well known that carrier mobility decreases with temperature; therefore, if the drain current is constant and the temperature rises, the $|v_{GS}|$ will increase. Otherwise, $|V_t|$ is reduced with temperature increases, which produces a decrease in $|v_{GS}|$. Mobility degradation is stronger at higher currents, and the thermal dependence of $|v_{GS}|$ dominates; however, at low currents the reduction in $|V_t|$ dominates, causing a decrease in $|v_{GS}|$. As it has studied, these opposing effects are cancelled in an intermediate

current region known as the Zero-Temperature-Coefficient zone, where the temperature dependence of $|v_{GS}|$ is minimal.

Equation (2.39) is valid for nMOS and pMOS transistors, considering the absolute value of the drain-source voltage, $|v_{DS}|$, and the threshold voltage $|V_t|$. In order to generalize for n- and p-channel transistors the $|v_{DS}|$ is renamed V_X for simplicity's sake. Using this equation, the threshold voltage can be calculated at two different drain currents, I_{D1} and I_{D2}, as it was previously studied in section 1.6.3:

$$|V_t|(T) = V_{X1}(T) - \sqrt{2I_{D1}}\sqrt{\frac{1}{\beta(T)}} \tag{5.1}$$

$$|V_t|(T) = V_{X2}(T) - \sqrt{2I_{D2}}\sqrt{\frac{1}{\beta(T)}} \tag{5.2}$$

where $V_{Xi}=|v_{DS,i}|$ for i=1,2; valid for nMOS and pMOS transistors. Matching (5.1) and (5.2) and operating, gives:

$$\sqrt{\frac{1}{\beta(T)}} = \frac{V_{X1}(T) - V_{X2}(T)}{\sqrt{2I_{D1}} - \sqrt{2I_{D2}}} \tag{5.3}$$

Replacing (5.3) in (5.1), it is obtained

$$|V_t(T)| = V_{X1}(T) - \frac{V_{X1}(T) - V_{X2}(T)}{1 - \sqrt{\frac{I_{D1}}{I_{D2}}}} \tag{5.4}$$

Equation (5.4) determines the threshold voltage from the drain-source voltage in absolute value measured at two different drain currents.

The linear modelling of the thermal dependence of electrical parameters is a very common practice in thermal models (Reverter and Altet 2013, Carvajal et al. 2011, Angelov, Bengtsson and Garcia 1996, Sadi and Schwierz 2010). In small signal or Scattering models, non-linear corrections could be necessary (Sadi and Schwierz 2013, Kyoungmin, Hyun-Min and Songcheol 2002), however the model presented is intended to DC drain currents and voltages. On the other hand, if the drain current is high, the self-heating must be considered (Sadi, Kelsall and Pilgrim 2006, Jong-Wook and Webb 2004). Let us consider that the variation of V_X ($|V_{DS}|$) with temperature can be approximated to a linear model, as follows (Reverter and Altet 2013, Carvajal et al. 2011):

$$V_X(T) = V_X(T_0) + \alpha(I_D)(T - T_0) \tag{5.5}$$

where $\alpha(I_D)$ is the thermal coefficient of the absolute value of source-drain voltages measured at drain current I_D. In the same way, the thermal dependence of the threshold voltage can be modelled using a linear dependence (Sze 1981, Tsividis 1987):

$$|V_t(T)| = |V_t(T_0)| + \alpha_{|V_t|}(T - T_0) \tag{5.6}$$

where α_{Vt} is the thermal coefficient of the threshold voltage. If (5.5) is evaluated for $I_D=I_{D1}$ and $I_D=I_{D2}$, the difference of voltage measured at these currents will be obtained as:

$$V_{X1}(T) = V_{X1}(T_0) + \alpha\,(I_{D1})(T - T_0) \tag{5.7}$$

$$V_{X2}(T) = V_{X2}(T_0) + \alpha\,(I_{D2})(T - T_0) \tag{5.8}$$

Replacing $V_{X1}(T)$ and $V_{X2}(T)$ in (5.4) and operating yields:

$$|V_t(T)| = V_{X1}(T_0) + \frac{V_{X2}(T_0) - V_{X1}(T_0)}{1 - \sqrt{\frac{I_{D2}}{I_{D1}}}} + \left[\alpha(I_{D1}) + \frac{\alpha(I_{D2}) + \alpha(I_{D1})}{1 - \sqrt{\frac{I_{D2}}{I_{D1}}}}\right](T - T_0) \tag{5.9}$$

Comparing (5.9) with (5.6), it can be concluded that:

$$\alpha_{|V_t|} = \alpha(I_{D1}) + \frac{\alpha(I_{D2}) - \alpha(I_{D1})}{1 - \sqrt{\frac{I_{D2}}{I_{D1}}}} \tag{5.10}$$

If (5.10) is rewritten for an arbitrary drain current $I_{D1}=I_D$, and $I_{D2}=I_{ZTC}$, where $\alpha(I_{ZTC})=0$, the following equation can be obtained:

$$\alpha(I_{D1}) = \alpha_{|V_t|}\left(\sqrt{\frac{I_D}{I_{ZTC}}} - 1\right) \tag{5.11}$$

This equation was found in section 3.6.3 from the increment of source and threshold voltage. However in the present section voltage values (no shifts) has been used to obtain the thermal model. Thus in this section an extension of expressions shows in section 3.6.3 concerning to thermal dependence has been generalized.

Therefore, from (5.11) the thermal coefficient of the source-drain voltage as a function of the drain current can be calculated from only two parameters, $\alpha_{|Vt|}$ and I_{ZTC}. The number of parameter of proposed model is similar to others thermal models related with MOS transistors. For example, the model proposed by (Angelov et al. 1996) for small signal parameters, or the model of (Sadi and Schwierz 2013) for the study of intermodulation distortion in III–V HEMTs and Si LDMOSFETs, used at least two thermal parameters. Moreover, in this case the parameters of the proposed model, $\alpha_{|Vt|}$ and I_{ZTC}, can be found experimentally. Then, the drain current can be chosen in order to

achieve the desired thermal coefficient of the source-drain voltage, making, moreover, easy the design of temperature sensor, as it will be shown at the end of this chapter.

A new procedure based on the previous developed two current method used for thermal compensation of the threshold voltage and this novel thermal model is found: an algorithm to reduce the impact of the I_{ZTC} shift in the dose extraction from the threshold voltage measurements of dosimeters based on MOSFET. The proposed method obtains the thermally compensated source voltage shift as performing measurements of the increase in the source voltage at two drain currents, considering I_{ZTC} known (Carvajal et al. 2011). Hereafter, the proposed method will be named as two current method (2CM). Specially focusing on pMOS transistors, which are the traditional dosimeters, the equation (5.5) can be particularized as (Sze 1981, Asensio et al. 2006, Tsividis 1987):

$$\Delta V_S = \Delta V_S^0 + \alpha(I_D)\Delta T$$

where ΔV_S^0 represents the increase in the absolute value of the source voltage due to some external factor as for example ionizing radiation, which is independent of temperature. The thermal coefficient was labelled as TC by others authors (Haran et al. 2004, Holmes-Siedle et al. 2007, Sarrabayouse and Siskos 2008). Applying this model with two currents, I_{D1} and I_{D2}:

$$\Delta V_{S1} = \Delta V_{S1}^0 + \alpha(I_{D1})\Delta T \quad (5.12)$$

$$\Delta V_{S2} = \Delta V_{S2}^0 + \alpha(I_2)\Delta T \quad (5.13)$$

Therefore, combining equations (5.12) and (5.13); ΔT it is obtained:

$$\Delta T = \frac{(\Delta V_{S2} - \Delta V_{S1}) - (\Delta V_{S2}^{0} - \Delta V_{1}^{0})}{\alpha(I_{D2}) - \alpha(I_{D1})} \quad (5.14)$$

From (2.39), if the changes in β produced by the radiation can be considered negligible, the threshold voltage shift due to radiation , $\Delta|V_T^0|$, could be approximate to the source-voltage shift, ΔV_S^0 (Buehler et al. 1993, Sarrabayrouse and Siskos 1998).

$$\Delta\left|V_T^0\right| \sim \Delta\left|V_{S1}^0\right| \sim \Delta\left|V_{S2}^0\right| \quad (5.15)$$

Including equation (5.15) in (5.14),

$$\Delta T = \frac{\Delta V_{S2} - \Delta V_{S1}}{\alpha(I_{D2}) - \alpha(I_{D1})} \quad (5.16)$$

Therefore using equations (5.12) and (5.13) in (5.16), the source voltage shift caused by radiation is:

$$\Delta V_{S1}^0 = \Delta V_{S1} + \frac{\Delta V_{S2} - \Delta V_{S1}}{1 - \frac{\alpha(I_{D2})}{\alpha(I_{D1})}} \quad (5.17)$$

Furthermore, using the linear thermal coefficient from equation (5.11), and evaluating this expression for I_{D2} and I_{D1}, the ratio $\alpha\ (I_{D2})\ /\alpha\ (I_{D1})$ can be obtained. Substituting it into equation (5.17), the thermally compensated source voltage shift can be found as a function of electric magnitudes that can be easily measured not requiring the temperature value:

$$\Delta V_T^0 \approx \Delta V_{S1}^0 = \Delta V_{S1} + (\Delta V_{S2} - \Delta V_{S1}) \frac{\sqrt{I_{D1}} - \sqrt{I_{ZTC}}}{\sqrt{I_{D1}} - \sqrt{I_{D2}}} \quad (5.18)$$

Equation (5.18) was successfully applied to significantly reduce the influence of the temperature on dose measurements with MOSFETs but without taking into account possible I_{ZTC} shifts (Carvajal et al. 2011). It must be taken into account that the 2CM algorithm (to thermal compensation) is equivalent to use 3CM (thermal compensation and enhancement of linear range) in the MOSFETs that

the contribution of ΔV_t due to $\Delta\beta$ is negligible, as happens in the most type of RADFETs. Now, it is proposed an election of the two drain currents to reduce the impact of this I_{ZTC} shift. To reduce the I_{ZTC} contribution in equation (5.18) the currents have to be selected as:

$$I_{D1} \gg I_{ZTC}$$

$$I_{D1} > I_{D2}$$

With this selection the quotient in the expression (5.18) is designed to be minimal and the contribution of I_{ZTC} could be neglected. To model the influence of the possible fluctuation of I_{ZTC}, the expression (5.17) is derived with the variation in temperature. From this, the fluctuations of I_{ZTC} will be denoted like ΔI_{ZTC}. Only the source voltage shifts are dependent on temperature and when they are derived the thermal coefficient at those currents are obtained.

$$\frac{\partial V_{S1}^{0}}{\partial T} = \alpha_{S1}^{0} = \alpha'(I_{D1}) + \frac{\alpha'(I_{D2}) - \alpha'(I_{D1})}{1 - \frac{\alpha(I_{D2})}{\alpha(I_{D1})}} \tag{5.19}$$

where α_{S1}^{0}, is the new thermal coefficient of source voltage after a I_{ZTC} shift, $\alpha'(I_{D1})$ and $\alpha'(I_C)$ are the modified thermal coefficients for the I_{D1} and I_C respectively with the change of I_{ZTC}.

5.2.1 Experimental validation of the theoretical thermal model

Firstly, the experimental validation of the proposed thermal model need to be done, checking (5.11) with the experimental data. The temperature dependence of two commercially available lateral n- and p-channel enhancement-mode MOSFETs is studied. The 3N170 is a general purpose enhancement-mode nMOS manufactured by Linear Systems (USA), and the 3N163 is pMOS already widely studied in this

thesis, but in this case, samples different to the others irradiated in the previous chapter. Both types are encapsulated in a TO-72 nickel package whose terminals were connected according to Figure 5.1a (3N170) and Figure 5.1b (3N163).

A set of five transistors per type were introduced into the climate chamber VCL4006 for characterizing their responses to temperature. To measure transistor temperature more accurately, an NAW880EXL thermometer was placed inside the chamber near the devices. The experiment involved heating and cooling from -40°C to 85°C, measuring 5°C increments, with no hysteresis in MOSFET performance noticed. A total of 26 temperatures were studied extracting the I_D-V_{GS} curves for each transistor and temperature. A new thermal studied of 3N163 was carried out, because the samples belong to a new batch of production, to check the thermal behaviour known until now, and to have the same range of temperature both nMOS and pMOS types for this study.

The type presented above in (5.11) is appropriate for lateral transistors that present an I_{ZTC} point. In order to check this proposed thermal model for the lateral transistors studied (3N163 and 3N170), an exhaustive thermal characterization was carried out with the aim of calculating parameters $\alpha_{|Vt|}$ and I_{ZTC}. This is done by comparing the values of these magnitudes using the standard model given by (5.6) and those extracted from the proposed model given by (5.11).

Method 1: Using equation (5.6)

If the linear fit of the experimental $I_D^{1/2}$ versus V_{GS} is carried out, the value of $|V_t|$ can be obtained as the intercept of the linear regression with the abscissa axis; according to equation 2.39 (see

Figure 5.2). This process is carried out for each transistor between -40ºC and 85ºC, in the current ranges from 15 to 700 μA for 3N163 and from 0.1 mA to 5 mA for 3N170. Both current ranges ensure the strong inversion regime of the MOSFETs where 2.39 is valid, as Figure 5.2 shows.

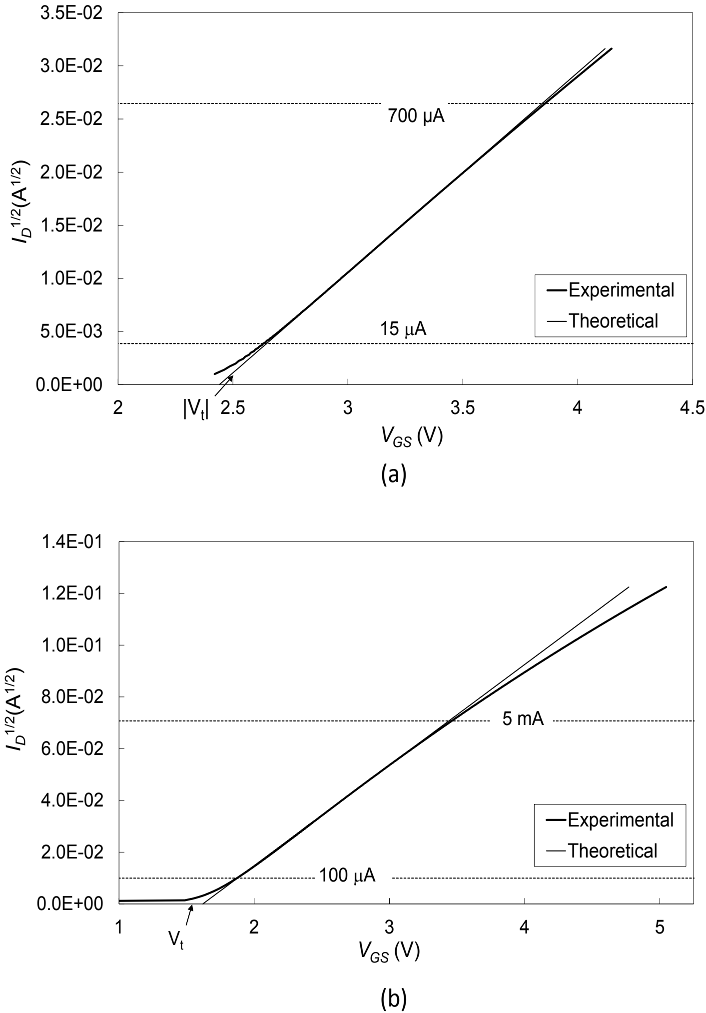

Figure 5.2 *I-V* characteristics of transistors at 20ºC: a) 3N163_T1 b) 3N170_T1.

In Figure 5.3, the thermal dependence of V_t for transistor number T1 of the set 3N163 and 3N170 is displayed, showing linear behaviour in the temperature range studied. The value of $\alpha_{|Vt|}$ was obtained as the slope of the linear fit. The individual and average parameters are summarized in Table 5.1. As can be observed, the standard deviation of $\alpha_{|Vt|}$ in the set of transistors is relatively low at 2.2% and 2.8% for 3N163 and 3N170 respectively.

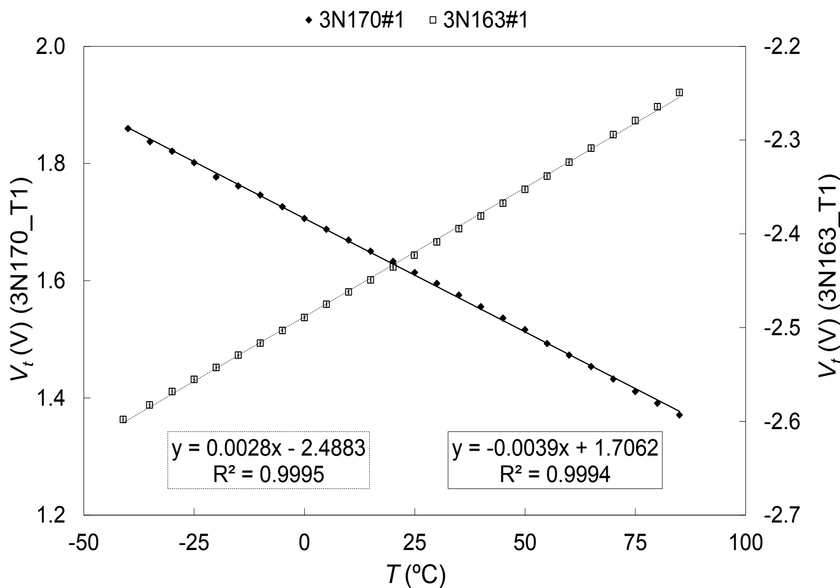

Figure 5.3 Threshold voltages as a function of the temperature of the transistors T1 of the groups 3N163 and 3N170.

To complete the thermal study, the I_{ZTC} was experimentally found as in previous thermal studies of this thesis, for all the transistors as the cross point of the current vs. voltage curves at several temperatures (see Figure 5.4). These values are also displayed in Table 5.1.

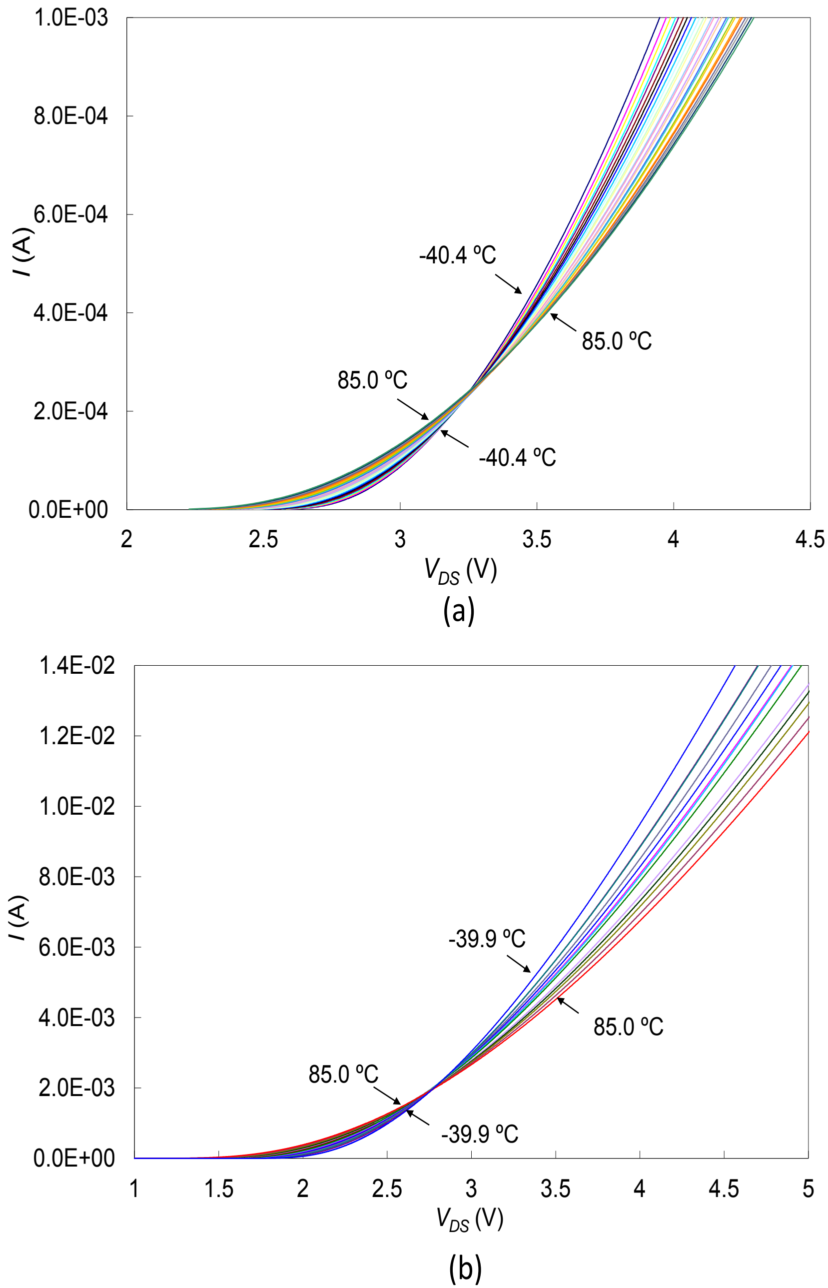

Figure 5.4 *I*-*V* characteristics for MOSFSET T1 for I_{ZTC} extraction: a) 3N163 b) 3N170.

Method 2: Using proposed model equation (5.11)

The second method for calculating $\alpha_{|V_T|}$ and I_{ZTC} consists on fitting the experimental results to (5.11). To do so, the temperature coefficient of source-drain voltage as a function of drain current ($\alpha(I_D)$) was fitted as the $I_D^{1/2}$ function as **Figure 5.6** shows for transistors 3N163_T1 and 3N170_T 1. The current range used for linear fitting depends on the transistor type, therefore for 3N163, the thermal coefficient was from 20 μA to 1 mA, and from 200 μA to 5mA for 3N170. In these current ranges, the dependence of $\alpha(I_D)$ with $I_D^{1/2}$ is approximately linear, as can be seen in **Figure 5.6**. From the slopes of the fitted curves to (5.5), $\alpha(I_D=20\mu\text{A})$ and $\alpha(I_D=1\text{mA})$ were calculated. Repeating the same process for the entire current range and all the studied MOSFETs, the thermal coefficients, $\alpha(I_D)$, were found.

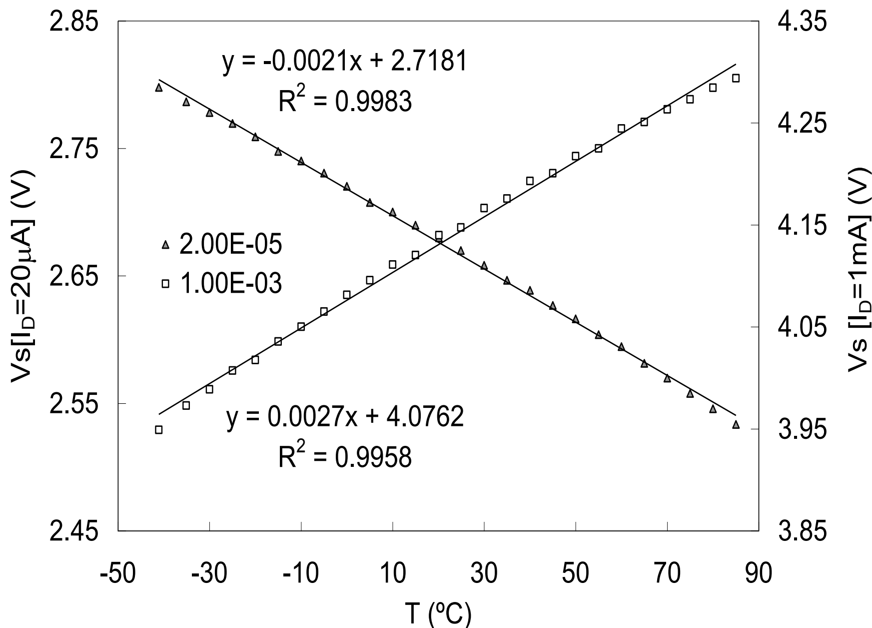

Figure 5.5 V_S for 3N163_T1 measured at 20 and 1000 μA.

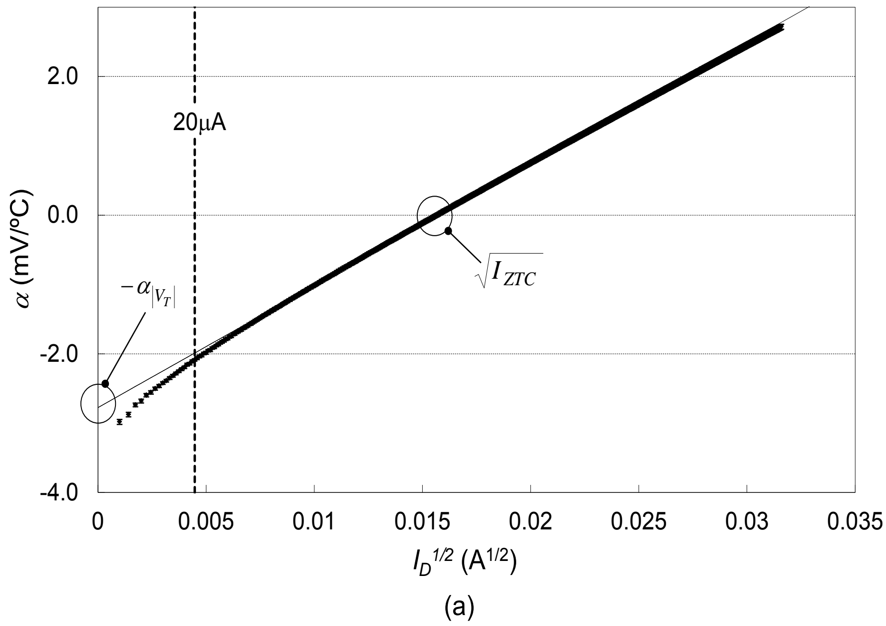

(a)

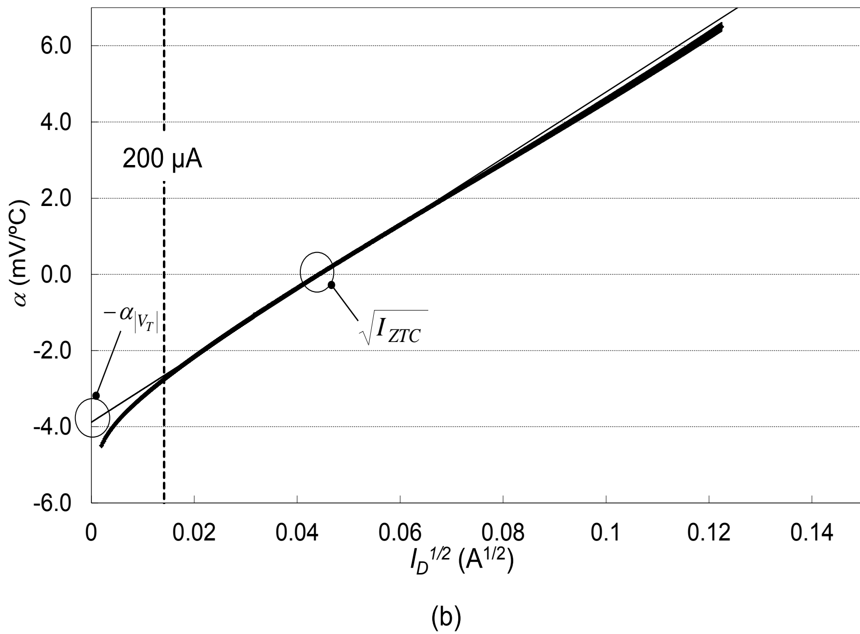

(b)

Figure 5.6 α(ID) as a function of $ID^{1/2}$ for transistors 3N163_T1 and 3N170_T1. The dots represent experimental data and the thin black line is the theoretical model.

Figure 5.6 shows $\alpha(I_D)$ for transistor 1 for the two groups of MOSFETs. Fitting these curves to (5.11), $-\alpha_{|Vt|}$ was extracted from the intercept of $\alpha(I_D)$ versus $I_D^{1/2}$, an I_D and I_{ZTC} was calculated as the value of I_D that makes $\alpha(I_D)=0$. Similar results were found in the rest of the transistors.

		Sensor					
		#1	**#2**	**#3**	**#4**	**#5**	**Average**
Method 1	$\alpha_{\|V_T\|}$ **(mV/ºC)**	-2.782	-2.666	-2.768	-2.803	-2.663	-2.74
	$\Delta\alpha_{\|V_T\|}$ **(mV/ºC)**	0.013	0.015	0.014	0.016	0.013	0.07
	Iztc (μA)	247	237	246	247	238	243
	ΔIztc (μA)	5	5	5	5	5	7
Method 2	$\alpha_{\|V_T\|}$ **(mV/ºC)**	-2.775	-2.660	-2.731	-2.797	-2.683	-2.73
	$\Delta\alpha_{\|V_T\|}$ **(mV/ºC)**	0.003	0.002	0.002	0.002	0.002	0.06
	Iztc (μA)	248.7	237.0	243.4	245.9	241.6	243
	ΔIztc (μA)	0.6	0.6	0.5	0.6	0.5	4

Table 5.1 Thermal parameters, $\alpha_{|Vt|}$ and I_{ZTC}, and their uncertainties in transistors 3N163 using linear fit (method 1) and the proposed thermal model (method 2).

In Table 5.1 and Table 5.2 the values of $\alpha_{/Vt/}$ and I_{ZTC} and their uncertainties obtained by both methods are summarized together. A good agreement between measurements and theoretical results has

been found, pointing out the validity of the proposed model in these conditions.

		Sensor					
		#1	**#2**	**#3**	**#4**	**#5**	**Average**
Method 1	$\alpha_{\lvert V_T \rvert}$ **(mV/ºC)**	-3.92	-3.75	-3.80	-3.63	-3.71	-3.92
	$\Delta\alpha_{\lvert V_T \rvert}$ **(mV/ºC)**	0.04	0.03	0.03	0.03	0.04	0.12
	Iztc (µA)	2.04	2.05	2.02	1.97	2.08	2.03
	ΔIztc (µA)	0.05	0.05	0.05	0.05	0.05	0.06
Method 2	$\alpha_{\lvert V_T \rvert}$ **(mV/ºC)**	-3.880	-3.693	-3.769	-3.593	-3.674	-3.72
	$\Delta\alpha_{\lvert V_T \rvert}$ **(mV/ºC)**	0.003	0.002	0.002	0.002	0.002	0.11
	Iztc (mA)	2.004	2.041	1.988	1.919	2.085	2.01
	ΔIztc (mA)	0.005	0.004	0.004	0.004	0.005	0.06

Table 5.2 Thermal parameters, $\alpha_{|Vt|}$ and I_{ZTC}, and their uncertainties in transistors 3N170 using linear fit (method 1) and the proposed thermal model (method 2).

Similar studies was previously done with the 3N163 type by (Asensio et al. 2006, Carvajal et al. 2010) to obtain the thermal parameters, which have been previously used in this thesis. They also calculated the thermal coefficient of threshold voltage and the I_{ZTC} were obtained, with values of -3.5±0.4 mV/°C and 230±3 μA respectively. The thermal coefficient is slightly higher than the obtained values for both methods; however the I_{ZTC} is lightly smaller

than in the current study. In both cases, the differences can be due to the fact that the samples belong to different batch, even different years of production.

To set the valid range of the thermal model, it has been also compared the experimental data (symbols) with the linear function given by (5.11) (lines) in Figure 5.6. The theoretical model and experimental data agree in certain current ranges. At low currents, the thermal model is not valid because a strong inversion is not achieved, and at high currents, the modulation channel effects are not negligible and increase the source-drain voltage. In both cases, equation 2.39 and the proposed model are no longer valid. From Figure 5.6, the drain current ranges where the thermal model can be applied is from 20 to 1000 μA for pMOS 3N163; and from 200 μA up to 5 mA for nMOS 3N170, where the experimental data present a reasonable agreement with the model.

The limits are not the same due to the different mobility of the electrons and holes and other technological parameters. Therefore, within a suitable current range, the transistor can be polarized in order to achieve a given source-drain thermal coefficient according to (5.11). In fact, this thermal model makes the thermal compensation in MOSFET sensors possible, for example, for MOSFET-based dosimeters (Carvajal et al. 2011) and as it has been previously used in this thesis. It could also be extended to other types of sensors based on MOS structures, such as CHEMFET or ISFET. In the sections below, the procedure to reduce the thermal drift of source voltage when I_{ZTC} shift happens and the development of a novel temperature sensor based on MOSFETs are described.

5.3 Thermal drift reduction with changes in I_{ZTC}

In the present section, the application of the proposed thermal model and the 2CM to reduce the thermal drift of different RADFETs types with changes in the ZTC current is presented based on equation (5.19). RADFETs were characterized with photon beams produced by a linear accelerator, over a range of doses until 275 Gy in case of t_{ox} =100 nm and 55 Gy to the rest of RADFETs types. After this irradiation process, they were annealed with different temperature cycles. To help to understand how to calculate parameters for evaluate (5.19), in Figure 5.7 the thermal coefficients of the source voltage as a function of drain current are depicted when a I_{ZTC} shift happens.

$$\frac{\partial V_{S1}^{0}}{\partial T} = \alpha_{S1}^{0} = \alpha'(I_{D1}) + \frac{\alpha'(I_{D2}) - \alpha'(I_{D1})}{1 - \frac{\alpha(I_{D2})}{\alpha(I_{D1})}}$$

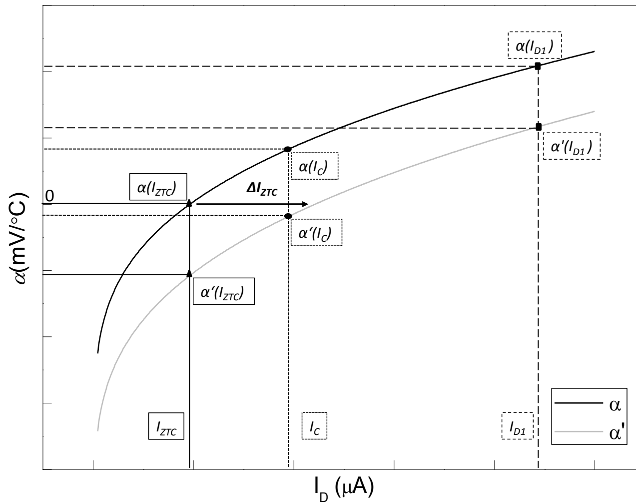

Figure 5.7 Thermal coefficients of the drain currents of interest with a ΔI_{ZTC}. The black line represents before the I_{ZTC} shift and grey line after.

Given an experimental $\alpha(I_D)$ curve, this is shifted in the horizontal axis an amount of ΔI_{ZTC}, obtaining the new thermal

coefficients in the vertical axis for I_C and I_{D1} which are the biasing currents during readout in the proposed two current method. In case of not to apply Eq. 10 and to consider the traditional biasing with a unique invariant I_{ZTC}, the new thermal coefficient will be given by $\alpha'(I_{ZTC})$ as indicated in the vertical axis of Figure 5.7. In the next section, these procedures will be carried out considering different I_{ZTC} shifts.

5.3.1 Experimental procedure

The samples used in this study were Al-gate p-channel MOS transistor manufactured by the Tyndall National Institute, with channel width and length of W =300 μm and L =50 µm, respectively. A total 20 individual RADFETs, four of each type, were analysed. It will be studied the I_{ZTC} shift of these RADFTEs due to similar causes than in space applications: integrated dose and thermal cycles. Therefore, to simulate this situation, it have been designed an experiment where RADFETs are first irradiated and next they are heated and cooled

As in the previous studies; all types were characterized in the unbiased single mode and with all the terminals short-circuited during radiation period. The linear accelerator Mevatrons KDS with transistors situated at the isocentre, at 100 cm from the source, with a normal beam incidence was the setting used. To control the stability of the accelerator, the PTW23332 ionization was selected. Sensor modules were irradiated with a dose of 2.05 Gy or 4.24 Gy for 400 nm and 1 μm and 10.48 Gy and 23.03 Gy for 100 nm and in each session, achieving a total accumulated dose around 55 Gy for 400 nm and 1 μm and 275 Gy for 100 nm RADFETs. A build-up of 1.5 cm was used over the

RADFETs to reach the electronic equilibrium. During the characterization and to minimize fading effects, voltage measurements were carried out ten minutes after irradiations. It has been used our readout system to perform the dosimetric measurements.

The thermal cycles were carried out after the last irradiation season as follows: RADFETs were heated in the climatic chamber from 10 to 80°C in steps of 10°C with a duration of this heating process of 14 hours, then they remained at 80°C during 12 hours; next they were cooled from 80 to 10°C again in steps of 10°C with the same duration of the heating process. I_{ZTC} were measured four times: i) before the first irradiation season, ii) after the set of irradiations, iii) during the heating cycle and, iv) during the cooling cycle. For all experimental data in this section, the calculated error represents the square propagation error of one standard deviation of the transistor sets and the experimental error.

The measurement of I_{ZTC} has been carried out only with temperatures between 10-50°C to avoid the possible influence of high temperatures during the calculations.

5.3.2 Experimental results

Thermal characterization

The different thermal studies for every RADFET type were carried out to calculate the I_{ZTC} after different process that could change the pre-irradiation value of this current. Figure 5.8 shows $\alpha(I_D)$ for pre-irradiated RADFETs. Fitting theses curves to the equation (5.11), I_{ZTC} was calculated as the value of I_D that makes $\alpha(I_D)=0$. Similar curves were found in the rest of the transistors.

In Figure 5.9 the experimental thermal coefficient $\alpha(I_D)$ are depicted for one RADFET with t_{OX} =1 μm. A negative curve shift is observed caused by the integrated dose of 55 Gy and positive shifts by the heating and the cooling cycles. In this case, the total shift was 104%. From this figure, the ΔI_{ZTC} is extracted as the relative difference in percentage of the curves to the initial pre-irradiated curve.

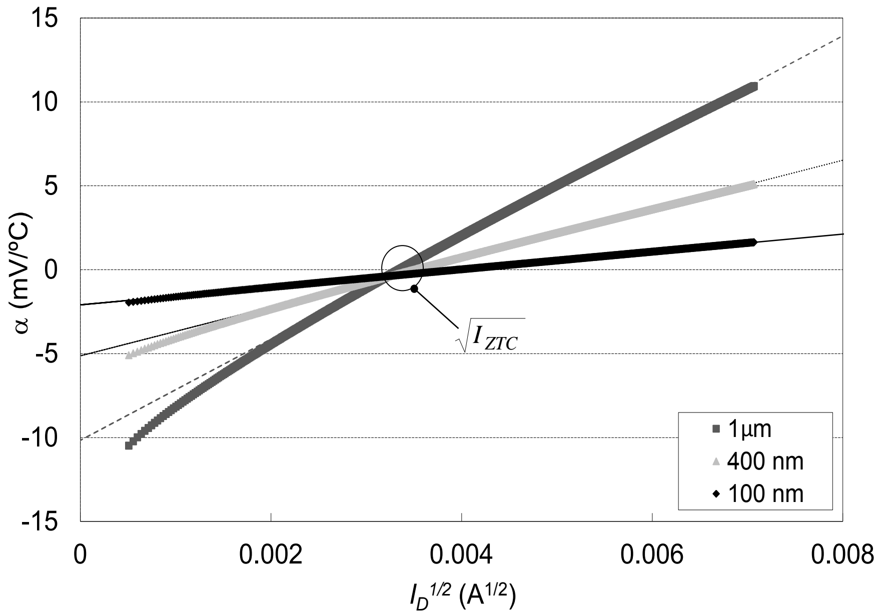

Figure 5.8 $\alpha(I_D)$ as function of $I_D^{1/2}$ for RADFETs with different t_{OX} . The sample of 400 nm is form the 400nm_W8 type. The dots represent experimental data and the thin black line is the theoretical model given by equation (5.11).

Table 5.3 summarizes I_{ZTC} and its shifts in percentage after irradiation and the two thermal cycles for each RADFET type. Uncertainties are given with a coverage factor k=1. Several facts can be extracted from Table 1:

i. Measured values of I_{ZTC} of pre-irradiated samples have very little scattering sample to sample inside each type and are in

very good agreement with previously obtained values (Haran et al. 2004, Benson et al. 2004, Jaksic et al. 2002).

ii. In accordance with previous works (Sarrabayouse and Siskos 2008, Holmes-Siedle et al. 2007) a I_{ZTC} shift is observed in irradiated RADFETS. A previous work also reported a similar I_{ZTC} shift for 400 nm and 500 nm gate oxide RADFETs irradiated in the unbiased mode as well (O'Sullivan et al. 1990). Moreover, a slight increase happens for the 100 nm RADFETs irradiated with 275 Gy and a decrease in the rest of types which were irradiated with 55 Gy.

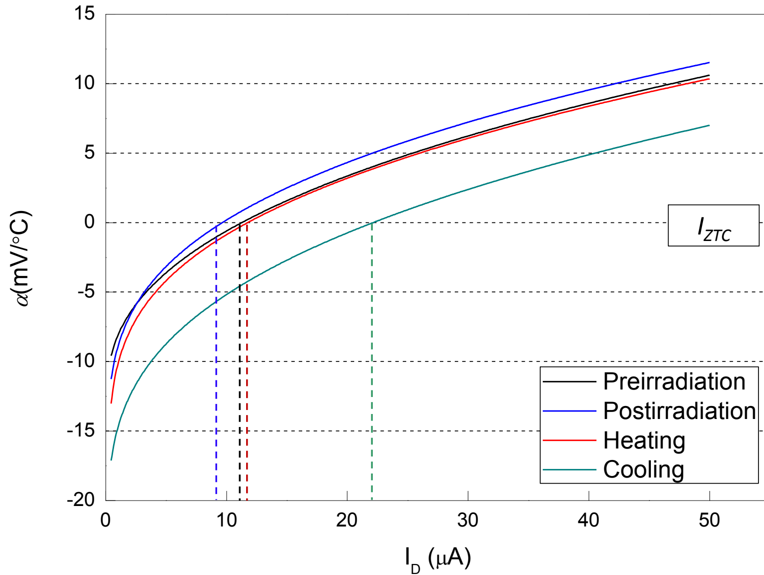

Figure 5.9 Experimental thermal coefficients as a function of I_D for a RADFET with t_{OX}=1 μm, showing the shifts due to irradiation and the thermal cycles. Uncertainties (with a coverage factor *k=1*) in mV/ºC are smaller than the size of symbol used.

iii. Positive I_{ZTC} shifts are always measured after each thermal cycle and for every RADFET type, observing a bigger shift in case of the thicker gate oxide. RADFET with a gate oxide of 1 μm is the most influenced by the temperature cycles, because

after finishing the second cycle, I_{ZTC} was almost doubled. On the other hand, the rest of type showed a similar behaviour with shifts around 25-30%.

iv. From these results, it is clear that, at least, after thermal cycles I_{ZTC} changes should not be neglected for the studied samples. Using these RADFETs as radiation dosimeters, if doses were extracted assuming a constant I_{ZTC}, without any other correction, it may induce a degradation of the measurement accuracy.

RADFET Type	**I_{ZTC} (μA)**	**ΔI_{ZTC} (%)**		
	Preirradiated samples	**Post-Irradiation**	**Heating cycle**	**Cooling cycle**
100nm_W8	16 ± 1	5 ± 9	32 ± 12	32 ± 13
400nm_W5	12.2 ± 0.3	-8 ± 3	10 ± 3	29 ± 3
400nm_W7	10.8 ± 0.1	-15 ± 7	5 ± 4	30 ± 1
400nm_W8	11.2 ± 0.3	-8 ± 4	0 ± 5	24 ± 3
1 μm	10.99 ± 0.09	-15 ± 6	5 ± 5	83 ± 15

Table 5.3 I_{ZTC} and its shift, ΔI_{ZTC}, in percentage for each RADFET type and size and. Uncertainties are given with a coverage factor k=1.

Comparison between readout methods

Once it has been shown that shifts I_{ZTC} can be significant, let's calculate the influence of this fact on the thermal drift of source voltage used as dosimetric parameter. To do that, it will be compared these thermal coefficients considering the two readout methods as described above. To apply the two current method (2CM), remembering the equation (5.18) the current I_C and I_1 must be selected to make minimal the influence of I_{ZTC}. Selecting I_C and I_1 much higher than the value of I_{ZTC} the impact of its possible fluctuations can be reduced. Considering a trade-off between this and avoiding high

currents which can modify the radiation-induced oxide charge, for these RADFETs the selected current values have been:

$$I_{D1} \simeq 20 \cdot I_{ZTC}$$
$$I_{D2} \simeq 4 \cdot I_{ZTC}$$

Table 5.4 shows thermal coefficients, α, obtained biasing with the pre-irradiated I_{ZTC} (designed as I_{ZTC} method) and the proposed two current method (biasing with I_C and I_{D1} during readout, 2CM) for a negative shift of -15% and two positive shifts of 25% and 65% of I_{ZTC} according to results of Table 5.3. Moreover, to translate these values to dose drifts, the dose coefficient per °C, δ, are also shown in Table 5.4. These values were calculated dividing the thermal coefficient by the sensitivity (mV/Gy) of every type calculated in a previous chapter, in section 4.4, The values of sensitivity used for every type were 180 mV/Gy for 1µm type, 1.50 mV/Gy for 100 nm, 60 mV/Gy, 67 mV/Gy and 46 mV/Gy in case of 400 nm_W5, 400 nm_W7 and 400 nm_W8 respectively. All sensitivities are calculated in 2.01 Gy, except in the case of 100 nm with a dose of 11.48 Gy.

From Table 5.4, several conclusions can be extracted:

i. As expected from the theoretical basis, the proposed 2CM provide a significantly lower thermal drift compared with the traditional I_{ZTC} method. In our study, this happens in all considered I_{ZTC} shifts and RADFET types.
ii. This thermal coefficient decrease goes from 33% (100 nm and +25% I_{ZTC}) to around 80% (400nm_W5 and -15% I_{ZTC}). Although remaining thermal coefficients are not still negligible, 2CM allows a remarkable improvement of the dose measurement accuracy in this kind of situations.

Type	Method	ΔI_{ZTC}					
		-15% I_{ZTC}		25% I_{ZTC}		65% I_{ZTC}	
		α (mV/ºC)	δ (cGy/ºC)	α (mV/ºC)	δ (cGy/ºC)	α (mV/ºC)	δ (cGy/ºC)
100 nm	I_{ZTC}	0.15 ± 0.11	10 ± 7	-0.3 ± 0.1	-18 ± 7	-0.8 ± 0.1	-57 ± 6
	2CM	0.07 ± 0.09	4 ± 6	-0.2 ± 0.1	-12 ± 7	-0.4 ± 0.1	-28 ± 6
400nm _W5	I_{ZTC}	0.39 ± 0.04	0.66 ± 0.07	-0.65 ± 0.05	-1.03 ± 0.08	-2.2 ± 0.1	-3.39 ± 0.11
	2CM	0.07 ± 0.17	0.12 ± 0.28	-0.38 ± 0.16	-0.6 ± 0.2	-1.03 ± 0.14	-1.69 ± 0.22
400nm _W7	I_{ZTC}	0.38 ± 0.04	0.58 ± 0.07	-0.64 ± 0.03	-0.96 ± 0.05	-2.11 ± 0.03	-3.17 ± 0.06
	2CM	0.1 ± 0.2	0.17 ± 0.37	-0.37 ± 0.18	-0.5 ± 0.3	-0.9 ± 0.1	-1.4 ± 0.2
400nm _W8	I_{ZTC}	0.35 ± 0.08	0.71 ± 0.17	-0.67 ± 0.06	-1.45 ± 0.14	-2.14 ± 0.07	-4.6 ± 0.2
	2CM	0.21 ± 0.15	0.4 ± 0.3	-0.4 ± 0.2	-0.8 ± 0.3	-0.99 ± 0.15	-2.1 ± 0.3
1um	I_{ZTC}	0.58 ± 0.05	0.32 ± 0.03	-1.56 ± 0.05	-0.86 ± 0.03	-4.63 ± 0.08	-2.58 ± 0.05
	2CM	0.21 ± 0.49	0.11 ± 0.27	-0.75 ± 0.21	-0.41 ± 0.11	-2.03 ± 0.20	-1.13 ± 0.11

Table 5.4 Linear thermal coefficients expressed in mV/ºC and cGy/ºC using two methods of dose readout for different I_{ZTC} shifts.

5.4 Application as temperature sensor

As consequence of this study the thermal model is applied to design a temperature sensor based on differential measurements of source-drain voltages in a pair of MOSFETs. The proposed transistor configuration has also been proposed for radiation measurement applications (Soubra et al. 1994, Thomson 1987).

Temperature dependence of semiconductor devices has been extensively studied, especially with the *p-n* junction (Szmyrka-Grzebyk and Lipiński 1993), bipolar transistors (Wang et al. 2012, Meijer 1986), and field-effect transistors (Sze 1981, Tsividis 1987). These works have also examined the use of these devices as temperature sensors. In fact, it is very desirable in different applications to include a temperature sensor in an integrated circuit, for example, for thermal protection, thermal compensation, or to maximize system performance (Altet et al. 2013, Aldrete-Vidrio et al. 2010). A *p-n* junction is commonly used for temperature sensing, with the forward diode voltage as the parameter measured to monitor temperature (Ocaya 2006, Ocaya 2013).

Today, CMOS (Complementary Metal-Oxide-Semiconductor) technology is the most widely used in fabrication technology of integrated circuits, with the possibility of manufacturing different types of temperature sensors. Different parameters can be used for temperature measurements, such as the delay in CMOS inverters (Poki et al. 2005) or the leakage current of a capacitor placed between two CMOS inverters (Ituero, Ayala and Lopez-Vallejo 2008). In addition, the thermal dependence of MOSFET electrical parameters has been used for temperature monitoring. For example, in a MOSFET configured as a diode (gate, bulk, and source grounded) and biased at constant current, the drain voltage exhibits a linear dependence with temperature (Souri et al. 2011). Another possibility to implement a temperature sensor in CMOS technology is to use the parasitic bipolar transistor that appears in the MOSFET fabrication process (Bakker and Huijsing 1996, Bianchi et al. 2000, Li, Weisheng and Youlin 2010). However, building a temperature sensor on a parasitic device might not be optimal because all the technological parameters may not always be properly characterized (Szekely et al. 1997). Therefore, a

temperature sensor that consists of a MOS transistor in weak inversion (Ueno, Asai and Amemiya 2011, Kölling et al. 1990, Sasaki, Ikeda and Asada 2008) or strong inversion (Poki et al. 2005, Sasaki et al. 2008) might be a more reliable way to obtain a well-controlled manufactured sensor. In the subthreshold region, the drain current and gate-source voltage of a MOSFET exhibit an exponential dependence, like bipolar transistors (Souri et al. 2011). However, at very low drain currents, the inaccuracy of the threshold voltage and carrier mobility can produce an imprecision of up to 3°C, as reported in (Ueno et al. 2011) for a range of 10–80°C. Therefore, a MOSFET used as a temperature sensor that operates at higher currents can improve resolution. In this regard, certain authors recently used a MOSFET biased in the saturation region as a temperature sensor that operates in the industrial temperature range with a linear error of around 7% (Reverter and Altet 2013).

5.4.1 Results

Once the thermal model has been verified and its range determined, it has been applied to achieve a temperature sensor based on MOSFETs. To measure V_X is easier than V_t as Figure 5.1 shows; in addition, the thermal coefficient of V_X can be known by using equation (5.11). Thus the source-drain voltage can be used as a signal proportional to temperature, V_{PT} (see Figure 5.5). Moreover, it can be possible to increase the sensor sensitivity to temperature by differential measurements of source-drain voltage, using two transistors. Figure 5.10 shows two possible temperature sensors, using a pair of transistors of the same type (two pMOS in this case) or using a complementary (p and n MOSFETs) pair.

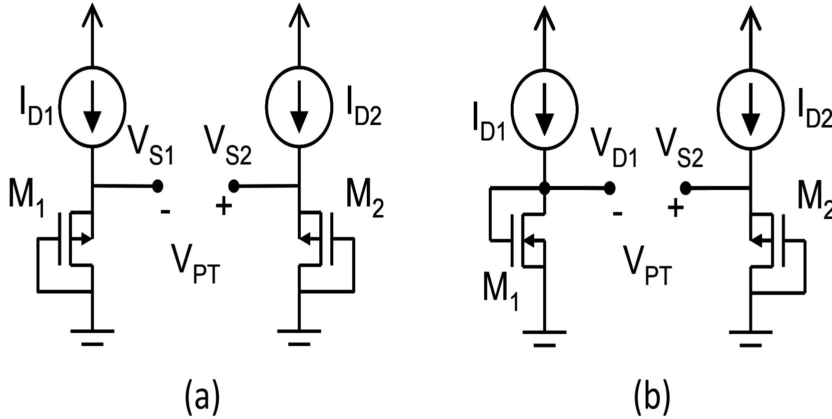

Figure 5.10 Temperature sensor schemas for differential measurements: a) Two pMOS b) Two complementary MOSFETs.

In this section, these two configurations have been analysed in order to achieve a total sensitivity (change of V_{PT} per degree Celsius) of around 5 mV/ºC , enough to obtain an resolution of 1°C in a 10-bit analog-to-digital conversion with an analog voltage range from 0 to 5V.

Therefore, let us consider the measurement of V_{S2}-V_{X1} for both configurations, whose thermal dependence is given by the linear coefficient,

$$\alpha_T = \alpha_{M2}(I_{D2}) - \alpha_{M1}(I_{D1}) \tag{5.20}$$

where the additional subscripts indicate the transistor M_1 or M_2. In order to maximize this thermal coefficient, the MOSFET position and the bias currents have to be carefully selected in the structures depicted in Figure 5.10. Thus, I_{D1} was selected as the lowest value below the I_{ZTC} of transistor M_1 ($I_{D1} < I_{ZTC,M1}$). The minimum value of $\alpha_{M1}(I_{D1})$ would be reached if I_{D1}=0 and then, according to (5.11), $\alpha_{M1}(I_{D1}=0)=-\alpha^{M1}{}_{|Vt|}$; however, the thermal model is not valid in the subthreshold region. Therefore, I_{D1} was selected to be equal to the minimum current of the valid range of the thermal model for transistor

M_1. In the same way, I_{D2} was selected to be higher than the I_{ZTC} of transistor M_2 ($I_{D2} > I_{ZTC,M2}$), and as high as possible taking into account the limit of the thermal model studied and the power consumption. If I_{D2} were $4I_{ZTC}$, then the thermal coefficient of α $(I_{D2}=4I_{ZTC,\,M2}) = \alpha^{M2}{}_{|Vt|}$, according to (5.11). Finally, with this selection of currents, the sensitivity will be

$$\alpha_T \approx \alpha_{|V_t|}^{M_2} + \alpha_{|V_t|}^{M_1} \qquad \textbf{(5.21)}$$

For transistor 3N163 I_{D2}=4$I_{ZTC,M2}$=976 μA, keeping power consumption low and reducing measurement error by self-heating. However, for 3N170, the drain current is I_{D2}=4$I_{ZTC,M2}$=8.04 mA, which is outside of the current range where the thermal model is valid. Therefore, in this case, transistor M_2 must be a 3N163. Transistor M_1 can be another 3N163 (dual pMOS temperature sensor) or a 3N170 (complementary pair temperature sensor). The configuration of dual pMOS transistors, Figure 5.10a, was studied with a 3N163 biased at I_{D1}=20 μA and I_{D2}=976 μA. The complementary pair configuration, Figure 5.10b, was tested with a 3N163 as M_2, biased at 976 μA, and 3N170 as M_1, biased at 200 μA. The values of the drain-source voltage were extracted from the I-V characteristic shown in Figure 5.4, and the thermal coefficient of the drain-source voltage was calculated as the slope of the linear fit, as described above.

The thermal coefficients of the source-drain voltages for the currents of 20 μA and 976 μA for the 3N163 and 200 μA for 3N170 are summarized in Table 5.5, where the error represents the standard deviation. The linearity errors, shown in Table 5.5, are calculated as the maximum distance from the experimental data to the linear fits and normalized to the full temperature range [-40°C, +85°C]. The predicted values are also displayed, using (5.11) and the averaged

thermal parameters given in Table 5.1. It can be observed that the theoretical and experimental values are both in agreement.

	I_D (μA)	Parameter	Experimental						Pre-dicted
			#1	#2	#3	#4	#5	Ave-rage	
3N163	20	$\alpha_{\lvert Vt\rvert}$ (mV/ºC)	-2.089	-1.99	-2.07	-2.11	-1.99	-2.05	-1.95
		$\Delta\alpha_{\lvert Vt\rvert}$ (mV/ºC)	0.017	0.02	0.02	0.02	0.02	0.06	0.04
		Linear error	2.7%	3.7%	3.3%	3.1%	3.1%	3.2%	--
	976	$\alpha_{\lvert Vt\rvert}$ (mV/ºC)	2.654	2.67	2.71	2.71	2.65	2.68	2.74
		$\Delta\alpha_{\lvert Vt}$ (mV/ºC)	0.036	0.04	0.04	0.04	0.03	0.05	0.10
		Linear error	4.6%	4.0%	4.3%	5.2%	3.6%	4.3%	--
3N170	200	$\alpha_{\lvert Vt\rvert}$(mV/ºC)	-2.760	-2.62	-2.66	-2.52	-2.62	-2.64	-2.55
		$\Delta\alpha_{\lvert Vt}$ (mV/ºC)	0.019	0.02	0.02	0.02	0.02	0.09	0.08
		Linear error	1.4%	1.2%	1.1%	1.1%	1.5%	1.2%	--

Table 5.5 Experimental and predicted sensitivity of the source-drain voltage of a MOS transistor biased at current of interest. Predicted values using the thermal model and the averaged thermal parameters values are given in Table 5.1.

The temperature coefficient of the 3N163 transistors at I_D=4$I_{ZTC,M2}$=976 μA is approximately equal to $\alpha_{|Vt|}$ of the value obtained by the methods described above and summarized in Table 5.1, as expected. On the other hand, the thermal coefficient of I_{D1}=20 μA is higher than -$\alpha_{|Vt|}$, and therefore the differential thermal coefficient is lower than 2$\alpha_{|Vt|}$. In the same way for 3N170, the thermal coefficient at 200 μA (Table 5.5) is lower than $\alpha_{|Vt|}$ (Table 5.1).

In order to experimentally test the two configurations of the temperature sensor, the transistors studied in the previous section were coupled in five pairs, both dual pMOS and complementary MOS configurations. The results and the transistors used for each configuration are summarized in Table 5.6. As an example, in Figure 5.11 the results of the pMOS transistor pair 3N163 1 and 2 and the complementary MOS pair 3N170 and 3N163 1, are plotted.

	Sensor configuration	$\alpha_{/Vt/}$ (mV/ºC)	$\Delta\alpha_{/Vt/}$ (mV/ºC)	Linear error (%)
Dual pMOS	**P#1 & P#2**	4.76	0.02	1.2
	P#2 & P#3	4.66	0.02	1.0
	P#3 & P#4	4.78	0.02	0.9
	P#4 & P#5	4.76	0.02	1.0
	P#5 & P#1	4.65	0.02	1.0
	Average	4.72	0.06	1.0
	Predicted by (5.11)	4.69	0.11	--
cMOS pair	**P#1 & N#1**	5.37	0.03	0.9
	P#2 & N#2	5.25	0.04	1.1
	P#3 & N#3	5.34	0.05	1.5
	P#4 & N#4	5.30	0.04	1.1
	P#5 & N#5	5.26	0.03	0.8
	Average	5.30	0.06	1.1
	Predicted by (5.11)	5.27	0.13	--

Table 5.6 Temperature coefficients of the differential source voltage and errors of the temperature sensors for the two proposed configurations.

The average temperature coefficient (change of V_{PT} per grade) for the 3N163 pair was 4.72±0.06 mV/°C; and 5.27±0.06 mV/°C, for the complementary pair of 3N170 and 3N163. Both experimental values fit the predicted values of the thermal model (see Table 5.6).

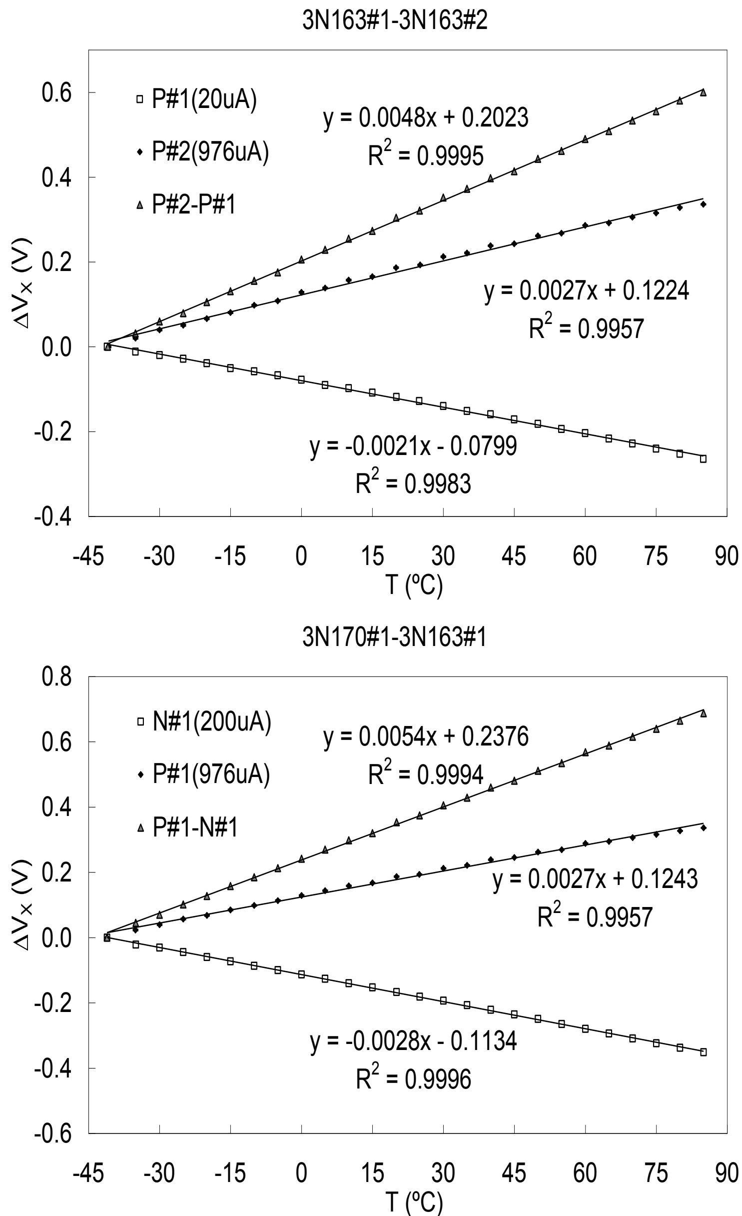

Figure 5.11 Source voltages at I_{D1}, I_{D2} and differential voltage, V_{PT}, as a function of temperature, for the dual pMOS (top figure) and the complementary MOS (bottom figure) sensor configurations.

Therefore, the thermal model can be used to design this type of temperature sensors. The linearity, quantified by the linear error of pairs of transistors, has been increased with respect to the single pMOS transistors and it is similar to the linearity provided by the single nMOS transistor. In addition, the temperature coefficient of the dual pMOS and complementary MOSFET sensors (Table 5.6) are twice the single transistor configuration (Table 5.5). As a result, the two MOSFET configurations improve the linearity and sensitivity of a single transistor. The linear error of both configurations was around 1.0% of the full temperature range, equivalent to 1.3°C.

6

Conclusions

The work here carried out consists of two main lines of research: the study of the response to ionizing radiation of pMOS transistors and the effects of temperature on them when they are used as dosimeters. Also additional results from this work have been obtained as the design of a MOSFET-based temperature sensor. The main conclusions of the work are written in this chapter.

6.1 Response to ionizing radiation

In this first study, the response of different commercial MOSFET transistors and RADFETs to photon and electron beams has been described, in order to check their capabilities as radiation sensors. Furthermore, a study of the degradation of the subthreshold swing has been carried out to evaluate its use as dosimetric parameter.

First of all a validation of dosimetric system was done, where it has been shown the good agreement between our readout system and a commercial semiconductor analyser. Once our system has been valid, a thermal study for every type was carried out. From this thermal study is concluded the lateral transistor 3N163, the integrated circuit CD4007 and for all types of RADFETs, a ZTC current was found.

However for the case of vertical transistor, I_{ZTC} was not found in the studied range.

For the MOSFETs with I_{ZTC}, the 3CM algorithm could be applied. The I_{ZTC} was not found in the DMOS transistors, thus the 2CM algorithm was used in order to enhance the linear range, and afterwards a numerically thermal compensation was applied.

6.1.1 Commercial transistors

Different techniques to increase the sensitivity of the commercial MOSFETs have been presented, to demonstrate their potential as dosimetry sensors to both electrons beams and gamma radiation. Different commercially available vertical and lateral pMOSs have been irradiated under normal incidence with 6 MV photon and electron beams. It has been checked single and two stacked transistor configurations in unbiased and biased modes during irradiation. As it has been expected, all cases the sensitivity increased when two transistors were stacked and for the biased mode. The objective was to select the best candidate and configuration for each kind of radiotherapy.

In case of gamma radiation the selected types were the lateral 3N163, the vertical ZVP3306 and a preliminary characterization with the CD4007. The conclusions of this study were:

1. All the analysed types transistors showed a linear performance with the received dose, with sensitivity range between 4.1 and 62 mV/Gy; depending on the pMOS type and the configuration.
2. With the MOSFETs 3N163 the improvement is almost lineal; the values of the sensitivity are higher than the ZVP3306 type.

3. Although the ZVP3306 has lowest dispersion, it is needed a thermal characterization in depth to find an algorithm that permit to compensate the dose measurement not only with a linear coefficient.
4. The fading results of the biased 3N163 indicate that, after 270 s, V_t has not yet stabilized. As it was expected, the fading with bias is higher than in the case of unbiased mode. A shift of threshold voltage between -16 mV to -30 mV, with 5 V and 10 V respectively was found, using 6 mints as elapsed time.
5. Finally the optimal configuration for gamma radiation was the two stacked biased mode for the 3N163 transistor, with the higher sensitivity of 62±3 mV/Gy, almost comparable to the sensitivity of a RADFET.
6. A preliminary characterization for the integrated circuit CD4007 was done to check their reliability as dosimetry sensor face to be used with electron beams because their nonmetallic encapsulation.

For electron beams, also the response of several pMOS transistors in different configurations was tested; CD4007 and three types of DMOS transistor: ZVP3306, ZVP4525 and BS250. For this type of beam, also energy typically used in IORT has been characterized. The main conclusions can be summarized as follows:

1. High linear response and low dispersion have been found in all the cases analysed with sensitivities in the range between 3 and 13 mV/Gy depending on the pMOS and the configuration. The linearity and uncertainty achieved are comparable to commercial RADFETs although the sensitivity is lower than the radiation sensitive transistors.

2. As expected, in all cases the sensitivity increased when two transistors were stacked and for the biased mode.
3. Analysed vertical pMOS (BS250F, ZVP3306 and ZVP4525) did not show zero temperature regions in their *I*-*V* curves, therefore thermal compensation algorithms were not able to be applied. This prevents to use this kind of pMOSs as reliable radiation sensors without an *in situ* temperature monitoring.
4. The fading results for the more promising DMOS show the transistor is established around 200 s, with a maximum threshold voltage shift of -6 mV, for a bias of 10 V. The case of the integrated circuits shows a variation of threshold voltage between -1 and 1.6 mV.
5. CD4007 shows a promising behaviour as radiation sensor for electron beams (with doses around 20 Gy), having a maximum sensitivity of 12.7 mV/Gy with two stacked transistors and biased with 0.6 V during irradiation.

With the correct electronic amplification and filtering and using the techniques describe in this thesis, these transistors in biased mode can be used *in vivo* dosimetry for clinical control in radiotherapy, extending control in radiotherapy treatments and increasing the safety of the patient.

Subthreshold swing

It has been carried out the study of the subthreshold swing shift, *S*, of a commercial MOSFET as a dosimetric parameter in the same manner as is usually done for the threshold voltage.

The results show it to be a reliable parameter based on the analysis of the linearity, sensitivity, reproducibility compared with the threshold voltage shift under gamma rays from a ^{60}Co source up to 56

Gy, typical in radiotherapy treatments. The linear behaviour of S with temperature is also very helpful for easy modelling and the required compensation of the temperature influence. One weak point from the point of view of the practical implementation is the greater difficulty in measuring S, requiring at least two currents in the subthreshold current region and the additional polarization of drain. Another weak point is the higher scattering of individual sensitivities but this is likely not a significant drawback due to the required individual calibration of sensors as in the case of the threshold voltage shift. This electrical magnitude could be measured to provide data complementary to the threshold voltage shift, providing enhanced reliability for the dose verification of radiotherapy treatments. Taking into account the current capability of electronics for signal processing, it would be possible to design a reader unit that implements the measurement of both dosimetric parameters. Data from the two electrical magnitudes would provide more robust results of the delivered dose, which would enhance the confidence of dose verification systems based on MOSFETs.

6.1.2 RADFETs transistors

A comparative study of RADFET transistors response to photon and electron beams has been carried out in reference conditions. Both types of beams have been applied to RADFETs of several gate oxide thicknesses, sizes and technological processes manufactured by Tyndall National Institute (Cork, Ireland). The 3CM, does not improve the response in linearity and reproducibility for these models. As it has been mentioned, this is due to the 3CM improve the linearity, taking into account $\Delta\beta$. In RADFETs ΔV_t is mainly caused by the oxide traps. As this type of transistors has a thick oxide the effect of oxide traps hide the possible improvement over the interface traps, so only

the thermal compensation could be solved, therefore, finally for simplicity, it has been decided to use the method of constant current $I_{ZTC.}$

Experimental results demonstrate that the response of RADFETs in electron beams (sensitivity, linearity and short-term fading) is very similar, within experimental uncertainty, to photon beams in reference conditions (electronic equilibrium in the sensing volume). Influence of the temperature has been minimized by biasing RADFETs at zero temperature coefficient drain current during readout process.

The short-term fading results have shown that it can be neglected in case of t_{OX} =100 nm and 400 nm for both radiation beams, showing a threshold voltage drift always below 1% after 360 s. However, in case of 1 μm the influence of fading is important and decreasing when the accumulate dose increases. Similarly to the commercial transistors, there are two competing effects, the density of oxide trapped charge decreases monotonically after irradiation by annealing; while the density of interface traps exhibits the initial increase. As it has been discussed, when the device has an concrete accumulated dose the induced positive charge by interface state build-up become comparable and even higher than the annealing of oxide traps and the fading show negative values (Price et al. 2004a, Jaksic et al. 2002, Ristic et al. 1996).

The general behaviour has been shown for devices fabricated with several gate oxide thicknesses, sizes and technological processes. Therefore, it can be concluded that RADFETs manufactured by Tyndall National Institute are well suitable for dosimetry when electron beams are used. Moreover, this similarity of the experimental results makes us consider that most of the conclusions from previous

research to characterize these devices in photon beams could be valid in electron beams, within the limits of our study. Therefore analysed RADFETs can be suitable to be used for dose verification in radiation therapies where electron beams are used such as intra-operative radiotherapy (IORT).

6.2 Effects of temperature on MOSFET as dosimeter

A model of the effects of the temperature on MOSFETs when they are used as dosimeters is presented. Firstly, a compact and empirical model of the temperature performance of MOS transistors has been described, justified, and experimentally tested with commercially available types of pMOS (3N163) and nMOS (3N170) transistors. The validation of the model was done, with data fit the theoretical model in different current ranges, depending on the transistor: from 15 to 700 μA for 3N163, and from 0.2 to 5 mA for 3N170. In these current ranges, the thermal coefficient of the source-drain voltage can be predicted with a good agreement with the experimental results. Therefore, the drain current can be calculated in order to obtain the desired thermal coefficient for different purposes, for example for thermal compensation or for designing a temperature sensor.

Afterward, a method based on this thermal model and biasing a MOSFET with two drain currents during readout is shown. This method provides a significant reduction of the linear temperature coefficient of the source voltage compared to biasing with the pre-irradiated I_{ZCT} when a shift of this magnitude occurs due to the integrated dose and thermal cycles. This one MOSFET procedure can

be an alternative to the measurement with two MOSFETs. The proposed method has been tested with five types of RADFETs with three different gate oxide thicknesses, showing very good results. Compared with the traditional biasing at I_{ZCT}, thermal coefficients decrease goes from 33% (100 nm and +25% I_{ZTC}) to around 80% (400nm_W5 and -15% I_{ZTC}). Although remaining thermal coefficients of the source voltage are not still negligible, 2CM allows a remarkable improvement of the dose measurement accuracy in this kind of situations

As a result of the thermal study, the application of a temperature sensor was carried out. It has been developed a thermometer based on MOSFETs in the saturation region, two configurations have been proposed: one using two pMOS transistors, and another configuration using two complementary MOSFETs. Using the latter configuration, a mean sensitivity of 5.27 mV/°C was achieved, with a linearity error of 1.1% in the industrial temperature range (from -40 to +85°C).

6.3 Scientific Contributions

6.3.1 Journal papers

- Banqueri J., Carvajal M., Martínez-García M. S., Morales D.P., Palma A.J. (2012). *Study of the subthreshold swing of a pMOSFET as dosimetric parameter.* Sensor & Actuators: A. Physical 187, 16-21.

- Martínez-Martí F., Martínez-García M.S., García-Díaz S.G., García-Jiménez S. G., Palma A.J., Carvajal M.A. (2013)

Embedded sensor insole for wireless measurement of gait parameters. Journal of Australasian Physical & Engineering Sciences in Medicine 37, 1-11.

- Martínez-García M.S., Simancas F., Palma A.J., Lallena A.M., Banqueri J., Carvajal M.A. (2014) *General purpose MOSFETs for the dosimetry of electron beams used in intra-operative radiotherapy.* Sensors and Actuators A: Physical 210, 175-181.

- Carvajal M. A., Martínez-García M.S., Martínez-Olmos A., Banqueri J., Palma A.J. (2014). *A simplified thermal model for lateral MOSFET and its application to temperature monitoring.* Semiconductor Science Technology, 210, 175-181.

6.3.2 Journal papers submission

- Martínez-García M.S., Torres del Río J., Palma A.J., Lallena A.M., Jaksic A., Carvajal M.A. (September 2014). *Comparative study of MOSFET response to photon and electron beams in reference conditions.* Sensors and Actuators A: Physical.

- Martínez-García M.S., Palma A.J., Lallena M., Jaksic A., Banqueri J., Carvajal M.A. (September 2014) Method to accuracy improvement of MOSFET dosimeters in case of thermal parameters variation. *IEEE Transaction on Nuclear Science.*

6.3.3 International Conferences

- Banqueri J., Carvajal M.A., Vilches M., Guirado D., Martínez-García M.S., Lallena A.M., Palma A.J. *An alternative measurement method for MOSFET dosimeters.* The First International Conference on Radiation and Dosimetry in various fields of research (RAD2012), April, 2012. Nis, Serbia.

- Carvajal M.A., Guirado D., Banqueri J., Vilches M., Martínez-García M.S., Lallena A.M., Palma A.J. *Evaluation of DMOS transistor as electron beams dosimeter.* The First International Conference on Radiation and Dosimetry in various fields of research (RAD2012), April, 2012. Nis, Serbia.

- Banqueri J Carvajal M.A., Martínez-García M.S., Palma A.J. Vilches M., Lallena A.M. *Subthreshold response of a MOSFET to radiation effect.* 9th Spanish Conference of Electron Device (CDE2013), February 2013.Valladolid, Spain.

- Martínez-Martí F.,García-Díaz S.G., García-Jiménez J., Martínez-García M.S., Martínez-Olmos A., Carvajal M.A. *Instrumented Insoles with Pressure and Acceleration Sensors.* International Work-Conference on Bioinformatics and Biomedical Engineering (IWBBIO 2013). March 2013. Granada, Spain.

- Martínez-García M.S., Carvajal M.A., Simancas F., Banqueri J., Lallena A.M., Palma A.J. *Techniques to increase the sensitivity for dosimetry sensors.* International Work-

Conference on Bioinformatics and Biomedical Engineering (IWBBIO 2013). March, 2013. Granada, Spain.

- Martínez-García M.S., Simancas F., Guirado D., Lallena A., Banqueri J.,Palma A.J., Carvajal M.A. *Commercial pMOS as reliable radiation sensor.* International Conference on Biotechnology, Bioengineering and Nanoengineering (ICBBN2013). November, 2014. Málaga, Spain.

- Martínez-García M.S., Torres Del Río J., Palma A.J., Jaksic A., Banqueri J., Carvajal M. A. *Multiple current applied to characterization of RADFETs.* The First Int. Conf on Radiation and Dosimetry in various fields of research (RAD2014), Mayo, 2014. Nis, Serbia.

- Martínez-García M.S., Simancas F., Palma A.J., Lallena M., Banqueri J., Carvajal M.A.. *Commercial pMOS as Radiation Sensor for IORT.* The First Int. Conf on Radiation and Dosimetry in various fields of research (RAD2014). Mayo, 2014. Nis, Serbia.

- Martínez-García M.S., Torres del Río J.., Lallena M., Jaksic A., Palma A.J., Carvajal M.A. *Commercial MOSFETs and RADFETs electrical and dosimetric characterization.* Micro-mini & nano dosimetry and prostate cancer treatment workshop (MMND-IPCT2014). October, 2014. Port Douglas, Queensland, Australia.

7

Conclusiones

El trabajo llevado a cabo está orientado en dos líneas de investigación: el estudio de la respuesta de transistores pMOS a la radiación ionizante y los efectos de la temperatura sobre ellos cuando son usados como dosímetros. Además han sido obtenidos resultados adicionales derivados de este trabajo, como el diseño de un sensor de temperatura basado en MOSFET. Las principales conclusiones de esta tesis son escritas en este capítulo.

7.1 Respuesta a la radiación ionizante

En el primer estudio es descrita la respuesta de diferentes transistores comerciales y RADFETs con haces de electrones y fotones, para comprobar sus capacidades como sensores de radiación. Además, ha sido llevado a cabo un estudio de la degradación de la pendiente subumbral, para evaluar su uso como parámetro dosimétrico.

En primer lugar fue hecha la validación del sistema dosimétrico, donde se ha observado concordancia entre el sistema de medida de la UGR y un analizador de semiconductores comercial. Una vez que la validación del sistema ha sido realizada, se hizo un estudio térmico de cada tipo de transistor. De este estudio se concluye que se ha

encontrado I_{ZTC} para el transistor lateral 3N163, el circuito integrado CD4007 y todos los tipos de RADFETs, Sin embargo en el caso de los transistores verticales, no se encontró I_{ZTC} en el rango de corriente estudiado.

Para los MOSFET, donde la I_{ZTC} fue hallada, se aplicó el algoritmo de 3CM. En los transistores DMOS; se utilizó el algoritmo 2CM con compensación térmica adicional.

7.1.1 Transistores comerciales

Han sido presentadas, diferentes técnicas para incrementar la sensibilidad de transistores comerciales MOFETs, para demostrar su potencial como sensores dosimétricos tanto para fotones como para electrones. Para ello, se han probado diferentes pMOS comerciales, disponibles en el mercado, con geometría tanto vertical como lateral. La caracterización se ha realizado con una energía de 6 MV con incidencia normal tanto para fotones como para electrones. Las configuraciones probadas han sido simples y dobles estacadas, con y sin polarización. Como era de esperar, en todos los casos estacados y polarizados la sensibilidad ha aumentado. El objetivo era seleccionar la mejor configuración posible y el tipo de transistor para cada clase de radioterapia.

Para la radiación gamma, varios tipos de MOSFETs han sido seleccionados: el transistor lateral 3N163, el vertical ZVP3306 y se realizó una caracterización preliminar del CD4007. Las conclusiones de este primer estudio se exponen a continuación:

1. Todos los transistores analizados muestran un comportamiento lineal con la dosis recibida, y tienen un rango de sensibilidad

entre 4.1 y 62 mV/Gy; dependiendo de la configuración y el tipo de transistor.

2. La mejora del MOSFET 3N163 es prácticamente lineal; además sus valores de sensibilidad son mayores que en el caso del transistor ZVP3306.
3. Aunque el tipo ZVP3306 tiene baja dispersión, es necesaria una caracterización térmica en profundidad para encontrar un algoritmo que permita compensar las medidas de la dosis, no solo con el coeficiente lineal.
4. Los resultados del fading del transistor 3N163 polarizado indican que, después de 270 segundos, V_t no se ha estabilizado. Como era de esperar el fading de la configuración polarizada es mayor que en el caso sin polarizar. El desfase de la tensión umbral varía de -16 a -30 mV, con polarizaciones de 5 y 10 V respectivamente.
5. Finalmente, la mejor configuración propuesta para haces de fotones fue la doble polarizada con el transistor 3N163, con la mayor sensibilidad obtenida de 62±3 mV/Gy, valor casi comparable con la sensibilidad de un transistor RADFET.
6. Se realizó además, una caracterización preliminar con fotones para el circuito integrado CD4007, para comprobar su viabilidad como sensor dosimétrico, de cara a ser utilizado posteriormente con haces de electrones, ya que tiene un encapsulado no metálico.

Para haces de electrones se realizó un estudio similar. Los transistores candidatos fueron: CD4007 y tres tipos de transistores DMOS; ZVP3306, ZVP4525 y BS250. En este tipo de haz, también energías típicas de RIO (Radioterapia Intraoperatoria) fueron estudiadas. Las principales conclusiones son:

1. Todos los tipos de transistores han mostrado alta linealidad y baja dispersión; con sensibilidades en el rango entre 3 y 13 mV/Gy en función de la configuración y el transistor utilizado. En este caso la linealidad y la incertidumbre son comparables a transistores RADFETs comerciales, sin embargo la sensibilidad es menor.
2. Como era de esperar, en todos los tipos de transistores la sensibilidad ha mejorado con la configuración doble y polarizada.
3. Los transistores verticales (BS250F, ZVP3306 y ZVP4525) no mostraron I_{ZTC} en sus curvas *I-V*, por los tanto, los algoritmos de compensación térmica no pudieron ser aplicados. Este hecho hace que estos transistores no sean adecuados como sensores de radiación sin usar una compensación de temperatura *in situ*.
4. Los resultados de fading, para el más prometedor de los transistores DMOS, el ZVP3306, muestra que se establece tras unos 200 s, con un máximo desfase de la tensión umbral de -6 mV, para la polarización de 10 V. En el caso del circuito integrado CD4007, se muestra una variación de la tensión umbral entre -1 y 1.6 mV.
5. El CD4007 muestra un prometedor comportamiento como sensor de radiación para haces de electrones. Para dosis alrededor de 20 Gy, muestra una sensibilidad de 12.7 mV/Gy con dos transistores apilados y una polarización de 0.6 V durante la irradiación.

Utilizando una adecuada amplificación y filtrado, y con el uso de las técnicas descritas en esta tesis, estos tipos de transistores en modo polarizado pueden ser usados en dosimetría in vivo para control clínico de radioterapia, aumentando el control y la seguridad del paciente.

Pendiente subumbral

Se ha realizado, el estudio del incremento de la pendiente subumbral, *S*, de un transistor comercial MOSFET para ser propuesto como parámetro dosimétrico. El estudio se ha realizado de la misma forma en la que normalmente se analiza la tensión umbral.

Los resultados muestran que es un parámetro fiable, basado en el análisis de su linealidad, su sensibilidad y su reproducibilidad comparada con el incremento de la tensión umbral producida por rayos gamma. Dicha energía, proviene de una fuente de ^{60}Co. Se realizó hasta una dosis acumulada de 56 Gy, que es un rango típico en los tratamientos de radioterapia. El comportamiento lineal del parámetro, *S*, con la temperatura es muy útil para un fácil modelado y llevar a cabo la compensación térmica debido a la influencia de la temperatura. Un punto débil desde el punto de vista de la implementación práctica es la gran dificultad en la medida de *S*; ya que se requiere al menos dos corrientes en región subumbral junto con la correspondiente polarización. Otro inconveniente sería la elevada dispersión de las sensibilidades individuales; sin embargo no es un problema importante debido a que se requiere la calibración individual de los sensores, de la misma forma que en el caso del incremento de la tensión umbral. Esta magnitud eléctrica podría ser medida para proporcionar una información complementaria al ΔV_t, aumentando la fiabilidad en la verificación de la dosis de los tratamientos de radioterapia.

Teniendo en cuenta las limitaciones de producir pequeñas corrientes en electrónica; sería posible diseñar una unidad lectora que implemente la medida de ambos parámetros dosimétricos. Si los datos provienen de dos magnitudes eléctricas, los resultados proporcionados

de las dosis repartidas, son más robustos, y se aumentaría la seguridad en la verificación de los sistemas basados en MOSFET.

7.1.2 Transistores RADFETs

Además se ha realizado un estudio comparativo de la respuesta de transistores RADFETs para ambos tipos de haces bajo condiciones de referencia. Ambas energías, han sido aplicadas a RADFETs de varios espesores de óxido de puerta, tamaño y diferentes procesos tecnológicos fabricados por el Instituto Nacional Tyndall, (Cork, Irlanda). Para estos modelos el algoritmo de 3CM no mejora la respuesta de los transistores en linealidad y reproducibilidad. Como se ha explicado anteriormente, esto es debido a que dicha mejora se obtiene teniendo en cuenta el incremento de $\Delta\beta$. En los RADFET, el incremento de la tensión umbral ΔV_t es principalmente causado por las trampas en el óxido de puerta. Esto es debido al grueso espesor de óxido, que hace las trampas en el óxido enmascare la posible mejora sobre las trampas de interfase con el 3CM. Por tanto, finalmente por simplicidad, se decidió usar el método de polarización a corriente constante I_{ZTC}.

Los resultados experimentales demuestran que la respuesta de los RADFETs para haces de electrones (sensibilidad, linealidad y fading a corto plazo) es muy similar, dentro de la incertidumbre experimental, a la de haces de fotones en condiciones de referencia (equilibrio electrónico en el volumen sensible). La influencia de la temperatura ha sido minimizada polarizando los RADFETs en su I_{ZTC} durante el proceso de lectura.

Los resultados del fading a corto plazo han mostrado que se puede considerar despreciable en los casos de t_{OX} =100 nm y 400nm para ambos tipos de energías, mostrando una deriva del voltaje

subumbral por debajo del 1%, tras 360 s. Sin embargo, para el caso de 1 μm la influencia del fading es importante, y disminuye conforme aumenta la dosis acumulada. De forma equivalente a como ocurre con los transistores comerciales, hay dos efectos competitivos, la densidad de cargas atrapadas en el óxido que disminuye monótonamente después de la irradiación mediante recuperación a temperatura ambiente; mientras la densidad de cargas de interfase exhibe un crecimiento inicial. Como ha sido previamente discutido, cuando el dispositivo tiene una concreta dosis acumulada las cargas positivas inducidas por los estados de interfase llegan a ser comparables e incluso mayores que las cargas en el óxido y por ello el fading muestra valores negativos (Price et al. 2004a, Jaksic et al. 2002, Ristic et al. 1996).

Por tanto, se ha expuesto que el comportamiento de los dispositivos fabricados con varios espesores de óxido, tamaño y procesos de fabricación con diferentes tipos de haces. Por lo tanto, puede ser concluido que los RADFETs fabricados por el Instituyo Nacional Tyndall son válidos para dosimetría con electrones. Además, la similitud con fotones de los resultados experimentales hace posible considerar que la mayoría de las conclusiones de trabajos previos de investigación para caracterizar estos dispositivos con fotones, puede ser extendidas para haces de electrones, dentro de los límites del estudio. Así, los RADFETs analizados son válidos para ser usados como verificación de la dosis en técnicas de radioterapia, donde se usen electrones como por ejemplo RIO.

7.2 Efectos de la temperatura en MOSFET como dosímetros

En este capítulo, es presentado un modelo de los efectos de la temperatura en transistores MOSFET, cuando ellos son usados como dosímetros. En primer lugar, ha sido expuesto, un modelo empírico y compacto de la influencia de la temperatura en el transistor MOS. Además ha sido justificado y probado experimentalmente con transistores comerciales disponibles en el mercado: un pMOS (3N163) y un nMOS (3N170). Después, se ha realizado la validación del modelo, mostrando el ajuste de los datos experimentales al modelo teórico en diferentes rangos de temperatura, que varían dependiendo del tipo de transistor: desde 15 a 700 μA para el 3N163, y desde 0.2 a 5 mA para el 3N170. En estos rangos de corriente, el coeficiente térmico del voltaje fuente-drenador podría ser predicho con una buena precisión con los resultados experimentales. Por lo tanto, la corriente de drenador puede ser calculada para obtener el coeficiente térmico deseado en función del propósito, por ejemplo para compensación térmica o para diseño de un sensor de temperatura.

A continuación, se ha expuesto un método basado en este modelo térmico y en la polarización de un MOSFET con dos corrientes durante la lectura. Este método presenta una importante mejora en el coeficiente lineal de voltaje de fuente con la temperatura en comparación a polarizar con valor de la I_{ZCT} previo a la irradiación, debido a que este valor sufre un desfase debido a la dosis acumulada y a ciclos térmicos. Este proceso puede ser alternativo a la medida con dos MOSFET. El método propuesto ha sido probado con cinco tipos de RADFETs con tres espesores de óxido de puerta, mostrando muy buenos resultados. Comparando en el tradicional método de

polarización con la I_{ZCT}, la disminución del valor de los coeficientes va desde el 33% (100 nm y +25% I_{ZTC}) hasta alrededor del 80% (400nm_W5 y -15% I_{ZTC}). Aunque los coeficientes térmicos de voltaje de fuente obtenidos no son despreciables, 2CM permite una importante mejora de la precisión en la medida de la dosis en este tipo de situaciones.

Como resultado del estudio térmico, se ha llevado a cabo la aplicación de un sensor de temperatura. Se ha desarrollado un termómetro basado en MOSFET trabajando en la región de saturación. Se han propuesto dos configuraciones: usando dos transistores pMOS, y otra usando dos transistores MOSET complementarios. Con esta última configuración, se ha conseguido una sensibilidad media de 5.27 mV/°C, con un error de linealidad del 1.1% en el típico rango de temperatura usado en el ámbito industrial (desde -40 hasta +85°C).

Bibliography

Agilent, T. (2014). Agilent B1500A Semiconductor Device Analyzer-Self pace Training Manual. Insitution. (Report).

Aldrete-Vidrio, E., D. Mateo, J. Altet, M. A. Salhi, S. Grauby, S. Dilhaire, M. Onabajo & J. Silva-Martinez (2010) Strategies for built-in characterization testing and performance monitoring of analog RF circuits with temperature measurements. *Meas. Sci. Technol.,* 21**,** 1-10.

Altet, J., D. Gomez, X. Perpinyà, D. Mateo, J. L. González, M. Vellvehi & X. Jordà (2013) Efficiency determination of RF linear power amplifiers by steady-state temperature monitoring using built-in sensors. *Sens. Actuator A-Phys.,* 192**,** 49-57.

Amin, N. M., R. Heaton, B. Norrlinger & M. K. Islam (2011) Small field electron beam dosimetry using MOSFET detector. *J. Appl. Clin. Med. Phys,* 12**,** 50-57.

Angelov, I., L. Bengtsson & M. Garcia (1996) Extensions of the Chalmers nonlinear HEMT and MESFET model. *IEEE Trans. Microw. Theory Techn.,* 44**,** 1664-1674.

Aristu, J., F. Calvo, R. Martínez, J. Dubois, M. Santos, S. Fisher & I. Azinovic (1999) Lung cancer. *Intraoperative irradiation. Techniques and results***,** 437-53.

Asensio, L. J., M. A. Carvajal, J. A. López-Villanueva, M. Vilches, A. M. Lallena & A. J. Palma (2006) Evaluation of a low-cost comercial mosfet as radiation dosimeter. *Sens. Actuator A-Phys.,* 125**,** 288-295.

Asensio, L. J., M. A. Carvajal & A. J. Palma López Dosimetric method and system. (2008) WO-2008123091A1. (Patent)

Babcock, J. A., J. L. Titus, R. D. Schrimpf & K. F. Galloway (1991) Effects of Ionizing Radiation on the Noise Properties of DMOS Power Transistors. *IEEE Trans. Nucl. Sci.,* 38.

Bakker, A. & J. H. Huijsing (1996) Micropower CMOS temperature sensor with digital output. *IEEE J. of Solid-State Circuits,* 31, 933-937.

Banqueri, J. (1994). Estudio experimental de la movilidad efectiva de los electrones en transistores metal-oxido-semiconductor. *Electrónica y Tecnología de Computadores.* Universidad de Granada. Granada. (PhD. Thesis)

Banqueri, J., M. A. Carvajal, M. S. Martínez-García, D. P. Morales & A. J. Palma (2012) Study of the subthreshold swing of a pMOSFET as a dosimetric parameter. *Sens. Actuator A-Phys.,* 187, 16-21.

Banqueri, J., F. Gamiz, J. E. Carceller, P. Cartujo & J. A. Lopez-Villanueva (1993) Influence of the inerface-state density on the electron mobility in silicon inversion layers. *J. Electron. Mater.,* 22, 1519-1164.

Benedetto, J. M. & H. E. Boesch (1986) The Relationship between ^{60}Co and 10keV X-Ray Damage in MOS Devices. *IEEE Trans. Nucl. Sci.,* 33, 1318-1323.

Benson, C., A. Albadri, M. J. Joyce & R. A. Price (2006) The empirical dependence of radiatiation-induced charge neutralization on negative bias in dosimeters based on the metal-oxide-semiconductor fild-effect transistor. *J. Appl. Phys.,* 100, 044505-5-044505-6.

Benson, C., R. A. Price, J. Silvie, A. Jaksic & M. J. Joyce (2004) Radiation-induced statistical uncertainty in the threshold voltage measurement of MOSFET dosimeters. *Phys. Med. Biol.,* 49, 3145-3159.

Best, S., A. Ralson & N. Suchowerska (2005) Clinical Application One Dose^{TM} patient dosimetry system for total body irradiation. *Phys. Med. Biol.,* 50, 5909-19.

Bianchi, R. A., J. M. Karam, B. Courtois, R. Nadal, F. Pressecq & S. Sifflet (2000) CMOS-compatible temperature sensor with digital output for wide temperature range applications. *Microelectr. J.,* 31, 803-810.

Black, R. OneDose. Disposable Single -Use External Dosimeters for use in Radiation Therapies. (2003) WO 03/047694 A2. (Patent)

Black, R. D., G. G. Mann, S. R. Widener, P. M. Lehman & J. Carrall Disaposable single-use internal dosimeters for detecting radiation in medical procedures/therapies. (2005) US-2005/0010110A1. (Patent)

Bloemen-van Gurp, E., A. W. H. Minken, B. J. Mijnheer, C. J. G. Dehing-Obergye & P. Lambin (2006) Clinical implementation of MOSFET detectors for dosimetry in electron beams. *Radiother. Oncol.,* 80**,** 288-295.

Boesch, H. E., F. B. McLean, J. M. Benedetto, J. M. McGarrity & W. E. Bailey (1986) Saturation of Threshold Voltage Shift in MOSFET's at High Total Dose. *IEEE Trans. Nucl. Sci.,* 33**,** 1191-1197.

Brady, L. W., A. M. Markone, B. Micaily, S. Fisher & F. Lamm (1990) Innovative Techniques in Radiation Oncology. *Clinical Research Programs to Improve Local and Regional Control in Cancer,* 65.

BS250F. Diodes Incorporated. (Datasheet)

Buehler, M. G., B. R. Blaes, G. A. Soli & G. R. Tardio (1993) On-Chip p-MOSFET Dosimetry. *IEEE Trans. Nucl. Sci.,* 40**,** 1442-1449.

Canada, B. M. (2014). MOSFET Dosimetry . (Best Medical Canada). 5/8/2014. http://www.mosfet.ca/. (Web Page)

Carvajal, M. A. (2008). Diseño de un sistema dosimétrico portatil. *Electrónica y Tecnología de Computadores.* Universidad de Granada. Granada. (PhD. Thesis)

Carvajal, M. A., S. García-Pareja, D. Guirado, M. Vilches, M. Anguiano, A. J. Palma & A. M. Lallena (2009) Monte Carlo simulation using the PENELOPE code with an ant colony algorithm to study MOSFET detectors. *Phys. Med. Biol.,* 54**,** 6263-6276.

Carvajal, M. A., A. Martínez-Olmos, D. P. Morales, J. A. Lopez-Villanueva, A. Lallena & A. Palma (2011) Thermal drift reduction with multiple bias current for MOSFET dosimeter. *Phys. Med. Biol.***,** 3535-3550.

Carvajal, M. A., F. Simancas, D. Guirado, M. Vilches, A. M. Lallena & A. J. Palma (2012) A Compact and Low Cost Dosimetry

System Based On MOSFET For In-Vivo Radiotherapy. *Sens. Actuator A-Phys.*, 146-152.

Carvajal, M. A., M. Vilches, D. Guirado, A. Lallena, J. Banqueri & A. J. Palma (2010) Redaout techniques for linearity and resolution improvements in MOSFET dosimeters. *Sens. Actuator A-Phys.*, 178-184.

Carvajal Rodríguez, M. A., M. S. Martínez-García, A. Martínez-Olmos, J. Banqueri & A. J. Palma López (2014) A simplified thermal model for lateral MOSFET and its application to temperature monitoring. *Semicond. Sci. Technol.,* 29.

Castellanos, M. E. (2006) Las nuevas tecnologías: necesidades y retos en radioterapia en América Latina. *Panamá Salud Publica,* 20, 143-50.

CD4007UB. Texas Instruments. (Datasheet)

Ciocca, M., V. Piazzi, R. Lazzari, A. Vavassori, A. Luini, P. Versonesi , V. Galimberti, M. Intra, A. Guido, G. Tosi, U. Veronesi & R. Orecchia (2006) Real-Time in vivo dosimetry using micro-MOSFET detectors during intraoperative electron beam radiation therapy in early-stage breast cancer. *Radiother. Oncol.,* 78, 213-216.

Consorti, R., A. Petrucci, F. Fortunato, A. Soriani, S. Marzi, G. Iaccarino, V. Landoni & M. Benassi (2005) In Vivo Dosimetry with MOSFETs : Dosimetric Characterization and First Clinical Results in Intraoperative Radiotherapy. *Int. J. Radiat. Oncol. Biol. Phys.,* 63, 952-960.

Cox, J. D. (1994). *Moss' Radiation Oncology.* M. editors.

Cheng, C.-W., M. Wolanski, Q. Zhao, L. Fanelli, A. Gautam, D. Pack & I. J. Das (2010) Dosimetric characteristics of a single use MOSFET dosimeter for in vivo dosimetry in proton therapy. *J. Med. Phys.,* 37, 4266-4273.

De las Heras González, M. (2008). Mini manuales prácticos. Radioterapia. Secondary Author. (Manual)

Dozier, C. M., D. B. Brown, R. K. Freitag & J. L. Throckmorton (1986) Use of the Subthreshold Behavior to Compare X-Ray and CO-60 Radiation-Induced Defects in MOS Transistors. *Ieee Trans. Nucl. Sci.,* 33, 1324-1329.

Edgecock, R., J. Matheson, M. Weber, E. Giulio Villani, R. Bose , A. Khan , D. R. Smith, Adil-, I. Adil-Smith & A. Gabrielli (2009) Evaluation of commercial programmable floating gate devices as radiation dosimeters. *J. Instrum.,* 4, 1-10.

Falco, M., M. D'Andrea, A. Bosco, M. Rebuzzi, E. Ponti, B. Tolu, G. Tortorelli, R. Barbarino, L. Di Murro & R. Santoni (2012) Is the in vivo dosimetry with the OneDosePlusTM system able to detect intra-fraction motion? A retrospective analysis of in vivo data from breast and prostate patients. *Radiation Oncology,* 7, 1-10.

Foty, D. P. & S. L. Titcomb (1987) Thermal effects in n-channel enhancement MOSFET's operated at cryogenic temperatures. *IEEE Trans. Electron Devices,* 34, 107-113.

Freeman, R. & A. Holmes-Siedle (1978) A Simple Model for Predicting Radiation Effects in MOS Devices. *IEEE Trans. Nucl. Sci.,* 25, 1216-1225.

Gnana Prakash, A. P., S. C. Ke & K. Siddappa (2003) High-energy radiation effects on subthreshold characteristics, transconductance and mobility of n-channel MOSFETs. *Semicond. Sci. Technol.,* 18, 1037-1042.

Gwynne, N. Semiconductor Dosimeter. (1993) GB-2263196A. (Patent)

Halvorsen, P. H. (2005) Dosimetric evaluation of a new design MOSFET in vivo dosimeter. *Med. Phys.,* 32, 110-117.

Haran, A., A. Jaksic, N. Refaeli, A. Eliyahu, D. David & J. Barak (2004) Temperature Effects and Long Term Fading of Implanted and Unimplanted Gate Oxide RADFETs. *IEEE Trans. Nucl. Sci.,* 51, 2917-2921.

Holmes-Siedle, A. (1999). REM's integrating dosimeter systme based on the radfet: an introduction. Insitution. (Report).

Holmes-Siedle, A. & L. Adams (1986) RADFET : A review of the use of metal-oxide-silicon devices as integrating dosimeters. *Int. J. Radiat. Appl. Instrum., Part C. Radiat. Phys. Chem.,* 28, 235-244.

Holmes-Siedle, A. & L. Adams. (1993). *Handbook of radiation effects.* O. U. Press. New York: Oxford Science Publications.

Holmes-Siedle, A., F. Ravotti & M. Glaser (2007) The Dosimetric Performance of RADFETs in Raditaion Test Beams. *Radiation*

Effects Data Workshop, 2007 IEEE Honolulu, HI, 47-57. (Conference Proceeding)

Hughes, R. C., D. Huffman, J. V. Snelling, T. E. Zipperian, A. J. Ricco & C. A. Kelsey (1988) Miniature radiation dosimeter for in vivo radiation measurements. *Int. J. Radiat. Oncol. Biol. Phys.,* 14, 963-967.

Ituero, P., J. L. Ayala & M. Lopez-Vallejo (2008) A Nanowatt Smart Temperature Sensor for Dynamic Thermal Management. *IEEE Sensors J.,* 8, 2036-2043.

Jaffe, G. (1929) Zur Theorie der Ionisation in Kolonnen. *Ann. Phys.,* 42, 303.

Jaksic, A., R. G., M. Pejovic, A. Mohammadzadeh, C. Sudre & W. Lane (2002) Gamma-Ray Irradiation and Post-Irradiation Responses of High Dose Range RADFETs. *IEEE Trans. Nucl. Sci.,* 49, 1356-1363.

Jaksic, A., Y. Kimoto, A. Mohammadzadeh & W. Hajdas (2005) RADFET Response to Proton Irradiation Under Different Biasin Configurations. *Radiation and its Effects on Component, RADECS*. (Conference Proceeding)

Jaksic, A., M. Pejovic, G. Ristic & S. Rakivic (1998) Latent Interface-Trap Generation in Commercial Power VDMOSFETs. *IEEE Trans. Nucl. Sci.,* 45, 1365-1371.

Johnson, G. H., W. T. Kemp, R. D. Schrimpf, K. F. Galloway, M. R. Ackermann & R. D. Pugh (1994) The effects of ionizing radiation on commercial power MOSFETs operated at cryogenic temperatures. *Ieee Trans. Nucl. Sci.,* 41, 2530-2535.

Jong-Wook, L. & K. J. Webb (2004) A temperature-dependent nonlinear analytic model for AlGaN-GaN HEMTs on SiC. *IEEE Trans. Microw. Theory Techn.,* 52, 2-9.

Kahilainen, J. Radiation Detector. (1998) US-005739541-A. (Patent)

Kelleher, A., W. Lane & L. Adams (1995) A Design Solution to increasing the sensitivity of pMOS Dosimeters: The Stacked RADFET Approach. *IEEE Trans. Nucl. Sci.,* 42, 48-51.

Kelleher, A., M. O'Sullivan, J. Ryan, B. O'Neill & W. Lane (1992) Development of the radiation sensitivity of PMOS dosimeters. *Ieee Trans. Nucl. Sci.,* 39, 342-346.

Keysight, T. The B1500 Semiconductor Device Analyzer. 17/8/2014. http://www.keysight.com/. (Web Page)

Khan, F. (1984). *The physics of Radiotherapy.* Lippincott.

Kimoto, Y., H. Koshiishi, H. Matsumoto & T. Goka (2003) Total dose orbital data by dosimeter onboard Tsubasa (MDS-1) satellite. *IEEE Trans. Nucl. Sci.,* 50, 2301-2306.

Kinhikar, R. A., P. K. Sharma, C. M. Tambe, U. M. Mahantshetty, R. Sarin, D. D. Deshpande & S. K. Shrivastava (2006) Clinical application of a OneDose MOSFET for skin dose measurements during internal mammary chain irradiation with high dose rate brachytherapy in carcinoma of the breast. *Phys. Med. Biol.,* 51, 263-268.

Kishi, T. Radiation dosimeter. (1997) *U.S. Patent Office,* US-5949075A. (Patent)

Knoll, G. F. (2000). *Radiation Detection and Measurement.* New York: John Wiley & Sons.

Knoll, M. & D. Bräunig MOS dosimeter. (1988) US-4788581. (Patent)

Kölling, A., F. Bak, P. Bergveld & E. Seevinck (1990) Design of a CMOS Temperature Sensor with Current Output. *Sens. Actuator A-Phys.*, 645-649.

Kronenberg, S. & A. Bard Radiation sensor dosimetry circuit. (1995) US-5477050A. (Patent)

Kwan, I. S., A. B. Rosenfeld, Z. Y. Qi, D. Wilkinson, M. L. F. Lerch, D. L. Cutajar, M. Safavi-Naeni, M. Butson, J. A. Bucci, Y. Chin & V. L. Perevertaylo (2008) Skin dosimetry with new MOSFET detectors. *Radiat. Meas.,* 43, 929-932.

Kwan, I. S., D. Wilkinson, D. Cutajar, M. Lerch, A. Rosenfeld, A. Howie, J. Bucci, Y. Chin & V. L. Perevertaylo (2009) The effect of rectal heterogeneity on wall dose in high dose rate brachytherapy. *Med. Phys.,* 36, 224-232.

Kyoungmin, K., P. Hyun-Min & H. Songcheol (2002) A spline large-signal FET model based on bias-dependent pulsed I-V measurement. *IEEE Trans. Microw. Theory Techn.,* 50, 2598-2603.

Lee, N. H., J. W. Cho, S. H. Kim & G. U. Youk (2000) Development of Electronic Radiaiton Dosimeter Using Commercial Power pMOSFET. *J. Nucl. Sci. Technol.,* 1, 803-807.

Li, J., X. Weisheng & Y. Youlin (2010) Accurate operation of a CMOS integrated temperature sensor. *Microelectr. J.,* 41, 897-905.

Lin, Y. S. & G. Buehler (1991) CRRES Microelectronic Test Chip. *IEEE Trans. Nucl. Sci.,* 38, 1678-1685.

Ma, T. P. & P. V. Dressendorfer. (1989). *Ionizing Radiation Effects in MOS Devices and Circuits.* New York: John Wiley & Sons.

Mackay, G. F., I. Thomson, A. Ng & N. Sultan (1997) Applications of MOSFET dosimeters on MIR and BION satellites. *IEEE Trans. Nucl. Sci.,* 44, 2048-2051.

Manic, I., Z. Pavlovic, Z. Prijic, V. Davidovic & N. Stojadinovic (2001) Analytical modelling of electrical characteristics in gamma-irradiated power VDMOS transistors. *Microelectr. J.,* 32, 485-490.

Manigandan, D., G. Bharanidharan, P. Aruna , K. Devan, D. Elangovan, V. Patil, R. Tamilarasan, S. Vasanthan & S. Ganesan (2009) Dosimetric characteristics of a MOSFET dosimeter for clinical electron beams. *Phys. Medica*, 141-147.

Martínez-García, M. S., F. Simancas, A. J. Palma, A. M. Lallena, J. Banqueri & M. A. Carvajal (2014) General purpose MOSFETs for the dosimetry of electron beams used in intra-operative radiotherapy. *Sens. Actuator A-Phys.,* 210, 175-181.

McWhorter, P. J. & P. S. Winokur (1986) Simple techn Simple technique for separating the effects of interface traps and trapped-oxide charge in metal-oxide-semiconductor transistors. *Appl. Phys. Lett.,* 48, 133-135.

Medical, A. (2014). Alliance Medical. Intelligent imaging. 26-7-2014. http://www.alliancemedical.it/. (Web Page)

Medical, B. (2004). Operator's Manual MOSFET 20. Insitution. (Report).

Meijer, G. C. M. (1986) Thermal sensors based on transistors. *Sensors Actuators,* 10, 103-125.

Metcalfe, P., A. Quinn, K. Loo, M. Lerch, M. Petasecca, J. Wong, N. Hardcastle, M. Carolan, J. McNamara, D. Cutajar, I. Fuduli, A. Espinoza, C. Porumb & A. Rosenfeld (2013) Review of four novel dosimeters developed for use in radiotherapy. *Journal of Physics: Conference Series (JPCS),* 444, 1-7.

Nurul Amin, M., R. Heaton, B. Norrlinger & M. K. Islam (2011) Small field electron beam dosimetry using MOSFET detector. *J. Appl. Clin. Med. Phys,* 12, 50-57.

O'Connell, B., A. Kelleher, W. Lane & L. Adams (1995) Stacked RADFETs for Increased Radiation Sensitivity. *Radiation and its Effects on Component , RADECS 95, Arcachon*, 481 - 486. (Conference Proceeding)

O'Sullivan, M., A. Kelleher, J. Ryan & B. L. O'Neil (1990) Temperature compensation of PMOS dosimeters. *ESA Electronic Components Conf., The Netherlands*, 81-285. (Conference Proceeding)

Ocaya, R. O. (2006) An experiment to profile the voltage, current and temperature behaviour of a P–N diode. *Eur. J. Phys.,* 27, 625-633.

Ocaya, R. O. (2013) A linear, wide-range absolute temperature thermometer using a novel p–n diode sensing technique. *Measurement,* 46, 1464-1469.

Oldman, T. R. (1999). *Ionizing Radiation Effects in MOS Oxides.* W. S. Publishing.

Onsager, L. (1938) Initial recombination of ions. *Phys. Rev.,* 54, 554.

Ortega Aramburu, X. & J. Jorba Bisbal. (1994). *Radiaciones ionizantes: Utilización y riesgos - I.* E. UPC. Barcelona: Insititut de Tècniques Energètiques.

Ortega Aramburu, X. & J. Jorba Bisbal. (1996). *Radiaciones ionizantes: Utilización y riesgos - II.* E. UPC. Barcelona: Institut Tèchniques Energètiques.

Overstraeten, R. J. V., G. J. Declerck & P. A. Muls (1975) Theory of MOS Transistor in Weak Inversion-New Method to Determine the Number of Surface States. *IEEE Trans. Electron Devices,* 5, 282-288.

Panettieri, V., M. A. Duch, N. Jornet, M. Ginjaume, P. Carrasco, A. Badal, X. Ortega & M. Ribas (2007) Monte Carlo simulation of MOSFET detectors for high-energy photon beams using the PENELOPE code. *Phys. Med. Biol.,* 52, 303-316.

Pejović, M., A. Jakšić & G. Ristić (1998) The behaviour of radiation-induced gate-oxide defects in MOSFETs during annealing at 140°C. *J. Non-Cryst. Solids,* 240, 182-192.

Pejovic, M., M. Pejovic & A. Jaksic (2012) Contribution of fixed oxide traps to sensitivity of pMOS dosimeters during gamma ray irradiation and annealing at room and elevated temperature. *Sens. Actuator A-Phys.,* 174, 85-90.

Pejovic, M., G. Ristic & A. Jaksic (1997) Formation and passivation of interface traps in irradiated n-channel power VDMOSFETs during thermal annealing. *Appl. Surf. Sci.,* 108, 141-148.

Pejovic, M. M., M. M. Pejovic & A. Jaksic (2013a) Response of pMOS Dosemeters on Gamma-Ray Irradiation During its Re-use. *Radiat. Prot. Dosim.,* 4, 394-403.

Pejovic, M. M., M. S. Pejovic, E. C. Dolicanin & D. Lazarevic (2011) Gamma-Ray Irradiation and Post-Irradiation at Room and Elevated Temperature Response of pMOS Dosimeters with Thick Gate Oxides. *Nuclear Technology & Radiation Protection,* 26, 261-265.

Pejovic, S., P. Bosnjakovic, O. Ciraj-Bjelac & M. Pejovic (2013b) Charactestic of a pMOSFET suitable for use radiotherapy. *Appl. Radiat. Isot.,* 77, 44-49.

Podgosak, E. B. (2006). *Radiation Physics for Medical Physicist.* Springer. Berlin Heidelberg.

Poki, C., C.-C. Chen, T. Chin-Chung & L. Wen-Fu (2005) A time-to-digital-converter-based CMOS smart temperature sensor. *IEEE J. Solid-State Circuits* 40, 1642-1648.

Polishchuk, V. Personal dosimeter on the base of radiation integrated circuit. (2012) US-2011260070. (Patent)

Price, R. A. (2005) Towards an optimum design of a p-MOS radiation detector for use in high-energy medical photon beams and neutron facilities: Analysis of Activation Materials. *Radiat. Prot. Dosim.,* 115, 386-390.

Price, R. A., C. Benson, M. J. Joyce, D. J. Kestell & J. Silvie (2004a) Novel Developments in the Mosfet Dosemeter for Neutron Dosimetry Applications. *Radiat. Prot. Dosim.,* 110, 283-290.

Price, R. A., C. Benson, M. J. Joyce & K. Rodgers (2004b) Development of a RadFET Linear Array for Intracavitary in vivo Dosimetry External Beam Radiotherapy and Branchytherapy. *IEEE Trans. Nucl. Sci.,* 4, 1420-1426.

Qi, Z. Y., X. W. Deng, S. M. Huang, J. Lu, M. Lerch, D. Cutajar & A. Rosenfeld (2007) Verification of the plan dosimetry for high dose rate brachytherapy using metal-oxide-semiconductor field effect transistor detectors. *Med. Phys.,* 34, 2007-2013.

Reverter, F. & J. Altet (2013) MOSFET temperature sensors for on-chip thermal testing. *Sens. Actuator A-Phys.,* 203, 234-240.

Ristic, G. (2008) Influence of ionizing radiation and hot carrier injection on metal-oxide-semiconductor transistors. *J. Phys D: App. Phys.,* 41, 1-19.

Ristic, G. (2009) Thermal and UV annealing of irradiated pMOS dosimetric transistors. *J. Phys D: App. Phys.,* 42.

Ristic, G., S. Golubovic & M. Pejovic (1993) pMOS transistors for dosimetric application. *Electron. Lett.,* 29, 1644-1646.

Ristic, G., S. Golubovic & M. Pejovic (1996) Sensitivity and fading of pMOS dosimeters with thick gate oxide. *Sens. Actuator A-Phys.,* 51, 153-158.

Ristic, G., A. Jaksic & M. Pejovic (1997) pMOS dosimetric transitors with two-layer gate oxide. *Sens. Actuator A-Phys.,* 63, 129-134.

Ristic, G., N. D. Vasovic, M. Kovacevic & A. Jaksic (2011) The sensitivity of 100 nm RADFETs with zero gate bias up to dose of 230 Gy (Si). *Nucl. Instrum. Meth. B,* 269, 2703-2708.

Rosenfeld, A. Radiation sensor and dosimeter. (2008) WO/2008/148150 (Patent)

--- (2014a) Advances in Radiation Dosimetry. *Radiation Dosimetry Workshop.* (Conference Proceeding)

--- Radiation sensor and dosimeter. (2014b) US-8742357 B2. (Patent)

Rosenfeld, A. B. (2002) MOSFET Dosimetry on Modern Radiation Oncology Modalities. *Radiat. Prot. Dosim.,* 101, 393-398.

Rosenfeld, A. B., M. L. F. Lerch, T. Kron, E. Brauer-Krisch, A. Bravin, A. Holmes-Siedle & B. J. Allen (2001) Feasibility study of online high-spatial-resolution MOSFET dosimetry in static and pulsed X-ray radiation fields. *IEEE Trans. Nucl. Sci.,* 48, 2061-2068.

Russell, K. J. Portable solid-state remote dosimeter. (2006) US-2004/0200967A1. (Patent)

Sadi, T., R. Kelsall & N. Pilgrim (2006) Simulation of Electron Transport in InGaAs/AlGaAs HEMTs Using an Electrothermal

Monte Carlo Method. *IEEE Electron Device Lett.,* 53, 1768-1774.

Sadi, T. & F. Schwierz (2010) A continuous physics-based electrothermal compact model for the study of non-linearities in III-V HMETs. *Solid-State Device Research Conference (ESSDERC)*, 432-435. (Conference Proceeding)

Sadi, T. & F. Schwierz (2013) Improved empirical non-linear compact model for studying intermodulation in HEMTs and LDMOSFETs. *Solid-State Electron.,* 81, 91-100.

Sarrabayouse, G. & S. Siskos (2008) Temperature effects and accuray of MOS radiation dosimeters. *7th WSEAS International Conference on Microelectronics, Nanoelectronics, Optoelectronics, Istanbul, Turkey.* (Conference Proceeding)

Sarrabayrouse, G. & S. Siskos (1998) Radiation dose measurement using MOSFEs. *IEEE Instrum. Meas. Mag.*, 26-34.

Sasaki, M., M. Ikeda & K. Asada (2008) A Temperature Sensor With an Inaccuracy of -1/+0.8ºC Using 90-nm 1-V CMOS for Online Thermal Monitoring of VLSI Circuits. *IEEE Trans. Semicond. Manuf.,* 21, 201-208.

Savic, Z., B. Radjenovic, M. Pejovic & N. Stojadinovic (1995) The contribution of border traps to the threshold voltage shift in pMOS dosimetric transistors. *IEEE Trans. Nucl. Sci.,* 42, 1445-1454.

Sexton, F. W. & J. R. Schwank (1985) Correlation of Radiation Effects in Transistors and Integrated Circuits. *IEEE Trans. Nucl. Sci.,* 32, 3975-3981.

Shaw, D. C., L. Lowry, K. P. MacWilliams & C. E. Barnes (1992) Observation of radiation induced changes in stress and electrical properties in MOS devices. *IEEE Trans. Nucl. Sci.,* 39, 2146-2151.

Shin, Y. H., K. W. Min, J. G. Rhee, D. H. Lee, S. H. Kim, H. S. Kim, S. D. Park, D. K. Sung & S. D. Choi (1999) Analysis of anomalous TDE data on-board the KITSAT-1. *IEEE Trans. Nucl. Sci.,* 46, 1586-1594.

Shoucair, F., W. Hwang & P. Jain (1984a) Electrical characteristics of large scale integration (LSI) MOSFETs at very high

temperatures part I: Theory. *Microelectron. Reliab.,* 24**,** 465-485.

--- (1984b) Electrical characteristics of large scale integration (LSI) MOSFETs at very high temperatures part II: Experiment. *Microelectron. Reliab.,* 24**,** 487-510.

Sicel, T. (2005). "OneDose User's Manual". Pre-production draft version , rev. P01. Sicel Technologies Inc. . Morrisville, NC.

Siebel, O. F., J. G. Pereira, M. C. Schneider & C. Galup-Montoro (2014) A MOSFET dosimeter built on an off-the-shelf component for in vivo radiotherapy applications. *Circuits and Systems (LASCAS), 2014 IEEE 5th Latin American Symposium on***,** 1-4. (Conference Proceeding)

Siliconix, V. 3N163 datasheet. Insitution. (Report).

Soli, G. A., B. R. Blaes, M. G. Buehler, K. Ray & Y. S. Lin (1992) CRRES microelectronic test chip orbital data. II. *IEEE Trans. Nucl. Sci.,* 39**,** 1840-1845.

Soubra, M., J. Cygler & G. Mackay (1994) Evaluation of a dual bias dual metal oxide-silicon semiconductor field effect transistor detector as radiation dosimeter. *Med. Phys.***,** 567-572.

Souri, K., C. Youngcheol, Y. Ponomarev & K. A. A. Makinwa (2011) A precision DTMOST-based temperature sensor. *ESSCIRC (ESSCIRC), 2011 Proceedings of the***,** 279-282. (Conference Proceeding)

Sung-Joon, K., M. Kyoung-Wook, S. Young-Hoon & S. Jong-Ho (2002) Model-data comparison of total dose experiment on KITSAT-1. *IEEE Trans. Nucl. Sci.,* 49**,** 2818-2821.

Sze, S. M. (1981). *Physics on Semiconductor Devices.* n. edn. New York: Wiley.

Szekely, V., C. Marta, Z. Kohari & M. Rencz (1997) CMOS sensors for on-line thermal monitoring of VLSI circuits. *IEEE Trans. Very Large Scale Integr. (VLSI) Syst.,* 5**,** 270-276.

Szmyrka-Grzebyk, A. & L. Lipiński (1993) Low temperature current - voltage characteristics of silicon diodes used as thermometers. *Cryogenics,* 33**,** 222-225.

Tarr, N. G. & I. Thomson Method of monitoring radiation using a floating gate field effect transistor dosimeter, and dosimeter for use therein. (2001) US 6172368B1. (Patent)

Teimouri Sichani, B. & M. Sohrabpour (2004) Monte Carlo source model for photon beam radiotherapy: photon source characteristics. *Med. Phys.,* 31**,** 3106.

Thomson, I. Direct reading dosimeter (Thomson&Nielsen). (1984) US-4484076. (Patent)

--- Dosimeter (Thomson&Nielsen). (1987) US-4678916. (Patent)

Thomson, I., A. Hartshorn, M. Brown, L. Adams, R. Nickson, A. Ng, T. Cousins & T. Jones (1998) Dose-Depth and SEU Monitors for the STR V-1c Satellite. *IEEE Trans. Nucl. Sci.,* 45**,** 2765-2769.

Thomson, I., G. F. Mackay & M. P. Brown Direct Reading Dosimeter (Thomson&Nielsen). (1991) EP-0471957A2. (Patent)

Tsividis, Y. (1987). *Operation and Modelling of the MOS Transistor* n. edn. Singapore: McGraw-Hill.

Ueno, K., T. Asai & Y. Amemiya (2011) Low-power temperature-to-frequency converter consisting of subthreshold CMOS circuits for integrated smart temperature sensors. *Sens. Actuator A-Phys.,* 165**,** 132-137.

Vettese, F., C. Donichak & P. Bourgeault. (1996). Assessment of a new p-Mosfet usable as a dose rate insensitive gamma dose sensor. Insitution. (Report).

Vötsch. (2014). VCL4006 Climate Chamber. 14/8/2014. http://www.v-it.com/. (Web Page)

Wang, R. L., C. W. Yu, C. Yu, T. H. Liu, C. M. Yeh, C. F. Lin, H. H. Tsai & Y. Z. Juang (2012) Temperature sensor using BJT-MOSFET pair. *Electron. Lett.,* 48**,** 503-504.

Willet, C. G., L. L. Gunderson, P. M. Busse, J. E. Tepper & F. A. Calvo. (1999). *Intraoperative irradiation.* Towota, New Jersey: Humana Press.

Yilmaz, E., I. Doğan & R. Turan (2008) Use of Al2O3 layer as a dielectric in MOS based radiation sensors fabricated on a Si substrate. *Nucl. Instrum. Methods in Physics Research Section B: Beam Interactions with Materials and Atoms,* 266**,** 4896-4898.

Yilmaz, E., B. Kaleli & R. Turan (2007) A systematic study on MOS type radiation sensors. *Nucl. Instrum. Methods in Physics*

Research Section B: Beam Interactions with Materials and Atoms, 264, 287-292.

Yilmaz, E. & R. Turan (2008) Temperature cycling of MOS-based radiation sensors. *Sens. Actuator A-Phys.,* 141, 1-5.

ZVP3306. Diodes Incorporated. (Datasheet)

ZVP4525. Diodes Incorporated. (Datasheet)